The Dynamics of Discs and Stars in Multiple Systems

Krisada Rawiraswattana

Department of Physics & Astronomy
The University of Sheffield

A dissertation submitted in candidature for the degree of Doctor of Philosophy at the University of Sheffield

October 2012

Declaration

I declare that no part of this thesis has been accepted, or is currently being submitted, for any degree or diploma or certificate or any other qualification in this University or elsewhere. This thesis is the result of my own work unless otherwise stated.

Chapter 4 has been based on Rawiraswattana et al. 2012. *MNRAS* **419**, 2025–2030.

Acknowledgements

I would like to thank my supervisor Simon Goodwin for his invaluable guidance, fantastic ideas, and infinite patience over the past four incredible years. I am deeply indebted to him for accepting me as his student.

Many thanks to David Hubber for his help with SPH and very useful suggestions for this thesis, especially in Chapter 6.

Many thanks must also go to Paul Kerry for all his computing support.

I would like to thank all past and present members of the astronomy group for making my time in Sheffield so enjoyable. I feel lucky to be part of the group.

Thanks to Prince of Songkla University for its financial support.

Special thanks to my family in Thailand for always supporting me.

Summary

Young stars have discs and are usually found in binary or multiple systems. In this thesis, we are interested in (a) the dynamical evolution of young stars in a multiple system and (b) the evolution of a circumprimary disc in a misaligned binary system.

In a young multiple star system, a close encounter between two stars may result in either an ejection of the least massive star or a collision. We perform N-body simulations to investigate the frequencies of both ejections and collisions in young coplanar triple systems. We find that the chance of a collision among the members is generally high, at least a few per cent in most configurations. From this finding, it is possible that collisions among young stars are responsible for some uncommon features found in young star systems such as an apparent non-coevality of members.

The evolution of a circumprimary disc in a misaligned binary system is, in several ways, affected by the companion. Dynamically, the disc is tilted by tidal effects from the companion. We perform SPH simulations to study the tilting process of the disc. We find that the disc precesses and, in most cases, is brought towards alignment with the binary orbit. The key findings include: (a) a significantly misaligned disc may not be aligned with the binary orbit within an estimated disc lifetime ($\sim 10^6$yr) and (b) the dispersal timescale of a misaligned disc could be of order the precession period of the disc. These findings would constrain the formation of planets in misaligned binary systems. For an alignment process that is driven by an alignment torque(s), our semi-analytic approach shows that the torque is mainly proportional to the change in the binary semi-major axis. In this work, we suggest a possible formation scenario for a spin-orbit misaligned planetary system around a single star that the system could form from a disc in a misaligned binary system which is later disrupted by dynamical interactions with other star in the cluster.

Additionally, we also perform SPH simulations to study several properties of low-mass discs. We investigate the influence of resolution, temperature structure, and artificial viscosity on the stability of those low-mass discs. We find that our low-mass discs are all stable against gravitational instabilities.

Contents

List of Figures

List of Tables

Chapter 1

Introduction

Understanding star formation is a fundamental problem in astronomy. Not only does star formation tell us how individual stars form, it also tells us about the formation of multiple star systems and planetary systems. Theoretical studies of star formation are based on the principal idea that stars form out of a collapsing cloud of gas and dust. So far, this idea agrees rather well with observations. With advances in computing power, numerical studies of star formation become increasingly powerful in enabling us to model the star formation process. The influence of several parameters can be explored in detail. However, the formation process involves much complicated physics that has not been fully understood. Modelling star formation with correct physics is thus an extremely difficult task.

Observations have found many interesting features of stars. In this work, we focus on two coexisting features. The first feature is that stars are typically found in multiple systems. The multiplicity of stars implies that most stars may originally form as multiple systems and later dissolve via close encounters. Although the dominant mode of close encounters is disruption, there is a non-zero chance for the encounters to end up with a collision. The chances of stellar collisions could be higher when the stars are younger, as younger stars have larger radii. Collisions among young stars are interesting as they will affect the evolution of the objects.

The second interesting feature of stars is that young stars have discs. Circumstellar discs are found in stages before the central stars start to burn hydrogen in their cores and become main-sequence stars. That many main-sequence stars including the Sun are found with orbiting planets suggests that planets somehow form from the progenitor discs. Also, in young multiple systems where discs are commonly found, the evolution of a disc would be affected in many ways by the stellar members.

From those two interesting points, we ask two questions: *(1) How frequently do collisions occur during close encounters among young stars in multiple systems?* and *(2) How do circumstellar discs surrounding the components in binary stars evolve, especially in systems where the orbital plane of the binary is not the same as that of the disc(s)?* The answer to the first question would tell us how likely that stellar collisions may be an explanation for some stars which are observed with uncommon properties, for example, infrared companions found in some young binaries. We find out this answer in Chapter 4. For the second question, although it has been known that discs in inclined binary systems are tilted towards alignment, the numerical investigations are still not thorough. We thus perform simulations to explore the mechanism in more detail in Chapter 6.

In this chapter, we provide a brief review of the star formation process from molecular clouds to pre-main-sequence stars in Section 1.1. The observations, formation mechanisms, and evolution of binary stars are given in Section 1.2. In Section 1.3, we talk about properties and evolution of circumstellar discs. Planet formation mechanisms are presented in Section 1.4. Finally, we give an overview of this thesis in Section 1.5.

1.1 Star formation

The Milky Way Galaxy is estimated to have a total mass of $\sim 10^{12} M_{\odot}$ (e.g. McMillan 2011). Most of the mass is in the form of dark matter while stars and the interstellar medium (gas and dust), which are observable, comprise only $\sim 10^{11} M_{\odot}$. Most stars are low-mass M-dwarfs with masses $\sim 0.1 - 0.5 M_{\odot}$ (e.g. Lada 2006). Most stars are also found as binaries or multiples, especially in young populations (see Section 1.2.1). It is believed that stars form as a product of collapsing gas clouds consisting mostly of molecular hydrogen (H_2). Young stars are usually found in dense parts of giant molecular clouds (GMCs). GMCs have typical diameters of a few to several tens of parsecs and masses of $\sim 10^5 - 10^6 M_{\odot}$. The density structures inside GMCs are irregular (preferentially filamentary) and hierarchical (e.g. Williams et al. 2000; Könyves et al. 2010; André et al. 2010; Molinari et al. 2010), as shown in Figure 1.1. A giant molecular *cloud* may consist of several *clumps* of densities $\sim 10^3 - 10^4\,\mathrm{cm}^{-3}$[†], or

[†]For convenience, extremely low density gas is usually discussed in terms of the *number density* (n, the number of atoms or molecules per unit volume) rather than the *mass density* (ρ, mass per unit volume). The relation between the two is given by $\rho = \bar{\mu} m_{\mathrm{H}} n$, where $\bar{\mu}$ is the mean molecular weight ($\bar{\mu} \simeq 2.35$ for a cloud with $\sim 70\%$ H_2 and $\sim 30\%$ other heavier elements, see Section 5.2.4) and $m_{\mathrm{H}} \simeq 1.67 \times 10^{-24}$g is the hydrogen mass. That is, for example, $n = 10^4 \mathrm{cm}^{-3}$ would correspond to $\rho \simeq 3.9 \times 10^{-20} \mathrm{g/cm}^3$.

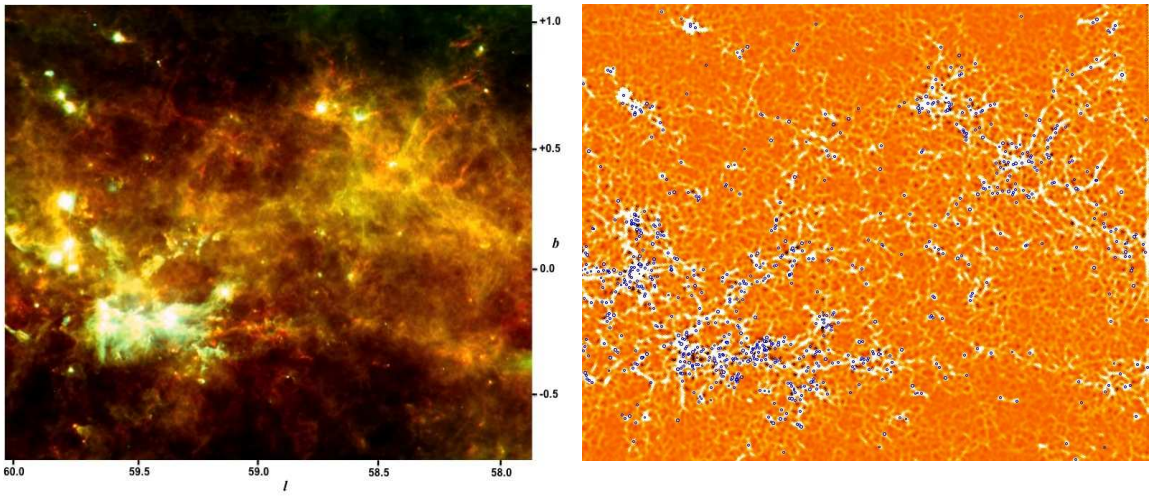

Figure 1.1 A molecular cloud complex in a $2°\times2°$ field centred at $[l, b] \simeq [59°, 0°]$ (galactic coordinates). Showing on the left figure is the three-colour image of the cloud while the right figure is the colour-enhancement version of the same image revealing the filamentary structure of the cloud. The blue dots on the right image locate the compact sources detected at wavelength of 250μm. The images are taken from the Hi-GAL survey which is the *Herschel* program to map the inner Galactic plane of the Milky Way.

roughly, with masses of a few hundred $M_\odot$ and $\sim$1pc in extent. Each clump may consist of several prestellar *cores* of even higher densities, i.e. with masses of $\sim 1M_\odot$ in less than $\sim$0.2pc across (Ward-Thompson et al. 2007). Some of the prestellar cores may be dense enough to collapse gravitationally to form a single or multiple star system.

1.1.1 Formation of prestellar cores

Prestellar cores are dense stellar-mass fragments in molecular clumps. They are gravitationally bound and tend to collapse to form stellar objects. Despite consisting mostly of H_2, the molecule cannot be detected directly as it has no excitable state in environments with temperatures as low as 10K. Instead, the abundance of H_2 can be traced by other coexisting molecules such as CO and NH_3 (e.g. Evans 1999).

Prestellar cores are observed mostly in submillimetre (submm) to millimetre wavelengths of dust continuum emission and some molecular tracers of high density such as NH_3 (e.g. Benson and Myers 1989; Ward-Thompson et al. 1994). Fragments that are similar to prestellar cores but show no significant tendency to collapse are starless (or pre-protostellar) cores (e.g. Gregersen and Evans 2000). Figure 1.2 shows a submm dust continuum map of NGC 2068 where evolved prestellar cores containing young stellar objects (YSOs, marked by star symbols) and starless cores (marked by cross

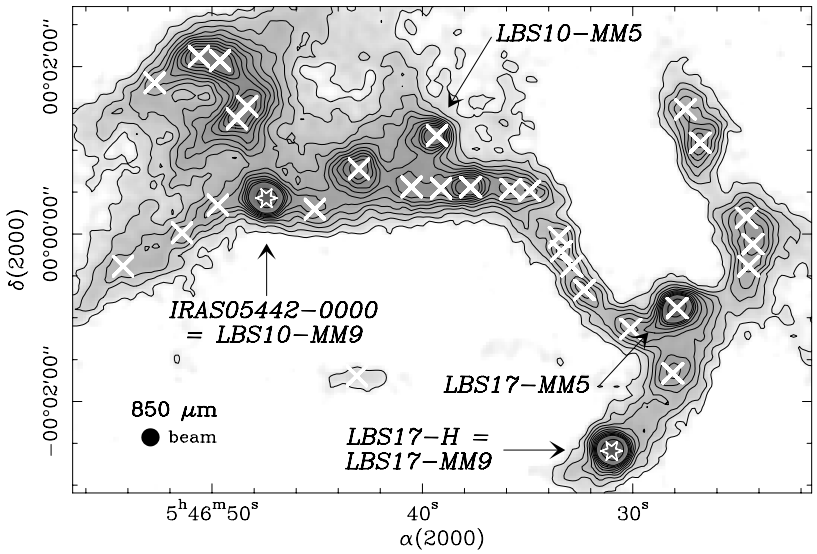

Figure 1.2 A submm dust continuum map of NGC 2068 showing a number of evolved prestellar cores containing YSOs (marked by star symbols) and starless cores (marked by cross symbols). The image is taken from Motte et al. (2001).

symbols) are observed (Motte et al. 2001). In addition, although starless cores are likely to be transient, some of them might be able to evolve further to the prestellar core stage.

How prestellar cores actually form or fragment out of a molecular cloud is still unknown. Along with improvements in observations, two major models have been proposed: (a) the standard model and (b) the turbulent fragmentation model. In the standard model of star formation suggested by Shu et al. (1987), prestellar cores are slowly condensed out of a gas cloud by the interplay between gravity and interstellar magnetic fields. The magnetic fields play a major role in preventing local contractions in the cloud which is considered as weakly ionized (containing a small fraction of ions and electrons). Charged particles in the cloud can be tied to the magnetic field lines, causing difficulty to the neutral gas particles in the cloud to flow through. This process is known as *ambipolar diffusion* (e.g. Mestel and Spitzer 1956). The model approximates the star formation timescale to be from a few to tens of Myr depending on the strength of the magnetic fields. However, this timescale does not seem to agree with observational evidence obtained over the past two decades. A survey by Lee and Myers (1999), for example, suggests that a typical lifetime of starless cores of $\sim 0.3 - 1.6$Myr, much shorter than that predicted by the model by a factor of $2 - 44$. From other observations, the star formation timescales seem to be rather short, i.e. within a few crossing times of the clouds, implying that mechanisms to delay the

gravitational collapse may not be required (Elmegreen 2000). Nevertheless, it is still debated if the star formation process is slow (Tan et al. 2006; Krumholz and Tan 2007).

In contrast to the standard model, the turbulent fragmentation model offers a shorter timescale by suggesting that prestellar cores are formed as a consequence of shocks generated by supersonic turbulence in a molecular cloud (e.g. Padoan and Nordlund 2002; Ballesteros-Paredes et al. 2007; Hennebelle and Chabrier 2008). In a typical molecular cloud where the density is extremely low ($\sim 10^2 - 10^3\,\mathrm{cm}^{-3}$), the velocity dispersion (σ, in km/s) is found to be supersonic and scales with the size of the cloud (L, in pc) as a power law function: $\sigma \propto L^{\beta}$, where $\beta \sim 0.5$ (Larson 1981). In such a situation, supersonic turbulence has a major role in creating shock-compression regions while supporting the whole cloud against monolithic gravitational collapse. Once dense regions have been created from shocks, the velocity dispersions in those regions become subsonic, allowing the condensation of prestellar cores to occur. This model suggests a star formation timescale to be less than a few Myr.

1.1.2 Prestellar evolution of low-mass stars

A prestellar core may collapse and fragment to form one or several stars, depending on parameters such as the core mass, density structure, and turbulence (Goodwin et al. 2004a,b; Delgado-Donate et al. 2004; Walch et al. 2010). To be able to collapse in the first place, the self-gravity of the core must overcome at least the thermal pressure. In terms of mass, a threshold for the core to collapse is generally given by the Jeans mass

$$M_{\mathrm{Jeans}} \simeq \frac{6c_{\mathrm{s}}^3}{G^{3/2}\rho^{1/2}}, \tag{1.1}$$

where G is the gravitational constant, c_{s} the sound speed, and ρ the average density of the core. The sound speed represents the temperature of the gas as

$$c_{\mathrm{s}} = \left(\frac{\gamma k_{\mathrm{B}} T}{\bar{\mu} m_{\mathrm{H}}}\right)^{1/2}, \tag{1.2}$$

where γ is the ratio of specific heats, k_{B} is Boltzmann's constant, T is the temperature, $\bar{\mu}$ the mean molecular weight, and m_{H} is the hydrogen mass. A prestellar core is able to collapse if its mass is greater than the Jeans mass.

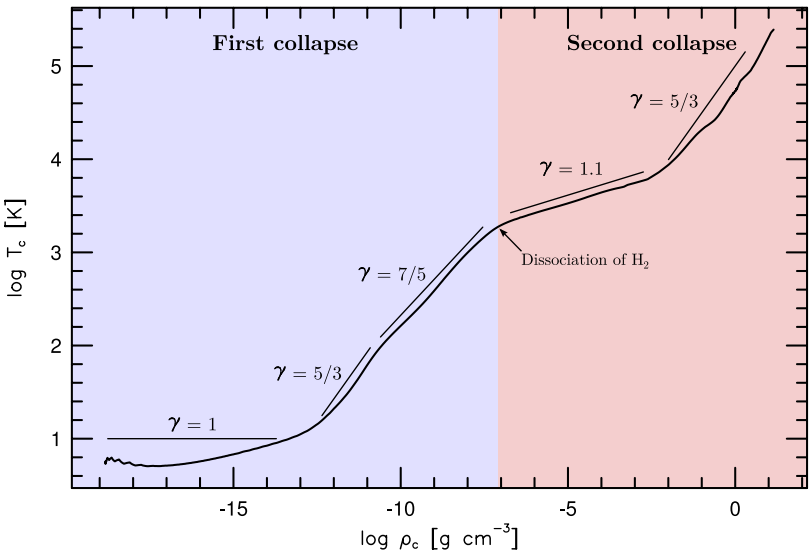

Figure 1.3 Plotting the change of temperature T_c against density ρ_c at the centre of a collapsing cloud core simulated by Masunaga and Inutsuka (2000). The collapse is divided into the *first collapse* and *second collapse* phases, corresponding to the *first core* and the *second core*, respectively. The two phases are separated by the onset of molecular hydrogen dissociation at $T_c \sim 2000$K. Also depicted along the curve is the *effective* ratio of specific heats γ, i.e. the approximate slope of each segment is $\gamma - 1$.

To illustrate the thermal evolution of the central core during collapse, let us consider the simulation of a collapsing cloud core performed by Masunaga and Inutsuka (2000). Figure 1.3 shows a plot between the temperature T_c and density ρ_c at the centre of the core. Changes in the temperature according to density can be approximately described by the equation of state $T_c \propto \rho_c^{\gamma-1}$, i.e. $\gamma - 1$ is approximately the slope of the curve in Figure 1.3. At the early stage of collapse, a prestellar core is optically thin with densities as low as $\sim 10^{-19}\,\mathrm{g/cm^3}$. Compressional heat from contraction can be efficiently removed by the thermal coupling of gas and dust. This maintains the temperature of the core to be approximately constant at ~ 10K. During this isothermal stage, the ratio of specific heats is effectively unity ($\gamma = 1$). The Jeans mass decreases as the density increases. The timescale for a prestellar core to collapse to stellar densities is given by the free-fall time:

$$t_{\mathrm{ff}} = \left(\frac{3\pi}{32 G \rho_\circ}\right)^{1/2}. \tag{1.3}$$

When the density of the central core reaches a value of $\sim 10^{-13}\,\mathrm{g/cm^3}$, the core becomes opaque, reducing the efficiency of cooling by dust (Larson 1969; Masunaga et al. 1998; Masunaga and Inutsuka 2000). As a consequence, the temperature (T_c) at

the central core starts to increase significantly. The state of gas begins to change from isothermal to adiabatic. In early adiabatic phase where the central core temperature is below ~ 100K (see the second slope in Figure 1.3), the molecular hydrogen still behaves like a monatomic gas with $\gamma = 5/3$, as the rotational state of the gas has not yet been excited. During this phase, the decreasing Jeans mass makes a turning point with a minimum value of $M_{\rm min} \sim 10^{-2} M_{\odot}$. Fragmentation may be encouraged to occur in a core whose mass is much greater than $M_{\rm min}$. Once the rotational state is excited, the gas behaves as a diatomic gas with $\gamma = 7/5$ (the third slope in Figure 1.3). The Jeans mass increases as the density increases, reducing the chances of core fragmentation. Suppression of the fragmentation during this phase is known as the opacity limit for fragmentation (Low and Lynden-Bell 1976).

So far, the core has undergone the *first collapse* phase to form the *first core* (see Figure 1.3). The adiabatic collapse (with $\gamma = 7/5$) proceeds rather slowly until the central temperature reaches ~ 2000K where the dissociation of molecular hydrogen begins. The dissociation process absorbs energy and enhances the *second collapse*. The core is then called the *second core* or *protostar*, which is enshrouded by an optically thick envelope of gas and dust. The ratio of specific heats in this phase is $\gamma = 1.1$ (the fourth slope in Figure 1.3); the collapse is nearly isothermal. The protostar then continues to evolve to a pre-main sequence star.

From observations, the evolutionary stages of young low-mass stars may be classified by the spectral features of the objects in infrared (IR) wavelengths. These features indicate the evolving characteristics of the disc and envelope surrounding young stars. Four major *Classes* (from Class 0 to Class III) are presented to distinguish those stages. Class I-III are defined by the values of the spectral index $\alpha_{\rm IR}$ obtained from spectral energy distributions (SEDs) of the stars. An SED of a young star is a log-log plot of the observed flux (λF_{λ}) against the observed wavelengths (λ), as shown in Figure 1.4 for the DL Tau system. The spectral index is the slope of the SED measured in the mid-IR wavelengths ($2 \lesssim \lambda \lesssim 100 \mu$m) where the SED is approximately linear, i.e. $\log_{10}(\lambda F_{\lambda}) \propto \alpha_{\rm IR} \log_{10} \lambda$. The stages from Class I to III were introduced by Lada (1987) while Class 0 was introduced later by Andre et al. (1993) to include younger stellar objects that are very bright in submm wavelengths. In addition to the main classification, Greene et al. (1994) introduced an intermediate stage separating Class I and Class II called *flat spectrum*. The sketch of an SED for each stage is illustrated in Figure 1.5 and the details are described as follows.

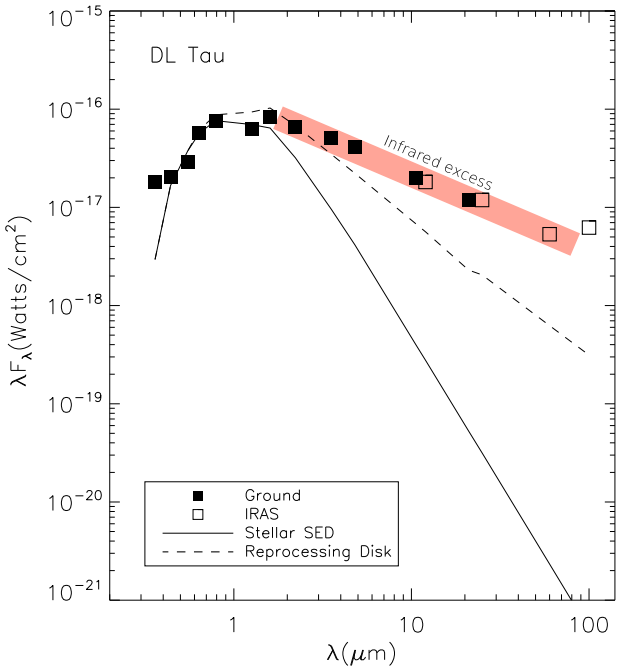

Figure 1.4 Spectral energy distribution (SED) of DL Tau. The SED plots the flux (λF_λ) against wavelength (λ). The spectral index ($\alpha_{\rm IR}$) is the slope of the SED in the mid-IR wavelengths shown as the red shaded area. The solid curve shows the black body fit of the central star. The dashed curve shows an SED predicted by the flat disc model (see Section 1.3). The image is taken and modified from Kundurthy et al. (2006).

Class 0. The earliest stage of YSOs where the central protostar is dense and hot but still embedded in its optically very thick envelope. Reprocessing of radiation from the centre by the dusty envelope makes Class 0 sources very bright in submm wavelengths, corresponding to a bolometric temperature of $T_{\rm bol} < 80$K. During this stage, material from the more massive envelope keeps falling onto the less massive protostar at the centre. Strong bipolar outflows are another feature observed in Class 0 sources more frequently than in Class I sources (e.g. Bontemps et al. 1996). The lifetime of the Class 0 stage is less than a few times 10^5yr (e.g. Evans et al. 2009; Enoch et al. 2009).

Class I. The intrinsic angular momentum of the core plays its role in building up a rotational plane of material, i.e. a disc. As more material from the envelope is accreted onto the disc, the envelope becomes optically thin to far-IR wavelengths, giving a positive spectral index (measured in the mid-IR) of $\alpha_{\rm IR} > 0.3$. This stage may last up to $\sim 10^6$yr. During this phase, it is possible for some systems that the rate of mass infalling from the envelope onto the disc may be higher than that of

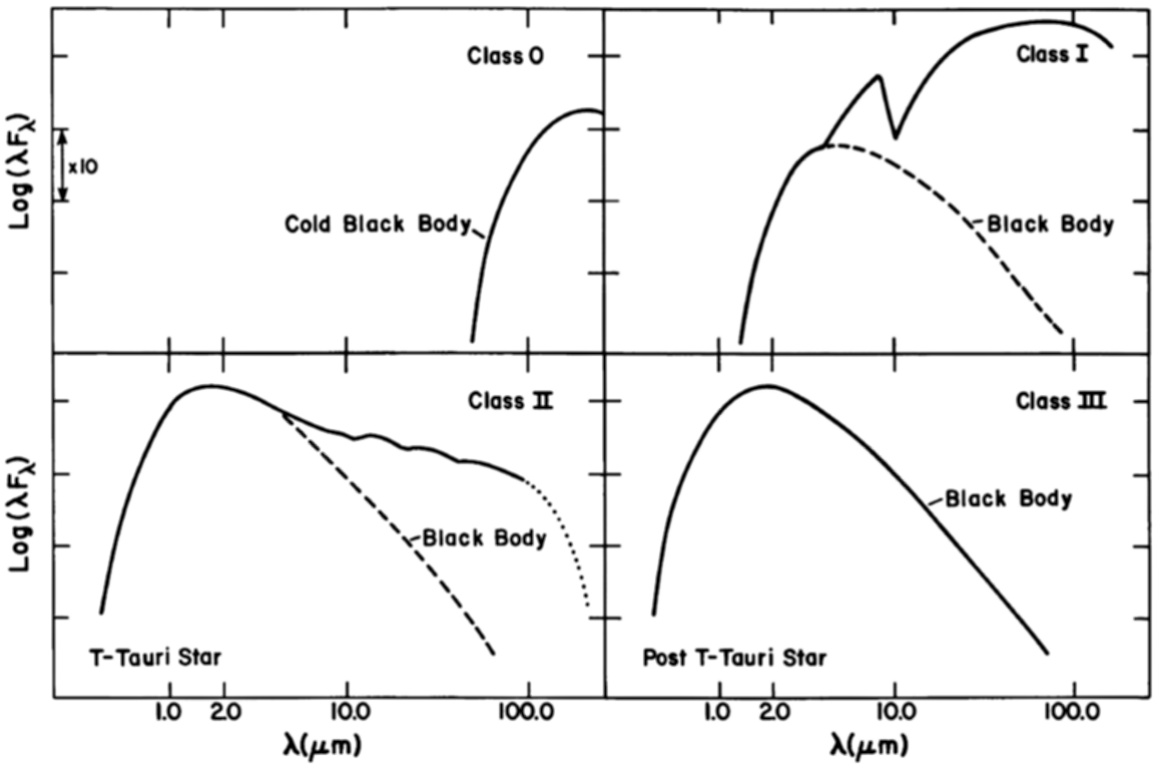

Figure 1.5 Spectral energy distributions (SEDs) of young stellar objects in different evolutionary stages. Heavily embedded Class 0 sources have SEDs peaking in the submm wavelengths (upper left subfigure). Class I sources show a large amount of IR excess (the solid line above the dashed line in the upper right subfigure). The spectral index (or slope) $\alpha_{\rm IR}$ of the excess in the mid-IR wavelengths ($2 \lesssim \lambda \lesssim 100\mu$m) is positive in this stage. Class II and III sources have the peak of the central young star shifting towards the optical (lower left and lower right subfigures). The spectral index of Class III sources is more negative than that of Class II as the amount of IR excess is much lesser or almost disappeared. The image is adapted from Lada (1987).

the mass accreting onto the central star. The disc becomes heavy and would need to find a way to maintain the stability, probably, by occasionally dumping some amount of the excess mass onto the star. This may cause a sequence of eruptive changes in the brightness of the central star. The stellar brightness may increase rapidly by a few orders of magnitude within a short period of time from $\sim$1 to a few years; it may decrease slowly afterwards within a period of time from several years to several decades. Class I sources that exhibit this eruptive phenomenon are classified as FU Orionis objects. A lightcurve example of FU Orionis objects (V1057 Cyg) is shown in Figure 1.6.

Flat spectrum. This stage is intermediate between Class I and Class II. Flat-spectrum sources begin to be optically visible while still exhibiting a large amount of IR excess, which flattens the SED profile in the mid-IR wavelengths and provides

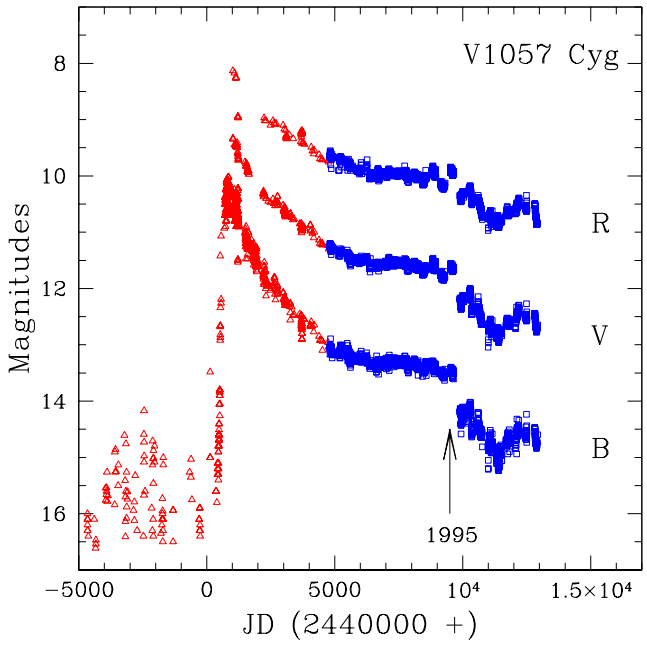

Figure 1.6 Lightcurves in different wavebands of V1057 Cyg showing an abrupt increase of the brightness, followed by the slow decline. Symbols and colours denote the data compiled different sources of data. The image is taken from Clarke et al. (2005).

the spectral index $-0.3 < \alpha_{\rm IR} < 0.3$. The excess may be produced from the remaining envelope or comes from a heavily extincted companion in the case of binaries.

Class II. Young stars of Class II are optically visible as most of the envelope mass has been accreted by the disc. The spectral index of Class II sources lies in the range $-1.6 < \alpha_{\rm IR} < -0.3$. Radiation from the central star is still reprocessed to the mid- to far-IR by dust in the disc. Class II sources are also known as Classical T Tauri stars (CTTSs). CCTSs have protoplanetary discs out of which planets are thought to be formed. This stage may last for a few times 10^6yr.

Class III. In this stage, most of the disc mass has been accreted onto the central star and dispersed by some mechanisms discussed in Section 1.3.6. The spectral index $\alpha_{\rm IR} < -1.6$. The disc material may also be depleted by planets that form in the disc. Class III sources are bright in the optical wavelengths with a small amount of IR excess of the remaining (or debris) disc. The objects of this stage are also known as Weak-lined T Tauri stars (WTTSs). A PMS star may take a few times 10^7yr to become a main-sequence (MS) or hydrogen-burning star.

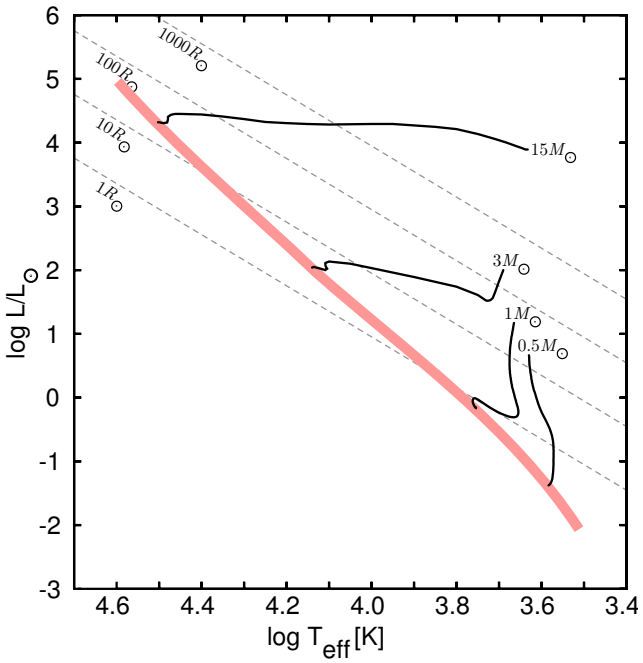

Figure 1.7 Pre-main-sequence evolutionary tracks on the Hertzsprung-Russell diagram. The main sequence is shown as the thick red line. The dashed lines mark the stages of equal radius. The image is adapted from Yorke and Sonnhalter (2002).

From a theoretical point of view, pre-main sequence evolution is usually described by evolutionary tracks on the Hertzsprung-Russell diagram shown in Figure 1.7. The key parameter to determine the evolution of a young star is the stellar mass, i.e. the higher the mass the faster the evolution toward the main sequence (the red stripe in Figure 1.7). For example, a star with mass $15M_{\odot}$ (see Figure 1.7) would spend only 0.062×10^{6}yr evolving towards the main sequence while a star with mass $0.5M_{\odot}$ would take 155×10^{6}yr (e.g. Iben 1965). The PMS tracks shown in Figure 1.7 begin at the points where the contracting protostars are close to the hydrostatic equilibrium (slow contraction). In low- to intermediate-mass stars (masses less than a few $M_{\odot}$), the contraction continues with an approximately constant surface temperature; the luminosity of stars thus decreases with the decreasing radius. The evolutionary curve during this phase is nearly vertical and is known as the *Hayashi track* (Hayashi 1961, 1966). Stars with masses below $\sim0.5M_{\odot}$ continue their slow contraction along the Hayashi track until reaching the main sequence. For stars with higher masses, the evolution along the Hayashi track ends once the temperature is high enough for radiative transport to dominate the convective. The contraction continues on the nearly horizontal path, called the *Henyey track* (Henyey et al. 1955), towards the main sequence (see Figure 1.7 for stars with masses $>0.5M_{\odot}$).

1.2 Binary star systems

Binary and multiple star systems are very important in the theory of star formation. Their existence implies that the majority of stars may originally form in multiples before dynamically dissolving into single stars and binaries (Goodwin and Kroupa 2005; Goodwin et al. 2007). Typically, binary stars are of the most interest as they outnumber the other (higher-order) multiple systems. In this section, we summarize the general statistics of binaries and briefly review the mechanisms by which binaries are formed.

1.2.1 Observations

Observations of binary and multiple star systems are usually focused in the Galactic field and nearby star-forming regions. Studying differences in binary statistics among these environments may help to shape the theory of star formation (Goodwin 2010).

Binaries in the Galactic field are sampled from solar neighbourhood stars within $\sim 20-22$pc. The surveys of binaries in the field are thus more complete than those in other regions faraway. The major surveys of the field stars have been conducted by Duquennoy and Mayor (1991) for G-dwarf stars with masses $0.84 \leq M \leq 1.2 M_{\odot}$; Metchev and Hillenbrand (2009) and Raghavan et al. (2010) for solar-type stars of spectral type from F6 to K3; Mayor et al. (1992) for K-dwarf stars with masses $0.47 \leq M \leq 0.84 M_{\odot}$; Fischer and Marcy (1992) for M-dwarf stars with masses $0.08 \leq M \leq 0.47 M_{\odot}$; and Bergfors et al. (2010) for southern M-dwarf stars (M0 − M6) within 52pc of the Sun. In general, the abundance of multiple systems from a survey can be indicated by the multiplicity fraction

$$f_{\rm mult} = \frac{B + T + Q + ...}{S + B + T + Q + ...}, \tag{1.4}$$

where S, B, T, Q, etc. are the number of single, binary, triple, quadruple, etc. systems. Those field surveys suggest $f_{\rm mult} \sim 0.57$ for G-dwarfs, ~ 0.45 for K-dwarfs, and ~ 0.42 for M-dwarfs; that is, roughly a half of stars are found in multiple systems.

Other binary parameters from those surveys are the distributions of mass ratio ($q = M_2/M_1$, where $M_2 \leq M_1$) and separation. For G-dwarf stars, the mass ratio distribution peaks at $q = 0.2$ (Duquennoy and Mayor 1991), while stars of lower-mass types have rather flat distribution profiles (see references above). The separation distribution is found to be peaking at ~ 30AU, corresponding to a period of ~ 164yr (or $\sim 10^{4.8}$d) for a binary star with total mass of $\sim 1 M_{\odot}$.

Unlike the Galactic field, star-forming regions contain mostly PMS stars. Many star-forming regions have been surveyed over the last few decades: for example, Taurus (e.g. Leinert et al. 1993; Simon et al. 1995; Köhler and Leinert 1998; Kraus et al. 2011); Orion (e.g. Prosser et al. 1994; Padgett et al. 1997; Simon et al. 1999; Scally et al. 1999; Reipurth et al. 2007); and Ophiuchus (e.g. Simon et al. 1995; Barsony et al. 2003; Duchêne et al. 2004; Ratzka et al. 2005). Star-forming regions usually have a multiplicity fraction higher than (or at least similar to) that of the field, depending on the number density of stars in the regions, i.e. the lower the number density the higher the multiplicity fraction (Mathieu 1994; Patience et al. 2002; Goodwin 2010; King et al. 2012). In low-density star-forming regions such as Taurus, for example, the multiplicity fraction of PMS stars in the separation range $18.2 \leq a \leq 1820$AU is roughly a factor of two higher than that of MS stars in the field. Lower multiplicity fractions are found in higher-density clusters such as Orion (e.g. Petr et al. 1998; Köhler et al. 2006; Reipurth et al. 2007) and IC348 (Duchêne et al. 1999). Combining the observations from several star-forming regions suggests that young binaries also have a rather wider separation (~ 100AU) than stars in the field (e.g. Mathieu 1994).

1.2.2 Formation mechanisms

Currently, binary stars are thought to be formed by *core* and/or *disc fragmentation* during the early adiabatic collapse phase (e.g. Tohline 2002; Goodwin et al. 2007). Dating back to the time of low computing power, theories of binary star formation include *fission* and *capture*. These mechanisms are now out of favour as they are ruled out by modern simulations and by the extensive range of binaries that they are unable to explain. Nevertheless, we present all the mechanisms here for completeness.

Fission

Fission mechanism suggests that a binary system may be created from a rapidly rotating protostar that breaks into two parts at some critical point. Although this idea has a long history back to the 19th century, modern simulations (e.g. Durisen et al. 1986; Williams and Tohline 1988; Tohline and Durisen 2001, and references therein) have shown that a rapidly rotating protostar does not split into two parts but instead forms a bar-like structure as a consequence of angular momentum transport. The protostar remains stable. Fission mechanism, if does occur, may only produce close binaries according to the sizes of protostars. This clearly disagrees with the observations.

Capture

Capture mechanism pairs up two independently formed single stars to create a binary system by means of dynamical encounters. For this mechanism to work, however, the presence of a third object is required in order to remove the excess energy and angular momentum between the two stars which are usually unbound (e.g. Clarke 1992). For this reason, the possibility of the mechanism depends on the likelihood of a three-body encounter which, in typical environments, is extremely low. The dynamical capture mechanism is thus clearly unable to produce the large binary fractions in both the field and cluster environments; not to mention the population of close and low-eccentricity binaries that are very unlikely to be formed by the mechanism. Furthermore, the age independence of the binary components suggested by the mechanism seems not to agree with observations suggesting that stars in binaries are of the same age (e.g. White and Ghez 2001).

An alternative capture scenario with the assistance of protostellar discs has also been presented for pairing up young stellar objects. The mechanism operates in a close encounter between a young star with disc and a passing star with an approximately parabolic orbit. In a relatively wide-orbit encounter where the periastron radius is longer than the disc radius, tide occurring on the disc may slightly dissipate the excess orbital kinetic energy, changing the orbit from parabolic to highly eccentric. If the periastron radius is shorter than the disc radius, the passing star can plough through the disc, dissipating a larger amount of the excess kinetic energy. In some situations such as in retrograde encounters (Heller 1995) and in a massive disc surrounding a massive star (Moeckel and Bally 2007), the efficiency of the energy dissipation can be even higher; the passing star may be effectively captured. The possibility of the disc-capture process could be high in young star clusters where the members still have large discs and the encounter rates are high. Nevertheless, the binary formation rate from this mechanism has been shown to be very low even in very dense cluster environments (Clarke and Pringle 1991). Furthermore, it is clear that capture mechanism may only be able to produce very wide binary population since typical discs are capable of dissipating only a small fraction of the excess orbital energy; the deviation of the orbital eccentricity after encounter is rather small (e.g. Forgan and Rice 2009). With more support from some numerical works such as Boffin et al. (1998) and Kroupa and Burkert (2001), the disc capture mechanism is by no means a major mode of binary star formation.

Fragmentation

Fragmentation has two major modes: (a) core fragmentation and (b) disc fragmentation. The occurrence of each mode depends on several factors including the influence of external triggers.

Core fragmentation. As mentioned in Section 1.1.2, fragmentation of a collapsing prestellar core is most likely to occur during the transition from isothermal to adiabatic phases, i.e. at $\rho_{\rm c} \sim 10^{-13}\,{\rm g/cm^3}$. Nevertheless, one of the important factors to determine the fragmentation of an isolated core is the rotation. The influence of rotation is usually quantified by the rotational energy ratio $\beta = E_{\rm rot}/\left|E_{\rm grav}\right|$ and the thermal energy ratio $\alpha = E_{\rm therm}/\left|E_{\rm grav}\right|$, where $E_{\rm rot}$ is the rotational energy, $E_{\rm therm}$ the thermal energy, and $E_{\rm grav}$ the gravitational potential energy. For a prestellar core with solid-body rotation, it has been found that fragmentation occurs when the product $\alpha\beta \lesssim 0.12 - 0.15$ (e.g. Goodwin et al. 2007, and references therein). The efficiency of core fragmentation can be increased in cores that have differential rotation (Myhill and Kaula 1992; Boss and Myhill 1995). In a radially symmetric core with differential rotation, for example, the centrifugal support begins to play its role in clearing the central part of the core when the value of β is approaching unity. The material bouncing back radially outwards from the centre facing with the material from the outer part creates a shock front of a ring-like shape. The density ring may be unstable to fragmentation (Bonnell and Bate 1994; Cha and Whitworth 2003).

Another key factor is turbulence in the core. The internal turbulence helps preparing the core ready for fragmentation by generating a complex structure of high-density regions that are prone to be gravitationally unstable. Simulations have shown that cores with different levels of turbulence fragment and produce different number of stars (e.g. Bate et al. 2002a,b, 2003; Delgado-Donate et al. 2004; Goodwin et al. 2004a,b, 2006). Other than the influences of rotation and turbulence, core fragmentation may occur as a result of collision between two prestellar cores (e.g. Bhattal et al. 1998; Kitsionas and Whitworth 2007).

Disc fragmentation. A collapsing prestellar core can be flattened by its intrinsic rotation, forming a centrally dense protostar surrounded by disc and envelope. Under some conditions, density enhancement occurred on the disc may grow up and become gravitationally unstable, leading the disc to fragmentation (Shu et al. 1990; Heemskerk et al. 1992; Woodward et al. 1994; Bonnell 1994). Fragmentation of a disc, despite

depending on several parameters, is usually determined from Toomre parameter (Q, Toomre 1964) and a cooling time parameter (β, Gammie 2001). The value of $Q(R)$ represents how gravitationally stable the disc is at a given radius R, the higher the value the higher the stability. The value of $\beta(R)$ represents the ability of the disc at radius R to cool down, the higher the value the poorer the cooling rate the higher the stability. We explain these parameters in more details in Section 1.4.2. The regions where Q and β are satisfied are rather restricted, i.e. not too close to the central star as the temperature is very high and not too far out to the edge of the disc as the density is very low. Indeed, Whitworth and Stamatellos (2006) have shown that the radius where a disc surrounding a star of mass $M_\star$ may be able to fragment should be greater than $\sim 150(M_\star/M_\odot)^{1/3}$AU. This has been verified later by Stamatellos et al. (2007) and Stamatellos and Whitworth (2009a).

In young cluster environments where the chances of close encounters among the members are not negligible, gravitational instabilities in a protostellar disc may be induced by tidal perturbations during close encounters. This has been shown to be the case in simulations of young stars with a massive extended disc, i.e. as massive as the central star with radius of several hundred AU, (Boffin et al. 1998; Watkins et al. 1998a,b; Thies et al. 2010). However, simulations performed by Lodato et al. (2007) and Forgan and Rice (2009) for young stars with a typical-size disc (a protoplanetary disc of radius $\lesssim 100$AU and mass $\sim 0.1M_\odot$) show no fragmentation even in the cases where the periastron is smaller than the disc radius. The authors point out that disc fragmentation depends mainly on cooling process than other factors such as external perturbation (see also Stamatellos et al. 2011). In addition to disc fragmentation by stimuli, it is also possible for a circumbinary disc to be gravitational unstable under the influence of its own binary star (Bonnell and Bate 1994). Fragmentation of a circumbinary disc may produce one or several objects that later have dynamical interaction with the binary components.

Although disc fragmentation seems to be more efficient in producing binaries than the other non-fragmentation mechanisms mentioned above, it cannot be a major mode of binary formation. There are two main reasons for this. First, there seems to be a disagreement between the masses of most secondary stars which are $\gtrsim 0.1M_\odot$ (e.g. Duquennoy and Mayor 1991) and the masses of the discs surrounding young stars which are $\sim 0.001 - 0.1M_\odot$ (e.g. Beckwith et al. 1990; Osterloh and Beckwith 1995). Second, this mechanism may only contribute binaries with separations in the order of a few to several hundred AU.

1.2.3 Modification of binary properties

Based on the fragmentation model, one prestellar core may form a small-N system of stars. From considering the observed properties of multiple systems, Goodwin and Kroupa (2005) suggest that one typical core would form only 2 to 3 stars. In general, non-hierarchical multiple systems with $N \geq 3$ are unstable to dynamical decay. Close encounters among the members preferentially result in the least massive being ejected (e.g. Anosova 1986; Sterzik and Durisen 1998, and references therein). Disintegration would eventually leave the two most massive stars as a tightly bound binary system. For a triple system, the decay timescale is estimated to be within ~ 100 crossing times ($t_{\rm cr}$), given by

$$t_{\rm cr} \sim 0.16 \left(\frac{\bar{R}^3}{M_{\rm tot}}\right)^{1/2} \text{yr}, \tag{1.5}$$

where $\bar{R}$ is the characteristic size of the system in AU and $M_{\rm tot}$ is the total mass of the system in $M_\odot$ (Anosova 1986).

In young star clusters that consist of many small-N systems (or subclusters), binary properties can also be altered by dynamical interactions between stars from different subclusters. Dynamically, binaries can be categorized into three types: soft, dynamically active, and hard binaries (Heggie 1975; Hills 1975, also see Parker and Goodwin 2012). In fact, the criteria to distinct those types depend largely on the environment where the binaries live. Soft binaries are those with relatively wide orbits and are easily disrupted. When considering binaries as a simplified one-body system, the reduced mass of a soft binary system moves with speed much lower than the velocity dispersion of the cluster or the environment it lives. Soft binaries may be disrupted even in gentle encounters. In contrast, hard binaries have relatively close orbits. The reduced mass of a simplified hard-binary system moves with speed much higher than the velocity dispersion. Hard binaries are very stable to dynamical disruption.

Between hard and soft binaries is a type of dynamically active binaries. The evolution of active binaries can be varied by the intense of interactions the system experienced (Parker and Goodwin 2012). Binaries of this type play a key role in distributing energy in star clusters. Heggie (1975) and Hills (1975) have found that, in cluster environments, dynamical interactions tend to harden the hard binaries and soften the soft binaries (the Heggie-Hills law).

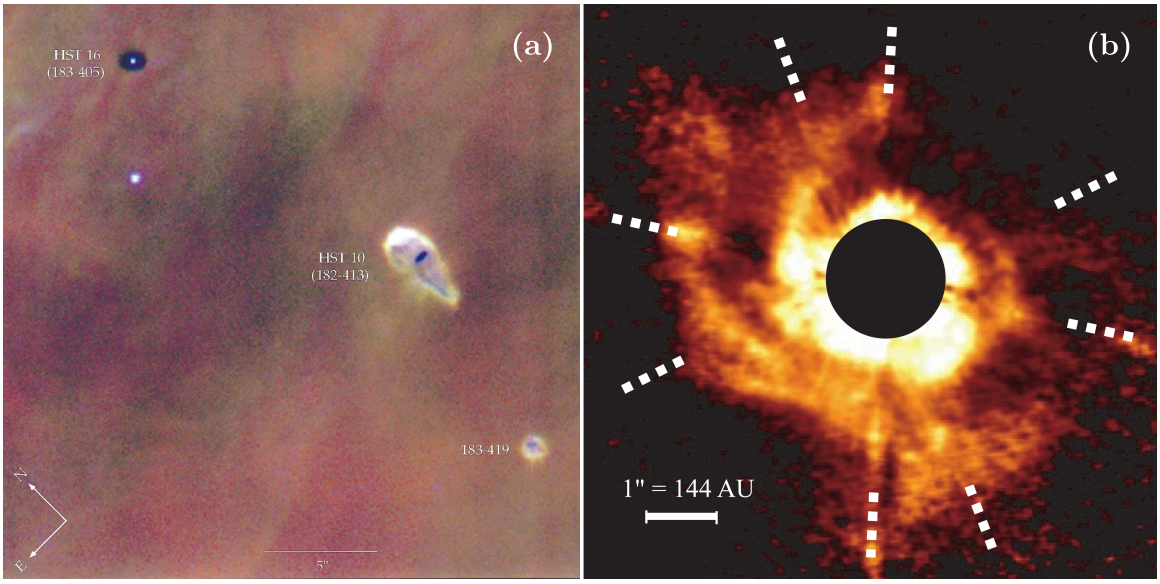

Figure 1.8 Images of young stars with discs. (a) Circulmstellar discs (dark area) around the objects 183-405, 182-413, and 183-419 in the Orion Nebula. The estimate radius are $\sim$289AU, $\sim$165AU, and $\sim$103AU, respectively. The image was taken with the Hubble Space Telescope (HST) by Bally et al. (1998). (b) An extended disc surrounding AB Aur star showing spiral structure. The image was taken with the Subaru telescope by Fukagawa et al. (2004).

1.3 Circumstellar discs

Observations in the IR, submm, and mm wavelengths imply the existence of circumstellar discs around young stars. Various properties of the discs can be investigated from the observations in those wavelengths (e.g. Strom et al. 1989; Weintraub et al. 1989; Beckwith et al. 1990). The first resolved disc around a young star is of HL Tauri, obtained from radio maps of ^{13}CO emission line (Sargent and Beckwith 1987). However, undoubted observations of disc morphology are conducted in optical wavelengths following the work of O'dell and Wen (1994) using the Hubble Space Telescope (HST). As examples, Figure 1.8 shows images of discs surrounding (a) young stellar objects (YSOs) in the Orion Nebula (Bally et al. 1998) and (b) AB Aur star (Fukagawa et al. 2004).

Several properties of circumstellar discs can be drawn from observational data using simple model in which the disc is assumed to be completely flat (e.g. Adams et al. 1987; Beckwith et al. 1990). In this section, the main properties of circumstellar discs are described.

1.3.1 Mass

Circumstellar discs consist of gas and dust with a gas-to-dust ratio generally assumed to be $f_{\rm g:d} = M_{\rm gas}/M_{\rm dust} \sim 100$. Despite contributing only a small fraction to the disc mass, dust is used as a tracer of gas in the disc; the mass of the disc can then be estimated. The amount of dust can be quantified from the observed flux (λF_λ) in submm-to-mm wavelengths ($10\mu{\rm m} \lesssim \lambda \lesssim 1{\rm cm}$) where dust emission is optically thin (Hildebrand 1983; Adams et al. 1987; Beckwith et al. 1990; Andrews and Williams 2005). For simplicity, the disc is assumed be flat and vertically isothermal. Therefore, the flux observed from a disc surrounding a star at distance d with rotational axis deviated from the line of sight by an angle i can be written as

$$\lambda F_\lambda = \frac{\cos i}{d^2} \int_{r_{\rm d}}^{R_{\rm d}} \lambda B_\lambda(T) \Big[1 - \exp\Big(-\frac{\tau_\lambda}{\cos i}\Big)\Big] 2\pi R \, {\rm d}R, \tag{1.6}$$

where $B_\lambda(T)$ is the Planck function (as a function of wavelength λ and temperature T) and τ_λ is the vertical optical depth at wavelength λ (e.g. Hartmann 2009, and references therein). Note that the temperature is varying with radius R, i.e. $T = T(R)$, and the integration considers the disc from its inner radius $r_{\rm d}$ to outer radius $R_{\rm d}$.

For the optically thin regime in which $\tau_\lambda \ll 1$, Equation 1.6 becomes

$$\lambda F_\lambda = \frac{2\pi}{d^2} \int_{r_{\rm d}}^{R_{\rm d}} \lambda B_\lambda(T) \tau_\lambda R \, {\rm d}R, \tag{1.7}$$

since the exponential term can be approximated by that $\exp(-x) \simeq 1 - x$ for any variable $x \ll 1$. In the long-wavelength emission of dust, an approximation can be made to B_λ by adopting the Rayleigh-Jeans law, i.e.

$$B_\lambda(T) \simeq \frac{2ck_{\rm B}T}{\lambda^4}, \tag{1.8}$$

where c and $k_{\rm B}$ are the speed of light and the Boltzmann constant, respectively. By assuming that the optical depth (τ_λ) in Equation 1.7 is dominated by the dust opacity (κ_λ), we have

$$\tau_\lambda = \kappa_\lambda \Sigma_{\rm dust} = \frac{\kappa_\lambda \Sigma}{f_{\rm g:d}}, \tag{1.9}$$

where $\Sigma_{\rm dust}$ and Σ are the dust and gas-plus-dust surface densities of the disc at radius R. Now, for Equation 1.7 to be integrable, we need to express the temperature

in Equation 1.8 and surface density in Equation 1.9 in terms of R. Several authors have used a power-law function of R for both T and Σ, i.e.

$$T(R) = T_\circ \left(\frac{R}{R_\circ}\right)^{-q}, \tag{1.10a}$$

$$\Sigma(R) = \Sigma_\circ \left(\frac{R}{R_\circ}\right)^{-p}, \tag{1.10b}$$

where $T_\circ$ and $\Sigma_\circ$ are respectively the temperature and surface density at radius $R = R_\circ$; p and q are the power-law indices. Substituting B_λ and τ_λ as a function of R into Equation 1.7 gives us

$$\lambda F_\lambda \simeq \frac{4\pi c k_{\rm B} \kappa_\lambda \Sigma_\circ T_\circ R_\circ}{\lambda^3 d^2} \int_{r_{\rm d}}^{R_{\rm d}} \left(\frac{R}{R_\circ}\right)^{1-p-q} {\rm d}R. \tag{1.11}$$

By assuming that the inner radius is much smaller than the outer, $r_{\rm d} \ll R_{\rm d}$, we have

$$\lambda F_\lambda \simeq \frac{4\pi c k_{\rm B} \kappa_\lambda \Sigma_\circ T_\circ R_\circ^2}{\lambda^3 d^2 (2-p-q)} \left(\frac{R_{\rm d}}{R_\circ}\right)^{2-p-q}, \tag{1.12}$$

for $p + q \neq 2$. Since the total mass of the disc is

$$M_{\rm d} = \int_{r_{\rm d}}^{R_{\rm d}} 2\pi R \Sigma \, {\rm d}R = \frac{2\pi \Sigma_\circ R_\circ^2}{2-p} \left(\frac{R_{\rm d}}{R_\circ}\right)^{2-p}, \tag{1.13}$$

Equation 1.14 can be rearranged to

$$\lambda F_\lambda \simeq \frac{2 c k_{\rm B} \kappa_\lambda}{\lambda^3 d^2} \frac{2-p}{2-p-q} M_{\rm d} T(R_{\rm d}). \tag{1.14}$$

From this equation, the mass of a disc can be found if we know the values of κ_λ, p, q, $R_{\rm d}$, and $T_\circ$. Among these parameters, the dust opacity κ_λ can cause the most uncertainty to the inferred result (for details, see Hartmann 2009). The dust opacity is generally assumed to be a power-law function (Beckwith et al. 1990):

$$\kappa_\lambda = \kappa_\circ \left(\frac{\lambda}{\lambda_\circ}\right)^{-\beta}, \tag{1.15}$$

where $\beta = 1$, $\kappa_\circ = 0.1 {\rm cm}^2/{\rm g}$, and $\lambda_\circ = 300 \mu{\rm m}$ (corresponding to frequency $\nu_\circ = 10^{12}{\rm Hz}$ given by the authors). However, the values of β and $\kappa_\circ$ are not absolute. Disc observations in the Taurus-Auriga star forming region by Andrews and Williams (2007) have

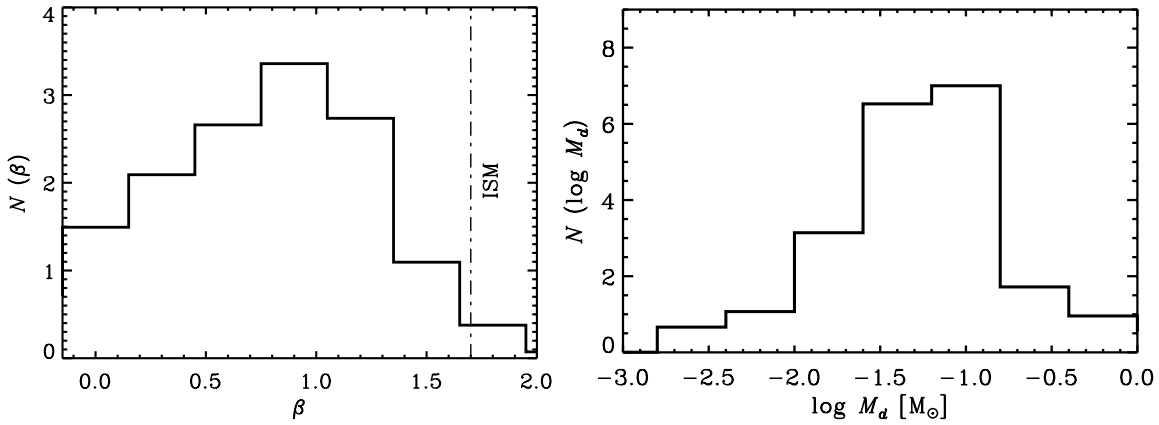

Figure 1.9 Distributions of the power-law index β (left) and disc masses (right) of circumstellar discs in the Taurus-Auriga star forming region (Andrews and Williams 2007). In figure (right), the dashed line marks on the value $\beta \simeq 1.7$ for the interstellar medium (Hildebrand 1983).

shown, in Figure 1.9(left), that the distribution of β is rather scattered, though with a median of ~ 1 in agreement with β suggested by Beckwith et al. (1990). We can see from Figure 1.9(left) that most discs have a value of β lower than that of the ISM ($\beta \simeq 1.7$, marked by the dashed line in the figure, Hildebrand 1983). This is believed to be the effect of grain growth within the disc (Testi et al. 2001; Natta et al. 2004). That the value of κ_λ cannot be obtained without uncertainty is a major source of error in the disc mass estimation; it is likely that most disc masses are underestimated (Hartmann et al. 2006).

Typically, circumstellar discs are relatively less massive than their central star. Andrews and Williams (2005) have found that most young low-mass stars ($M_\star \lesssim 1 M_\odot$) in the Taurus-Auriga star forming region are surrounded by discs of masses from $\sim 10^{-4}$ up to $\sim 0.1 M_\odot$. The distribution of disc masses for low-mass stars are rather scattered about the median mass of $\sim 0.06 M_\odot$, as shown in Figure 1.9(right), for the Taurus-Auriga and Ophiuchus-Scorpius star forming regions (Andrews and Williams 2007). In Orion Nebula Cluster, a number of low-mass stars with relatively massive discs ($\sim 0.2 - 0.5 M_\odot$) are observed (Eisner and Carpenter 2006; Eisner et al. 2008). Massive discs surrounding low-mass stars are believed to be susceptible to gravitational instabilities (see Section 1.2.2).

For very low-mass stars and brown dwarfs ($M_\star \lesssim 0.08 M_\odot$), the disc masses range from < 1 up to a few Jupiter masses (Scholz et al. 2006). In contrast, young massive stars with mass below $\sim 20 M_\odot$ are commonly found with massive discs of comparable masses (e.g. Cesaroni et al. 2007). All these mass ranges of young stars, from brown

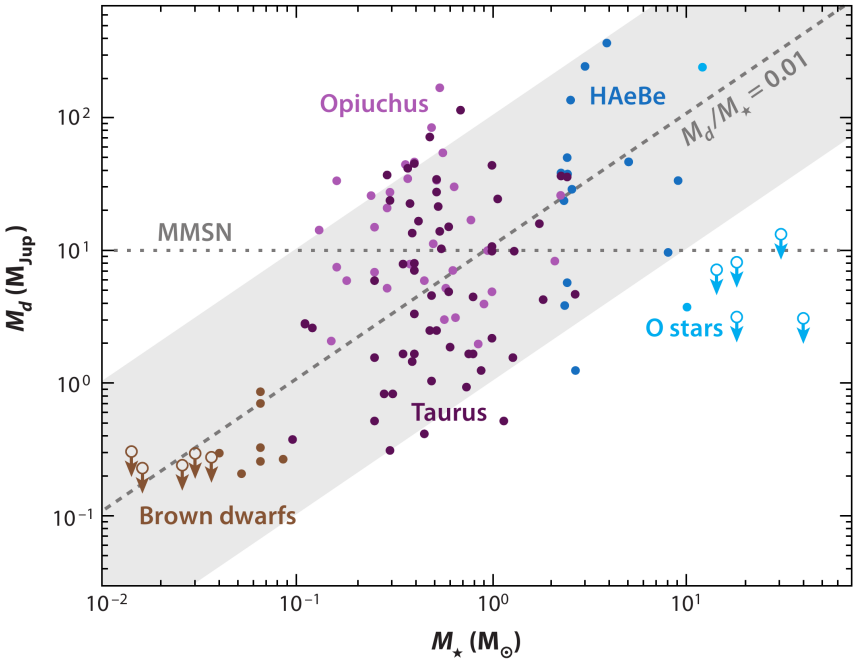

Figure 1.10 Scattered trend of star-disc mass dependence. The plot suggests that, for young stars with masses of $M_\star = 0.04 - 10 M_\odot$, $M_\mathrm{d}/M_\star \sim 0.01$ with ± 1dex about the median (the grey shaded area). The dotted horizontal line marks on the minimum mass solar nebula (MMSN), the lowest mass required to form the planets in the Solar System, i.e. $\sim 0.01 - 0.07 M_\odot$ or $\sim 10 - 70 M_\mathrm{Jup}$ (Kusaka et al. 1970; Weidenschilling 1977a). The plot is taken from Williams and Cieza (2011).

dwarfs to high-mass stars, seem to suggest that the disc mass may correlate with the mass of the central star (e.g. Natta et al. 2000). A compilation of several data sources suggests a roughly constant ratio between disc mass and stellar mass, i.e. $M_\mathrm{d}/M_\star \sim 0.01$ (Williams and Cieza 2011). The trend is shown in Figure 1.10.

1.3.2 Radius

In order to determine the disc radius, the disc has to be spatially resolved. The angular extent of a disc may be measured directly if the object is silhouetting against an optically bright background such as HII region (e.g. McCaughrean and O'dell 1996). An example of disc silhouettes in the Orion Nebula is shown in Figure 1.11. For discs in other environments, interferometry may be used instead (e.g. Dutrey et al. 1996).

Typical radii of discs surrounding young low-mass stars range from several tens up to a thousand of AU. Discs in the Taurus-Auriga star forming region, for example, have a radius distribution as shown in Figure 1.12 with a median value of ~ 200AU (Andrews and Williams 2007). As well as the disc mass, the disc radius also seems to

Figure 1.11 Disc silhouettes in the Orion Nebula showing the clear extent of the discs (Bally et al. 2000). Note that the disc of the $294-606$ object is seen edge-on.

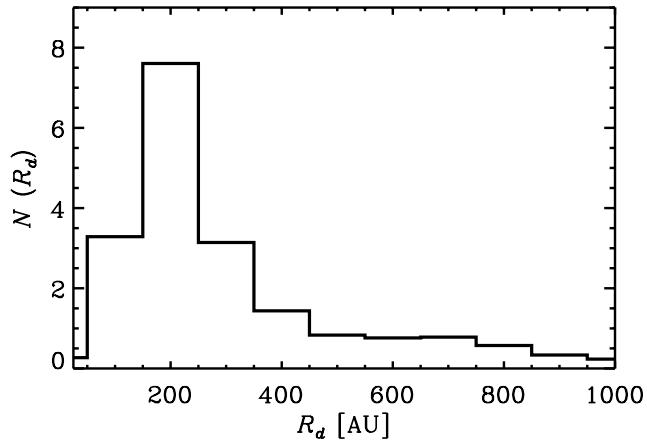

Figure 1.12 Distribution of disc radii in the Taurus-Auriga and Ophiuchus-Scorpius star forming regions (Andrews and Williams 2007).

scale with the mass of the central star. For brown dwarfs in the Taurus star forming region, the discs are observed to have radii of a few to several tens of AU (Scholz et al. 2006). Discs surrounding young massive stars are found to have radii from $\sim 10^3$ up to 10^5AU (e.g. Cesaroni et al. 2007).

1.3.3 Density structure

The power-law index (p) of the surface density profile (Equation 1.10b) is difficult to determine. In general, the value of p is assumed to be 1 in the α-disc model (Shakura and Sunyaev 1973) and 1.5 in the solar nebula model of Solar System formation (Weidenschilling 1977b; Hayashi et al. 1985). An early attempt to confine the range of p was made by Mundy et al. (1996) for the disc around HL Tau. They found that $0 \leq p \leq 1$. This range of p was found to be consistent with that obtained from a survey

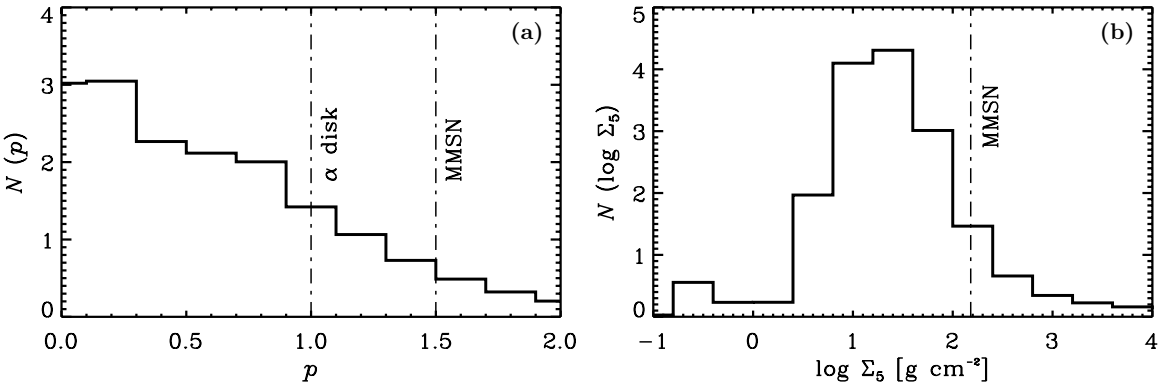

Figure 1.13 Distributions of (a) the power-law index (p) and (b) surface density at $R = 5$AU (Σ_5) of the discs in the Taurus-Auriga star forming region (Andrews and Williams 2007).

of T Tauri stars in Taurus by Kitamura et al. (2002). Andrews and Williams (2007) were later able to constrain the values of p and Σ_5 (i.e. $\Sigma_\circ$ defined at $R = 5$AU) from a circumstellar disc survey of the Taurus-Auriga star forming region. The distributions of p and Σ_5 are shown in Figure 1.13. From the distributions, the median values are $p \sim 0.5$ and $\Sigma_5 \sim 14\mathrm{g/cm}^2$.

1.3.4 Temperature structure

According to the power-law assumption of the temperature profile (Equation 1.10a), the temperature structure of the disc is characterized by the value of q and $T_\circ$. The power-law index q can be obtained from comparing the spectral index α_{IR} measured in the mid-IR wavelengths with the exponent of wavelength in the expression derived from Equation 1.6. In this case, we consider Equation 1.6 in the optically thick regime in which $\tau_\lambda \gg 1$. The observed flux can be written as

$$\lambda F_\lambda = \frac{\cos i}{d^2} \int_{r_\mathrm{d}}^{R_\mathrm{d}} \lambda B_\lambda(T) 2\pi R \, \mathrm{d}R. \tag{1.16}$$

To simplify the integration, let us consider the Planck function

$$B_\lambda(T) = \frac{2hc^2}{\lambda} \frac{1}{\exp(hc/\lambda k_\mathrm{B} T) - 1}. \tag{1.17}$$

By using T from Equation 1.10a, the argument of the exponential function may be defined as a new variable

$$x = \left(\frac{hc}{\lambda k_\mathrm{B} T}\right)^{1/q} = \left(\frac{hc}{\lambda k_\mathrm{B} T_\circ}\right)^{1/q} \frac{R}{R_\circ}, \tag{1.18}$$

and thus

$$R = \left(\frac{\lambda k_{\rm B} T_\circ}{hc}\right)^{1/q} R_\circ x. \tag{1.19}$$

Rewriting Equation 1.16 in terms of x gives

$$\lambda F_\lambda = \frac{2\pi \cos i}{d^2} \frac{2hc^2}{\lambda^4} \left(\frac{\lambda k_{\rm B} T_\circ}{hc}\right)^{2/q} R_\circ^2 \int_{x_{\rm min}}^{x_{\rm max}} \frac{x}{\exp(x^q) - 1}\, {\rm d}x. \tag{1.20}$$

The limits of the integration can be considered from that, for a wide range of wavelengths, most of the observed flux is a contribution from the intermediate radii of the disc, i.e. $r_d \ll R \ll R_d$ (Beckwith et al. 1990). Therefore, an approximation can be made by using the limits from 0 to ∞ for $x_{\rm min}$ and $x_{\rm max}$, respectively. The flux can now be written as

$$\begin{aligned} \lambda F_\lambda &\simeq \frac{2\pi \cos i}{d^2} \frac{2hc^2}{\lambda^4} \left(\frac{\lambda k_{\rm B} T_\circ}{hc}\right)^{2/q} R_\circ^2 \int_0^{\infty} \frac{x}{\exp(x^q) - 1}\, {\rm d}x \\ &\simeq \mathcal{C}(q) \frac{4\pi hc^2 R_\circ^2 \cos i}{d^2} \left(\frac{k_{\rm B} T_\circ}{hc}\right)^{2/q} \lambda^{2/q-4}, \end{aligned} \tag{1.21}$$

where $\mathcal{C}(q)$ is the outcome value of the integral term for a given value of q. Since $\mathcal{C}(q)$ is constant, we have

$$\lambda F_\lambda \propto \lambda^{2/q-4}. \tag{1.22}$$

By comparing the exponent of the RHS term with that of the observed flux in the mid-IR wavelengths, i.e.

$$\lambda F_\lambda \propto \lambda^{\alpha_{\rm IR}}, \tag{1.23}$$

we then come up with

$$q = \frac{2}{4 + \alpha_{\rm IR}}. \tag{1.24}$$

Note that, for an SED which is plotted in terms of frequency rather than wavelength,

$$q = \frac{2}{4 - \alpha_{\rm IR}}. \tag{1.25}$$

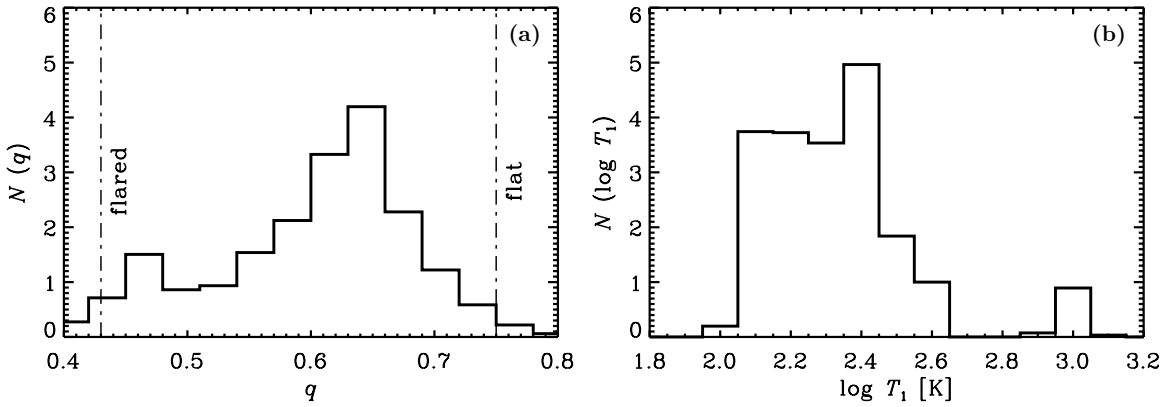

Figure 1.14 Distributions of (a) the temperature profile index (q) and (b) the disc temperature at 1AU (T_1) of circumstellar discs in Taurus-Auriga star forming region (Andrews and Williams 2007). The dot-dash lines in figure (a) mark on the values of q that are usually assumed in the flat disc model ($q \sim 0.75$) and the flared disc model ($q \sim 0.43$).

Once we have a value of the temperature profile index q, we may find the value of $T_\circ$ from substituting q back into Equation 1.21, provided that the other parameters are already known or assumed.

Although Equation 1.21 provides a good fit for typical SEDs in mid-IR wavelengths up to a few 10μm, it usually fails to fit the flux at longer wavelengths; for example, the SED of DL Tau shown in Figure 1.4. This implies that the outer radii of the disc are hotter than that has been assumed in the flat disc model. It has been suggested that the shape of most discs would rather be flared than flat especially at the outer parts (Kenyon and Hartmann 1987). This is simply because the influence of gravity from the central star to keep the warm material in a thin plane decreases with radius. Hence, the thickness of the disc increases as a function of distance from the central star. Chiang and Goldreich (1997) have shown that the height of the visible photosphere above the disc midplane is proportional to $\sim R^{58/45}$. The details of the flared disc model can be found in, for example, Calvet et al. (1992) and Chiang and Goldreich (1997).

Observations have found that the value of the index q is in between the theoretical values for the flat (thin) disc ($q = 0.75$, Pringle 1981; Adams et al. 1987) and flared disc ($q = 0.43$, Chiang and Goldreich 1997); mostly, $q \sim 0.5$ (e.g. Beckwith et al. 1990; Henning et al. 1993; Osterloh and Beckwith 1995). Submm survey of circumstellar discs in Taurus-Auriga star forming region by Andrews and Williams (2007), for example, is able to show the distribution of q and T_1 (disc temperature at 1AU) in Figure 1.14. From the figure, the median values are $q \sim 0.62$ and $T_1 \sim 200$K.

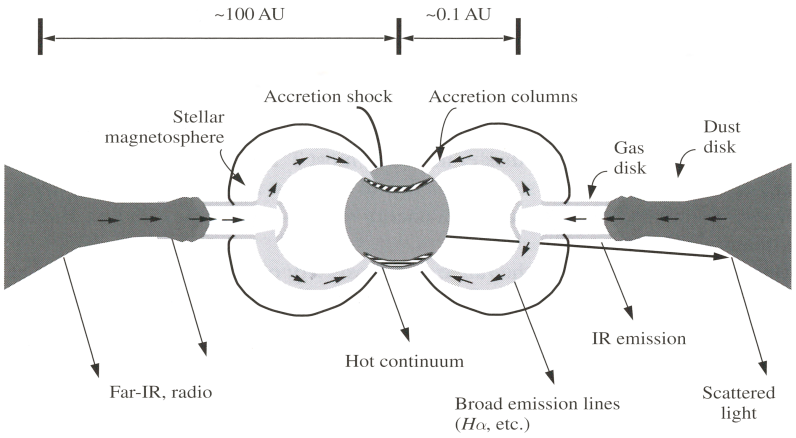

Figure 1.15 Diagram illustrating the magnetospheric accretion model for discs in T Tauri stars. The inner disc material (light grey shaded areas) falls along the magnetic field lines (accretion columns) onto the stellar surface. The accretion shock at the surface emits the hot continuum excess in UV wavelengths. The diagram is taken from Hartmann (2009).

1.3.5 Mass accretion rate

Young stars accrete mass from the inner part of their discs. The disc material landing on the stellar surface produces the UV continuum excess (Lynden-Bell and Pringle 1974). It is suggested that the stellar magnetic field may play a major role in channelling the disc material onto the stellar surface (Uchida and Shibata 1984, 1985; Bertout et al. 1988; Königl 1991; Shu et al. 1994). This magnetospheric accretion model can be illustrated in Figure 1.15. The luminosity of the excess emission from the accretion process, once distinguished from the stellar photospheric emission, can be used to estimate the mass accretion rate ($\dot{M}$) onto the central star (e.g. Hartmann 2009). In the magnetospheric accretion model, the accretion luminosity is given by

$$L_{\rm acc} \simeq \frac{GM_\star \dot{M}}{R_\star}\left(1 - \frac{R_\star}{R_{\rm in}}\right), \tag{1.26}$$

where $M_\star$ and $R_\star$ are the stellar mass and radius, and $R_{\rm in}$ is the inner radius of the disc. The value of $R_{\rm in}$ is typically around the value of the co-rotation radius, which is $\sim 5 - 6R_\star$ (Gullbring et al. 1998). Once the other parameters in Equation 1.26 are known, the mass accretion rate $\dot{M}$ can be calculated.

Surveys of star forming regions such as done by Gullbring et al. (1998) for the Taurus and Calvet et al. (2004) for the Taurus and Orion have found the typical values of $\dot{M}$ from $\sim 10^{-9}$ to $10^{-7} M_\odot$/yr for T Tauri stars. Very low-mass stars and brown dwarfs have lower mass accretion rates ranging from $\sim 10^{-11}$ up to $10^{-9} M_\odot$/yr

(e.g. Natta et al. 2004), while high-mass stars with masses $\geq 8M_{\odot}$ have higher mass accretion rates from $\sim 10^{-4}$ to $10^{-3}M_{\odot}$/yr or even higher (e.g. Fuller et al. 2005; Keto and Wood 2006). This apparently indicates a relation between the accretion rate and stellar mass. Indeed, for T Tauri stars and brown dwarfs, it is found that the mass accretion rate scales quadratically with the stellar mass, i.e. $\dot{M} \propto M_{\star}^{2}$ (Hartmann et al. 2006, and references therein). In addition, the accretion rate also changes with the age of the system due to the dissipation of the disc over time. It is found that the accretion rate changes roughly as a power-law function of time: $\dot{M} \propto t^{-\eta}$, where $\eta \sim 1.5 - 2.8$ (Hartmann et al. 1998).

1.3.6 Lifetime

In theories of planet formation (Section 1.4) in which planets are thought to from out of circumstellar discs, the disc lifetime is a fundamental parameter for constraining the formation timescale of the planets. Disc lifetime can be estimated from the assumption that young star clusters of different ages would have different fractions of stars surrounded by discs. That is, the fraction should decrease with the age of the cluster. From a survey of stars with IR excess in star clusters aged $2.5 - 30$Myr compiled with other previous observations, Haisch et al. (2001) have found a relation between the fraction of stars with disc and the age of the clusters, as shown in Figure 1.16. The trend in the figure suggests a disc lifetime of ~ 6Myr. This extrapolated value is in agreement with the disc lifetime from a few to ~ 10Myr suggested by other studies (e.g. Strom et al. 1989; Skrutskie et al. 1990; Hillenbrand et al. 1998; Jayawardhana et al. 1999; Lada et al. 2000; Sicilia-Aguilar et al. 2005; Uzpen et al. 2009).

Circumstellar discs may be dispersed by various mechanisms during the transition from Class II (CTTS) to Class III (WTTS). Observations have found a number of young stars which exhibit spectral excess in mid- to far-IR wavelengths similar to typical CTTSs but lack of near IR excess. These young stars are interpreted as having their disc on the process of disc clearing, so called *transition discs*. The objects are believed to be representing the beginning of the transition phase from CTTS to WTTS. However, the number of young stars with transition discs is very low compared to that of CTTSs and WTTSs found in the same region (e.g. Persi et al. 2000; Hartmann et al. 2005; Padgett et al. 2006). This implies that the transition phase is short-lived, possibly as short as $< 10^{5}$yr (Simon and Prato 1995). Viscous accretion alone cannot clear the whole disc within this very short timescale nor do other mechanisms such as grain growth, stellar winds and outflows, and photoevaporation

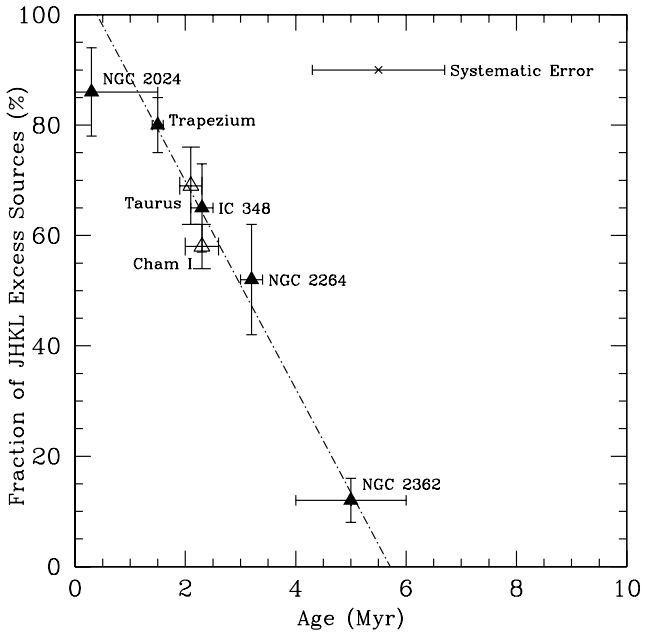

Figure 1.16 Correlation between the fraction of stars with discs in young clusters and the age of the clusters. The extrapolation suggests a disc lifetime of $\sim$6Myr. The plot is taken from Haisch et al. (2001).

from nearby massive stars, which also have their own limitations (e.g. Alexander 2008; Hartmann 2009). The more efficient mechanism seems to be from combining viscous accretion with photoevaporation from the central star (Clarke et al. 2001; Alexander et al. 2006a,b). The photoevaporation of a disc becomes important in increasing the mass-loss rate of the disc in the late stage of disc evolution. The disc clearing process begins when the mass-loss rate due to photoevaporation at the gravitational radius $R_{\rm g}$, beyond which the ionized gas escapes as a wind, exceeds the viscous accretion rate (see Alexander et al. 2006b). As a consequence, the outer disc beyond $R_{\rm g}$ is unable to replenish the disc inside $R_{\rm g}$. Viscous accretion of the inner disc onto the star then leaves a hole of radius $R_{\rm g}$. The UV radiation from the central star can now reach the inner rim of the outer disc and starts to evaporate the disc from the inside out. The disc clearing process occurs rapidly within $\sim 10^5$yr, consistent with the estimated transition timescale.

1.3.7 Timescales

Disc timescales indicate roughly how efficient the disc is in adjusting itself back to an equilibrium after some perturbation has occurred. In this aspect, the timescales may be used as the instability criteria for a disc. Among all the disc timescales we

are discussing here, the *dynamical timescale* ($t_{\rm dyn}$) is the shortest one. The dynamical timescale of the disc at any radius R is defined as

$$t_{\rm dyn} = \frac{R}{v_\theta} = \frac{T}{2\pi} = \Omega^{-1}, \tag{1.27}$$

where v_θ is the local azimuthal velocity, T the local time period, and Ω the local angular speed. For a Keplerian disc in which the disc mass is negligible compared to the stellar mass, we have

$$t_{\rm dyn} \simeq \sqrt{\frac{R^3}{GM_\star}}, \tag{1.28}$$

where $M_\star$ is the mass of the central star. The dynamical timescale more or less reflects the influence of the centrifugal force in bringing the disc, at a given radius, back to centrifugal balance, i.e. a circular orbit.

In a non-self-gravitating disc where the gravity of the central star dominates the internal gravity of the disc, the timescale required for pressure forces to adjust the disc to a vertical hydrostatic equilibrium is represented by the *vertical timescale*

$$t_{\rm z} = \frac{H}{c_{\rm s}}, \tag{1.29}$$

where H and $c_{\rm s}$ are respectively the local scale height and local sound speed of the disc. For a Keplerian disc, this timescale is approximately equal to the dynamical timescale.

In thermal evolution of the disc, the time required for the disc to cool down or heat up to its thermal equilibrium is given by the *thermal timescale* (Gammie 2001):

$$t_{\rm th} = \frac{4}{9}\frac{1}{\gamma(\gamma-1)\alpha_{\rm ss}\Omega}, \tag{1.30}$$

where γ is the ratio of the specific heats and $\alpha_{\rm ss} \lesssim 1$ is the viscosity parameter in the α-disc model (Shakura and Sunyaev 1973). By comparing with the dynamical timescale, we find that

$$t_{\rm th} \sim \frac{t_{\rm dyn}}{\alpha_{\rm ss}} \gg t_{\rm dyn}. \tag{1.31}$$

Furthermore, in thermal equilibrium, the thermal timescale is equal to the cooling and heating timescales of the disc.

Finally, the timescale for the disc to adjust its surface density is the *viscous timescale*, given by

$$t_\nu = \frac{R^2}{\nu} = \frac{1}{\alpha_{\rm ss}\Omega}\left(\frac{R}{H}\right)^2, \tag{1.32}$$

where ν is the viscosity. Since the disc scale height (H) is much smaller than the radius (R), we have $(R/H)^2 \gg (4/9)(\gamma(\gamma-1))^{-1}$; that is, the viscous timescale is much greater than the thermal timescale. In comparison, we have

$$t_\nu \gg t_{\rm th} \gg t_{\rm z} \sim t_{\rm dyn}. \tag{1.33}$$

The details of deriving the thermal and viscous timescales can be found in, for example, Lodato (2008).

1.4 Planet formation

The formation of planets is intimately linked to star formation processes. Current theories of planet formation agree on that planets are formed out of protoplanetary discs around young stars, T Tauri stars in particular. Two formation models that have been proposed as a formation mechanism are (a) the core accretion model (e.g. Mizuno 1980; Pollack et al. 1996) and (b) the disc instability model (e.g Cameron 1978; Boss 1997, 2000; Durisen et al. 2007). The major difference of the two model is the process of building up a planet: core accretion builds planets up gradually ($\sim 10^7$yr) from dust particles while disc instability can rapidly ($\sim 10^3$yr) produce heavy planetary seeds to begin with. Of course, both models still have their own pros and cons. In this section, we summarize the main aspects and briefly discuss the problems of the models.

1.4.1 Core accretion model

In the core accretion model, planet formation begins with the coagulation of dust and small solid grains of submicron-sizes into larger particles. The early growth phase is to become a centimetre-size pebble and settle down as a thin layer in the disc mid-plane. The pebbles aggregate further via inelastic collisions to form kilometre-size agglomerates or *planetesimals* which, by now, have decoupled from the gas and move in nearly circular orbits. The process of building up a planetesimal may take $\sim 10^4$yr

(Weidenschilling and Cuzzi 1993). As a planetesimal being sufficiently massive, its gravity begins to play a key role in gathering more mass from surrounding objects. Since the gathering rate depends on the mass and size of the planetesimal and the distribution of the surrounding neighbours, the planetesimal grows up with an increasing rate. This rapid accumulation of mass is known as the *runaway growth* (e.g. Wetherill and Stewart 1989; Kokubo and Ida 1996). Eventually, when the number of small planetesimals drops, the growth rate of the remaining largest bodies decreases. Many accumulated bodies may now be large enough to be considered as a *planetary core* or *protoplanet*. The estimate building-up timescale of protoplanets via the runaway growth is $\sim 10^6$yr (Wetherill and Stewart 1989; Aarseth et al. 1993; Weidenschilling et al. 1997). For protoplanets that orbits near the central star where the temperature is high, the further growth process by capturing the disc gas may progress very slowly. These protoplanets evolve towards terrestrial planets, i.e. with iron-silicate composition. Protoplanets at larger radii (several AU), on the other hand, are able to accrete more mass from the surrounding disc gas. These protoplanets may take another $\sim 10^7$yr (e.g. Wuchterl et al. 2000) to evolve to gas giant planets.

During the accumulation process of a planetesimal, gravitational interaction with the surrounding gas can change the angular momentum of the object. This causes the planetesimal to have an orbital *migration* in either radially inward or outward directions. In this stage where the planetesimal is not massive enough to open a gap in the disc, the migration is known as *Type I migration* which generally moves the body towards the central star (Ward 1997). For a protoplanet in the later stages, however, the object may be massive enough to clear the disc material in its orbit. The migration of a protoplanet with an opening gap is called *Type II migration*. Sample simulations of planetary migration Type I and II are shown in Figure 1.17. In addition, the inward migration rate of Type I is rather higher than that of Type II (e.g. Ward 1997; D'Angelo et al. 2010).

Core accretion is an extremely slow process for building up a planet. One major issue of this model is the formation timescale of giant planets which exceeds the estimated disc lifetime of ~ 6Myr (Section 1.3.6). A long period of time is spent on growing the gaseous envelope in which the heat generated by the gravitational collapse is inefficiently removed due to the high dust opacity. However, Podolak (2003) has found that the dust opacity is significantly lower than that of previously estimated because of the rapid growth and settling of dust grains once entering the protoplanetary envelope. Using lower values of dust opacity in modelling the accumulation of the envelope, it is found that the formation timescale can be shorter and consistent with

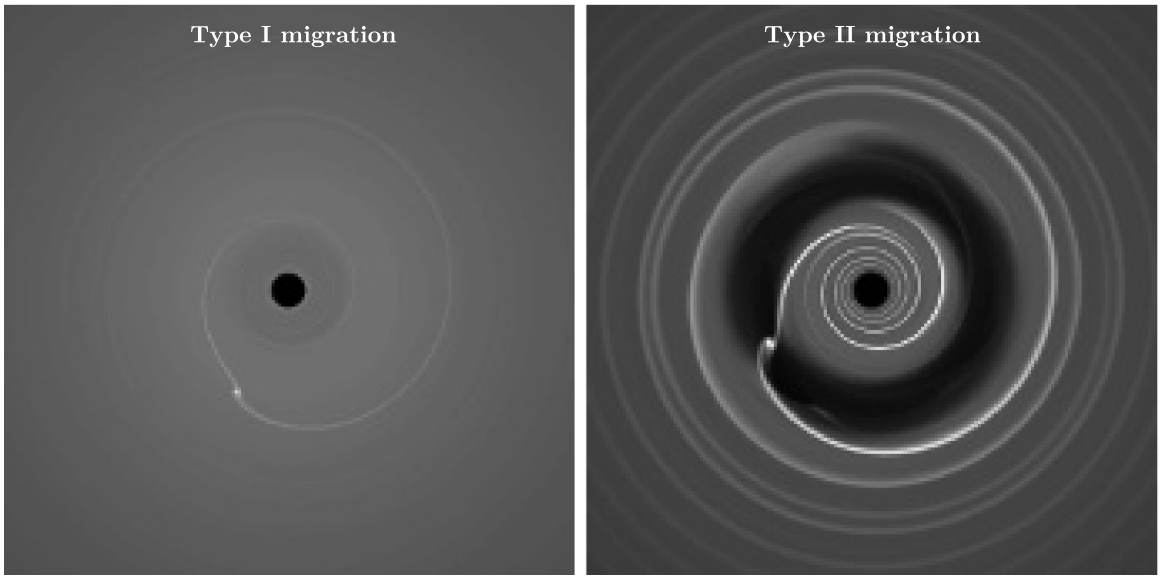

Figure 1.17 Disc simulations showing the main distinctive characteristic between Type I (left) and Type II (right) migrations. Type I migration progresses without creating a gap in the disc while Type II does. The image is taken from Armitage (2009).

the estimate disc lifetime (Hubickyj et al. 2005). Nevertheless, another important issue of core accretion model is the formation mechanism of planetesimals. Although collision provides a constructive effect in the coagulation of micron-size grains up to centimetre-size pebbles, it tends to provide destructive effect to objects with larger sizes (Dominik et al. 2007).

1.4.2 Disc instability model

Disc instability model suggests that protoplanetary mass objects is created from gravitational instabilities in a sufficiently massive protoplanetary discs. This model is essentially a smaller scale of multiple star formation via fragmentation of a massive extended disc, mentioned in Section 1.2.2. The onset of gravitational instabilities depends mainly on two parameters: (a) the Toomre parameter (Toomre 1964) and (b) the cooling time parameter (Gammie 2001). The Toomre parameter of a thin disc at radius R is given by

$$Q(R) = \frac{c_{\rm s}(R)\kappa(R)}{\pi G\Sigma(R)}, \tag{1.34}$$

where $c_{\rm s}$, κ, and Σ are the local sound speed, epicyclic frequency, and surface density, respectively. The disc at radius R becomes susceptible to gravitational instabilities

when $Q(R) \lesssim 1$. Each variable in Equation 1.34 has its own role in controlling the local stability. First, for an adiabatic disc, the local sound speed is given by

$$c_{\rm s} = \sqrt{\frac{\gamma \mathcal{R} T}{\mu}} \tag{1.35}$$

where γ, $\mathcal{R}$, T, and μ are the ratio of heat capacities, the specific gas constant, the temperature, and the mean molecular weight, respectively. It is clear that high temperature would tend to increase the value of Q, hence increasing the local stability of the disc. Second, for a Keplerian disc, the epicyclic frequency κ is equal to the local angular velocity $\Omega(R)$ or equivalently a reciprocal of the local dynamical timescale (Equation 1.27 and 1.28). The value of κ thus describes how fast a local region changes dynamically. In other words, significant dynamical changes such as clumping of the disc material have to occur within the dynamical timescale, otherwise would be smeared out by the centrifugal balance. Finally, for the disc to become unstable by the Toomre criterion, the product of $c_{\rm s}(R)$ and $\kappa(R)$ in Equation 1.34 has to be smaller than the denominator term dominated by the local surface density $\Sigma(R)$.

In more realistic situations, consideration of the Toomre parameter alone may not suffice to justify the likelihood of gravitational instabilities. That is, in order to promote the instabilities, the disc has to be able to efficiently remove excess heat from compression and other sources. This ability can be represented by the cooling time parameter, defined as

$$\beta_{\rm cool}(R) = t_{\rm cool}(R)\Omega(R), \tag{1.36}$$

where $t_{\rm cool}$ is a local cooling time required for removing heat occurs in a region at radius R from the central star. Stated otherwise, the cooling time parameter is a ratio between the local cooling time and the local dynamical timescale (Equation 1.27). For a thin disc, gravitational instabilities are likely to occur when $\beta_{\rm cool} \lesssim 3$ (Gammie 2001); the value may vary in discs with more realistic conditions (e.g. Rice et al. 2003, 2005).

It seems very promising that disc instability model is able to form giant planets within the disc lifetime and may only be a formation mode for giant planets at large orbital radii including those that found to have orbits exceeding 100AU (e.g. Lafrenière et al. 2008; Kalas et al. 2008). Nevertheless, it is found to be unlikely for disc fragmentation to occur in typical protoplanetary discs with radii smaller than 100AU because the cooling timescales in those discs are too long for gravitational

instabilities to be encouraged (Rafikov 2005). Although some earlier disc simulations have found the possibility of disc fragmentation in the protoplanetary discs (e.g. Boss 2000; Mayer et al. 2002), recent numerical works using more sophisticated radiation treatments confirm that the fragmentation is unlikely (e.g. Boley et al. 2006; Stamatellos and Whitworth 2008). In summary, even if the disc instability model is feasible, it may only be responsible for the formation of rather massive giant planets at large radii (i.e. several tens or a hundred of AU) while giant planets at smaller radii are formed by core accretion (Boley 2009).

1.5 Overview of thesis

In this thesis, we study (a) the dynamical evolution of young triple systems, (b) the evolution of isolated star-disc systems, and (c) the evolution of circumprimary discs in binary systems. Relevant background for this work have been provided in this chapter. In Chapter 2, we describe the methods for solving the N-body problem in the later chapters. Chapter 3 provides the description for the method of smoothed particle hydrodynamics (SPH). We use this method for our hydrodynamic disc simulations. In Chapter 4, we perform N-body simulations to investigate the dynamical evolution of young triple systems, particularly looking at the chance of collisions in coplanar systems. In Chapter 5, we move on to perform hydrodynamic simulations of isolated star-disc systems to investigate the behaviour of the discs prior to their quasi-equilibrium state. The discs are set up with various initial conditions and evolved up to the limit of particle resolution. In Chapter 6, we use one of the star-disc systems prepared in Chapter 5 to create star-disc-companion systems. The systems are initialized with various orbital configurations of the companion, especially inclined orbits. The perturbation from the inclined companion onto the disc in the systems causes the disc to precess and adjust the relative inclination angle. Our explanation to the behaviour of the disc is also provided in this chapter. Finally, we give a conclusion to our work in Chapter 7.

Chapter 2

Numerical methods for solving the N-body problem

In this chapter, we describe the numerical integration methods used for solving the N-body problems in our work. We begin this chapter with an outline of N-body problem in Section 2.1. The basic procedure for solving the problem with the Euler method is described in Section 2.2. Section 2.3 explains a second-order method known as the leapfrog integrators. The leapfrog method will be used for hydrodynamic simulations of circumstellar discs in Chapter 5 and Chapter 6. Section 2.4 explains a fourth-order Adams-Bashfourth-Moulton predictor-corrector method used for the N-body problem in Chapter 4. Finally, we summarize this chapter in Section 2.5.

2.1 N-body problem

The N-body problem concerns the evolution of a system consisting of N point-mass particles interacting with each other via only gravitational forces. By Newton's laws of motion and gravity, the motion of a particle of mass m_i in the system can be described by the equation of motion

$$\frac{\mathrm{d}^2\mathbf{r}_i}{\mathrm{d}t^2} = \mathbf{a}_i = -G\sum_{\substack{j=1\\ j\neq i}}^{N} \frac{m_j}{|\mathbf{r}_{ij}|^2}\hat{\mathbf{r}}_{ij} \tag{2.1}$$

where G is the gravitational constant, $\mathbf{a}_i$ the acceleration of particle i, and $\mathbf{r}_{ij} = \mathbf{r}_i - \mathbf{r}_j$ the relative position between particle i and j. Once the initial positions and velocities of all particles are known, the position $\mathbf{r}_i(t)$ and velocity $\mathbf{v}_i(t)$ of particle i at any time t can be solved by integrating Equation 2.1.

2.2 Basic numerical integration

Apart from systems with $N \leq 2$ and a handful of very special few-body systems, Equation 2.1 can be integrated only numerically. There are many numerical methods available with different degrees of accuracy and efficiency. However, the basic principle of most methods are similar. Suppose that we are to integrate a first-order differential equation

$$y'(x) = f(x, y(x)), \quad a \leq x \leq b; \tag{2.2}$$

with the initial condition

$$y(a) = y_0. \tag{2.3}$$

First of all, the interval from a to b needs to be divided into n_{tot} smaller steps, each with size of $\Delta x = (b-a)/n_{\text{tot}}$. The step size Δx must be small enough so that the value of y at step $n+1$ can be approximated by

$$y_{n+1} \simeq y_n + f(x_n, y_n)\Delta x, \tag{2.4}$$

where $0 \leq n < n_{\text{tot}}$. This basic method is also known as the Euler method. It provides a first-order approximation in which the error is of the order of Δx or $\mathcal{O}(\Delta x)$. Since the Euler method uses only the information from step n to approximate the solution at step $n+1$, it is also classified as a one-step method.

From Equation 2.4, the position and velocity of particle i at time $t = t_{n+1}$ can be written as

$$\mathbf{r}_{i,n+1} = \mathbf{r}_{i,n} + \mathbf{v}_{i,n}\Delta t, \tag{2.5a}$$

$$\mathbf{v}_{i,n+1} = \mathbf{v}_{i,n} + \mathbf{a}_{i,n}\Delta t, \tag{2.5b}$$

where $\mathbf{a}_{i,n}$ is obtained from Equation 2.1.

In N-body simulations, error in the approximation at timestep t_n is usually measured by the fractional error of the total energy defined as

$$\Delta E_n = \left| \frac{E_n - E_0}{E_0} \right|, \tag{2.6}$$

where E_0 and E_n are the total energy at $t = t_0$ and $t = t_n$, respectively. The total

energy of an N-body system can be calculated from

$$E = \sum_{i=1}^{N} \frac{1}{2} m_i v_i^2 - \sum_{i=1}^{N-1} \sum_{j=i+1}^{N} \frac{G m_i m_j}{r_{ij}}. \tag{2.7}$$

In this chapter, we will focus on two numerical methods used in this thesis: the second-order leapfrog and the fourth-order predictor-corrector methods. The second-order method provides a sufficient accuracy and speed for solving problems that require a huge number of particles, e.g. hydrodynamic problems in Chapter 5 and Chapter 6. The second-order method will be used together with the method of smoothed particle hydrodynamics described in Chapter 3. The fourth-order method, on the other hand, will be used for the N-body simulations in Chapter 4 since the nature of the problem requires higher accuracy.

2.3 Leapfrog method

Leapfrog integrators can be derived from Hamilton's equations (e.g. Binney and Tremaine 2008). Basically, a leapfrog integrator consists of two steps of integration called `drift` and `kick`. The `drift` step advances position while the `kick` step advances velocity. Therefore, one needs to combine both `drift` and `kick` steps to advance both position and velocity with a timestep size of Δt. A `drift-kick` integrator would thus sequentially perform

$$\mathbf{r}_{n+1} = \mathbf{r}_n + \mathbf{v}_n \Delta t, \tag{2.8a}$$

$$\mathbf{v}_{n+1} = \mathbf{v}_n + \mathbf{a}_{n+1} \Delta t, \tag{2.8b}$$

where $\mathbf{a}_{n+1}$ is calculated from Equation 2.1 using the new positions $\mathbf{r}_{n+1}$ from Equation 2.8a. By similar manner, a `kick-drift` integrator would perform

$$\mathbf{v}_{n+1} = \mathbf{v}_n + \mathbf{a}_n \Delta t, \tag{2.9a}$$

$$\mathbf{r}_{n+1} = \mathbf{r}_n + \mathbf{v}_{n+1} \Delta t. \tag{2.9b}$$

Leapfrog integrators are symplectic in that they conserve phase-space when a fixed timestep size is used. This means that they are good at confining the oscillation in the energy error between integration timesteps. However, the leapfrog in Equation 2.8 and 2.9 provide only first-order accuracy, $\mathcal{O}(\Delta t)$.

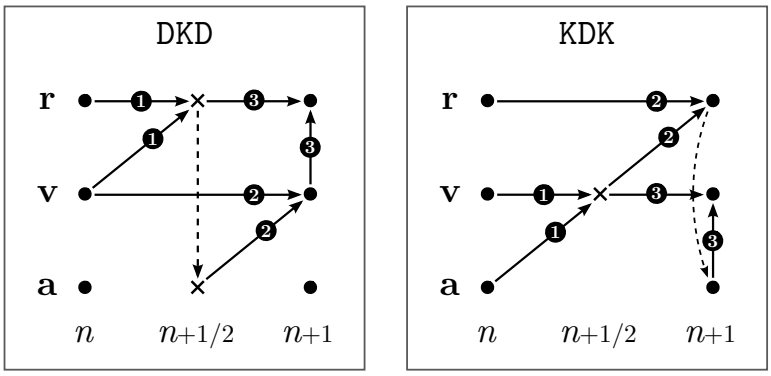

Figure 2.1 Diagrams illustrating three integration steps in the leapfrog DKD and KDK. Solid arrows link the relevant variables in each calculation step. The step numbers from 1 to 3 correspond to Equation 2.10a-c and Equation 2.11a-c. Dashed arrows show the intermediate step where forces (accelerations) are evaluated.

The higher-order leapfrog integrators can be obtained from the combinations `drift-kick-drift` (or DKD) and `kick-drift-kick` (or KDK). Both combinations consist of three integration steps: the first step advances position or velocity for $\Delta t/2$, the second step for Δt, and the third step for $\Delta t/2$. The leapfrog DKD integrator sequentially performs

$$\mathbf{r}_{n+\frac{1}{2}} = \mathbf{r}_n + \frac{1}{2}\mathbf{v}_n \Delta t \tag{2.10a}$$

$$\mathbf{v}_{n+1} = \mathbf{v}_n + \mathbf{a}_{n+\frac{1}{2}} \Delta t \tag{2.10b}$$

$$\mathbf{r}_{n+1} = \mathbf{r}_{n+\frac{1}{2}} + \frac{1}{2}\mathbf{v}_{n+1} \Delta t \tag{2.10c}$$

while the leapfrog KDK integrator performs

$$\mathbf{v}_{n+\frac{1}{2}} = \mathbf{v}_n + \frac{1}{2}\mathbf{a}_n \Delta t \tag{2.11a}$$

$$\mathbf{r}_{n+1} = \mathbf{r}_n + \mathbf{v}_{n+\frac{1}{2}} \Delta t \tag{2.11b}$$

$$\mathbf{v}_{n+1} = \mathbf{v}_{n+\frac{1}{2}} + \frac{1}{2}\mathbf{a}_{n+1} \Delta t. \tag{2.11c}$$

These integration steps are illustrated in Figure 2.1.

One advantage of the two integrators over many second-order integrators is that they require only one force calculation per timestep (at Equation 2.10b in DKD and at Equation 2.11c in KDK). Although both DKD and KDK perform equally well in hydrodynamic simulations, our preferred choice of integrator is the leapfrog KDK.

2.4 Adams-Bashfourth-Moulton method

In contrast to one-step methods such as the Euler and the leapfrog methods described above, multistep methods achieve a better approximation by considering the information from the previous timesteps in the integration. Our choice of the multistep method for this work is the fourth-order Adams-Bashfourth-Moulton predictor-corrector (ABM). This method provides fourth-order accuracy, $\mathcal{O}(\Delta t^4)$, with only two force evaluations per timestep required. As the name suggests, the method consists of two integrators: the predictor and the corrector. The ABM scheme uses the four-step, fourth-order Adams-Bashfourth

$$y_{n+1} = y_n + \frac{1}{24}[55f(t_n, y_n) - 59f(t_{n-1}, y_{n-1}) + 37f(t_{n-2}, y_{n-2}) - 9f(t_{n-3}, y_{n-3})]\Delta t \quad (2.12)$$

as the predictor, and the three-step, fourth-order Adams-Moulton

$$y_{n+1} = y_n + \frac{1}{24}[9f(t_{n+1}, y_{n+1}) + 19f(t_n, y_n) - 5f(t_{n-1}, y_{n-1}) + f(t_{n-2}, y_{n-2})]\Delta t \quad (2.13)$$

as the corrector (see e.g. Binney and Tremaine 2008). We can see that the corrector (Equation 2.13) is implicit in that the solution itself is required as a variable on the RHS of the equation. The advantage of this implicit method occurs in situations where an extremely small timestep size needs to be used if solved by an explicit method, i.e. the implicit method allows us to use a larger timestep size to achieve the same accuracy. Apparently, Equation 2.13 can not be solved directly. But, with the help of the predictor (Equation 2.12), the value of y_{n+1} required on the RHS of Equation 2.13 can be predicted and thus it can be used to evaluate y_{n+1} on the LHS.

The ABM predictor for N-body problems is given by

$$\mathbf{r}_{\text{P}} = \mathbf{r}_n + \frac{1}{24}(55\mathbf{v}_n - 59\mathbf{v}_{n-1} + 37\mathbf{v}_{n-2} - 9\mathbf{v}_{n-3})\Delta t, \quad (2.14a)$$

$$\mathbf{v}_{\text{P}} = \mathbf{v}_n + \frac{1}{24}(55\mathbf{a}_n - 59\mathbf{a}_{n-1} + 37\mathbf{a}_{n-2} - 9\mathbf{a}_{n-3})\Delta t, \quad (2.14b)$$

while the corrector is

$$\mathbf{r}_{\text{C}} = \mathbf{r}_n + \frac{1}{24}(9\mathbf{v}_{\text{P}} + 19\mathbf{v}_n - 5\mathbf{v}_{n-1} + \mathbf{v}_{n-2})\Delta t, \quad (2.15a)$$

$$\mathbf{v}_{\text{C}} = \mathbf{v}_n + \frac{1}{24}(9\mathbf{a}_{\text{P}} + 19\mathbf{a}_n - 5\mathbf{a}_{n-1} + \mathbf{a}_{n-2})\Delta t. \quad (2.15b)$$

Note that $\mathbf{a}_{\text{P}}$ in Equation 2.15b is calculated by using $\mathbf{r}_{\text{P}}$ from Equation 2.14a.

Before the ABM method can be used, the first four integration steps needs to be initiated. This can be done by using any one-step method with a sufficiently small and fixed timestep size. To obtain the same order of accuracy, we choose the fourth-order Runge-Kutta method in which its general form is given by

$$y_{n+1} = y_n + \frac{1}{6}(c_1 + 2c_2 + 2c_3 + c_4)\Delta t, \tag{2.16}$$

where

$$\begin{aligned} c_1 &= f(t_n, y_n)\,, \\ c_2 &= f(t_n + \Delta t/2, y_n + c_1/2)\,, \\ c_3 &= f(t_n + \Delta t/2, y_n + c_2/2)\,, \\ c_4 &= f(t_n + \Delta t, y_n + c_3)\,. \end{aligned}$$

In N-body simulations, the error of integration usually increases during a close encounter between particles. The situation can be worsened if a large timestep size is used. Using a smaller timestep size may help improve the accuracy, but it comes at the price of a longer simulation runtime. To overcome this problem, the timestep size of an integrator should be able to adjust according to the error. That is, a smaller timestep size should be used when the error tends to increase, otherwise use a larger size to speed up the calculation. In order to do this, some criteria are required to justify when the size should be changed to keep the balance between speed and accuracy. For the ABM method, the criterion for adjusting the timestep size is obtained from the truncation error of the method, given by

$$\epsilon = \frac{19}{270}\frac{y_{\mathrm{C},k+1} - y_{\mathrm{P},k+1}}{y_{\mathrm{C},k+1}}, \tag{2.17}$$

(Mathews and Fink 2004). The timestep size should be adjusted when the error is out of some specified tolerable range, i.e. $\epsilon_{\min} < \epsilon < \epsilon_{\max}$. In other words, the timestep size should be decreased to minimize the error when $\epsilon \geq \epsilon_{\max}$ and increased to speed up the calculation when $\epsilon \leq \epsilon_{\min}$. For our work in Chapter 4, we use our empirical error limits $\epsilon_{\min} = 8\times10^{-25}$ and $\epsilon_{\max} = 8\times10^{-17}$.

Since the ABM method needs even time-intervals for the contiguous steps from $n-3$ to n, resizing the timestep interval therefore needs adjustment for the values of those previous steps. This can be done by storing the values of y back to y_{n-6} and allowing the timestep size to be changed only by a factor of two, i.e. $\Delta t_{\mathrm{new}} = \Delta t_{\mathrm{old}}/2$

or $\Delta t_{\rm new} = 2\Delta t_{\rm old}$. When the timestep size is decreased, the values for the new set of previous timesteps can be interpolated by

$$\begin{aligned}
\tilde{y}_n &= y_n, \\
\tilde{y}_{n-1} &= \frac{1}{128}(35y_n + 140y_{n-1} - 70y_{n-2} + 28y_{n-3} - 5y_{n-4}), \\
\tilde{y}_{n-2} &= y_{n-1}, \\
\tilde{y}_{n-3} &= \frac{1}{128}(-5y_n + 60y_{n-1} + 90y_{n-2} - 20y_{n-3} + 3y_{n-4}),
\end{aligned}$$

where $\tilde{y}$ is an interpolated value of y, (Mathews and Fink 2004). The interpolation is easier in the case that the timestep size is increased, namely,

$$\begin{aligned}
\tilde{y}_n &= y_n, \\
\tilde{y}_{n-1} &= y_{n-2}, \\
\tilde{y}_{n-2} &= y_{n-4}, \\
\tilde{y}_{n-3} &= y_{n-6}.
\end{aligned}$$

2.5 Summary

We have described the numerical integration methods for using in our work. The methods will be used according to the nature of the problems. The second-order leapfrog `KDK`, which (as well as `DKD`) provides good approximation and speed for the problems that require a large number of particles (e.g. $> 10^4$), will be used for the hydrodynamic simulations performed in Chapter 5 and Chapter 6. The fourth-order Adams-Bashfourth-Moulton method that provides better approximation will be used for the N-body integration in Chapter 4 where the problem contains only three bodies but requires very high accuracy ($\Delta E_n \ll 10^{-5}$).

Chapter 3

Smoothed particle hydrodynamics

In this chapter, we describe a method for solving hydrodynamic problems. The method is known as smoothed particle hydrodynamics, or SPH for short. This method is now wildly used in many areas of science, including computational astrophysics. Being simple, adaptive to high density, and Galilean invariant make SPH a favourite choice for many star formation simulations. The formalism of SPH and some of its features that are used in this work will be described. However, some in-depth details of the method may be omitted as those can be found in a number of extensive reviews (e.g. Monaghan 1992; Cossins 2010; Price 2010).

This chapter begins with a brief introduction to Lagrangian hydrodynamics in Section 3.1, followed by the standard formalism of SPH in Section 3.2. The currently popular formalism of SPH (*grad-h* SPH) is described in Section 3.3. The equation of state that links thermal and dynamical quantities of the system together is described in Section 3.4. Timestepping and additional techniques used in this work are described respectively in Section 3.5 and 3.6. Finally, we briefly summarize this chapter in Section 3.7.

3.1 Lagrangian hydrodynamics

In fluid dynamics, there are two different approaches for describing fluid flow: the Eulerian and the Lagrangian approaches. The Eulerian approach describes a fluid flow with respect to fixed points on an equally-spaced grid spanning over the fluid volume. Fluid quantities at each point can be approximated by, for example, finite difference methods. In the Lagrangian approach, on the other hand, a fluid flow is traced by a number of movable particles. Fluid flow quantities are approximated at

the positions of the sampling particles which are moving along with the flow. SPH is one example of the particle-based methods that follow the Lagrangian approach. The advantages and disadvantages of both approaches have been demonstrated with several hydrodynamic codes (e.g. O'Shea et al. 2005; Agertz et al. 2007; Hubber et al. 2011).

Fluid dynamics are fundamentally shaped up by the conservation laws of mass, linear momentum, and energy. These three laws can be represented by three equations in Lagrangian form as

$$\textbf{Continuity equation:} \qquad \frac{\mathrm{d}\rho}{\mathrm{d}t} = -\rho\nabla\cdot\mathbf{v}, \tag{3.1a}$$

$$\textbf{Momentum equation:} \qquad \frac{\mathrm{d}\mathbf{v}}{\mathrm{d}t} = -\frac{\nabla P}{\rho} + \mathbf{f}, \tag{3.1b}$$

$$\textbf{Energy equation:} \qquad \frac{\mathrm{d}u}{\mathrm{d}t} = -\frac{P}{\rho}\nabla\cdot\mathbf{v}, \tag{3.1c}$$

where ρ is the density, P the pressure, $\mathbf{v}$ the velocity, $\mathbf{f}$ the non-pressure forces (e.g. gravity), and u the specific internal energy of the fluid. The principal idea of SPH is to turn Equation 3.1(a)-(c) into the discrete forms that can be solved numerically.

3.2 Standard formalism of SPH

The SPH method was introduced independently by Lucy (1977) and Gingold and Monaghan (1977). In SPH, a fluid is represented by a number of SPH particles distributed over the volume. Each SPH particle carries quantities such as mass, velocity, temperature, etc., of its current position in the volume. Other quantities such as density and pressure can be estimated by gathering the contribution from the surrounding or neighbouring particles. The amount of the contribution depends on the separation between the particle and its neighbours via an interpolating function.

The mathematical formulation of SPH is based on a weighted integral of a function $A(\mathbf{r})$ which is given by

$$A(\mathbf{r}) = \int A(\mathbf{r}')W(\mathbf{r}-\mathbf{r}', h)\,\mathrm{d}r', \tag{3.2}$$

where W is a weighting (or interpolating) function. In SPH, W is known as the *smoothing kernel* and the length h the *smoothing length*. The smoothing kernel describes how physical quantities distribute around the position $\mathbf{r}$, while the smoothing

length defines the extent covered by the kernel. In two and three dimensions, $\mathrm{d}r'$ in Equation 3.2 is replaced by $\mathrm{d}r'^2$ and $\mathrm{d}r'^3$, respectively. With Equation 3.2, a physical quantity at any point in the fluid volume can be estimated.

For consistency in the estimation, the smoothing kernel function has to be (a) an even function, i.e.

$$W(\mathbf{r}-\mathbf{r}',h) = W(|\mathbf{r}-\mathbf{r}'|,h); \tag{3.3}$$

(b) normalizable, so that

$$\int_0^\infty W(\mathbf{r}-\mathbf{r}',h)\,\mathrm{d}r' = 1; \tag{3.4}$$

(c) singular when $h \to 0$,

$$\lim_{h\to 0} W(\mathbf{r}-\mathbf{r}',h) = \delta(\mathbf{r}-\mathbf{r}'), \tag{3.5}$$

where $\delta(\mathbf{r}-\mathbf{r}')$ is the Dirac delta function; and finally (d) differentiable (or smooth) to at least the second derivative. One of the functions that satisfies these requirements and was also used in early years of SPH is a Gaussian function of the form

$$W(\mathbf{r}-\mathbf{r}',h) = \frac{1}{h^\nu \pi^{\nu/2}} \exp\left[-\frac{(\mathbf{r}-\mathbf{r}')^2}{h^2}\right], \tag{3.6}$$

where ν is the number of spatial dimensions.

Since a volume of fluid in SPH is represented by a finite number of particles, Equation 3.2, which holds for continuum distribution, needs to be modified to suit the discrete nature of a particle distribution. This can be done by turning Equation 3.2 into its equivalent summation form:

$$A(\mathbf{r}) \simeq \sum_i A(\mathbf{r}_i) W(\mathbf{r}-\mathbf{r}_i,h)\left(\frac{m_i}{\rho_i}\right), \tag{3.7}$$

where m_i/ρ_i represents the volume (three dimension). From this equation, the accuracy of the approximation depends on the number of SPH particles within the kernel, i.e. the higher the number the better the approximation.

In general, the points where the quantity A is estimated are chosen to be the same as the positions of the SPH particles. The estimated value of the quantity A_i

at particle i is then given by

$$A_i \simeq \sum_j m_j \frac{A_j}{\rho_j} W(\mathbf{r}_{ij}, h), \tag{3.8}$$

where $\mathbf{r}_{ij} = \mathbf{r}_i - \mathbf{r}_j$. The number of particles to be considered in the summation and the value of smoothing length will be discussed later in Section 3.3. A basic example of using Equation 3.8 in SPH is the estimation of density, i.e. $A = \rho$, at the position of particle i:

$$\rho_i \simeq \sum_j m_j W(\mathbf{r}_{ij}, h). \tag{3.9}$$

In typical simulations, every SPH particle has the same mass which is constant throughout the simulation. Selecting a value for the particle mass depends on a trade-off between the resolution and computing resources available. In star formation simulations, the resolution requirement may be set by the physical processes that need to be modelled properly. Fragmentation of a prestellar core, for example, is one of the processes that depend on resolution. Bate and Burkert (1997) suggest that, in order to resolve the fragmentation, the total mass of other particles neighbouring to one particle should be lower than the local Jeans mass (M_J, Equation 1.1) by a factor $f \simeq 1.5 - 2$. The mass required for each particle is therefore $m_\mathrm{sph} < M_\mathrm{J}/fN_\mathrm{neib}$, i.e. the lower the better.

For later references in deriving SPH, some useful expressions for the spatial derivatives (*gradient*, *divergence*, and *curl*) of Equation 3.8 are given as:

Gradient:
$$\nabla A_i \simeq \sum_j m_j \frac{A_j}{\rho_j} \nabla_i W(\mathbf{r}_{ij}, h) \tag{3.10a}$$

Divergence:
$$\nabla \cdot \mathbf{A}_i \simeq \sum_j m_j \frac{\mathbf{A}_j}{\rho_j} \cdot \nabla_i W(\mathbf{r}_{ij}, h) \tag{3.10b}$$

Curl:
$$\nabla \times \mathbf{A}_i \simeq -\sum_j m_j \frac{\mathbf{A}_j}{\rho_j} \times \nabla_i W(\mathbf{r}_{ij}, h) \tag{3.10c}$$

where ∇_i is the gradient with respect to the coordinates of particle i. Since it is clear that all SPH quantities are from estimations, the equals sign that will be used in all following SPH equations for convenience will actually mean *approximately equal*. Also, the smoothing kernel may be written in a concise form as W_{ij} for $W_{ij}(\mathbf{r}_{ij}, h)$ and $W_{ij}(h_i)$ for $W_{ij}(\mathbf{r}_{ij}, h_i)$.

3.2.1 Smoothing kernels

Using the Gaussian kernel in Equation 3.6 (suggested by Gingold and Monaghan (1977)), each particle needs to gather the contributions from the rest of the particles, even ones from large distances whose contribution can be negligible. This thus requires a huge computational effort in high-resolution simulations. To overcome this problem, a kernel function with compact support (i.e. $W = 0$ everywhere outside a certain range) may be used instead. One of the widely used kernels is the M4 cubic spline suggested by Monaghan and Lattanzio (1985):

$$W(r,h) = \frac{\sigma_\nu}{h^\nu} \begin{cases} 1 - \frac{3}{2}\left(\frac{r}{h}\right)^2 + \frac{3}{4}\left(\frac{r}{h}\right)^3 & \text{for} \quad 0 \le \frac{r}{h} < 1 \\ \frac{1}{4}\left(2 - \frac{r}{h}\right)^3 & \text{for} \quad 1 \le \frac{r}{h} < 2 \\ 0 & \text{for} \quad \frac{r}{h} \ge 2 \end{cases}, \tag{3.11}$$

where r is a separation between the particles, ν the number of spatial dimensions (1, 2, or 3), and σ_ν a normalization constant corresponding to the dimension; $\sigma_\nu = 2/3$, $10/7\pi$, and $1/\pi$ for $\nu = 1$, 2, and 3, respectively.

The gradient of the M4 kernel is

$$\nabla W(r,h) = -\frac{\sigma_\nu}{h^{\nu+1}} \left\{ \begin{array}{lll} 3\left(\frac{r}{h}\right) - \frac{9}{4}\left(\frac{r}{h}\right)^2 & \text{for} & 0 \le \frac{r}{h} < 1 \\ \frac{3}{4}\left(2 - \frac{r}{h}\right)^2 & \text{for} & 1 \le \frac{r}{h} < 2 \\ 0 & \text{for} & \frac{r}{h} \ge 2 \end{array} \right\} \hat{\mathbf{r}}, \tag{3.12}$$

where $\hat{\mathbf{r}}$ is the unit vector. For better results, however, one may use the modified version of the kernel gradient suggested by Thomas and Couchman (1992). The Thomas-Couchman M4 kernel gradient is given by

$$\nabla W(r,h) = -\frac{\sigma_\nu}{h^{\nu+1}} \left\{ \begin{array}{lll} 1 & \text{for} & 0 \le \frac{r}{h} < \frac{2}{3} \\ 3\left(\frac{r}{h}\right) - \frac{9}{4}\left(\frac{r}{h}\right)^2 & \text{for} & \frac{2}{3} \le \frac{r}{h} < 1 \\ \frac{3}{4}\left(2 - \frac{r}{h}\right)^2 & \text{for} & 1 \le \frac{r}{h} < 2 \\ 0 & \text{for} & \frac{r}{h} \ge 2 \end{array} \right\} \hat{\mathbf{r}}. \tag{3.13}$$

The flat piecewise at $0 \le r/h \le 2/3$ is to cope with the pairing instability in which the lowering of pressure force between a pair of particles calculated using the M4 kernel gradient often causes the two particles to pair up with each other; thus, sampling by the particles can be poor as particle distribution is not well dispersed. The comparison plots of the kernels and their derivatives are shown in Figure 3.1.

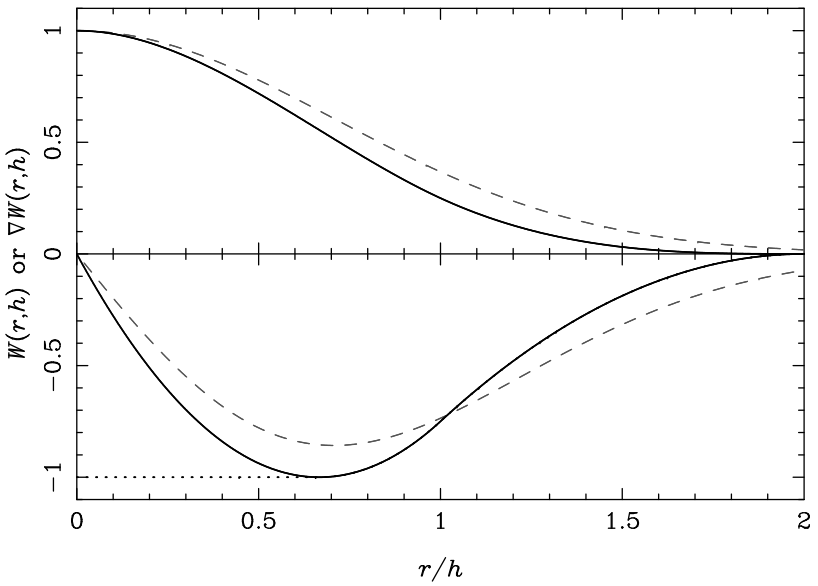

Figure 3.1 A comparison plot of un-normalized smoothing kernels. The solid curves are of the M4 kernel while the dashed curves are of the Gaussian. The kernels and their derivatives are on the positive and negative sides, respectively. The dotted straight line shows the aspect of the Thomas-Couchman M4 kernel derivative for $0 \leq r/h \leq 2/3$.

Additionally, the derivative of the M4 kernel with respect to the smoothing length is given by

$$\frac{\partial W}{\partial h}(r,h) = \frac{\sigma_\nu}{h^{\nu+1}} \begin{cases} -\nu + \frac{3}{2}(\nu+2)\left(\frac{r}{h}\right)^2 - \frac{3}{4}(\nu+3)\left(\frac{r}{h}\right)^3 & \text{for } 0 \leq \frac{r}{h} < 1 \\ -2\nu + 3(\nu+1)\left(\frac{r}{h}\right) - \frac{3}{2}(\nu+2)\left(\frac{r}{h}\right)^2 - \frac{3}{4}(\nu+3)\left(\frac{r}{h}\right)^3 & \text{for } 1 \leq \frac{r}{h} < 2 \\ 0 & \text{for } \frac{r}{h} \geq 2 \end{cases} . \quad (3.14)$$

This kernel derivative will be used in the variable smoothing length formalism described in Section 3.3.

3.2.2 Equation of motion

Most astrophysical fluid simulations are generally concerned with both hydrodynamic and gravitational forces. From the momentum equation of a fluid (Equation 3.1b), we may alternatively write the acceleration of an SPH particle i as

$$\frac{\mathrm{d}\mathbf{v}_i}{\mathrm{d}t} = \left[\left(\frac{\mathrm{d}\mathbf{v}_i}{\mathrm{d}t}\right)_{\text{pres}} + \left(\frac{\mathrm{d}\mathbf{v}_i}{\mathrm{d}t}\right)_{\text{visc}}\right]_{\text{hydro}} + \left(\frac{\mathrm{d}\mathbf{v}_i}{\mathrm{d}t}\right)_{\text{grav}}, \quad (3.15)$$

where the pressure term

$$\left(\frac{\mathrm{d}\mathbf{v}_i}{\mathrm{d}t}\right)_{\mathrm{pres}} = -\frac{\nabla_i P_i}{\rho_i}. \tag{3.16}$$

The gravity term can be determined from the N-body equation (Equation 2.1) with an extra consideration of kernel-softened gravity when the separation of the particles is shorter than the smoothing length (see below). The viscous force term will be described later in Section 3.2.4.

Pressure forces

The RHS of Equation 3.16 can be expressed in terms of SPH approximation by using the vector identity

$$\nabla\left(\frac{P}{\rho}\right) = \frac{\nabla P}{\rho} - \frac{P}{\rho^2}\nabla\rho.$$

Rearranging the terms and applying the SPH approximation (Equation 3.8) give us

$$\begin{aligned}
\frac{\nabla P_i}{\rho_i} &= \nabla_i\left(\frac{P_i}{\rho_i}\right) + \frac{P_i}{\rho_i^2}\nabla_i\rho_i \\
&= \nabla_i\left(\sum_j m_j \frac{P_j}{\rho_j^2} W_{ij}\right) + \frac{P_i}{\rho_i^2}\nabla_i\left(\sum_j m_j W_{ij}\right) \\
&= \sum_j m_j \frac{P_j}{\rho_j^2}\nabla_i W_{ij} + \frac{P_i}{\rho_i^2}\sum_j m_j \nabla_i W_{ij}.
\end{aligned}$$

The acceleration of particle i due to pressure forces then reads

$$\left(\frac{\mathrm{d}\mathbf{v}_i}{\mathrm{d}t}\right)_{\mathrm{pres}} = -\sum_j m_j\left(\frac{P_i}{\rho_i^2} + \frac{P_j}{\rho_j^2}\right)\nabla_i W_{ij}. \tag{3.17}$$

Gravitational forces

Since the mass of an SPH particle represents the mass inside the radius $2h$, the gravitational interaction between any pair of particles with separation $r_{ij} < 2h$ needs to be modelled consistently by accounting for the distribution of mass in that separation. In order to achieve this, let us consider the gravitational potential (Φ_i) at particle i

defined by

$$\Phi_i = G\sum_j m_j\phi_{ij}, \tag{3.18}$$

where $\phi_{ij} = \phi(\mathbf{r}_{ij}, h)$ is the softening kernel for gravitational potential. The kernel must have the same properties as the potential Φ_i: namely, (a) $\phi(r,h) < 0$ for all r and h, (b) $\nabla\phi(0,h) = 0$, and (c) $\lim_{r/h\to\infty}\phi(r,h) = -1/r$ (Cossins 2010). It can be shown that ϕ_{ij} is related to W_{ij} by considering Poisson's equation,

$$\nabla^2\Phi_i = 4\pi G\rho_i. \tag{3.19}$$

Substituting Φ_i from Equation 3.18 and ρ_i from Equation 3.9 gives us

$$\nabla^2\left(G\sum_j m_j\phi_{ij}\right) = 4\pi G\left(\sum_j m_j W_{ij}\right). \tag{3.20}$$

We can see that

$$\nabla^2\phi_{ij} = 4\pi W_{ij}. \tag{3.21}$$

As the extent of the particle is spherically symmetric, only radial component of the Laplacian needs to be considered, i.e.

$$\frac{\partial}{\partial r}\left(r^2\frac{\partial\phi}{\partial r}\right) = 4\pi r^2 W, \tag{3.22}$$

where $r = r_{ij}$ is used and the index variables are dropped for convenience. Integrating this equation gives us the gradient of ϕ,

$$\frac{\partial\phi}{\partial r} = \frac{4\pi}{r^2}\int_0^r r'^2 W(r')\,\mathrm{d}r'. \tag{3.23}$$

For the M4 kernel given by Equation 3.11, one can find that

$$\nabla\phi(r,h) = \frac{1}{h^2}\left\{\begin{array}{lll} \frac{4}{3}\left(\frac{r}{h}\right) - \frac{6}{5}\left(\frac{r}{h}\right)^3 + \frac{1}{2}\left(\frac{r}{h}\right)^4 & \text{for} & 0 \le \frac{r}{h} < 1 \\ \frac{8}{3}\left(\frac{r}{h}\right) - 3\left(\frac{r}{h}\right)^2 + \frac{6}{5}\left(\frac{r}{h}\right)^3 - \frac{1}{6}\left(\frac{r}{h}\right)^4 - \frac{1}{15}\left(\frac{h}{r}\right)^2 & \text{for} & 1 \le \frac{r}{h} < 2 \\ \left(\frac{h}{r}\right)^2 & \text{for} & \frac{r}{h} \ge 2 \end{array}\right\}\hat{\mathbf{r}}. \tag{3.24}$$

Now, the gravitational acceleration acting on particle i can be found from

$$\left(\frac{\mathrm{d}\mathbf{v}_i}{\mathrm{d}t}\right)_{\mathrm{grav}} = -\nabla\Phi_i = -G\sum_j m_j \nabla_i \phi_{ij}. \tag{3.25}$$

With the kernel gradient provided by Equation 3.24, the strength of gravity between particles will be softened when $r_{ij} < 2h$ and follows the usual inverse-square law when $r_{ij} \geq 2h$.

Before we move on, it is useful to find the expression for ϕ, as we will need to use it later in Section 3.4.4. This can be obtained from integrating Equation 3.23, i.e.

$$\phi = 4\pi \int_0^r \frac{1}{r'^2}\left[\int_0^r r'^2 W(r')\,\mathrm{d}r'\right]\mathrm{d}r'. \tag{3.26}$$

Rearranging the terms gives us

$$\phi = 4\pi\left[-\frac{1}{r}\int_0^r r'^2 W(r')\,\mathrm{d}r' + \int_0^r r' W(r')\,\mathrm{d}r'\right]. \tag{3.27}$$

For the same M4 kernel (Equation 3.11), we can find that

$$\phi(r,h) = -\frac{1}{h}\begin{cases} \frac{7}{5} - \frac{2}{3}\left(\frac{r}{h}\right)^2 + \frac{3}{10}\left(\frac{r}{h}\right)^4 - \frac{1}{10}\left(\frac{r}{h}\right)^5 & \text{for} \quad 0 \leq \frac{r}{h} < 1 \\ \frac{8}{5} - \frac{4}{3}\left(\frac{r}{h}\right)^2 + \left(\frac{r}{h}\right)^3 - \frac{3}{10}\left(\frac{r}{h}\right)^4 + \frac{1}{30}\left(\frac{r}{h}\right)^5 - \frac{1}{15}\frac{h}{r} & \text{for} \quad 1 \leq \frac{r}{h} < 2 \\ \frac{h}{r} & \text{for} \quad \frac{r}{h} \geq 2 \end{cases}. \tag{3.28}$$

3.2.3 Energy equation

In standard SPH, the RHS of Equation 3.1c can be expressed by two expressions derived from different vector identities. The first expression for the energy term is derived from the identity

$$\nabla\cdot(\rho\mathbf{v}) = \rho\nabla\cdot\mathbf{v} + \mathbf{v}\cdot\nabla\rho. \tag{3.29}$$

By multiplying both sides with P/ρ^2 and rearranging the terms, we have

$$\begin{aligned} \frac{P_i}{\rho_i}\nabla\cdot\mathbf{v}_i &= \frac{P_i}{\rho_i^2}\left[\nabla_i\cdot(\rho_i\mathbf{v}_i) - \mathbf{v}_i\cdot\nabla_i\rho_i\right] \\ &= \frac{P_i}{\rho_i^2}\left[\sum_j m_j\mathbf{v}_j\cdot\nabla_i W_{ij} - \sum_j m_j\mathbf{v}_i\cdot\nabla_i W_{ij}\right] \end{aligned}$$

$$= -\sum_j m_j \left(\frac{P_i}{\rho_i^2}\right) (\mathbf{v}_i - \mathbf{v}_j)\cdot\nabla_i W_{ij}.$$

The energy equation resulting from this derivation is then

$$\frac{\mathrm{d}u_i}{\mathrm{d}t} = \sum_j m_j \left(\frac{P_i}{\rho_i^2}\right) \mathbf{v}_{ij}\cdot\nabla_i W_{ij}. \tag{3.30}$$

where $\mathbf{v}_{ij} = \mathbf{v}_i - \mathbf{v}_j$.

The second expression is derived from the vector identity

$$\nabla\cdot\left(\frac{P\mathbf{v}}{\rho}\right) = \frac{P}{\rho}\nabla\cdot\mathbf{v} + \mathbf{v}\cdot\nabla\left(\frac{P}{\rho}\right). \tag{3.31}$$

From this, we have

$$\begin{aligned}
\frac{P_i}{\rho_i}\nabla\cdot\mathbf{v}_i &= \nabla_i\cdot\left(\frac{P_i\mathbf{v}_i}{\rho_i}\right) - \mathbf{v}_i\cdot\nabla_i\left(\frac{P_i}{\rho_i}\right) \\
&= \sum_j m_j \left(\frac{P_j}{\rho_j^2}\right) \mathbf{v}_j\cdot\nabla_i W_{ij} - \sum_j m_j \left(\frac{P_j}{\rho_j^2}\right) \mathbf{v}_i\cdot\nabla_i W_{ij} \\
&= -\sum_j m_j \left(\frac{P_j}{\rho_j^2}\right) (\mathbf{v}_i - \mathbf{v}_j)\cdot\nabla_i W_{ij}.
\end{aligned}$$

The energy equation becomes

$$\frac{\mathrm{d}u_i}{\mathrm{d}t} = \sum_j m_j \left(\frac{P_j}{\rho_j^2}\right) \mathbf{v}_{ij}\cdot\nabla_i W_{ij}. \tag{3.32}$$

Although Equation 3.30 and 3.32 can be used on their own, the average form is also preferred, i.e.

$$\left(\frac{\mathrm{d}u_i}{\mathrm{d}t}\right)_{\text{pres}} = \frac{1}{2}\sum_j m_j \left(\frac{P_i}{\rho_i^2} + \frac{P_j}{\rho_j^2}\right) \mathbf{v}_{ij}\cdot\nabla_i W_{ij}. \tag{3.33}$$

Note that the energy equations derived here are only for the change of energy due to pressure forces, the one that is associated with viscous forces is described in next section.

3.2.4 Artificial viscosity

When supersonic flows are colliding, a sudden increase in density (or a shock) is created. In the shock compressed regions, the kinetic energy of the flows is turned into heat. Modelling this phenomenon using the SPH method prescribed earlier fails as the pressure terms alone are inadequate to prevent SPH particles in a high-velocity flow passing through each other freely. In order to alleviate this problem, an artificial viscous force and its corresponding energy are added to the force equation (Equation 3.15) and the energy equation (Equation 3.33), respectively (e.g. Monaghan 1992, and references therein). The *artificial viscosity* that causes the artificial viscous force is given by

$$\Pi_{ij} = \begin{cases} \dfrac{-\alpha \bar{c}_{ij} \mu_{ij} + \beta \mu_{ij}^2}{\bar{\rho}_{ij}} & \text{for} \quad \mathbf{v}_{ij} \cdot \mathbf{r}_{ij} < 0 \\ 0 & \text{for} \quad \mathbf{v}_{ij} \cdot \mathbf{r}_{ij} \geq 0 \end{cases}, \tag{3.34}$$

where the parameter

$$\mu_{ij} = \frac{h \mathbf{v}_{ij} \cdot \mathbf{r}_{ij}}{|\mathbf{r}_{ij}|^2 + \eta^2} \tag{3.35}$$

specifies how the viscosity should behave, i.e. proportional to the relative velocity and the inverse of separation. The other parameters in Equation 3.34 and 3.35 are the average sound speed $\bar{c}_{ij} = (c_i + c_j)/2$, the average density $\bar{\rho}_{ij} = (\rho_i + \rho_j)/2$, and a constant $\eta \simeq 0.1h$ for preventing a singularity when $|\mathbf{r}_{ij}| \to 0$. The parameters α and β are for controlling the viscosity of the fluid at low and high relative velocities, respectively. Although Monaghan (1992) suggests $\alpha \simeq 1$ and $\beta \simeq 2$ for general SPH simulations, the values can be varied. In many works, keeping $\beta \simeq 2\alpha$ is usually preferred. The acceleration and energy terms due to the artificial viscosity can be written as

$$\left(\frac{\mathrm{d}\mathbf{v}_i}{\mathrm{d}t}\right)_{\mathrm{visc}} = -\sum_j m_j \Pi_{ij} \nabla_i W_{ij} \tag{3.36}$$

and

$$\left(\frac{\mathrm{d}u_i}{\mathrm{d}t}\right)_{\mathrm{visc}} = \frac{1}{2} \sum_j m_j \Pi_{ij} \mathbf{v}_{ij} \cdot \nabla_i W_{ij}, \tag{3.37}$$

respectively. The equations of the hydrodynamic acceleration and energy become

$$\left(\frac{\mathrm{d}\mathbf{v}_i}{\mathrm{d}t}\right)_{\mathrm{hydro}} = -\sum_j m_j \left(\frac{P_i}{\rho_i^2} + \frac{P_j}{\rho_j^2} + \Pi_{ij}\right) \nabla_i W_{ij} \tag{3.38}$$

and

$$\left(\frac{\mathrm{d}u_i}{\mathrm{d}t}\right)_{\mathrm{hydro}} = \frac{1}{2}\sum_j m_j \left(\frac{P_i}{\rho_i^2} + \frac{P_j}{\rho_j^2} + \Pi_{ij}\right) \mathbf{v}_{ij}\cdot\nabla_i W_{ij}. \tag{3.39}$$

respectively.

Besides the standard viscosity prescription, an alternative form which is based on Riemann solvers was suggested to provide a better viscosity modelling (Monaghan 1997; Price 2008). In this form, the acceleration equation is given by

$$\left(\frac{\mathrm{d}\mathbf{v}_i}{\mathrm{d}t}\right)_{\mathrm{visc}} = -\sum_j m_j \frac{\alpha v_{\mathrm{sig}} \mathbf{v}_{ij}\cdot\hat{\mathbf{r}}_{ij}}{\bar{\rho}_{ij}} \overline{\nabla_i W}_{ij}, \tag{3.40}$$

while the energy equation is

$$\left(\frac{\mathrm{d}u_i}{\mathrm{d}t}\right)_{\mathrm{visc}} = -\sum_j \frac{m_j}{\bar{\rho}_{ij}} \left[\frac{1}{2}\alpha v_{\mathrm{sig}} (\mathbf{v}_{ij}\cdot\hat{\mathbf{r}}_{ij})^2 + \alpha' v'_{\mathrm{sig}} (u_i - u_j)\right] \hat{\mathbf{r}}_{ij}\cdot\nabla_i W_{ij}, \tag{3.41}$$

where $\alpha' \simeq 1$. The first and the second terms in the square brackets on the RHS associate with the artificial viscosity and the artificial thermal conductivity, respectively. The parameters v_{sig} and v'_{sig} are signal speeds given by

$$v_{\mathrm{sig}} = c_i + c_j - \beta \mathbf{v}_{ij}\cdot\hat{\mathbf{r}}_{ij} \tag{3.42}$$

and

$$v'_{\mathrm{sig}} = \sqrt{\frac{|P_i - P_j|}{\bar{\rho}_{ij}}}, \tag{3.43}$$

respectively.

Even though the artificial viscosity helps improve modelling shocks, it can result in an unphysical transfer of angular momentum in shearing motions between particles such as found in disc simulations. Two methods were introduced to reduce the effect of the artificial shear viscosity. They are described as follows.

Balsara switch

Balsara (1995) suggests that the artificial viscosity should be fully active only in strong converging flows and completely vanished in strong shear flows. The amplitude of converging flows and shear flows can be represented by $|\nabla\cdot\mathbf{v}|$ and $|\nabla\times\mathbf{v}|$, respectively. These terms can be found from the identities

$$\nabla\cdot\mathbf{v} = \frac{1}{\rho}\left[\nabla\cdot(\rho\mathbf{v}) - \mathbf{v}\cdot\nabla\rho\right], \tag{3.44}$$

which is Equation 3.29, and

$$\nabla\times\mathbf{v} = \frac{1}{\rho}\left[\nabla\times(\rho\mathbf{v}) + \mathbf{v}\times\nabla\rho\right]. \tag{3.45}$$

With some manipulations using Equation 3.10a-c for the spatial derivatives in both identities, we have

$$\nabla\cdot\mathbf{v}_i = -\frac{1}{\rho_i}\sum_j m_j\mathbf{v}_{ij}\cdot\nabla_i W_{ij}, \tag{3.46}$$

and

$$\nabla\times\mathbf{v}_i = \frac{1}{\rho_i}\sum_j m_j\mathbf{v}_{ij}\times\nabla_i W_{ij}. \tag{3.47}$$

Weighting the influence of viscosity is done by multiplying the viscosity term Π_{ij} by a factor $\bar{f}_{ij} = (f_i + f_j)/2$, where

$$f = \frac{|\nabla\cdot\mathbf{v}|}{|\nabla\cdot\mathbf{v}| + |\nabla\times\mathbf{v}| + 0.0001c/h}. \tag{3.48}$$

With this factor, the viscosity will be minimized ($\bar{f}_{ij}\sim 0$) in shear dominated flows where $|\nabla\cdot\mathbf{v}| \ll |\nabla\times\mathbf{v}|$ and maximized ($\bar{f}_{ij}\sim 1$) in convergence dominated flows where $|\nabla\cdot\mathbf{v}| \gg |\nabla\times\mathbf{v}|$.

Time-dependent viscosity

This method allows each particle to have its own viscosity parameter α_i which varies as a function of time and the velocity divergence. Morris and Monaghan (1997) suggest

α_i obtained from the differential equation

$$\frac{\mathrm{d}\alpha_i}{\mathrm{d}t} = -\frac{\alpha_i + \alpha_{\min}}{\tau_i} + S_i, \tag{3.49}$$

where $\alpha_{\min}$ is the minimum viscosity parameter, τ_i the decay timescale for the viscosity, and S_i the source function given by

$$S_i = \mathrm{MAX}(-\nabla{\cdot}v_i, 0)(\alpha_{\max} - \alpha_i), \tag{3.50}$$

where $\alpha_{\max}$ is the maximum value of viscosity parameter. Typically, we use $\alpha_{\min} = 0.1$ and $\tau_i = h_i/\mathcal{C}c_i$, where $\mathcal{C} = 0.1 - 0.2$ and c_i is the local sound speed.

From Equation 3.49, α_i attenuates exponentially to $\alpha_{\min}$ within a timescale τ_i in a non-converging flow in which $\nabla{\cdot}v_i \geq 0$ and thus $S_i = 0$. Once a shock starts to form, i.e. $\nabla{\cdot}v_i < 0$ and thus $S_i > 0$, the source term can increase the value of α_i according to the intensity of the shock.

3.3 Variable smoothing length SPH

In early versions of SPH, every particle uses the same value of smoothing length, which is also held constant throughout the simulation. The problem arises when the density varies from region to region. That is, particles in very low density regions may have too few neighbouring particles, while particles in very high density regions have too many. This may severely reduce the accuracy of the approximation in very low density regions while unnecessarily causing longer calculation times in the other. To overcome this problem, particles should be allowed to have their own smoothing length which is adaptable to the local particle distribution.

One simple way is by forcing the smoothing length of each particle to vary with the extent of its own nearest neighbours. To do so, the number of neighbours N_{neib} is set to be globally constant, i.e. every particle has the same number of nearest neighbours. Typically, $N_{\mathrm{neib}} = 50$ is used for three-dimensional simulations. The smoothing length of any particle thus becomes a half of the distance between the particle and its outermost neighbour, $h_i = |\mathbf{r}_i - \mathbf{r}_{N_{\mathrm{neib}}}|/2$.

Once the particles have their own smoothing length, however, there comes a problem with momentum conservation due to particles having different smoothing lengths. In other words, if $h_i \neq h_j$, the forces acting on particles i and j due to one another can not be equal and opposite, violating Newton's third law of motion. In order to

guarantee the symmetry of pairwise forces, Hernquist and Katz (1989) suggest using the average smoothing kernel

$$\overline{W}(\mathbf{r}_{ij}) = \frac{W_{ij}(h_i) + W_{ij}(h_j)}{2},$$

while Benz (1990) suggest using the average smoothing length

$$\bar{h}_{ij} = \frac{h_i + h_j}{2}.$$

Nevertheless, Hernquist (1993) points out that the energy may not be conserved well from using either of these methods. Until recently, the more sophisticated *grad-h* method has been introduced to improve the situation.

3.3.1 The *grad-h* method

This method intends to ensure energy conservation in SPH whilst the smoothing length is varying. Springel and Hernquist (2002) and Price and Monaghan (2004) reformulate the momentum and energy equations from the Euler-Lagrangian equation and use an adaptive smoothing length that varies with the local density. The relation between the smoothing length h_i and local density ρ_i of particle i is given by

$$h_i = \eta \left(\frac{m_i}{\rho_i}\right)^{1/3}, \tag{3.51}$$

where η is a parameter valued between 1.2 and 1.5 (Gingold and Monaghan 1982; Price 2004; Monaghan 2005). This parameter η controls the average number of neighbours via $\bar{N}_{\rm neib} \simeq 2\mathcal{R}\eta$, $\pi(2\mathcal{R}\eta)^2$, and $(4\pi/3)(2\mathcal{R}\eta)^3$ for one, two, and three dimension, respectively. The parameter $\mathcal{R} = 2$ is used for the M4 kernel of Monaghan and Lattanzio (1985). The density in Equation 3.51 is obtained from

$$\rho_i = \sum_j m_j W_{ij}(h_i), \tag{3.52}$$

where only h_i is used in the kernel and the summation is over all particles including particle i itself. One can see that the smoothing length is now an implicit function which can be solved only by using an iterative method (see Price 2004).

Before we proceed to further derivations, it is useful to derive the expressions for the gradient and time derivatives of the separation r_{ij} and the kernel W_{ij}. First of

all, let us consider the gradient of $r_{ij} = |\mathbf{r}_i - \mathbf{r}_j|$ with respect to the coordinate of an arbitrary particle k,

$$\nabla_k r_{ij} = \frac{\partial}{\partial \mathbf{r}_k} |\mathbf{r}_i - \mathbf{r}_j| = \hat{\mathbf{r}}_{ij}(\delta_{ik} - \delta_{jk}), \tag{3.53}$$

where δ_{ik} and δ_{jk} are the Kronecker delta functions. If k is either i or j, we have

$$\nabla_k r_{ij} = \begin{cases} \hat{\mathbf{r}}_{ij} & \text{for} \quad k = i \\ -\hat{\mathbf{r}}_{ij} & \text{for} \quad k = j \end{cases}. \tag{3.54}$$

Therefore,

$$\nabla_i r_{ij} = -\nabla_j r_{ij}. \tag{3.55}$$

Similarly, with the help of Equation 3.53, one can find that the gradient of W_{ij} with respect to the coordinate of an arbitrary particle k is

$$\begin{aligned} \nabla_k W_{ij} &= \frac{\partial W_{ij}}{\partial \mathbf{r}_k} = \frac{\partial W_{ij}}{\partial r_{ij}} \frac{\partial r_{ij}}{\partial \mathbf{r}_k} = \frac{\partial W_{ij}}{\partial r_{ij}} \hat{\mathbf{r}}_{ij}(\delta_{ik} - \delta_{jk}) \\ &= \nabla_i W_{ij}(\delta_{ik} - \delta_{jk}). \end{aligned} \tag{3.56}$$

This gives us the relation

$$\nabla_i W_{ij} = -\nabla_j W_{ij}. \tag{3.57}$$

Since r_{ij} depends on both $r_i(t)$ and $r_j(t)$, its time derivative must be obtained by means of the total derivative

$$\begin{aligned} \frac{\mathrm{d}r_{ij}}{\mathrm{d}t} &= \frac{\partial r_{ij}}{\partial \mathbf{r}_i} \cdot \frac{\mathrm{d}\mathbf{r}_i}{\mathrm{d}t} + \frac{\partial r_{ij}}{\partial \mathbf{r}_j} \cdot \frac{\mathrm{d}\mathbf{r}_j}{\mathrm{d}t} \\ &= \frac{\partial r_{ij}}{\partial \mathbf{r}_i} \cdot \frac{\mathrm{d}\mathbf{r}_i}{\mathrm{d}t} - \frac{\partial r_{ij}}{\partial \mathbf{r}_i} \cdot \frac{\mathrm{d}\mathbf{r}_j}{\mathrm{d}t} \\ &= (\mathbf{v}_i - \mathbf{v}_j) \cdot \frac{\partial r_{ij}}{\partial \mathbf{r}_i} \\ &= \mathbf{v}_{ij} \cdot \nabla_i r_{ij}. \end{aligned} \tag{3.58}$$

With this expression, the time derivative of W_{ij} becomes

$$\begin{aligned}\frac{\mathrm{d}W_{ij}}{\mathrm{d}t} &= \frac{\partial W_{ij}}{\partial r_{ij}}\frac{\mathrm{d}r_{ij}}{\mathrm{d}t} \\ &= \frac{\partial W_{ij}}{\partial r_{ij}}\frac{\partial r_{ij}}{\partial \mathbf{r}_i}\cdot\mathbf{v}_{ij} \\ &= \mathbf{v}_{ij}\cdot\nabla_i W_{ij}. \end{aligned} \tag{3.59}$$

3.3.2 Equation of motion

To derive the equation of motion (see e.g. Price 2004; Rosswog 2009; Cossins 2010), let us consider the Lagrangian (L) of a fluid parcel

$$L = \int\left(\frac{1}{2}\mathbf{v}\cdot\mathbf{v} - u(\rho, s) - \frac{1}{2}\Phi\right)\rho\,\mathrm{d}V, \tag{3.60}$$

where $\mathbf{v}$ is the velocity of the fluid parcel, u the specific internal energy as a function of density ρ and specific entropy s, Φ the gravitational potential, and V the fluid volume. This Lagrangian can be expressed in terms of a summation over all SPH particles as

$$L_{\mathrm{sph}} = \sum_j m_j\left(\frac{1}{2}\mathbf{v}_j\cdot\mathbf{v}_j - u(\rho_j, s_j) - \frac{1}{2}\Phi_j\right). \tag{3.61}$$

By using a constant value of mass, L_{sph} satisfies the Euler-Lagrange equation

$$\frac{\mathrm{d}}{\mathrm{d}t}\left(\frac{\partial L_{\mathrm{sph}}}{\partial \mathbf{v}_i}\right) - \frac{\partial L_{\mathrm{sph}}}{\partial \mathbf{r}_i} = 0. \tag{3.62}$$

The first term on the LHS is the total rate of change of the linear momentum, i.e.

$$\begin{aligned}\frac{\mathrm{d}}{\mathrm{d}t}\left(\frac{\partial L_{\mathrm{sph}}}{\partial \mathbf{v}_i}\right) &= \frac{\mathrm{d}}{\mathrm{d}t}\left[\frac{\partial}{\partial \mathbf{v}_i}\sum_j m_j\left(\frac{1}{2}\mathbf{v}_j\cdot\mathbf{v}_j - u(\rho_j, s_j) - \frac{1}{2}\Phi_j\right)\right] \\ &= \frac{\mathrm{d}}{\mathrm{d}t}\left(\frac{1}{2}m_i\frac{\partial}{\partial \mathbf{v}_i}(\mathbf{v}_i\cdot\mathbf{v}_i)\right) \\ &= m_i\frac{\mathrm{d}\mathbf{v}_i}{\mathrm{d}t}, \end{aligned} \tag{3.63}$$

or the total force. The second term thus consists of the forces associated with the motion of particle i, i.e. pressure and gravity. For simplicity, we may split the

Lagrangian in Equation 3.61 into two terms of pressure and gravity:

$$L_{\text{sph}} = L_{\text{pres}} + L_{\text{grav}}, \tag{3.64}$$

where

$$L_{\text{pres}} = \sum_j m_j \left(\frac{1}{2} \mathbf{v}_j \cdot \mathbf{v}_j - u(\rho_j, s_j) \right) \tag{3.65}$$

and

$$L_{\text{grav}} = -\frac{1}{2} \sum_j m_j \Phi_j. \tag{3.66}$$

By writing the equation of motion as

$$\frac{\mathrm{d}\mathbf{v}_i}{\mathrm{d}t} = \left(\frac{\mathrm{d}\mathbf{v}_i}{\mathrm{d}t} \right)_{\text{pres}} + \left(\frac{\mathrm{d}\mathbf{v}_i}{\mathrm{d}t} \right)_{\text{grav}}, \tag{3.67}$$

we then have

$$\left(\frac{\mathrm{d}\mathbf{v}_i}{\mathrm{d}t} \right)_{\text{pres}} = \frac{1}{m_i} \frac{\partial L_{\text{pres}}}{\partial \mathbf{r}_i} \tag{3.68}$$

and

$$\left(\frac{\mathrm{d}\mathbf{v}_i}{\mathrm{d}t} \right)_{\text{grav}} = \frac{1}{m_i} \frac{\partial L_{\text{grav}}}{\partial \mathbf{r}_i}. \tag{3.69}$$

The pressure term. Substituting L_{pres} from Equation 3.65 into 3.68 gives us

$$\begin{aligned} \left(\frac{\mathrm{d}\mathbf{v}_i}{\mathrm{d}t} \right)_{\text{pres}} &= \frac{1}{m_i} \frac{\partial}{\partial \mathbf{r}_i} \left[\sum_j m_j \left(\frac{1}{2} \mathbf{v}_j \cdot \mathbf{v}_j - u(\rho_j, s_j) \right) \right] \\ &= -\frac{1}{m_i} \sum_j m_j \frac{\partial u_j}{\partial \mathbf{r}_i} \\ &= -\frac{1}{m_i} \sum_j m_j \frac{\partial u_j}{\partial \rho_j} \frac{\partial \rho_j}{\partial \mathbf{r}_i}, \end{aligned} \tag{3.70}$$

where $u_j = u(\rho_j, s_j)$. The partial derivative $\partial u / \partial \rho$ can be found from the first law of

thermodynamics where the entropy (S) of the system is considered to be constant, i.e. $\mathrm{d}S = 0$. The change of the internal energy (U) becomes

$$\mathrm{d}U = -P\mathrm{d}V. \tag{3.71}$$

Replacing $V = m/\rho$, or $\mathrm{d}V = -m/\rho^2\mathrm{d}\rho$, gives us

$$\mathrm{d}u = \frac{P}{\rho^2}\mathrm{d}\rho \tag{3.72}$$

or

$$\left.\frac{\partial u}{\partial \rho}\right|_s = \frac{P}{\rho^2}, \tag{3.73}$$

where $u = U/m$ and s denotes the constant specific entropy.

The expression for the gradient of the density ($\partial\rho/\partial\mathbf{r}$) in Equation 3.70 can be derived with the help of an additional index variable k, i.e.

$$\begin{aligned}
\frac{\partial \rho_j}{\partial \mathbf{r}_i} &= \frac{\partial}{\partial \mathbf{r}_i}\left(\sum_k m_k W_{jk}(h_j)\right) \\
&= \sum_k m_k \left(\frac{\partial W_{jk}(h_j)}{\partial \mathbf{r}_i} + \frac{\partial W_{jk}(h_j)}{\partial h_j}\frac{\partial h_j}{\partial \mathbf{r}_i}\right) \\
&= \sum_k m_k \left(\nabla_i W_{jk}(h_j) + \frac{\partial W_{jk}(h_j)}{\partial h_j}\frac{\partial h_j}{\partial \rho_j}\frac{\partial \rho_j}{\partial \mathbf{r}_i}\right).
\end{aligned}$$

Gathering the terms with $\partial\rho_j/\partial\mathbf{r}_i$ from both sides gives us

$$\frac{\partial \rho_j}{\partial \mathbf{r}_i} = \frac{1}{\Omega_j}\sum_k m_k \nabla_i W_{jk}(h_j), \tag{3.74}$$

where

$$\Omega_j = 1 - \frac{\partial h_j}{\partial \rho_j}\sum_k m_k \frac{\partial W_{jk}(h_j)}{\partial h_j}. \tag{3.75}$$

In the grad-h formalism, Ω acts more or less like a correction for quantities derived by the standard formalism; $\Omega = 1$ when h is constant. We can see that the index variables in the RHS of Equation 3.74 are not yet ready for the summation over j in Equation 3.70. This can be changed by invoking Equation 3.56 with the index

variables shifted from $i \to j$, $j \to k$, and $k \to i$, i.e.

$$\nabla_k W_{ij}(h_i) = \nabla_i W_{ij}(h_i)(\delta_{ik} - \delta_{jk}) \longrightarrow \nabla_i W_{jk}(h_j) = \nabla_j W_{jk}(h_j)(\delta_{ji} - \delta_{ki}). \tag{3.76}$$

The gradient of the density thus becomes

$$\frac{\partial \rho_j}{\partial \mathbf{r}_i} = \frac{1}{\Omega_j} \sum_k m_k \nabla_j W_{jk}(h_j)(\delta_{ji} - \delta_{ki}). \tag{3.77}$$

Substituting Equation 3.73 and 3.77 into Equation 3.70 gives us

$$\begin{aligned}
\left(\frac{\mathrm{d}\mathbf{v}_i}{\mathrm{d}t}\right)_{\text{pres}} &= -\sum_j m_j \frac{P_j}{\rho_j^2} \frac{1}{\Omega_j} \sum_k m_k \nabla_j W_{jk}(h_j)(\delta_{ji} - \delta_{ki}) \\
&= -\frac{1}{m_i}\left[m_i \frac{P_i}{\rho_i^2} \frac{1}{\Omega_i} \sum_k m_k \nabla_i W_{ik}(h_i) - \sum_j m_j \frac{P_j}{\rho_j^2} \frac{1}{\Omega_j} m_i \nabla_j W_{ji}(h_j) \right] \\
&= -\left[\frac{P_i}{\rho_i^2} \frac{1}{\Omega_i} \sum_j m_j \nabla_i W_{ij}(h_i) + \sum_j m_j \frac{P_j}{\rho_j^2} \frac{1}{\Omega_j} \nabla_i W_{ij}(h_j) \right]
\end{aligned}$$

or

$$\left(\frac{\mathrm{d}\mathbf{v}_i}{\mathrm{d}t}\right)_{\text{pres}} = -\sum_j m_j \left(\frac{P_i}{\Omega_i \rho_i^2} \nabla_i W_{ij}(h_i) + \frac{P_j}{\Omega_j \rho_j^2} \nabla_i W_{ij}(h_j) \right). \tag{3.78}$$

The gravity term. By considering that the local gravitational potential Φ_j in Equation 3.66 can expressed as

$$\Phi_j = G \sum_k m_k \phi_{jk}(h_j), \tag{3.79}$$

the acceleration due to gravity (Equation 3.69) becomes

$$\begin{aligned}
\left(\frac{\mathrm{d}\mathbf{v}_i}{\mathrm{d}t}\right)_{\text{grav}} &= -\frac{1}{m_i} \frac{\partial}{\partial \mathbf{r}_i} \left(\frac{1}{2} \sum_j m_j \Phi_j \right) \\
&= -\frac{1}{m_i} \frac{\partial}{\partial \mathbf{r}_i} \left(\frac{G}{2} \sum_j \sum_k m_j m_k \phi_{jk}(h_j) \right) \\
&= -\frac{1}{2} \frac{G}{m_i} \sum_j \sum_k m_j m_k \left(\nabla_i \phi_{jk}(h_j) + \frac{\partial \phi_{jk}(h_j)}{\partial h_j} \frac{\partial h_j}{\partial \mathbf{r}_i} \right),
\end{aligned}$$

or

$$\left(\frac{\mathrm{d}\mathbf{v}_i}{\mathrm{d}t}\right)_{\mathrm{grav}} = -\frac{1}{2}\frac{G}{m_i}\left[\sum_j\sum_k m_j m_k \nabla_i \phi_{jk}(h_j) + \sum_j\sum_k m_j m_k \frac{\partial \phi_{jk}(h_j)}{\partial h_j}\frac{\partial h_j}{\partial \rho_j}\frac{\partial \rho_j}{\partial \mathbf{r}_i}\right]. \quad (3.80)$$

In order to use this equation in practice, the double summations on the RHS of this equation have to be simplified to a single summation over j. The first double summation can be reorganized by using the same method of shifting indices in Equation 3.76 for $\nabla_i \phi_{jk}(h_j)$. That is,

$$\begin{aligned}\sum_j\sum_k m_j m_k \nabla_i \phi_{jk}(h_j) &= \sum_j\sum_k m_j m_k \nabla_j \phi_{jk}(h_j)(\delta_{ji} - \delta_{ki}) \\ &= m_i \sum_k m_k \nabla_i \phi_{ik}(h_i) - m_i \sum_j m_j \nabla_j \phi_{ji}(h_j) \\ &= m_i \sum_j m_j \left[\nabla_i \phi_{ij}(h_i) + \nabla_i \phi_{ij}(h_j)\right]. \end{aligned} \quad (3.81)$$

For the second double summation on the RHS of Equation 3.80, we can substitute Equation 3.77 for the density gradient term (with a new index variable l instead of k) to obtain

$$\begin{aligned}\sum_j\sum_k m_j m_k \frac{\partial \phi_{jk}(h_j)}{\partial h_j}\frac{\partial h_j}{\partial \rho_j}\frac{\partial \rho_j}{\partial \mathbf{r}_i} &= \sum_j\sum_k m_j m_k \frac{\partial \phi_{jk}(h_j)}{\partial h_j}\frac{\partial h_j}{\partial \rho_j}\left(\frac{1}{\Omega_j}\sum_l m_l \nabla_j W_{jl}(h_j)(\delta_{ji} - \delta_{li})\right) \\ &= \sum_k m_i m_k \frac{\partial \phi_{ik}(h_i)}{\partial h_i}\frac{\partial h_i}{\partial \rho_i}\frac{1}{\Omega_i}\sum_l m_l \nabla_i W_{il}(h_i) \\ &\quad - \sum_j\sum_k m_j m_k \frac{\partial \phi_{jk}(h_j)}{\partial h_j}\frac{\partial h_j}{\partial \rho_j}\frac{1}{\Omega_j} m_i \nabla_j W_{ji}(h_j) \\ &= m_i \sum_l m_l \left(\sum_k m_k \frac{\partial \phi_{ik}(h_i)}{\partial h_i}\frac{\partial h_i}{\partial \rho_i}\right)\frac{1}{\Omega_i}\nabla_i W_{il}(h_i) \\ &\quad + m_i \sum_j m_j \left(\sum_k m_k \frac{\partial \phi_{jk}(h_j)}{\partial h_j}\frac{\partial h_j}{\partial \rho_j}\right)\frac{1}{\Omega_j}\nabla_i W_{ij}(h_j). \end{aligned} \quad (3.82)$$

Since l and j run through the same values, we can use $l = j$ so that the terms can be grouped together. Equation 3.82 becomes

$$\sum_j\sum_k m_j m_k \frac{\partial \phi_{jk}(h_j)}{\partial h_j}\frac{\partial h_j}{\partial \rho_j}\frac{\partial \rho_j}{\partial \mathbf{r}_i} = m_i \sum_j m_j \left(\frac{\xi_i}{\Omega_i}\nabla_i W_{ij}(h_i) + \frac{\xi_j}{\Omega_j}\nabla_i W_{ij}(h_j)\right), \quad (3.83)$$

where ξ is defined such that

$$\xi_a = \sum_b m_b \frac{\partial \phi_{ab}(h_a)}{\partial h_a} \frac{\partial h_a}{\partial \rho_a}. \tag{3.84}$$

Substituting Equation 3.81 and Equation 3.83 back into Equation 3.80 and rearranging the terms give us the gravitational acceleration

$$\left(\frac{\mathrm{d}\mathbf{v}_i}{\mathrm{d}t}\right)_{\mathrm{grav}} = -\frac{1}{2}G\left[\sum_j m_j \left(\nabla_i \phi_{ij}(h_i) + \nabla_i \phi_{ij}(h_j)\right) + \sum_j m_j \left(\frac{\xi_i}{\Omega_i}\nabla_i W_{ij}(h_i) + \frac{\xi_j}{\Omega_j}\nabla_i W_{ij}(h_j)\right)\right]. \tag{3.85}$$

Apart from Equation 3.78 for pressure forces and Equation 3.85 for gravitational forces, the grad-h formalism uses the same artificial viscosity forces (Equation 3.40) as the standard formalism.

3.3.3 Energy equation

The energy equation in the grad-h formalism can be derived from Equation 3.1c with the substitution of $\nabla \cdot \mathbf{v}$ from Equation 3.1a. This gives us

$$\left(\frac{\mathrm{d}u_i}{\mathrm{d}t}\right)_{\mathrm{pres}} = \frac{P_i}{\rho_i^2}\frac{\mathrm{d}\rho_i}{\mathrm{d}t} \tag{3.86}$$

the energy equation associated with the pressure force. The time derivative of the density can be found from

$$\begin{aligned}
\frac{\mathrm{d}\rho_i}{\mathrm{d}t} &= \frac{\mathrm{d}}{\mathrm{d}t}\left(\sum_j m_j W_{ij}(h_i)\right) \\
&= \sum_j m_j \left(\frac{\partial W_{ij}(h_i)}{\partial r_{ij}}\frac{\mathrm{d}r_{ij}}{\mathrm{d}t} + \frac{\partial W_{ij}(h_i)}{\partial h_i}\frac{\mathrm{d}h_i}{\mathrm{d}t}\right) \\
&= \sum_j m_j \frac{\partial W_{ij}(h_i)}{\partial r_{ij}}\left(\mathbf{v}_{ij}\cdot\frac{\partial r_{ij}}{\partial \mathbf{r}_i}\right) + \sum_j m_j \frac{\partial W_{ij}(h_i)}{\partial h_i}\frac{\partial h_i}{\partial \rho_i}\frac{\mathrm{d}\rho_i}{\mathrm{d}t} \\
&= \sum_j m_j \mathbf{v}_{ij}\cdot\nabla_i W_{ij}(h_i) + \left(\frac{\partial h_i}{\partial \rho_i}\sum_j m_j \frac{\partial W_{ij}(h_i)}{\partial h_i}\right)\frac{\mathrm{d}\rho_i}{\mathrm{d}t}.
\end{aligned}$$

By gathering $\mathrm{d}\rho_i/\mathrm{d}t$ from both sides, we have

$$\frac{\mathrm{d}\rho_i}{\mathrm{d}t} = \frac{1}{\Omega_i}\sum_j m_j \mathbf{v}_{ij}\cdot\nabla_i W_{ij}(h_i), \tag{3.87}$$

where Ω_i is as defined by Equation 3.75. The energy equation associated with pressure forces becomes

$$\left(\frac{\mathrm{d}u_i}{\mathrm{d}t}\right)_{\mathrm{pres}} = \frac{P_i}{\Omega_i\rho_i^2}\sum_j m_j \mathbf{v}_{ij}\cdot\nabla_i W_{ij}(h_i). \tag{3.88}$$

In the grad-h formalism, the energy equation associated with viscous forces is given by Equation 3.41, as in the standard formalism.

3.4 Equation of state

In order to model gas dynamics in star formation properly, we need an equation of state to link the dynamical quantities to the thermal quantities. In star formation simulations where the gas is assumed to be ideal, the local state variables are connected through the ideal gas law of the form

$$P_i = \frac{k_{\mathrm{B}}\rho_i T_i}{\overline{m}} = (\gamma-1)\rho_i u_i, \tag{3.89}$$

where k_{B} is Boltzmann's constant, $\overline{m}$ the mean gas-particle mass, and γ the ratio of specific heats. This equation is generally used for an adiabatic process in which no heat is lost or gained from the system; for example, the optically thick stages of a collapsing molecular cloud core. In some situations, however, we may use the simplified equations of state such as the isothermal, the polytropic, and the barotropic. These equations of state do not need the energy equation to be solved as the pressure is a function of only density; thus, the simulation runtime can be reduced. Although SPH simulations in our work use a more sophisticated method described in Section 3.4.4 for treating the thermal processes, the descriptions of the simplified equations are still provided as follows.

3.4.1 Isothermal equation of state

In optically thin environments such as the early stage of protostellar cloud collapse, where thermal radiation produced from the collapse can get through the gas very

easily, the temperature of the whole cloud can be approximately constant. Under the isothermal approximation, the local pressure is linearly proportional to the density, i.e.

$$P_i = c_\circ^2 \rho_i, \tag{3.90}$$

where $c_\circ$ is the isothermal sound speed given by

$$c_\circ = \sqrt{\frac{k_\mathrm{B} T_\circ}{\overline{m}}}. \tag{3.91}$$

3.4.2 Polytropic equation of state

The polytropic equation of state is given by

$$P_i = K\rho_i^\eta = K\rho_i^{\left(1+\frac{1}{n}\right)}, \tag{3.92}$$

where K is the polytropic constant, η the polytropic exponent, and n the polytropic index. The value of η can be varied in order to model the change of state. In a collapsing cloud core, for example, η as a piecewise function of density can be used to follow the change of state from isothermal to early adiabatic (e.g. Bate 1998).

3.4.3 Barotropic equation of state

The barotropic equation of state can be used for modelling the change of state from isothermal to early adiabatic. The equation is given by

$$P_i = c_\circ^2 \rho_i \left[1 + \left(\frac{\rho_i}{\rho_\mathrm{crit}}\right)^{\gamma-1}\right], \tag{3.93}$$

where ρ_crit is the critical density at which the state of the gas changes from isothermal to adiabatic. The critical density is usually $\rho_\mathrm{crit} \sim 10^{-13}\,\mathrm{g\,cm^{-3}}$ (e.g. Larson 1969; Masunaga and Inutsuka 2000), while the ratio of specific heats for a monatomic gas is $\gamma \simeq 5/3$ (e.g. Goodwin et al. 2004a).

3.4.4 Radiative cooling method

The radiative cooling method was introduced by Stamatellos et al. (2007) to estimate the net radiative energy from heating and cooling processes occurring in a gas cloud.

In this method, the energy equation can be written as

$$\frac{\mathrm{d}u_i}{\mathrm{d}t} = \left(\frac{\mathrm{d}u_i}{\mathrm{d}t}\right)_{\mathrm{pres}} + \left(\frac{\mathrm{d}u_i}{\mathrm{d}t}\right)_{\mathrm{visc}} + \left(\frac{\mathrm{d}u_i}{\mathrm{d}t}\right)_{\mathrm{rad}}, \tag{3.94}$$

where the first two terms on the RHS are from Equation 3.88 and 3.41. The third term on the RHS is the change of energy associated with radiation, given by

$$\left(\frac{\mathrm{d}u_i}{\mathrm{d}t}\right)_{\mathrm{rad}} = \frac{4\sigma_{\mathrm{SB}}\left(T_{\mathrm{bg}}^4(r_i) - T_i^4\right)}{\bar{\Sigma}_i^2\bar{\kappa}_i(\rho_i, T_i) + \kappa_i^{-1}(\rho_i, T_i)}, \tag{3.95}$$

where σ_{SB} is the Stefan-Boltzmann constant, κ the opacity, $\bar{\kappa}$ the mass weighted opacity, and T_{bg} the background temperature. By using this equation, the local temperature T_i of the gas is maintained to be above the background temperature T_{bg} by the artificial heating process, i.e. that $T_i < T_{\mathrm{bg}}$ makes Equation 3.95 positive. On the other hand, the artificial cooling process begins when $T_i > T_{\mathrm{bg}}$, turning Equation 3.95 negative. In the case that $T_i \gg T_{\mathrm{bg}}$, the denominator of Equation 3.95 ensures that the equation is approximately valid in both optically thin and optically thick cooling regimes. That is, in the optically thin regime where $\bar{\Sigma}_i^2\bar{\kappa}_i \ll \kappa_i^{-1}$, Equation 3.95 reduces to

$$\left(\frac{\mathrm{d}u_i}{\mathrm{d}t}\right)_{\mathrm{rad}} \simeq -4\sigma_{\mathrm{SB}}\kappa_i(\rho_i, T_i)T_i^4; \tag{3.96}$$

while, in the optically thick regime where $\bar{\Sigma}_i^2\bar{\kappa}_i \gg \kappa_i^{-1}$, the equation becomes

$$\left(\frac{\mathrm{d}u_i}{\mathrm{d}t}\right)_{\mathrm{rad}} \simeq -\frac{4\sigma_{\mathrm{SB}}T_i^4}{\bar{\Sigma}_i^2\bar{\kappa}_i(\rho_i, T_i)}. \tag{3.97}$$

The opacities in Equation 3.95 can be calculated from considering that the particle i is embedded in a spherically symmetric pseudo-cloud. The particle's mean optical depth ($\bar{\tau}_i$), which plays a major role in heating and cooling processes, can be estimated from the local density (ρ_i), temperature (T_i), and gravitational potential (Φ_i, Equation 3.18). By modelling the pseudo-cloud with a polytrope of index $n = 2$ and solving the Lane-Emden equation (see Stamatellos et al. (2007) for the details), the pseudo-mean opacity is

$$\bar{\kappa}_i = \frac{\bar{\tau}_i}{\bar{\Sigma}_i}, \tag{3.98}$$

where $\bar{\Sigma}_i$ is the pseudo-mean column density given by

$$\bar{\Sigma}_i = \zeta_n \sqrt{\frac{\rho_i |\Phi_i|}{4\pi G}}. \tag{3.99}$$

According to Stamatellos et al. (2007), $\zeta_2 = 0.368$. For a fixed value of n, it is better to evaluate the values of the opacities in advance and tabulate them in a look-up table. The values can then be recalled when needed by interpolating from the table.

In this radiative cooling method, solving Equation 3.94 explicitly may lead to very short timesteps when some particles are rapidly thermalized to their equilibrium. Stamatellos et al. (2007) suggest that this situation can be avoided by using a semi-implicit scheme in which the thermalization timescale ($t_{\rm th}$) is considered in calculating the internal energy. That is, the internal energy $u_i(t+\Delta t)$ at time $t+\Delta t$ is controlled by

$$u_i(t+\Delta t) = u_i(t) \exp\left(-\frac{\Delta t}{t_{{\rm th},i}}\right) + u_{{\rm eq},i}\left[1 - \exp\left(-\frac{\Delta t}{t_{{\rm th},i}}\right)\right], \tag{3.100}$$

where $u_{{\rm eq},i}$ is the internal energy at equilibrium and $u_i(t)$ the internal energy calculated from solving Equation 3.94. To find $u_{{\rm eq},i}$ and $t_{{\rm th},i}$, let us consider the equilibrium state at particle i where

$$\frac{{\rm d}u_i}{{\rm d}t} = \left(\frac{{\rm d}u_i}{{\rm d}t}\right)_{\rm hydro} + \left(\frac{{\rm d}u_i}{{\rm d}t}\right)_{\rm visc} + \frac{4\sigma_{\rm SB}\left(T_{\rm bg}^4(r_i) - T_{{\rm eq},i}^4\right)}{\bar{\Sigma}_i^2 \bar{\kappa}_i(\rho_i, T_{{\rm eq},i}) + \kappa_i^{-1}(\rho_i, T_{{\rm eq},i})} = 0. \tag{3.101}$$

Solving this equation gives us the equilibrium temperature $T_{{\rm eq},i}$ which can be used in Equation 3.89 to find $u_{{\rm eq},i}$. The thermalization timescale can then be calculated from

$$t_{{\rm th},i} = (u_{{\rm eq},i} - u_i)\left(\frac{{\rm d}u_i}{{\rm d}t}\right)^{-1}. \tag{3.102}$$

In one extreme case where thermalization occurs in a very short time, i.e. $t_{{\rm th},i} \ll \Delta t$, the internal energy calculated from Equation 3.100 is quickly converged to the equilibrium value:

$$u_i(t+\Delta t) \simeq u_{{\rm eq},i}. \tag{3.103}$$

In the other extreme case where thermalization is very slow, i.e. $t_{{\rm th},i} \gg \Delta t$, the expo-

nential terms in Equation 3.100 become

$$\exp\left(-\frac{\Delta t}{t_{\mathrm{th},i}}\right) \simeq 1 - \frac{\Delta t}{t_{\mathrm{th},i}}. \tag{3.104}$$

The internal energy is thus

$$u_i(t+\Delta t) \simeq u_i(t) + [u_{\mathrm{eq},i} - u_i(t)]\frac{\Delta t}{t_{\mathrm{th},i}}. \tag{3.105}$$

3.5 Integration and timestepping

For our SPH simulations in this work, we use the second-order leapfrog `KDK` described in Section 2.3. Although a higher-order integration scheme can be used, the leapfrog method is sufficient as the error from the SPH interpolation is already second-order. In other words, there would be no point in using any higher-order scheme if it cannot reduce the interpolation error while costing considerably more computational effort. To optimize the integration, we employ adaptive timesteps and a hierarchical block timestep scheme. These are described as follows.

3.5.1 Adaptive timesteps

For more efficiency in the integration, particles are allowed to have their own timestep that is adaptive to the local conditions. In SPH, the timestep of each particle can be chosen from the smallest value among those provided by the Courant condition, the acceleration condition, and the energy condition (Hubber et al. 2011):

$$\Delta t_i = \mathrm{MIN}\left[\gamma_{\mathrm{C}}\frac{h_i}{(1+1.2\alpha)c_i + (1+1.2\beta)h_i\,|\nabla_i\cdot\mathbf{v}_i|},\ \gamma_{\mathrm{A}}\sqrt{\frac{h_i}{|\mathbf{a}_i|+\eta_{\mathrm{A}}}},\ \gamma_{\mathrm{E}}\frac{u_i}{|\dot{u}_i|+\eta_{\mathrm{E}}}\right] \tag{3.106}$$

where c_i is the local sound speed; γ_{C}, γ_{A}, and γ_{E} are constants for the Courant condition, the acceleration condition, and the energy condition, respectively; α and β are the viscosity parameters; η_{A} and η_{E} are small values for preventing the denominators being zero. Typically, $\gamma_{\mathrm{C}} = 0.3$, $\gamma_{\mathrm{A}} = 0.4$, and $\gamma_{\mathrm{E}} = 0.3$ are used. However, in this work, we omit the the energy condition term since the energy equation is not solved explicitly in the radiative cooling scheme (Section 3.4.4).

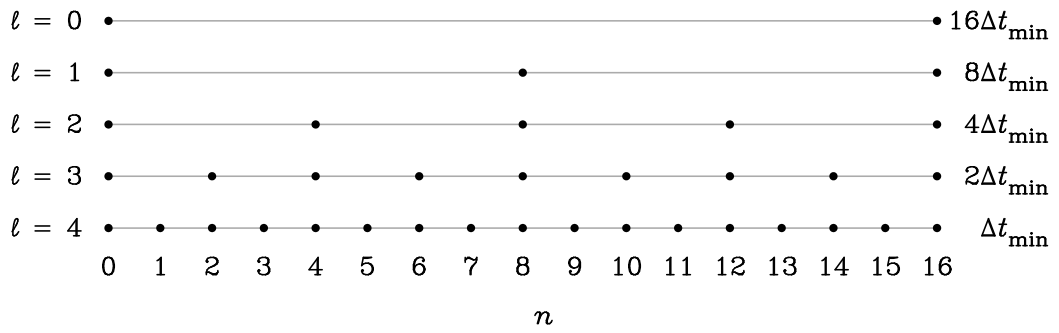

Figure 3.2 Diagram illustrating a block of five timestep levels, i.e. from $\ell = 0$ to 4. Each level ℓ has an associated timestep value of $\Delta t_\ell = \Delta t_{\rm min} 2^{\ell_{\rm max}-\ell}$ shown on the right. Time progressing inside the block is counted as an integer multiple (n) of the minimum timestep $\Delta t_{\rm min}$. The solid dots mark the complete timesteps in each level.

3.5.2 Hierarchical block timesteps

A hierarchical block timestep scheme (e.g. Binney and Tremaine 2008) is used for synchronizing the integration of an N-body system in which particles in the system have different timesteps. The procedure begins with creating a hierarchy of quantized timestep levels; each level ℓ has an associated timestep value of Δt_ℓ. To do this, we:

(1) calculate the timestep Δt_i for every particle using Equation 3.106

(2) find the minimum value ($\Delta t_{\rm min}$) among those timesteps of all particles

(3) assign a value of $\Delta t_\ell = \Delta t_{\rm min} 2^{\ell_{\rm max}-\ell}$ to each timestep level $\ell = 0, 1, 2, ..., \ell_{\rm max}$

(4) assign particle i to its appropriate level ℓ, where $\Delta t_i \geq \Delta t_\ell$ and $\Delta t_i - \Delta t_\ell$ is minimum, and reduce the timestep Δt_i to Δt_ℓ.

Note that the total number of the levels is $\ell_{\rm max} + 1$. In practice, a few more levels may be added below the bottom level ($\ell_{\rm max}$) for some particles that need even smaller timestep sizes ($\Delta t_i < \Delta t_{\rm min}$) during the integration. A block of five timestep levels ($\ell = 0 - 4$) is illustrated in Figure 3.2. In this figure, the integer time n denotes the multiple of the minimum timestep $\Delta t_{\rm min}$ of the block. The solid dots mark the complete timesteps in each level.

Once particles are assigned a quantized timestep, integration can proceed. As an example, let us consider the integration of particles in a block of three timestep levels using the leapfrog `KDK` integration scheme (Equation 2.11), as illustrated graphically in Figure 3.3. First of all, for the first `kick` step at $n = 0$, the half-step velocity of all particles are calculated by using Equation 2.11a with $\Delta t = \Delta t_\ell$. This `kick` step is

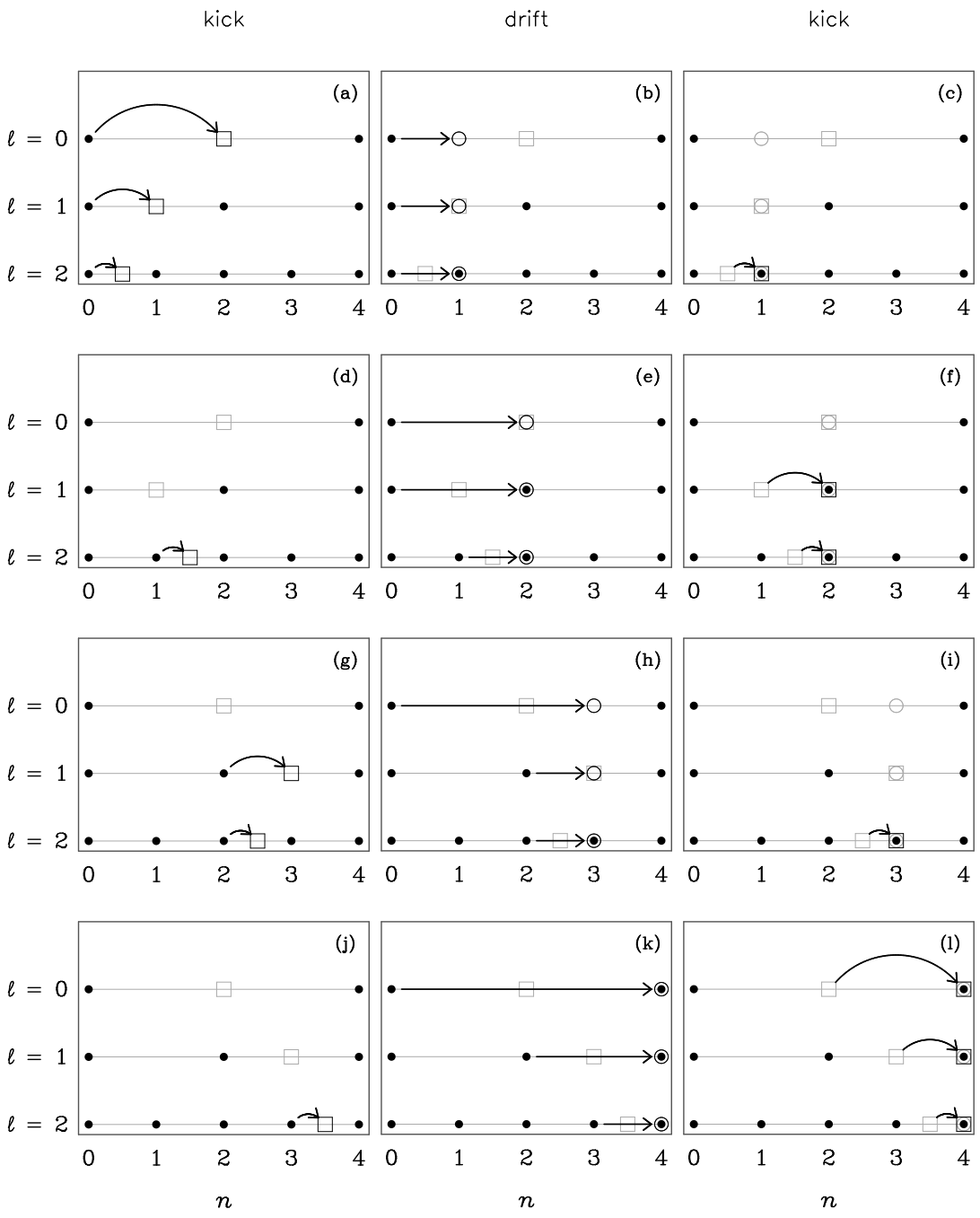

Figure 3.3 Leapfrog KDK integration in a simple block timestep with $\ell_{\max} = 2$. The curved and straight arrows represent `kick` and `drift` steps, respectively. The open squares mark the points in time where velocity is calculated, while the open circles mark where position is calculated. Note that, forces are calculated only in the second `kick` step (the third column) for each timestep.

illustrated by the curved arrows depicted in Figure 3.3(a). The points in time where the half-step velocity is calculated are marked by the open squares in the same figure. Then, in the following `drift` step (represented by the straight arrows in Figure 3.3(b)), the position of every particle is advanced to the integer time $n=1$ (marked by the open circles) by using Equation 2.11b with $\Delta t=\Delta t_2$ ($\ell=2$). To complete the first `KDK` cycle, the second `kick` step is performed only to particles in level $\ell=2$ by using Equation 2.11c with $\Delta t=\Delta t_2$. The particle positions for calculating all forces in this step are from the previous `drift` step. It is clear that not all particles need force calculations in every timestep. The integration is therefore speeded up.

For the remaining cycles of the integration, the key procedures are that (a) both `kick` steps at any integer time n are always performed only to particles in the levels marked by solid dots in Figure 3.3, (b) the timestep size for the `drift` step toward integer time n is obtained from $\Delta t_i=(n-n_{\mathrm{last},i})\Delta t_{\mathrm{min}}$, where $n_{\mathrm{last},i}$ is the last completed integer time of particle i, and (c) the new timesteps of all particles are calculated after finishing each cycle. The last procedure is for assigning particles to the appropriate levels before proceeding the next integration cycle. For a downward change of the level (i.e. $\ell_{\mathrm{new}}>\ell_{\mathrm{old}}$), particles are allowed to be assigned directly to any corresponding lower level as long as $\ell_{\mathrm{new}}\leq\ell_{\mathrm{max}}$. The particles moved to the new level are ready to be advanced in the next cycle. On the other hand, an upward change (i.e. $\ell_{\mathrm{new}}<\ell_{\mathrm{old}}$) needs to be done with two extra restrictions: (a) the particles are allowed to change by only one level upward at a time and (b) the changes are allowed only when the full-timestep on the old level is synchronized with that of the new one. The latter condition means that, from Figure 3.2, the solid dots on the two levels must be vertically aligned; if not, the particles must continue in their current levels until all conditions are satisfied.

3.6 Additional techniques and the code SEREN

In this section, we describe two widely used techniques for optimizing SPH simulations: sink particles and tree data structures. Both techniques improve the simulation speed considerably. We also briefly describe the SPH code SEREN which is used for performing our simulations.

3.6.1 Sink particles

In typical star formation simulations using SPH, interactions between gas particles become stronger when the gas begins to clump together. According to the acceleration condition in Equation 3.106, the timesteps of particles need to be shorter to maintain the accuracy; the computation time increases significantly as a consequence. At some point when the density of the clump is sufficiently high, e.g. when a protostar forms, the simulation may grind to a halt. To reduce such a high computational effort, Bate et al. (1995) introduce a method of replacing a high-density clump with a *sink particle* when the central density of the clump exceeds a threshold value, e.g. $\geq 10^{-11}\,\mathrm{g\,cm^{-3}}$. Sink particles have a spherical shape of a specified constant radius. The mass and momentum of the sink particle are calculated collectively and straightforwardly from the particles involved. Other gas particles can be accreted by sink particle if they are *inside and bound* to the sink. The masses and momenta of accreted particles are also contributed to the sink. Particles that form or are accreted by the sink are removed from the calculation, reducing the computational workload.

Nevertheless, the main problem of the standard sink particle is that it can interact with gas and other sink particles only gravitationally. With the lack of hydrodynamic pressure support around the surface, the sink particle may accrete gas particles too easily and unphysically. Therefore, this issue has to be considered when interpreting the simulation results.

3.6.2 Trees

Without any additional technique, the gravitational force calculation is no doubt the most computationally expensive part of SPH. High-resolution simulations with $N \gg 10^3$ are simply prohibited by the fact that the number of force calculations per timestep goes with $\mathcal{O}(N^2)$. To alleviate the situation, Barnes and Hut (1986) introduce the *tree* method for organizing the particles so that gravitational forces can be calculated efficiently. Using a tree can speed up the computation considerably as the number of force calculations per timestep is reduced to $\mathcal{O}(N \log N)$. Moreover, the tree is also beneficial to the neighbour searching procedure in the hydrodynamic part of SPH. With an adjustable trade-off between speed and accuracy, the method was soon adopted by the SPH community.

The standard tree algorithm uses a repetitive partitioning of spaces occupied by particles to create a hierarchical data structure of particle positions. In calculating gravitational forces acting on one particle, the tree data structure allows us to decide

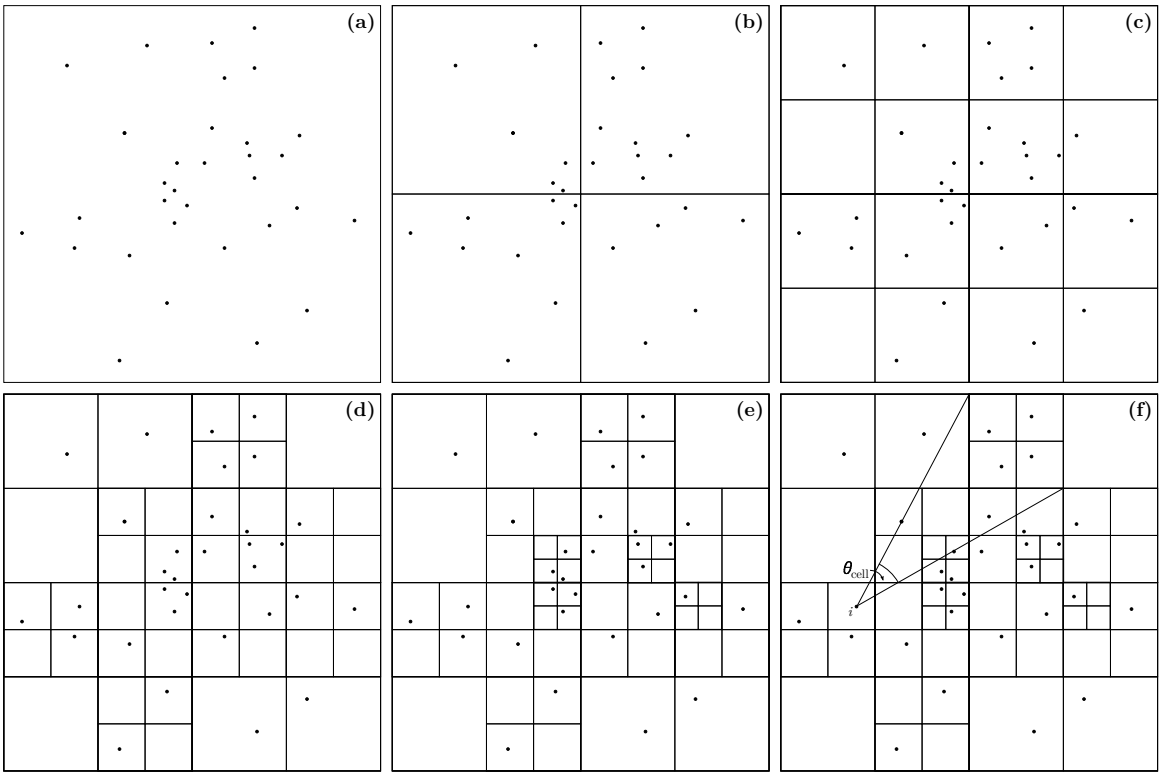

Figure 3.4 Spatial divisions for making a tree of two-dimensional particle distribution. See text for details.

whether other surrounding particles should be considered individually or grouped together so that they can be considered as a single object. A basic tree data structure can be created by the following steps, see Figure 3.4:

(1) Define the extent of all particles with a cubic bounding box labelled as the root cell of the tree (Figure 3.4(a)).

(2) Divide the cell equally into four quadrants (or eight octants for three dimensions), each one called a child cell (Figure 3.4(b)).

(3) Repeatedly perform step (2) for child cells containing particles more than a specified number (usually one or a few particles per cell, Figure 3.4(c)-(e)). Child cells containing a specified minimum number of particles is a leaf cell that requires no more division.

(4) From a leaf cell up to the root cell, calculate and record the mass, the centre of mass, multipole quantities (see below), and particle identifiers.

Structuring the data in this way makes it easy to find the nearest neighbours of a particle. More details can be found in, e.g., Pfalzner and Gibbon (1996).

Once a tree has been created, force calculations between particle i and the rest of the system are performed by (a) direct summation for nearby particles and (b) multipole expansion for clusters of distant particles. While the former can be performed directly, the latter involves more complicated procedures. First of all, it needs to be decided whether a child cell containing a cluster of particles is far enough away to be considered as a single object. The criterion for this is given as the angle subtended by the length of the cell

$$\theta_{\rm cell} \simeq \frac{s}{d}, \tag{3.107}$$

where s is the diagonal width of the cell and d is the distance between the centre of the cell and particle i, see Figure 3.4(f). That is, the cluster of particles in the cell can be thought of as a single object located at its centre of mass only if $\theta_{\rm cell}$ is smaller than some tolerable value, say $\theta_{\rm max}$; otherwise, the cell needs to be opened and the sub-cells are brought into consideration instead. The value of $\theta_{\rm max}$ controls the trade-off between the accuracy and efficiency of the tree; namely, the accuracy of the tree can be as good as the direct summation when a very small value of $\theta_{\rm max}$ is used, but this in turn reduces the efficiency of the tree as more cells need to be opened.

The force calculation can be made more accurate by including the higher-order terms of the multipole expansion. Generally, including just the quadrupole terms gives a sufficiently accurate result. With the quadrupole terms, the gravitational acceleration acting on particle i due to particles in cell k of total mass M_k is

$$\left(\frac{{\rm d}\mathbf{v}_{ik}}{{\rm d}t}\right)_{\rm grav} = -\frac{GM_k}{|\mathbf{r}_{ik}|^2}\hat{\mathbf{r}}_{ik} + \frac{G(\mathbf{Q}_k\cdot\hat{\mathbf{r}}_{ik})}{|\mathbf{r}_{ik}|^4} - \frac{5}{2}\frac{G(\hat{\mathbf{r}}_{ik}\cdot\mathbf{Q}_k\cdot\hat{\mathbf{r}}_{ik})}{|\mathbf{r}_{ik}|^4}\hat{\mathbf{r}}_{ik}, \tag{3.108}$$

where $\mathbf{Q}_k$ is the quadrupole moment tensor of the cell and $\mathbf{r}_{ik}$ is the position of the cell's centre of mass relative to particle i (Hernquist 1987). For a leaf cell, the quadrupole components Q_{pq} of the quadrupole moment tensor $\mathbf{Q}$ are defined as

$$Q_{pq} = \sum_l m_l \left(3x_{p,l}x_{q,l} - r_l^2\delta_{pq}\right), \tag{3.109}$$

where m_l is the mass of particle l, $\mathbf{r}_l = (x_{1,l}, x_{2,l}, x_{3,l}) = (x_l, y_l, z_l)$ are the coordinates of particle l relative to the centre of mass of the cell, and δ_{pq} is the Kronecker delta. For a cell that contains sub-cells, the quadrupole components are calculated collectively from that of the sub-cells. That is, the quadrupole components of cell k in

Equation 3.108 are obtained from

$$Q_{ab,k} = \sum_c m_c \left(3x_{a,c}x_{b,c} - r_c^2\delta_{ab}\right) + \sum_c Q_{ab,c}, \tag{3.110}$$

where m_c is the total mass of particles in sub-cell c and, in this case, the coordinates $\mathbf{r}_c = (x_{1,c}, x_{2,c}, x_{3,c}) = (x_c, y_c, z_c)$ represent the centre of mass of sub-cell c relative to that of cell k. Note that the quadrupole moment and related quantities of every cell and sub-cell are calculated in step (4) of the tree building process.

In summary, using the tree can speed up the simulation by reducing the number of force calculations per timestep from $\mathcal{O}(N^2)$ to $\mathcal{O}(N \log N)$. In simulations in which the positions of particles do not change considerably, one constructed tree may be used economically for several timesteps, e.g. $\lesssim 20$. During those timesteps, some information still needs to be updated in every timestep according to the motion of particles and that some particles may have been accreted by sink particles. Despite being economical, using the same tree for too many timesteps increases the overlaps between the cells, eventually reducing the efficiency of the tree.

3.6.3 The SPH code SEREN

SEREN is a high-performance SPH code created by Hubber et al. (2011) for modelling various astrophysical phenomena. The code is written in Fortran 95/2003 and is also parallelized with OpenMP, allowing it to utilize computational resources effectively to obtain maximum performance. The demonstrations of SEREN on several standard tests can also be found in Hubber et al. (2011).

3.7 Summary

SPH is an efficient method for solving hydrodynamic problems. We have described the method in both the standard and the grad-h formalisms. We will use the latter formalism for our SPH simulations in Chapter 5 and Chapter 6. The simulations will be performed by the SPH code SEREN with the radiative cooling scheme for radiation treatment and the leapfrog `KDK` as the integrator.

Chapter 4

Dynamical evolution of young triple systems

In this chapter, we perform N-body simulations to explore the dynamical evolution of young triple systems. Our triple systems consist of two low-mass companions orbiting around a relatively more massive primary in coplanar orbits. The possible outcomes of the evolution are ejections, collisions, and stable systems. We find that the chance of a collision between the two companions is generally high, at least a few per cent, in several configurations. Since a collision between young stars would change the evolution of the objects, we suggest that collisions among young stars might be responsible for some rare features found in young star systems such as apparently different ages between the members.

In Section 4.1, we provide a brief review of the age discrepancy problem in some young star systems. Details of the simulations are described in Section 4.2 followed by the results and analyses in Section 4.3. Finally, we discuss the role of collisions in stellar evolution in Section 4.4.

The work in this chapter has been published in the Monthly Notices of the Royal Astronomical Society (Rawiraswattana, Lomax, and Goodwin 2012).

4.1 Infrared companions in young star systems

Observations have found that most young stars are in binary or multiple systems (Section 1.2.1). According to the theory of star formation via fragmentation (Section 1.2.2), stellar components in binary and multiple systems are expected to have

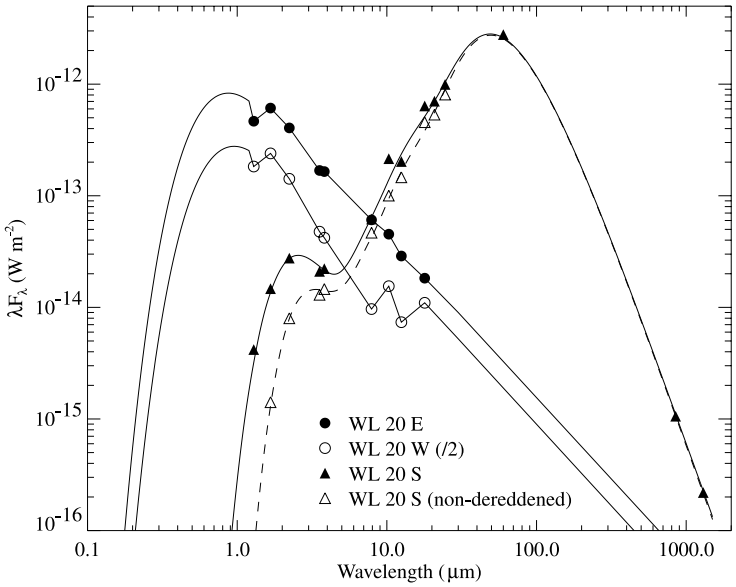

Figure 4.1 Spectral energy distribution (SED) of the young triple system WL 20. The system consists of WL 20 E, WL 20 W, and WL 20 S. The infrared companion WL 20 S (Class I) is much brighter in mid- to far-IR wavelengths than the other two components which are T Tauri stars (Class II). The plot is taken from Ressler and Barsony (2001).

roughly the same age. In observations, however, it is found that there are a number of young star systems that consist of a visually bright T Tauri star(s) (TTS) and a component(s) called *infrared companion* (IRC) which is bright in mid- to far-IR wavelengths (e.g. Hartigan et al. 1994; Koresko et al. 1997; Ressler and Barsony 2001; Hartigan and Kenyon 2003; Prato et al. 2003; Kraus and Hillenbrand 2009). The infrared excess of an IRC suggests that the object is less evolved (Class I) than other members (Class II or TTS) in the system. The system thus *appears* to be non-coeval. It is estimated by Zinnecker and Wilking (1992) that the population of IRCs could be around 10% of PMS binaries. An example of non-coeval systems is the young triple WL 20 (Ressler and Barsony 2001) which has spectral energy distribution (SED) as shown in Figure 4.1. The system consists of two TTSs (WL 20 E and WL 20 W) and an IRC (WL 20 S). The figure shows that WL 20 S (both filled and hollow triangles) is much brighter in mid- to far-IR wavelengths than the other two components (filled and hollow circles). WL 20 S is classified as a Class I object while WL 20 E and WL 20 W are classified as Class II objects or TTSs (Section 1.1.2).

It is still unclear whether an IRC is genuinely younger than other TTSs in the same system or just a peculiarly embedded typical TTS. As discussed in Koresko et al. (1997) and Duchêne et al. (2003), most explanations lean towards the latter possibility. Koresko et al. (1997), for example, suggest that the appearance of an IRC in a young

binary system may be due to that the object is enshrouded by material taken from the inner part of a circumbinary disc surrounding the system during apastron passage. Optical radiation from the central part of the IRC can be heavily absorbed by dust grains in the surrounding dusty envelope. Warm dust grains can cool down afterwards by radiating in longer wavelengths beyond near-IR. These absorption and re-radiation processes make the IRC appear to be cooler or less evolved than its counterpart.

In this work, we suggest an alternative explanation to the age discrepancy problem. The explanation is based on the results from Baraffe et al. (2009) which show that the evolution of a PMS star depends largely on the accretion history of the star and the efficiency in removing the accretion energy. A high accretion rate of various durations at the early stage of a young star can later shift the position of the star on the Hertzsprung-Russell diagram away from that predicted by non-accreting models. This situation seems to be applicable to the age discrepancy problem. In our point of view, however, the effect of the episodic accretion in a young star might also be obtained from an alternative process such as merging between two young progenitor stars in a collision. To provide some support for this idea, we investigate how common a collision is as a result of dynamical evolution in a young multiple system. We will show in our simulation results later that, for a coplanar triple system, a collision between low-mass components is quite common.

4.2 Simulation set-up

In this section, we describe the initial conditions of our simulations and the criteria for termination. Simulations in this chapter are performed by using the Adams-Bashforth-Moulton predictor-corrector method with the variable timestep size scheme described in Section 2.4. The fractional energy error (Equation 2.6) of the calculations is kept below 10^{-5}. A system with unacceptable error is reintegrated from the beginning with a more stringent limit for timestep size. If an error persists, the result is omitted from analyses; the number of the systems in the ensemble is reduced accordingly.

4.2.1 Initial conditions

We set up a three-body system of young stars in which two low-mass companions of masses M_2 and M_3 are orbiting around a primary star of a higher mass M_1. The companions are assumed to form from circumstellar disc fragmentation (e.g. Stamatellos

and Whitworth 2009a). However, our simulations ignore the presence of the remaining disc material to avoid the complicated hydrodynamic modelling. This assumption can be acceptable, regarding the results from Stamatellos and Whitworth (2009a) which show that the disc material is soon accreted by the forming objects and is reduced to a small fraction in only a few thousand years. The three-body system of young stars can be characterized by three sets of parameters:

Protostellar masses

Most of the simulation ensembles use $M_1 = 1M_\odot$ for the primary mass; some ensembles use $M_1 = 2M_\odot$. The companion masses are obtained from (a) the companion total mass, $M_2 + M_3 = 0.1 - 0.6M_\odot$ in steps of $0.05M_\odot$, and (b) the companion mass ratio, $M_2/M_3 = 0.25, 0.5$ and 1. This gives us 33 combinations of companion masses for each primary.

Protostellar radii

The radius of a young star in the systems is estimated and scaled from the mass-radius relation of low-mass main-sequence stars. In this work, we use the empirical mass-radius relation from Caillault and Patterson (1990) which is for stars of mass $\sim 0.1 - 0.5M_\odot$ in the Solar neighbourhood. We assume that the relation extends to very low-mass stars of a few tens of Jupiter mass. Since the PMS stars are young, their radius could be larger by a factor of $\alpha > 1$. The radius R of a PMS star of mass M is then given by

$$R = 0.918\alpha \left(\frac{M}{M_\odot}\right)^{0.796} R_\odot. \tag{4.1}$$

The values of α used in the simulations are selected from 1 up to 20: in steps of 0.5 for $\alpha = 1 - 10$, and in steps of 1 for $\alpha = 10 - 20$.

We also assume that the stellar radius is constant throughout simulations. This is reasonable as we will see later that most ejection and collisions occur on timescales $\lesssim 10^5$yr which is much shorter than the evolution timescale of low-mass PMS stars ($\sim 10^7 - 10^8$yr for stars with masses $\lesssim 1M_\odot$, see the change of radius in Figure 1.7).

Initial positions

The initial orbital radii of the companions are chosen to cover the range from which the results of disc fragmentation (Stamatellos and Whitworth 2009a) are consistent

with the observations of PMS binary separations. The simulations performed by Stamatellos and Whitworth (2009a) show that massive extended discs can fragment at large radii as estimated by Whitworth and Stamatellos (2006), i.e.

$$r_{\rm frag} \gtrsim 150 \left(\frac{M_\star}{M_\odot}\right)^{1/3} {\rm AU}. \tag{4.2}$$

The Stamatellos and Whitworth (2009a) disc fragments to form a number of low-mass objects, mostly with mass ranging between brown dwarfs to hydrogen-burning stars. Due to the dynamical interactions between the objects, the higher-mass objects that frequently form closer to the central star tend to move inwards to smaller radii of a few hundreds of AU, while the lower-mass objects that frequently form in the outer part of the disc tend to move outwards to larger radii. This agrees with the observations of PMS binaries in which most PMS binaries are with separations ranging from a few tens to a few hundreds of AU (e.g. Mathieu 1994; Patience et al. 2002; Konopacky et al. 2007; Goodwin 2010). We then perform simulations to cover three ranges of orbital radii: $20-100$AU, $100-200$AU, and $200-300$AU. For each value of M_1, M_2, M_3, and α we perform an ensemble of 5×10^3 simulations for the first range and 10^4 simulations for the second and the third ranges. The two companions are placed randomly in the given ranges measured from the primary in the same plane. Their angular separation is greater than 45° in order to avoid initial conditions which may result in a collision or ejection almost immediately. The companions are initiated with the correct velocities to orbit in the same direction.

We also perform simulations to test the effect of non-coplanar motion. This is done by giving the mass M_3 a small velocity component in the z-direction.

4.2.2 Termination criteria

The possible outcomes of the simulations are ejections, collisions, and stable systems. The criteria for these cases are described as follows.

Ejections

A companion that travels beyond 5000AU from the primary star is considered as an ejected component, even though it might not be moving with the escape speed and may still be weakly bounded to the primary. In a star cluster, this separation may be widely enough for an ejected component to be disrupted by other stars.

We also record the ejection timescale which defined as the time when the energy E_i of an ejecting component i is at its last maximum. The energy E_i is given by

$$E_i = \frac{1}{2} M_i v_i^2 - \frac{1}{2} \sum_{i \neq j} \frac{G M_i M_j}{r_{ij}} \tag{4.3}$$

where G is the gravitational constant, r_{ij} the distance between components i and j, and v_i the velocity of component i. Note that the total energy of the system is

$$E = \sum_{i=1}^{3} E_i. \tag{4.4}$$

Collisions

A collision occurs when any $r_{ij} \leq R_i + R_j$. There are two possible types of collisions that can occur and are counted separately: (a) collisions between companions or companion-companion collisions (CCCs) and (b) collisions between a companion and the primary star or companion-primary collisions (CPCs).

Stable systems

A system is stable if it evolves with no ejections or collisions for 5 Myr.

4.3 Results

The main outcome of the simulations is as expected by, for example, Anosova (1986) and Sterzik and Durisen (1998) in that most of the systems decay by ejection within ~ 100 crossing times and the least-massive member is preferentially ejected. However, a significant number of collisions are found in systems with radius factors $\alpha > 1$ (young systems). We also find that the distributions of both ejection and collision times are essentially similar (decaying exponentially), as shown in Figure 4.2 for a system with $M_1 = 1 M_\odot$, $M_2 = M_3 = 0.15 M_\odot$, and $\alpha = 5$.

4.3.1 Companion-companion collisions

Collisions between the companions (CCC) occur mostly in a coplanar system with equal-mass companions. In such system, the number of CCCs depends on the radius factor (α) as shown in Figure 4.3. The plots in the figure are of the ensembles with

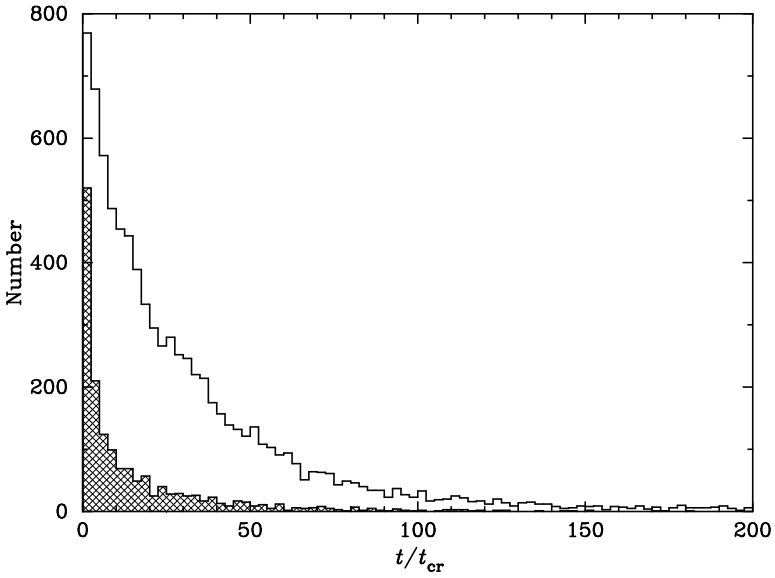

Figure 4.2 Distributions of ejection times (open histogram) and CCC times (cross-hatched histogram) of the system with $M_1 = 1M_\odot$, $M_2 = M_3 = 0.150M_\odot$, and $\alpha = 5$. The crossing time of the system is $t_{\rm cr} \sim 2\times10^4$ yr

primary mass $M_1 = 1M_\odot$ and companion mass ratio $M_2/M_3 = 1$. The number of collisions is shown by the lines with circle symbols, while the number of ejections by the lines with diamond symbols. The increasing thickness of the lines corresponds to $\alpha = 1, 5, 10, 15, 20$. This figure shows that CPCs and stable systems are very rare in systems with equal-mass companions. The increase in the number of CCCs with increasing values of α suggests that collisions among companions may be not uncommon in young systems in which the components still have large radii. However, the slow increase in the number of CCCs at high values of α tells us that, within a reasonable range of α assumed, CCCs cannot be very common.

Changes in the number of CCCs with α reveal to us an interesting aspect of the separation distribution of close encounters, as shown in Figure 4.4. The vertical axis of the plot in this figure is the probability $P(r_{23})$ of CCCs occurring at separation r_{23}, where $r_{23} = R_2 + R_3$. In other words, $P(r_{23})$ is a cumulative distribution function (CDF) of separation r_{23}. The selected ensembles shown in Figure 4.4 have the companion total mass of $M_2 + M_3 = 0.3M_\odot$ and mass ratios of $M_2/M_3 = 0.25$ (red circles) and 1.0 (black circles). Each point on the CDFs tells us the probability of the companions having a separation less than r_{23} during a close encounter if they are considered as point masses.

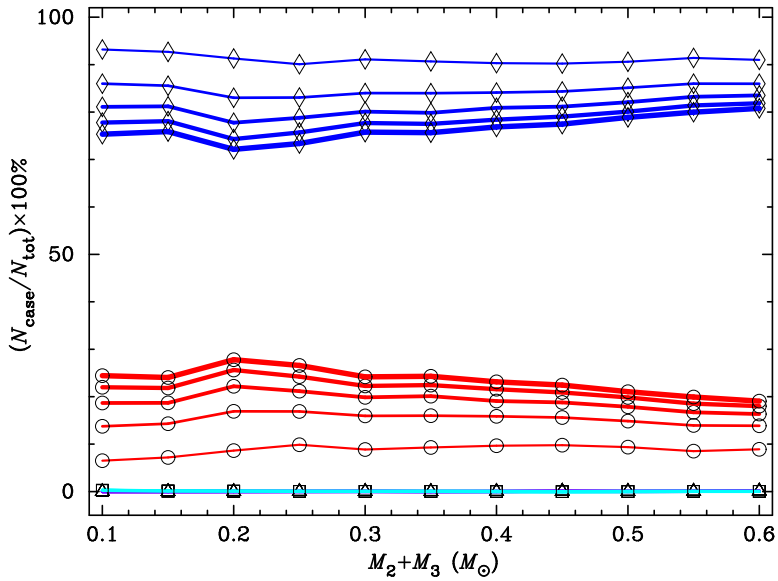

Figure 4.3 Effects of changing the radius factor (α) on the frequencies of ejections (blue lines with diamond symbols), CCCs (red lines with circle symbols), CPCs (purple lines with triangle symbols), and stable systems (cyan lines with square symbols). The frequencies are plotted against total companion-mass $M_2 + M_3$ of the ensembles. In all cases $M_1 = 1M_\odot$ and $M_2 = M_3$. Increasing line thicknesses correspond to increasing radius factors $\alpha = 1, 5, 10, 15, 20$. Note that the fractions of CPCs and stable systems are very small.

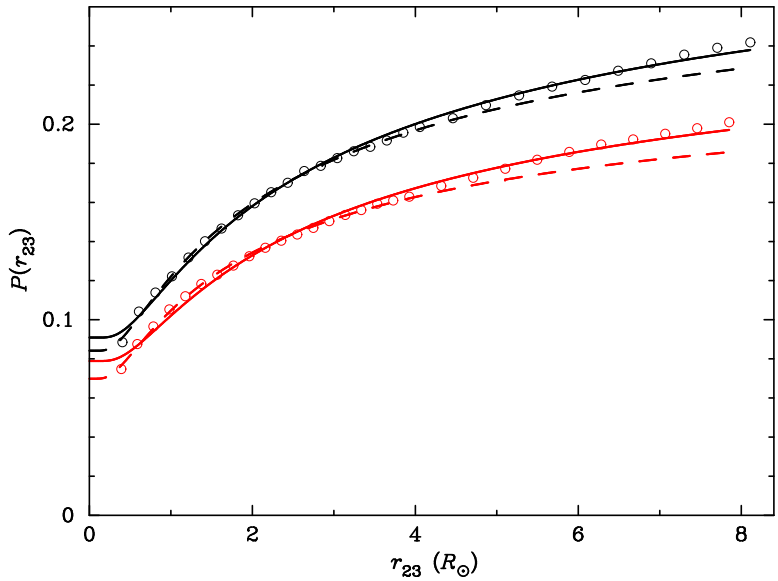

Figure 4.4 The probability of an encounter at companion separation $\leq r_{23}$, $P(r_{23})$, as measured by the frequency of CCCs with increasing α. In all cases $M_1 = 1M_\odot$ and $M_2 + M_3 = 0.3M_\odot$. Black circles are for systems with mass ratio $M_2/M_3 = 1$ and red circles for $M_2/M_3 = 0.25$. Solid lines are the fits from Equation 4.5 for all data, while dashed lines show the fits for only $\alpha = 1 - 10$.

The trends in Figure 4.4 can be fitted very well with Lévy's CDF (solid lines) of the form

$$P(r) = a\,\mathrm{erfc}\left(\sqrt{\frac{b}{r}}\right) + c, \tag{4.5}$$

where a, b, and c are constants; and $\mathrm{erfc}(x)$ is the complementary error function of variable x. This CDF provides the best fit with some meaningful properties, namely, $dP(r)/dr = 0$ at $r = 0$ and $\lim_{r \to \infty} P(r) = \text{constant}$. The values of the constants (a, b, and c) and the coefficient of determination ($\mathcal{R}^2$) corresponding to each data set are summarized in Table 4.1.

That the data are well fitted ($\mathcal{R}^2 \simeq 1$) by the Lévy distribution can be explained by assuming that (1) as $r_{23} \ll r_{12} \sim r_{13}$, the close encounter between the two companions is approximately a two-body problem and (2) the effects of a rotating frame of reference is small at small r_{23}. The problem can then be simplified to one body of a reduced mass $\mu = M_2 M_3/(M_2 + M_3)$ orbiting around a fixed central mass of $M = M_2 + M_3$. Let us now consider r_{23} as the separation between the masses μ and M at the pericentre of the orbit. At this turning point, as the radial velocity is zero, we assume further that (3) the tangential velocity (v_t) of the mass μ follows the one-dimensional Maxwell-Boltzmann distribution, i.e. $f(v_\mathrm{t}) \propto \exp(-v_\mathrm{t}^2/2\sigma^2)$, where σ is the velocity dispersion. The probability of the mass μ having v_t from that for a circular orbit to hyperbolic orbits around the fixed mass M may be written as

$$P(v_\mathrm{t} \geq v_\mathrm{cir}) \propto \int_{v_\mathrm{cir}}^{\infty} e^{-v_\mathrm{t}^2/2\sigma^2}\,\mathrm{d}v_\mathrm{t} \propto \mathrm{erfc}\left(\frac{v_\mathrm{cir}}{\sqrt{2}\sigma}\right) \tag{4.6}$$

By substituting $v_\mathrm{cir} = \sqrt{GM/r_{23}}$ into Equation 4.6, one can find that

$$P(r_{23}) = a\,\mathrm{erfc}\left(\sqrt{\frac{b}{r_{23}}}\right), \tag{4.7}$$

where a and b are constants. The constant c in Equation 4.5 is due to head-on collisions in which $v_\mathrm{t} \sim 0$.

In addition to the solid lines in Figure 4.4, the dashed lines show the fits of the data with $\alpha \leq 10$. Although these lines have better values of $\mathcal{R}^2$, as shown in Table 4.1, they tend to diverge from the data at higher α. These divergences may indicate some complicated dynamics that we have not included in our derivation above, for example, the effects of motion in rotating frame of reference.

Table 4.1 Constants in Equation 4.5 obtained from nonlinear regressions of the data in Figure 4.4. The goodness of fit is represented by the coefficient of determination $\mathcal{R}^2$ (closer to 1 is better).

α	M_2/M_3	a	b	c	$\mathcal{R}^2$
1-20	1.00	0.254	1.242	0.091	0.9971
	0.25	0.207	1.265	0.079	0.9945
1-10	1.00	0.232	0.972	0.084	0.9988
	0.25	0.180	0.847	0.070	0.9984

The differential of $P(r_{23})$ with respect to r_{23} is the probability density function (PDF) of the encounter having a separation at pericentre of r_{23},

$$p(r_{23}) = a\sqrt{\frac{b}{\pi}}\frac{e^{-b/r_{23}}}{r_{23}^{3/2}}. \tag{4.8}$$

The plots of $p(r_{23})$ from all fitted lines in Figure 4.4 are shown in Figure 4.5.

In addition to CCCs, the distribution of collision distances measured from the primary star is shown in Figure 4.6. The figure is for systems with $M_1 = 1M_\odot$, $M_2 = M_3 = 0.15M_\odot$, and $\alpha = 5$ in the three initial ranges of companion orbits: $20 - 100$AU (red histogram on the left), $100 - 200$AU (blue histogram in the middle), and $200 - 300$AU (black histogram on the right). In other cases, we find that the distance distribution does not depend on the companion mass ratio. Also, systems with more massive companions have similar distributions but with longer tails.

4.3.2 Systems of unequal-mass companions

The companion mass ratio (M_2/M_3) plays an important role in the energy distribution during close encounters between the companions. In an N-body system, the objects in the system tend to distribute kinetic energy equally (equipartition). The system tends to have slow-moving-high-mass and fast-moving-low-mass objects.

In our three-body system, the primary star is more massive than the companions. It therefore moves rather slowly compared to the companions which are, most of the time, also interacting with each other. For a system with unequal-mass companions ($M_2/M_3 < 1$), the equipartition of kinetic energy usually causes the least massive companion to be ejected from the system. For a system with equal-mass companions, in contrast, the companions need more close encounters to find themselves having unequal amounts of kinetic energy that are sufficient to send one of them out of the

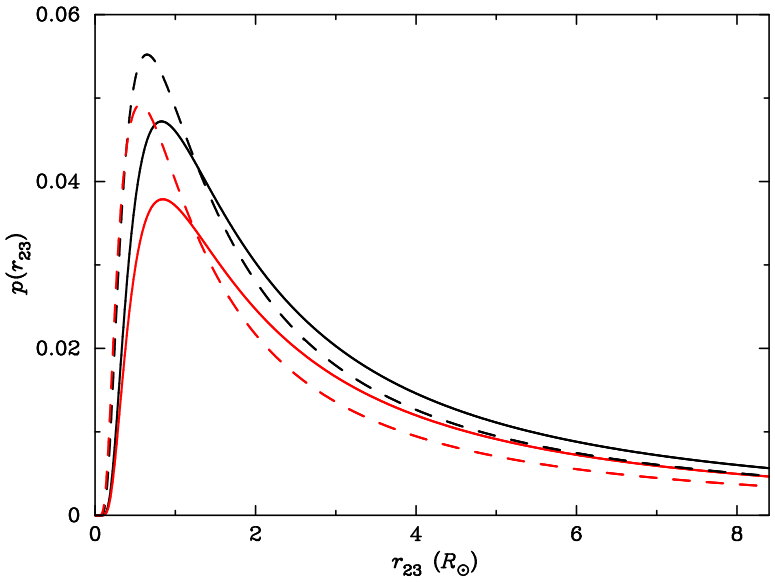

Figure 4.5 Probability density functions (PDFs) of the fitted lines in Figure 4.4. Colours and line styles are the same as in the previous figure.

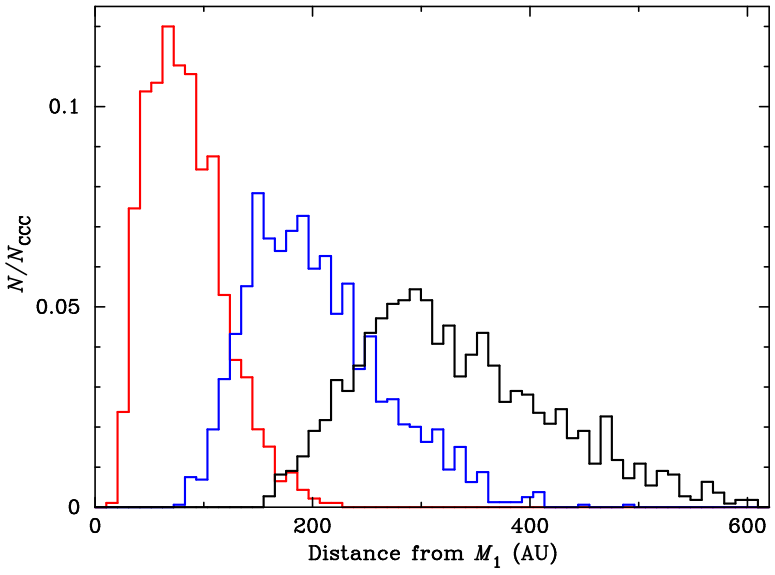

Figure 4.6 Distribution of collision distances measured from the primary star. The three histograms are of systems with $M_1 = 1M_\odot$, $M_2 = M_3 = 0.15M_\odot$, and $\alpha = 5$ in the three initial ranges of companion orbits: $20 - 100$AU (red histogram on the left), $100 - 200$AU (blue histogram in the middle), and $200 - 300$AU (black histogram on the right).

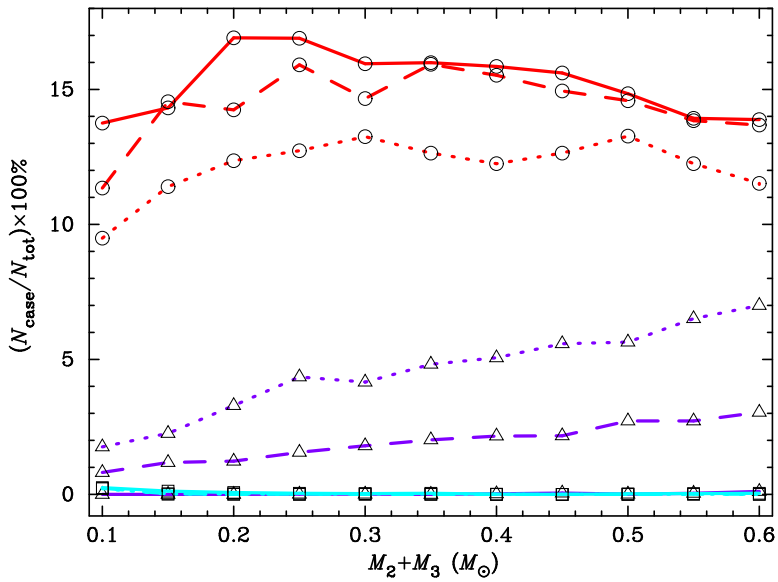

Figure 4.7 Effects of changing companion mass ratio (M_2/M_3) on the frequencies of CCCs (red lines with circle symbols), CPCs (purple lines with triangle symbols), and stable systems (cyan lines with square symbols). Different line styles represent different mass ratios: $M_2/M_3 = 0.25$ (dotted lines), 0.5 (dashed lines), and 1.0 (solid lines). In all cases, $M_1 = 1M_\odot$ and $\alpha = 5$.

system. The chance of collisions in an equal-mass system is therefore higher than in an unequal-mass system. We can see in Figure 4.7 that the number of collisions between companions (marked with circles) increases with the increasing mass ratio from $M_2/M_3 = 0.25$ (dotted lines) to $M_2/M_3 = 1.0$ (solid lines).

Figure 4.7 also shows an interesting feature of systems with unequal-mass companions, i.e. the increasing numbers of CPCs. We find that it is almost always the least-massive companion that collides with the primary star. This occurs after the least-massive companion has been regularly perturbed by the more-massive one whose orbit is larger. The least-massive loses angular momentum during each encounter with the more-massive, causing its orbit to become more and more eccentric. Eventually, the least-massive companion collides with the primary star. From our simulations, it is very likely that CPCs occur only in systems with unequal-mass companions.

4.3.3 The influence of other parameters

Apart from the radius factor (α) and the companion mass ratio, three other parameters can also affect the number of collisions: (1) the potential energy of the system, (2) the orbital separation between the companions, and (3) the coplanarity of the orbits.

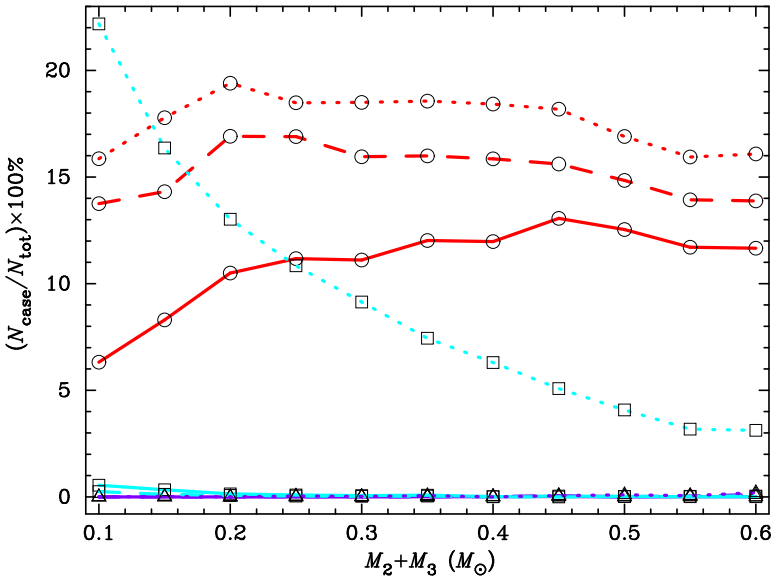

Figure 4.8 Effects of changing the initial orbital range of the companions on the frequencies of CCCs (red lines with circle symbols), CPCs (purple lines with triangle symbols), and stable systems (cyan lines with square symbols). Different line styles represent different ranges of the orbital radii: $20-100$AU (dotted lines), $100-200$AU (dashed lines), and $200-300$AU (solid lines). In all cases, $M_1=1M_\odot$, $M_2/M_3=1$, and $\alpha=5$.

Potential energy

To some extent, the potential energy sets how difficult an ejection is. In a particular configuration like our coplanar three-body system, an increase of the potential energy, either by increasing the primary mass or decreasing the range of companion orbits, produces less ejections but more CCCs and stable systems. The results are shown in Figure 4.8. We can see from the figure that the number of stable systems from the companion orbital range of $20-100$AU (dotted cyan line with square symbols) is much higher than that from the other two ranges. This is because the companions can hardly feel each others gravity while orbiting near the central star. The closest separation for a close encounter to result in ejection is decreased. This reduces the chance of ejections but increases the chance of collisions.

Separation between the companions

The companions cannot interact with each other to cause dramatic results if they are separated by too large a distance. We demonstrate this with three ensembles whose companion's initial orbits are restricted to be inside two widely-separated ranges of $r_2=50-60$ AU (for M_2) and $r_3=200-210$ AU (for M_3): (a) $M_2/M_3=0.5$, (b) $M_2/M_3=1$, and (c) $M_2/M_3=2$.

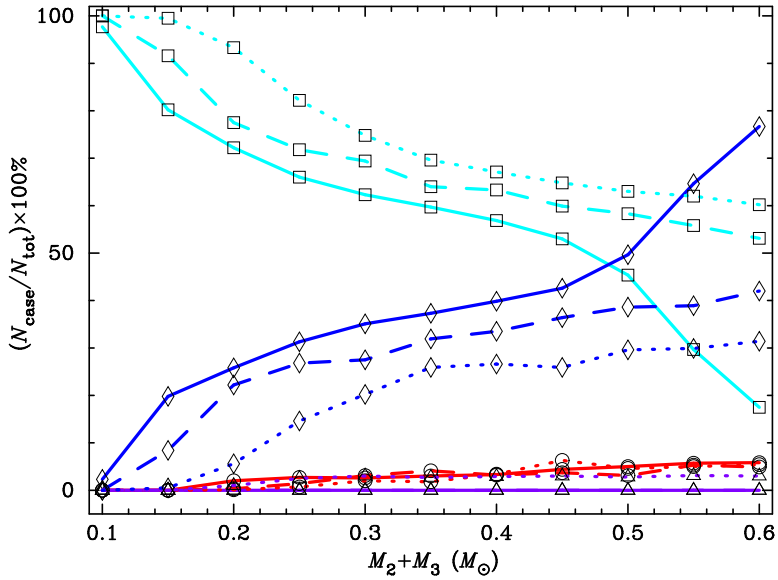

Figure 4.9 Effects of large initial separation between the companions (r_{23}) on the frequencies of ejections (blue lines with diamond symbols), CCCs (red lines with circle symbols), CPCs (purple lines with triangle symbols), and stable systems (cyan lines with square symbols). Dotted lines represent the systems with $M_2/M_3 = 0.5$ (the less massive in the smaller orbit), dashed lines with $M_2/M_3 = 1$, and solid lines with $M_2/M_3 = 2$ (the more massive in the smaller orbit). In all cases $M_1 = 1M_\odot$ and $\alpha = 5$.

We can see from Figure 4.9 that the systems initialized with widely-separated companions are very stable. The way in which the number of stable systems (cyan lines with square symbols) changes along the total companion-mass is almost exactly opposite to that of ejections (blue lines with diamond symbols). The systems tend to be more stable if the lower-mass companion is initialized with a smaller orbit ($M_2/M_3 < 1$), compare the dotted cyan line ($M_2/M_3 = 0.5$) with the dashed cyan line ($M_2/M_3 = 1$) and the solid cyan line ($M_2/M_3 = 2$) in Figure 4.9. CPCs occur only in systems with $M_2/M_3 < 1$ (the dotted purple line with triangle symbols). The number of CCCs drops significantly, especially in systems with low total masses of companions.

Coplanarity of the orbits

To test the effect of non-coplanarity, we perform some ensembles of simulations in which the companion M_3 is given a small velocity component in z-direction just enough to make its orbit initially inclined by $\sim 5°$ and $\sim 10°$. We find that the number of CCCs drops significantly as the inclination increases, as shown in Figure 4.10, from zero (solid line) to $\sim 5°$ (dashed line) and $\sim 10°$ (dashed line). Although the number of collisions decreases in non-coplanar configurations, it is still a non-negligible number.

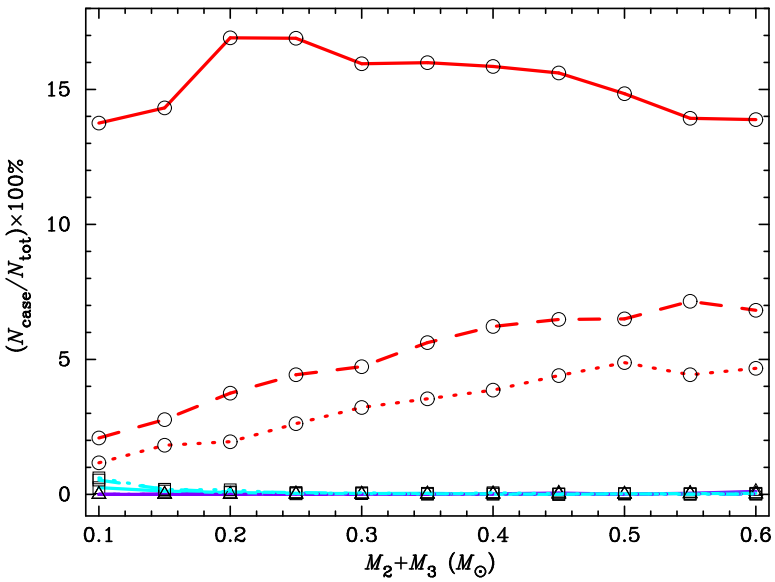

Figure 4.10 Effects of changing orbital coplanarity on the frequencies of CCCs (red lines with circle symbols), CPCs (purple lines with triangle symbols), and stable systems (cyan lines with square symbols). Different line styles represent different degrees of orbital inclination between the two companions: coplanar orbits (solid lines), $\sim 5°$ inclined orbits (dashed lines), and $\sim 10°$ inclined orbits (dotted lines). In all cases, $M_1 = 1M_\odot$, $M_2/M_3 = 1$, and $\alpha = 5$.

4.3.4 The remaining binary system

After one of the companions has been ejected, the remaining system becomes a binary system. The binary system has some interesting properties such as the distributions of the semi-major axis and eccentricity. The distribution of both quantities does not seem to vary significantly with the total mass of the companions but rather with mass ratio. Figure 4.11 and 4.12 show the distribution of the semi-major axis and eccentricity of systems with $M_1 = 1M_\odot$, $M_2 + M_3 = 0.3M_\odot$, and $\alpha = 5$. The initial range of the orbital radii for the systems is $100 - 200$AU. The red, blue, and black histograms are of the systems with mass ratio $M_2/M_3 = 0.25$, 0.5, and 1, respectively.

We can see from Figure 4.11 that the orbital range of the remaining companion is displaced from the initial range ($100 - 200$AU). The displacement increases with the increase of companion mass ratio (M_2/M_3). This result may be explained in terms of the energy partitioning during ejection. As the kinetic energy of a particle is also a function of mass, more massive escaper would take more energy from the system with it than the less massive one does. In a system with low companion mass ratio, the escaper is always the least massive companion; thus, only a small amount of energy would be taken from the system. This leaves the more massive companion with a

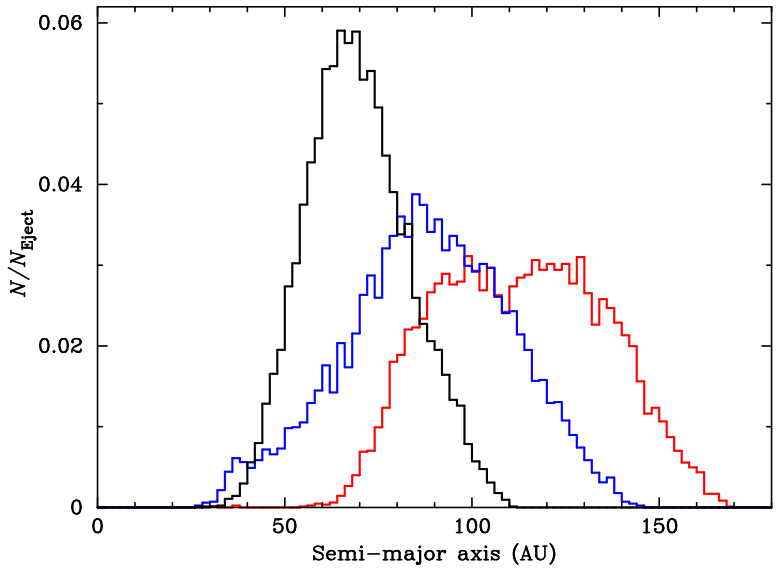

Figure 4.11 Distributions of the semi-major axis of the remaining binary system. The histograms are of systems with mass ratio $M_2/M_3 = 0.25$ (red), 0.5 (blue), and 1 (black), respectively. All systems have $M_1 = 1M_\odot$, $M_2 + M_3 = 0.3M_\odot$, and $\alpha = 5$.

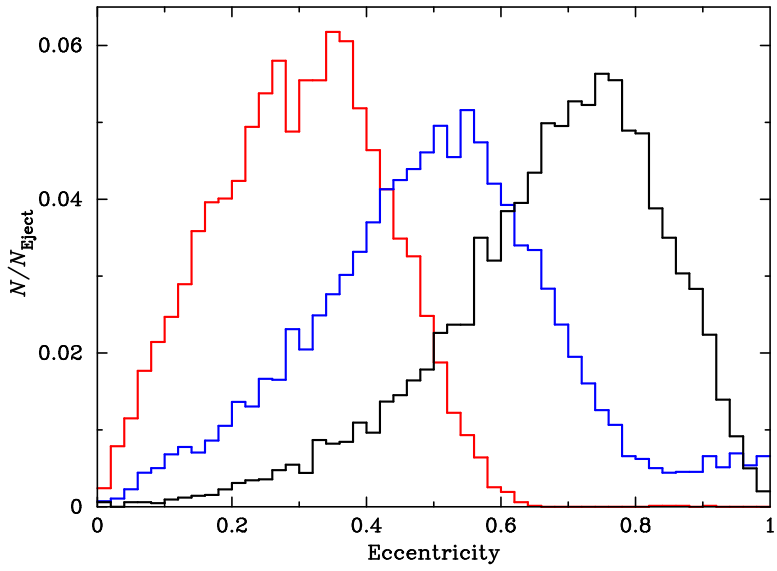

Figure 4.12 Distributions of the eccentricity of the remaining binary system. The histograms are of systems with mass ratio $M_2/M_3 = 0.25$ (red), 0.5 (blue), and 1 (black), respectively. All systems have $M_1 = 1M_\odot$, $M_2 + M_3 = 0.3M_\odot$, and $\alpha = 5$.

slightly shrunken orbit, i.e. small displacement in the orbital range of the remaining companion. The eccentricity of the remaining companion is also lower in systems with lower companion mass ratios, as shown in Figure 4.12.

4.4 Discussion

We have studied the dynamical evolution of young triple systems, in which collisions among the members are considered. We have found that the chance of a collision between the companions (CCC) is surprisingly high, especially in a compact, coplanar system with equal-mass companions. The chance of a collision between one of the companions and the primary (CPC) increases in a system with low companion mass ratio, but the chance is generally lower than that of a CCC. The radius of the components, which is assumed to be related to the ages, affects the chance of CCCs but not CPCs. We have also found that the separation distribution of close encounters can be described by the Lévy cumulative distribution function. The distribution shows us that the chance of head-on collisions is actually high. Although the chance of collisions in triple systems may be affected by several factors, it is still not negligible in most cases.

That the chance of collisions in young systems is high supports our idea that collisions may occasionally play a significant role in the early stages of multiple star formation. Collisions between two members in a young multiple system would result in the two components to merge and form a new object with different internal structure. Based on Baraffe et al. (2009), this restructuring process would more or less define a new evolutionary path to the object. At later times, the new object may look different from other components in the system. We suggest that this could be an explanation for the age discrepancy problem in some young star systems that are observed with infrared companions.

Chapter 5

Stable circumstellar discs

The main goal of this chapter is to simulate a number of isolated star-disc systems and study their properties under the variations of some parameters such as resolution, temperature structure, and viscosity. We focus our study on low-mass compact discs which are robust against gravitational instabilities. The purpose of this chapter is also to find a disc with suitable conditions for using as an initial disc in simulations performed in Chapter 6.

This chapter begins with a brief review of disc simulations in Section 5.1. The disc initialization is described in Section 5.2. The simulation details are provided in Section 5.3, followed by simulation results in Section 5.4. We then describe in Section 5.5 the criteria for choosing the disc to be used for simulations in the next chapter. Finally, we summarize this chapter work in Section 5.6.

5.1 Simulations of circumstellar discs

It is well known that circumstellar discs are a natural outcome of a collapsing cloud core with angular momentum. Disc formation has been investigated by means of hydrodynamic simulations since the early works of, for example, Larson (1972) and Tscharnuter (1975). Huge improvements in computing power over the last two decades provide us with the capability to perform three-dimensional simulations of astrophysical phenomena. Subsequent to the first three-dimensional simulation of a collapsing cloud core performed by Bate (1998), an increasing number of star formation simulations including disc evolution have been performed with various initial conditions and radiation treatments (e.g. Goodwin et al. 2004a,b, 2006; Boley et al. 2007; Attwood et al. 2009; Tscharnuter et al. 2009; Rice et al. 2010; Bate 2010; Walch et al. 2010;

Bate 2011; Machida et al. 2010; Machida and Matsumoto 2011). Some simulations also include complicated physics such as magnetic field (e.g. Machida et al. 2004; Hennebelle and Fromang 2008).

Circumstellar discs are thought to be a place out of which low-mass stars and planets may form. The formation of those objects depend largely on physical properties of the disc such as mass, density, and temperature. In simulations, it has been found that methods used for modelling physical processes are crucial to the outcomes. Stamatellos and Whitworth (2009b), for example, have shown that using different prescriptions to treat radiation transfer in the simulation of a massive extended disc can affect both the efficiency of disc fragmentation and the properties of the forming objects.

In general, numerical studies of instabilities in a disc focus on (a) massive extended discs with outer radii $\gtrsim 100$AU and mass comparable to that of the central star; (b) low-mass compact discs with outer radii of a few tens of AU and mass of a few per cent of the central star's mass; and (c) discs in multiple systems. The last category will be discussed later in Chapter 6.

For a massive extended disc, simulations performed by Stamatellos et al. (2007) and Stamatellos and Whitworth (2009a) have shown that a heavy disc of initial mass $M_{\rm d} = 0.7 M_{\odot}$ with outer radii $R_{\rm out} \sim 400$AU surrounding a $0.7 M_{\odot}$ star can fragment to form a number of low-mass hydrogen-burning stars, brown dwarfs, and planets. The fragmentation of the disc occurs rapidly within a few thousand years and preferentially occurs in the middle parts of the disc ($R \sim 100 - 200$AU). Just after the disc has fragmented, the newly forming objects begin to accrete material from the disc. Within several thousand years, the disc material is almost depleted and the objects are interacting dynamically with each other. On one hand, this simulation result seems to be consistent with observations in that only a small number of massive extended discs have been observed (Eisner et al. 2005; Eisner and Carpenter 2006; Eisner et al. 2008); that is, massive extended discs are short lived because of the fragmentation process. On the other hand, it is still unclear how those heavy discs were being formed without having been interrupted by instabilities on the way.

In contrast, more attention has been paid to numerical studies of low-mass compact discs which are often called *protoplanetary discs*. Low-mass discs tend to be robust against fragmentation or gravitational instabilities when the Toomre parameter and cooling timescale of the discs are considered (see Section 1.4.2). However, it has been argued that gravitational instabilities may be promoted by some cooling processes, leading to fragmentation of the disc. There are two candidates for the cooling mechanisms: convection and radiation. Boss (2004) and Mayer et al. (2007)

have suggested that convection may play a leading role in cooling the midplane of an optically thick disc where radiation transfer finds difficulty in operating. It is argued by Rafikov (2007) that convective cooling may not actually operate as fast as required by the cooling timescale, especially in the region within several tens of AU from the central star. Nevertheless, radiative cooling does not seem to be efficient either. Stamatellos and Whitworth (2008), for example, use the Stamatellos et al. (2007) radiative cooling method to show that a disc of mass $M_{\rm d} = 0.07 M_{\odot}$ with outer radii $R_{\rm out} \sim 40$AU surrounding a $0.5 M_{\odot}$ star is still stable even in the case in which only a background radiation temperature of 10K is considered throughout the disc.

In the following sections, we perform numerical simulations of low-mass discs to investigate their evolution under variations of resolution, temperature structure, and viscosity. The evolution of the discs will be considered in two stages: the early stage during which the discs become quasi-steady ($t = 0 - 2$kyr) and the rest ($t = 2 - 102$kyr). The latter is to verify that the discs are stable and can be used as an initial disc for the simulations in the next chapter.

5.2 Disc initialization

Our star-disc systems for SPH simulations are initialized by using similar initial conditions and methods described in Stamatellos and Whitworth (2008). An initial star-disc system consists of a central star of mass $M_{\rm s} = 0.5 M_{\odot}$ surrounded by a disc of mass $M_{\rm d} = 0.07 M_{\odot}$ with radius R extended from 0.5 to 40AU. We use a sink particle, described in Section 3.6.1, to represent the central star. The sink can accrete particles which are bound within the sink radius of $R_{\rm sink} = 0.5$AU. The disc is embedded in the background radiation field of $T_{\infty} = 10$K and assumed to be heated by the central star with a temperature profile described below.

5.2.1 Density and temperature profiles

Initial discs are assumed to have axial symmetry in mass distribution and temperature structure. A power-law function is often used for modelling the surface density (Σ) and temperature (T) of circumstellar discs (e.g. Beckwith et al. 1990). For surface density, we use Equation 1.10b from Section 1.3.1, i.e.

$$\Sigma(R) = \Sigma_{\circ} \left(\frac{R}{R_{\circ}} \right)^{-p} \tag{5.1}$$

where p is the power-law index and $\Sigma_\circ$ is the surface density at radius $R = R_\circ$. The value of $\Sigma_\circ$ can be calculated by supposing that the disc is flat, so that the mass of an annular strip with inner radius R and width $\mathrm{d}R$ is $\mathrm{d}M = 2\pi\Sigma R\mathrm{d}R$. By integration, we have

$$\begin{aligned} M(R) &= 2\pi\Sigma_\circ R_\circ^p \int_{R_{\min}}^{R} R^{1-p}\,\mathrm{d}R \\ &= \frac{2\pi}{2-p}\Sigma_\circ R_\circ^p \left(R^{2-p} - R_{\min}^{2-p}\right), \end{aligned} \tag{5.2}$$

where $R_{\min}$ is the inner radius of the disc. Integrating for the entire disc ($R = R_{\max}$) with $p = 1/2$ (see Section 1.3.3) and rearranging the terms give us

$$\Sigma_\circ = \frac{3}{4\pi}\frac{M_\mathrm{d}}{R_\circ^p\left(R_{\max}^{3/2} - R_{\min}^{3/2}\right)}. \tag{5.3}$$

By using $R_\circ = 1\mathrm{AU}$, $R_{\min} = 0.5\mathrm{AU}$, $R_{\max} = 40\mathrm{AU}$, and $M_\mathrm{d} = 0.07 M_\odot$, we then have $\Sigma_\circ = 6.615\times10^{-5} M_\odot/\mathrm{AU}^2$. We will see later in the simulations that the initial value of p is not crucial as the disc particles will be redistributed according to the effects of viscosity and temperature structure; the value of p changes accordingly.

Similar to the surface density profile, the temperature profile is also assumed to be a power-law function (Equation 1.10a). However, the profile that we use here is modified by including the background radiation temperature $T_\infty = 10\mathrm{K}$:

$$T(R) = T_\circ\left(\frac{R}{R_\circ}\right)^{-q} + T_\infty, \tag{5.4}$$

where q is the power-law index and $T_\circ$ the temperature at $R = R_\circ = 1\mathrm{AU}$. According to the observations discussed in Section 1.3.4, we explore the influence of temperature profile indices $q = 1/2$ (flared disc), 3/4 (flat disc), and (an extra steep) 1 on the disc evolution. We also investigate the effect of using the inner disc temperatures $T_\circ = 300\mathrm{K}$, 600K, and 1200K.

5.2.2 Distribution of SPH particles

To create a disc, SPH particles are distributed within a volume constrained by the density and temperature of the disc. For convenience, the positions are calculated in cylindrical coordinates (r, ϕ, z) and then transformed to rectangular coordinates (x, y, z). The distribution in each coordinate is described as follows.

Radial distribution

To obtain the radial distribution constrained by the surface-density profile (Equation 5.1), let us define the fraction between the disc mass enclosed by radius R and the disc total mass as

$$f_r = \frac{M(R)}{M_\mathrm{d}}. \tag{5.5}$$

Using Equation 5.2 with $p = 1/2$ for $M(R)$, one can find that

$$R = \left[\frac{3}{4\pi}\frac{M_\mathrm{d}}{\Sigma_\circ R_\circ^p} f_r + R_\mathrm{min}^{3/2}\right]^{2/3}. \tag{5.6}$$

Given f_r a set of random numbers valued between 0 and 1 (inclusive) and $R_\circ = 1\mathrm{AU}$, this equation provides us the radial distribution of particles.

Azimuthal distribution

Since the disc is axially symmetric in density, the azimuthal component (ϕ) of particles in the disc can directly be found from the azimuthal fraction $f_\phi = \phi/2\pi$, or

$$\phi = 2\pi f_\phi. \tag{5.7}$$

Similar to the distribution of the previous component, f_ϕ is chosen randomly from values between 0 and 1 (inclusive).

Vertical distribution

In order to find the distribution in this component, the vertical scale height ($z_\circ$), which represents the thickness of the disc, has to be determined first. This can be roughly approximated by considering that particles at vertical height $z_\circ(R)$ above the disc midplane is in an equilibrium of vertical forces (e.g. Stamatellos and Whitworth 2008). The balance of vertical accelerations (a_z) may be written as

$$[a_z]_\mathrm{sgrav} + [a_z]_\mathrm{dgrav} = [a_z]_\mathrm{dhydro}\,, \tag{5.8}$$

where $[a_z]_\mathrm{sgrav}$ is the gravitational acceleration due to the central star, $[a_z]_\mathrm{dgrav}$ the gravitational acceleration due to the self gravity between disc particles, and $[a_z]_\mathrm{dhydro}$ the hydrostatic acceleration in the disc. The two gravitational accelerations have

directions pointing towards the disc midplane, opposite to the directions of the hydrostatic acceleration.

By assuming that the disc is thin ($z_\circ(R) \ll R$) the gravitational acceleration from the central star may be approximated as

$$[a_z]_{\rm sgrav} = \frac{GM_{\rm s}}{R^2 + z_\circ^2(R)} \frac{z_\circ(R)}{\sqrt{R^2 + z_\circ^2(R)}} \simeq \frac{GM_{\rm s}}{R^2} \frac{z_\circ(R)}{R}. \tag{5.9}$$

The gravitational acceleration from the disc itself, on the other hand, is very difficult (if not impossible) to calculate directly. It may only be estimated by considering the disc as an infinite sheet, so that Gauss's law for gravity can be applied. One can find that the acceleration is

$$[a_z]_{\rm dgrav} \simeq 2\pi G\Sigma(R). \tag{5.10}$$

The vertical hydrostatic acceleration can be derived from the momentum equation of a fluid given by

$$[a_z]_{\rm dhydro} = -\frac{1}{\rho}\frac{\partial P}{\partial z}\bigg|_{z=z_\circ}, \tag{5.11}$$

where $P = P(R, z)$ is the local isothermal pressure,

$$P(R, z) = \rho(R, z) c_{\rm s}^2(R). \tag{5.12}$$

The isothermal sound speed $c_{\rm s} = c_{\rm s}(R)$ in Equation 5.12 is given by

$$c_{\rm s}(R) = \sqrt{\frac{k_{\rm B} T(R)}{\bar{\mu} m_{\rm H}}}, \tag{5.13}$$

where $k_{\rm B}$ is Boltzmann's constant, $T(R)$ the temperature at radius R (Equation 5.4), $\bar{\mu}$ the mean molecular weight (see Section 5.2.4), and $m_{\rm H}$ the hydrogen mass. The volume density $\rho(R, z)$ in Equation 5.12 is another parameter that is difficult to obtain an exact expression. Nevertheless, we may obtain its closest form from considering (for a moment) that the disc has no self gravity, i.e. $[a_z]_{\rm dgrav} = 0$. In this way, we can equate Equation 5.11 to Equation 5.9 (with $z_\circ \to z$). After rearrangement, we have

$$\frac{\partial \rho}{\partial z} = -\frac{GM_{\rm s} z}{c_{\rm s}^2 R^3} \rho. \tag{5.14}$$

The solution to this equation is simply a Gaussian function. If we assume that gravity from the central star dominates self gravity in the disc as $M_{\rm d} \ll M_{\rm s}$, approximating the volume density with a Gaussian profile may be acceptable. In our disc set-up, we employ a Gaussian function of the form

$$\rho(R,z) \simeq \rho(R,0)\exp\left[-\left(\frac{bz}{z_{\circ}(R)}\right)^2\right], \tag{5.15}$$

where $\rho(R,0)$ is the volume density at the midplane and b is an arbitrary constant. The hydrostatic acceleration (Equation 5.11) now becomes

$$\begin{aligned}
[a_z]_{\rm dhydro} &\simeq -\frac{c_{\rm s}^2(R)}{\rho(R,z)}\frac{\partial\rho(R,z)}{\partial z}\bigg|_{z=z_{\circ}} \\
&\simeq -\frac{c_{\rm s}^2(R)}{\rho(R,z)}\left\{-\frac{2b^2 z}{z_{\circ}^2(R)}\rho(R,0)\exp\left[-\left(\frac{bz}{z_{\circ}(R)}\right)^2\right]\right\}\bigg|_{z=z_{\circ}} \\
&\simeq \frac{2b^2 c_{\rm s}^2(R)}{z_{\circ}(R)}.
\end{aligned} \tag{5.16}$$

Rearranging the substitution of Equation 5.9, 5.10, and 5.16 into Equation 5.8 gives us the quadratic equation

$$z_{\circ}^2(R) + \left(\frac{2\pi\Sigma(R)R^3}{M_{\rm s}}\right)z_{\circ}(R) - \frac{2b^2R^3c_{\rm s}^2(R)}{GM_{\rm s}} = 0.$$

Solving this equation gives us the force-balanced scale height

$$z_{\circ}(R) \simeq -\frac{\pi\Sigma(R)R^3}{M_{\rm s}} + \left[\left(\frac{\pi\Sigma(R)R^3}{M_{\rm s}}\right)^2 + \frac{2b^2R^3c_{\rm s}^2(R)}{GM_{\rm s}}\right]^{1/2}. \tag{5.17}$$

The vertical distribution of particles can be obtained from the fraction of surface density defined as

$$f_z = \frac{\displaystyle\int_{-z}^{z}{\rm d}\Sigma}{\displaystyle\int_{-\infty}^{\infty}{\rm d}\Sigma} = \frac{\displaystyle\int_{-z}^{z}\rho(R,z)\,{\rm d}z}{\displaystyle\int_{-\infty}^{\infty}\rho(R,z)\,{\rm d}z}. \tag{5.18}$$

For convenience in integration, we use

$$\rho(R,z) \simeq \rho(R,0)\mathrm{sech}^2\left(\frac{bz}{z_\circ(R)}\right) \tag{5.19}$$

instead of Equation 5.15. This is because Equation 5.19 is an integrable function and also closely resembles the Gaussian. By substituting Equation 5.19 into Equation 5.18, we have

$$f_z = \tanh\left(\frac{bz}{z_\circ(R)}\right). \tag{5.20}$$

The vertical component of particles in the disc becomes

$$z = \frac{z_\circ(R)}{b}\tanh^{-1}(f_z). \tag{5.21}$$

The value of b roughly defines the initial thickness of the disc, namely, the bigger the value the thicker the disc. For our simulations, we simply use $b=1$. Note that the random number f_z in this case is $-1<f_z<1$ (exclusive), for both positive and negative sides of the disc.

5.2.3 Initial velocities

Particles are initiated with Keplerian velocities to move in circular orbits. The azimuthal velocity of a particle at radius R from the central star is given by

$$v_\phi = \left[\frac{G\left(M_\mathrm{s}+M(R)\right)}{R}\right]^{1/2}, \tag{5.22}$$

where, from Equation 5.2 with $R_\circ = 1\mathrm{AU}$ and $p=1/2$,

$$M(R) = \frac{4\pi}{3}\Sigma_\circ\left(R^{3/2}-R_\mathrm{min}^{3/2}\right) \tag{5.23}$$

is the mass of the interior disc enclosed by radius R. The velocities in the radial and vertical components are zero.

5.2.4 Composition

Our discs are assumed to be comprised of 70 per cent of molecular hydrogen and 30 per cent of helium with no other heavier elements. The mean molecular weight $\bar{\mu}$ for

using in SPH simulations can be obtained from

$$\frac{1}{\bar{\mu}} = \frac{X}{\mu_{\mathrm{H}_2}} + \frac{Y}{\mu_{\mathrm{He}}}, \tag{5.24}$$

where X is the fraction by weight of hydrogen, Y the fraction by weight of helium, μ_{H_2} the molecular weight of molecular hydrogen, and μ_{He} the molecular weight of a helium atom. Substituting $X = 0.7$, $Y = 0.3$, $\mu_{\mathrm{H}_2} = 2$, and $\mu_{\mathrm{He}} = 4$ gives us $\bar{\mu} \simeq 2.35$. The mean gas-particle mass in the ideal gas law Equation 3.89 is obtained from $\bar{m} = \bar{\mu} m_{\mathrm{H}}$, where m_{H} is the mass of hydrogen.

5.3 Simulations

We use the initial conditions described in the previous section to set up a number of circumstellar discs with different resolutions, viscosity parameters, and temperature profiles. Note again that all discs use the power-law index $p = 1/2$. The surface density profile of a disc that is created from 2×10^5 SPH particles is as shown in Figure 5.1(left). The light-green line in the figure is the theoretical profile with $p = 1/2$. We can see that the density profile of the generated disc agrees with that expected. This simply depends on the resolution of the disc, the higher the better.

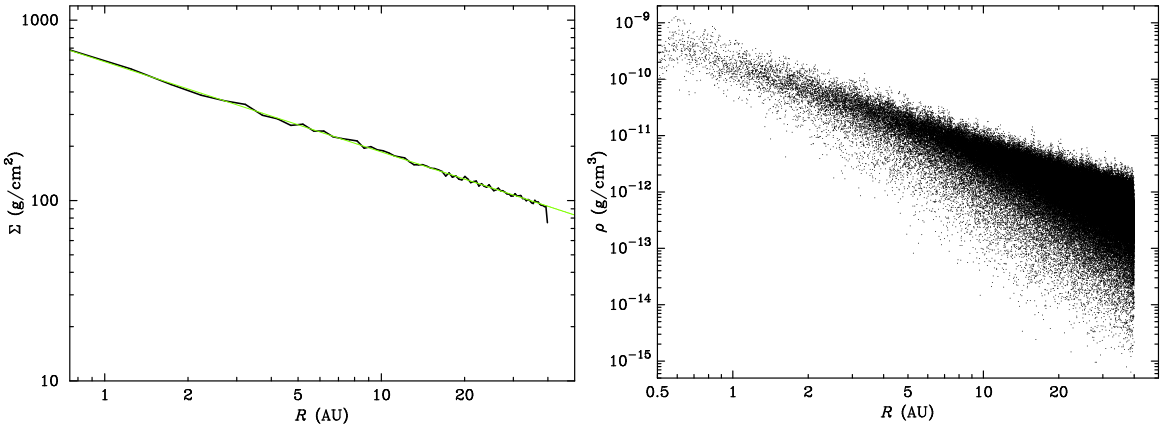

Figure 5.1 Surface density (left) and volume density (right) of a disc created from 2×10^5 SPH particles. The light-green line in the left subfigure is the expected profile of $p = 1/2$.

Although all of our discs use the same value of p, their vertical distributions may be different by the different value of q (the temperature profile index). A disc with flatter temperature profile (low q) may be thicker (or fluffier) than a disc with steeper temperature profile (high q).

At the beginning of each simulation, the smoothing length (h) and volume density (ρ) of all SPH particles are calculated. The volume density can be plotted as shown in Figure 5.1(right).

We perform a number of tests to investigate the influences of resolution, temperature structure, and viscosity parameters on the evolution of the discs. The specifications of the tests in this chapter are described as follows.

5.3.1 Resolution tests

In a numerical study of gravitational instabilities in a disc, resolution of the disc needs to be sufficiently high to ensure that the instabilities are not due to numerical effects. However, using higher resolution does cost more computational resources and is sometimes unnecessary for some problems. It is thus useful to be able to estimate the minimum resolution required by the system in question. In core fragmentation studies, the minimum resolution for an SPH simulation is suggested by Bate and Burkert (1997) (Section 3.2). For our disc simulations, we adopt the resolution requirement criterion used in Forgan and Rice (2009), i.e.

$$\frac{M_{\rm J}}{M_{\rm min}} \sim \frac{1}{2}\left(\frac{M_{\rm d}}{M_{\rm s}}\right)^2 \frac{N_{\rm tot}}{N_{\rm neib}}, \tag{5.25}$$

where $M_{\rm J}$ is the Jeans mass, $M_{\rm min}$ the minimum resolvable mass, $N_{\rm tot}$ the total number of particles in the disc, and $N_{\rm neib} \simeq 50$ the number of nearest neighbours. With $M_{\rm d} = 0.07 M_{\odot}$, $M_{\rm s} = 0.5 M_{\odot}$, and giving $M_{\rm J}/M_{\rm min} = 1$, we then have $N_{\rm tot} \sim 5102$ particles for the minimum resolution. Therefore, using 2×10^5 particles for our main disc simulations would be sufficient. In resolution tests, nevertheless, we perform simulations with various resolutions to investigate the effects of resolution on the mass accretion rate of the central star and the stability of the disc. The disc specifications for the resolution tests are given in Table 5.1.

5.3.2 Temperature tests

We perform nine tests to explore the effects of using different temperature profiles (q) and inner disc temperatures ($T_{\circ}$). The disc specifications for the temperature tests are given in Table 5.2.

Table 5.1 Disc specifications for the resolution tests. Five tests in total.

Number of particles ($\times 10^3$):	$N_{\rm sph} = 10, 50, 100, 200, 300$
Viscosity parameters:	$\alpha = 0.1$, $\beta = 0.2$
Balsara switch:	No
Disc temperature profile:	$q = \frac{1}{2}$
Disc temperature at 1AU:	$T_\circ = 300$K
Simulation time:	$t_{\rm end} = 2$kyr

Table 5.2 Disc specifications for the temperature tests. Nine tests in total.

Number of particles ($\times 10^3$):	$N_{\rm sph} = 200$
Viscosity parameters:	$\alpha = 0.1$, $\beta = 0.2$
Balsara switch:	No
Disc temperature profile:	$q = \frac{1}{2}, \frac{3}{4}, 1$
Disc temperature at 1AU:	$T_\circ = 300$K, 600K, $1200K$
Simulation time:	$t_{\rm end} = 2$kyr

5.3.3 Artificial viscosity tests

The artificial viscosity parameters α and β have a major role in controlling the artificial viscosity in a disc (Section 3.2.4). Viscous forces can cause an outward transfer of angular momentum in a disc (Lynden-Bell and Pringle 1974). The particles that gain angular momentum tend to move radially outwards while the ones that lose do the opposite. This would affect the mass accretion rate of the central star. However, choosing the values of α and β for simulations is rather empirical. For the high-resolution set of simulations that will also be used in the next chapter, we use $\alpha = 0.1$ and $\beta = 0.2$.

The effects of artificial viscosity are explored by the tests that use various values of viscosity parameters with and without Balsara viscosity switch (Balsara 1995, Section 3.2.4). The disc specifications for the viscosity tests are given in Table 5.3. Note for the viscosity parameters that, in all cases, we use $\beta = 2\alpha$. Therefore, in many places, only α is mentioned for convenience.

Table 5.3 Disc specifications for the viscosity tests. Twenty one tests in total.

Number of particles ($\times 10^3$):	$N_{\rm sph} = 200$
Viscosity parameters ($\beta = 2\alpha$):	$\alpha = 0, 0.01, 0.03, 0.05, 0.1, 0.2, 0.3, 0.4, 0.5, 1, 2$
Balsara switch:	Yes, for $\alpha > 0$.
Disc temperature profile:	$q = \frac{1}{2}$
Disc temperature at 1AU:	$T_\circ = 300$K
Simulation time:	$t_{\rm end} = 2$kyr

5.3.4 Stability tests

In the next chapter, we will study the evolution of a disc in a binary system. The star-disc system with $q = 3/4$, $T_\circ = 600$K, and resolution of 200k particles will be used as a circumprimary disc to be perturbed by the companion star in the binary system. In order tell that any change occurring in the disc is not from the disc itself but the perturbation from the companion, we evolve the star-disc system in isolation for the same length of simulation time (500kyr). In this chapter, however, we also evolve the remaining systems (of the same resolution) further from 2kyr up to 102kyr to study the evolution of the systems.

5.3.5 Numerical details

Our SPH simulations are performed by using the SPH code SEREN (Hubber et al. 2011) mentioned in Section 3.6.3. The grad-h scheme of SPH (Section 3.3.1) is used with the Thomas-Couchman M4 smoothing kernel (Thomas and Couchman 1992) (Section 3.2.1). Our preferential choice of integrator is the leapfrog `KDK` (Section 2.3). We use the Monaghan (1997) prescription for the artificial viscosity (Section 3.2.4). The radiation transfer is treated by the Stamatellos et al. (2007) radiative cooling scheme (Section 3.4.4). Finally, to reduce the time for building a particle tree, the particles whose distances from the central star are greater than 3000AU will be removed from the calculation.

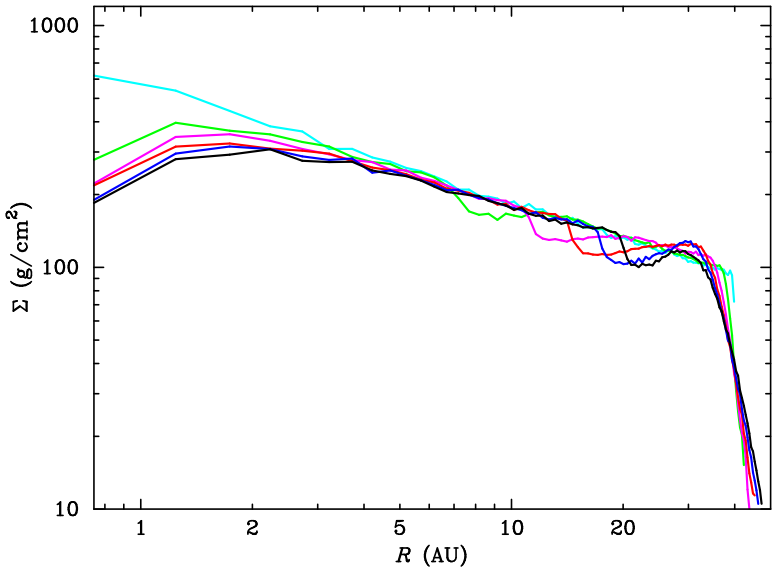

Figure 5.2 Outward propagation of density waves in the disc with $q = 3/4$, $T_\circ = 600$K, and $\alpha = 0.1$. Colours of the lines varying from cyan to black represent the time from $t = 0$ to 100yr in steps of 20yr.

5.4 Results

We find that, in all cases, the disc tends to adjust itself rapidly into a quasi-steady state in the first hundred years of its evolution. This creates a brief phase of an outward density propagation as found in other disc simulations (e.g. Boley et al. 2006). Figure 5.2 shows the outward propagation of density waves over time from $t = 0$ to 100yr in steps of 20yr represented by lines with colours varying from cyan to black. [†] Within a thousand years the disc is in a quasi-steady state where properties of the disc change gradually. The disc also expands slowly due to an outward transfer of angular momentum. Apparent spiral-arm patterns are found in discs with steep temperature profiles (high q) and low inner edge temperatures (low $T_\circ$), see Section 5.4.2.

The disc properties discussed in this section are the mass accretion rate of the central sink $\dot{M}_\mathrm{s}(t)$, surface density $\Sigma(R)$, temperature $T(R)$, Toomre parameter $Q(R)$ (Equation 1.34), and cooling parameter $\beta_\mathrm{cool}(R)$ (Equation 1.36). The cooling time t_cool required by Equation 1.36 can be obtained from that

$$\frac{\mathrm{d}u}{\mathrm{d}t} \simeq -\frac{u}{t_\mathrm{cool}}, \tag{5.26}$$

where $u = u(R)$ is the average specific internal energy of particles at radius R. Disc at

[†]For the rest of this thesis, the colour codes for any change from low to high, unless stated otherwise, are **Grey**, **Yellow**, **Orange**, **Cyan**, **Green**, **Magenta**, **Red**, **Blue**, and **Black**.

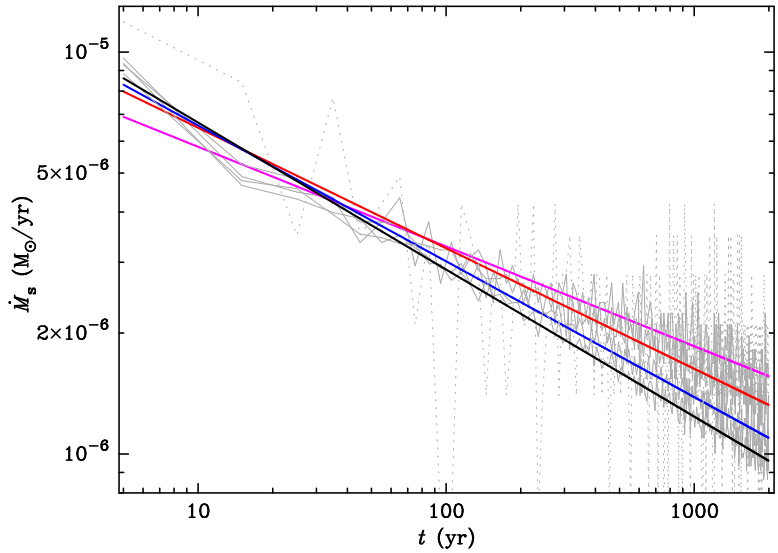

Figure 5.3 The influence of resolution on the mass accretion rate $\dot{M}_{\rm s}(t)$ of the central sink. Changes in mass accretion rates over time are plotted as grey lines. The straight lines are linear fits to the data of the discs with resolutions 50k (magenta), 100k (red), 200k (blue), and 300k (black) particles. The dotted grey line that cannot not be fitted is of the disc with 10k particles.

radius R may be gravitationally unstable if $Q(R) \lesssim 1$ (Toomre 1964) and $\beta_{\rm cool}(R) \lesssim 3$ (Gammie 2001).

5.4.1 Influence of resolution

The resolution of the disc affects the mass accretion rate $\dot{M}_{\rm s}$ of the central sink as shown in Figure 5.3 for discs with $q = 1/2$, $T_\circ = 300$K, and $\alpha = 0.1$. During this early stage ($t \leq 2000$yr), the change in the mass accretion rate with time on log-log scales is approximately linear, i.e.

$$\log_{10} \dot{M}_{\rm s} \propto -\log_{10} t, \tag{5.27}$$

suggesting that

$$\dot{M}_{\rm s} \propto t^{-\eta}, \tag{5.28}$$

where η is a positive constant, which is the absolute value of the slope obtained from a linear fit to $\log_{10} \dot{M}_{\rm s}$ versus $\log_{10} t$. From Figure 5.3, the coloured straight lines are linear fits on log-log scales to $\dot{M}_{\rm s}$ versus t of the discs with resolutions 50k (magenta), 100k (red), 200k (blue), and 300k (black) particles. The figure shows that the value

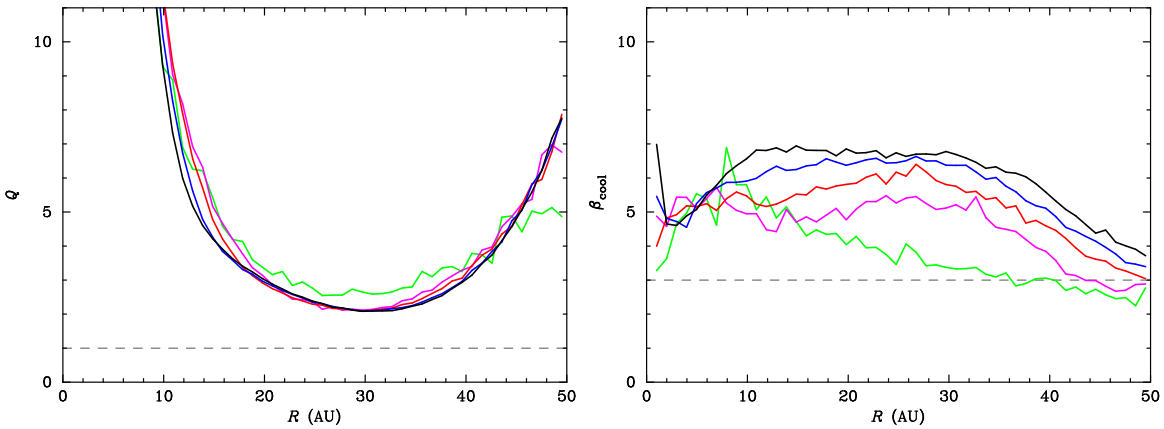

Figure 5.4 Radial profiles of the Toomre parameter Q (left) and cooling parameter $\beta_{\rm cool}$ (right) at $t = 2000$yr. The lines are of the discs with resolutions 10k (green), 50k (magenta), 100k (red), 200k (blue), and 300k (black) particles.

of η (higher is better) increases with resolution.

One of the factors that can affect the mass accretion rate of the central sink is the artificial transfer of angular momentum. This artificial effect may be amplified in a low-resolution disc where the nearest neighbours of a particle are sparsely distributed. Since a relative velocity between two particles in a disc depends on the radial distance between them (the longer the distance the larger the relative velocity), sparse distribution in a low-resolution disc may cause large relative velocities between a particle and its neighbours. Viscous forces acting on the particle could be high accordingly. Particles in a low-resolution disc would then experience more viscous torques than particles in a disc with higher resolution. More angular momentum would thus be transferred artificially in a low-resolution disc. Given that angular momentum is transferred outwards while mass moves inwards and gets accreted by the central sink, which is usually the case in isolated disc simulations, the sink in a lower-resolution disc would accrete more mass than that in a higher-resolution disc.

For the effect of resolution on the stability of a disc, Figure 5.4 compares the Toomre parameter Q (left) and cooling parameter $\beta_{\rm cool}$ of the discs with different resolutions at time $t = 2000$yr. We can see that resolution does not significantly affect the stability of the discs although it tends to reduce $\beta_{\rm cool}$ in the case of low resolution, e.g. the 10k-particle disc (green line). This is because the disc mass is very low compared to the star mass. Self gravity in the disc is thus overshadowed by gravity of the central star; this represents via the high values of Q above the critical value.

5.4.2 Influence of temperature

Discs quickly adjust themselves in the first few hundred years to their quasi-steady state where properties of the discs gradually change over time. Changes in temperature profiles of the discs are shown in Figure 5.5(top group). The large deviations of most temperature profiles (at $t = 2000$yr, black lines) from the background temperatures (green lines) could be due to the effect of artificial viscosity (see Section 5.4.3).

The disc's temperature structure has some influence on the particle distribution at outer radii ($R \gtrsim 10$AU) where the density is low. Significant changes can be seen from comparing the density profiles at outer radii in subfigure (g) with those in subfigure (i) (in the bottom group of Figure 5.5). The effect on vertical distribution of particles are shown as xz-cross-sectional plots in Figure 5.6; the plot layout is the same as Figure 5.5, i.e. same discs are labelled with the same letters. The plots in Figure 5.6 are rendered by the density of SPH particles near the xz-plane (within $2h$ from the plane), see Price (2007) for plotting methods. We can see from Figure 5.6 that the flatter the temperature profile the fluffier the disc.

The temperature structure does affect the stability of a disc. Here, we use the Toomre parameter Q and cooling parameter $\beta_{\rm cool}$ to indicate a disc's stability. Figure 5.8 shows changes in the radial profiles of Q (top group) and $\beta_{\rm cool}$ (bottom group) over the first 2000yr of evolution. From the figure, a thoroughly warm disc (with high $T_\circ$ and low q) such as that in subfigure (g) is more gravitationally stable than the other. In contrast, the disc in subfigure (c) (with low $T_\circ$ and high q) is marginally stable at $R \sim 30$AU since the value of Q is ~ 1; that it is still stable against gravitational instabilities is mainly because the cooling parameter is well higher than the critical value. In addition to this disc, a weak spiral density pattern can be observed as shown in Figure 5.7.

5.4.3 Influence of artificial viscosity

In disc simulations, artificial viscosity can cause artificial heat and affect the process of angular momentum transfer, altering the density structure of the disc and the mass accretion rate onto the central star. The influence of artificial viscosity on a disc's temperature and density structures can be seen from Figure 5.5. In the top group of Figure 5.5, the excess temperatures in most discs over the background temperatures (green lines) is mainly due to the artificial heating, occurring especially in the inner parts of the discs ($R \lesssim 20$AU) where particle's smoothing lengths are comparable or greater than the disc scaleheights (e.g. Forgan et al. 2011). The bottom group of

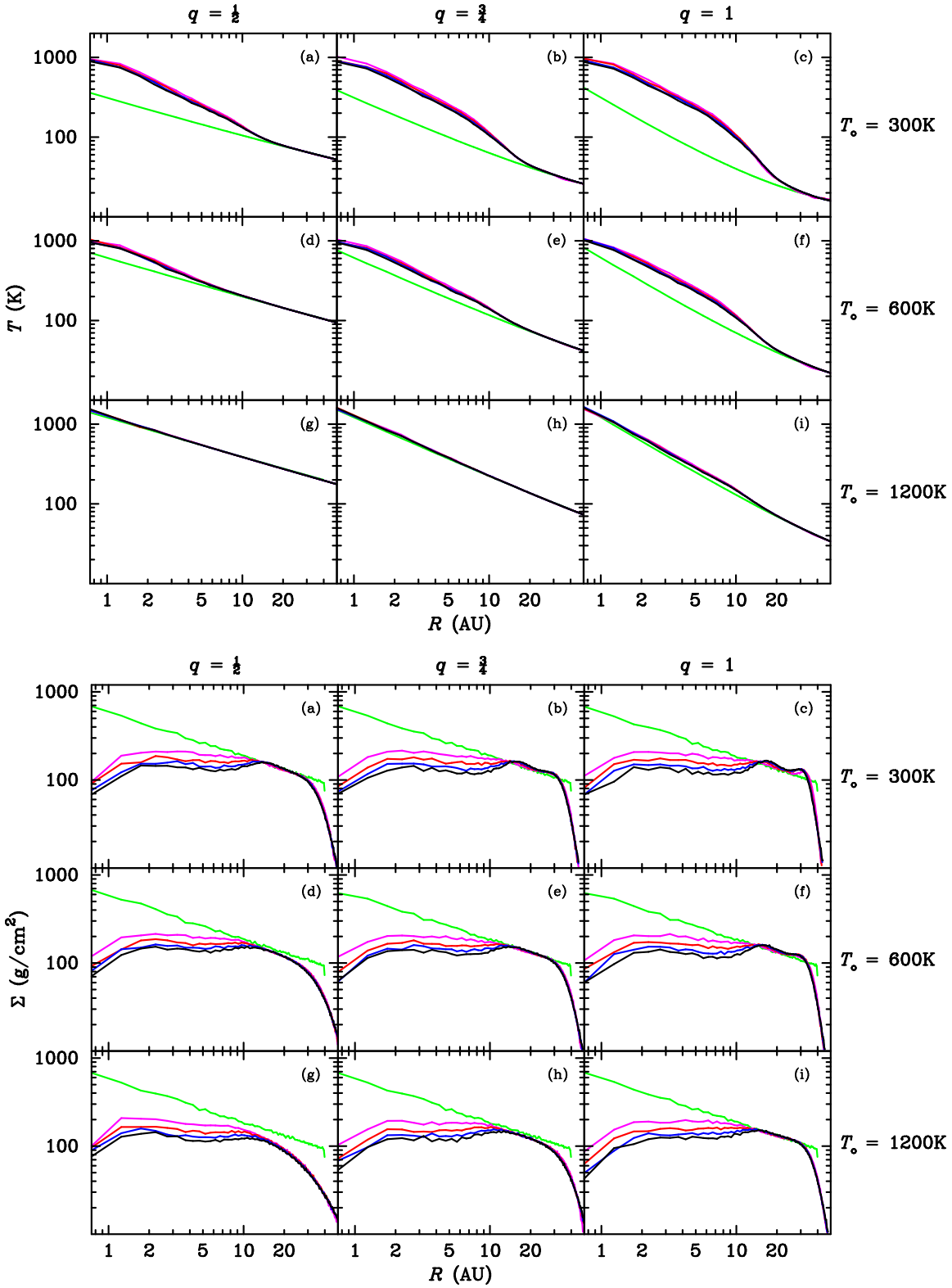

Figure 5.5 Changes in temperature profiles (top group) and surface density profiles (bottom group) of the discs with different values of q and $T_\circ$. Lines with different colours represent the profiles at the time from $t = 0$ (green) to 2000yr (black) in steps of 500yr.

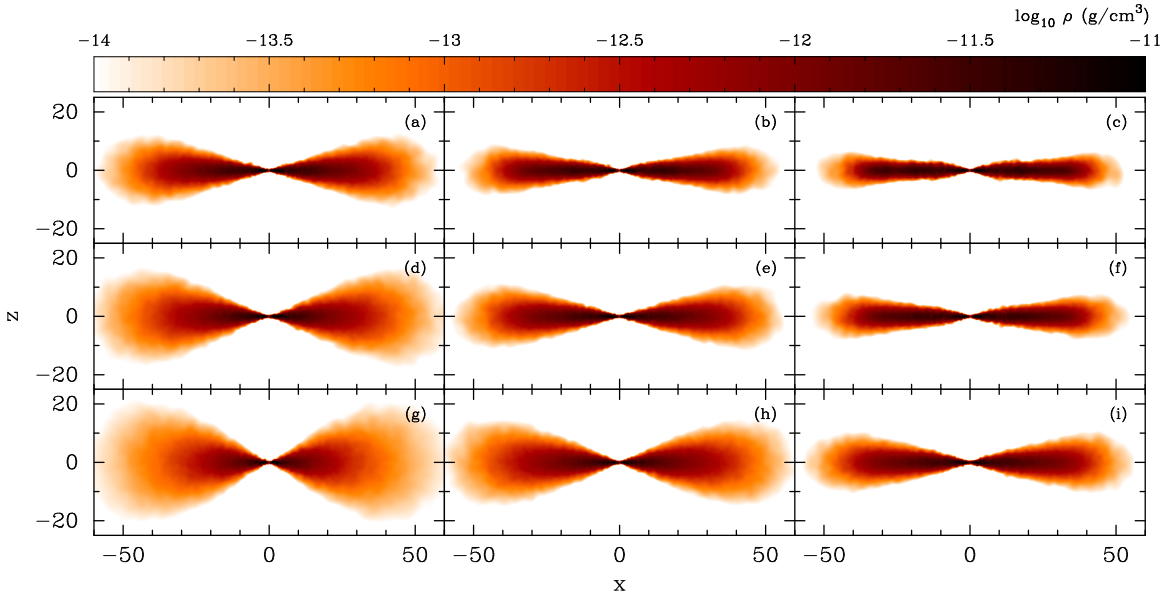

Figure 5.6 Cross-sectional plots of the discs in Figure 5.5(a)-(i) (labelled with the same letters) at $t = 2000$yr. The plots are rendered by the density of SPH particles around the xz-plane. The value of the density is indicated by the colour bar on the top.

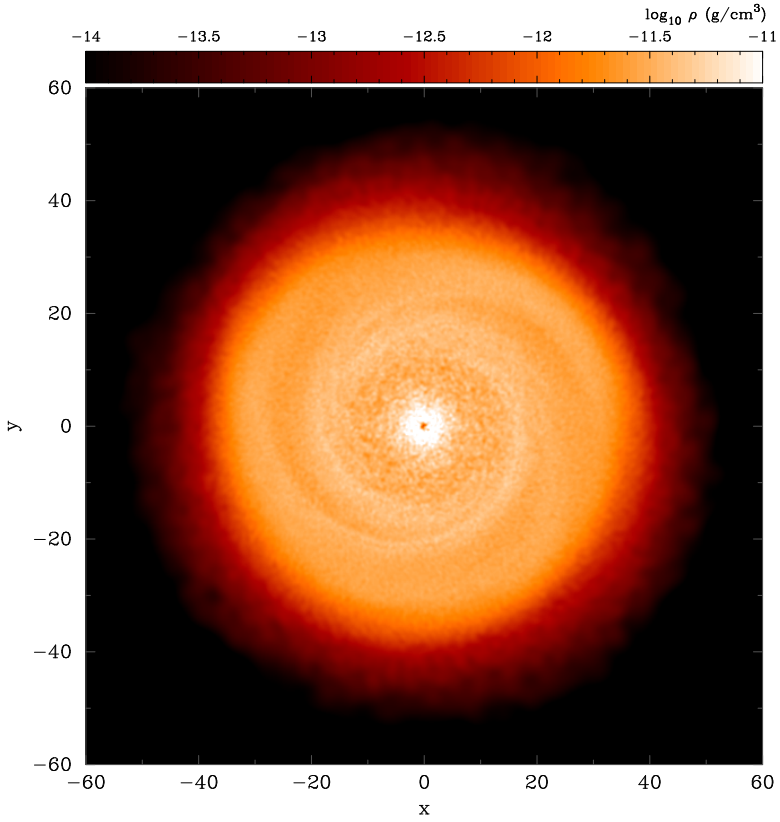

Figure 5.7 Cross-sectional plot of the disc in Figure 5.5(c) showing a weak spiral pattern of the midplane density. The plots are rendered by the density of SPH particles around the xy-plane.

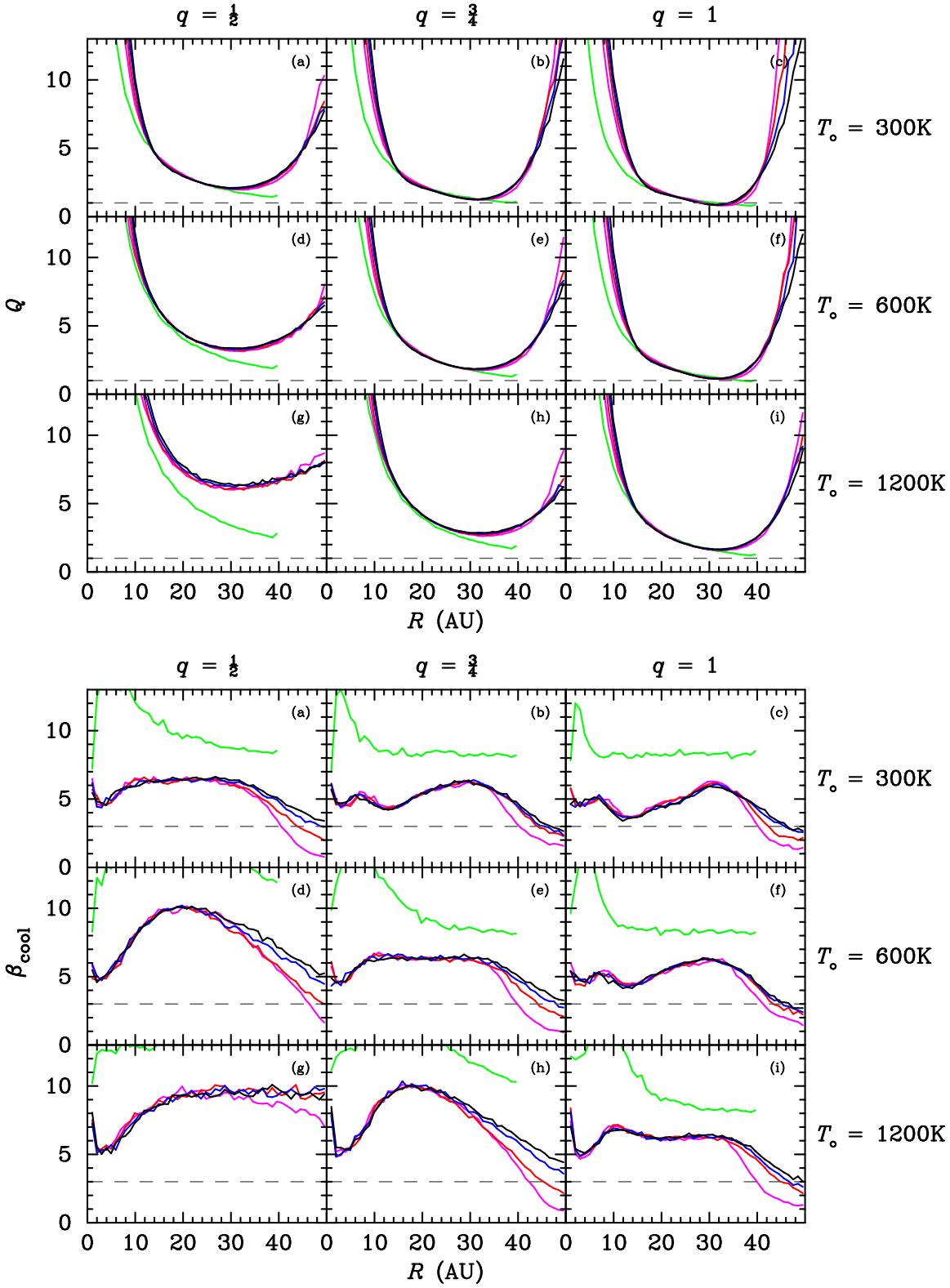

Figure 5.8 Changes in radial profiles of Toomre parameter (top) and cooling parameter (bottom) of the discs with different values of q and $T_\circ$. Line colour description is the same as Figure 5.5.

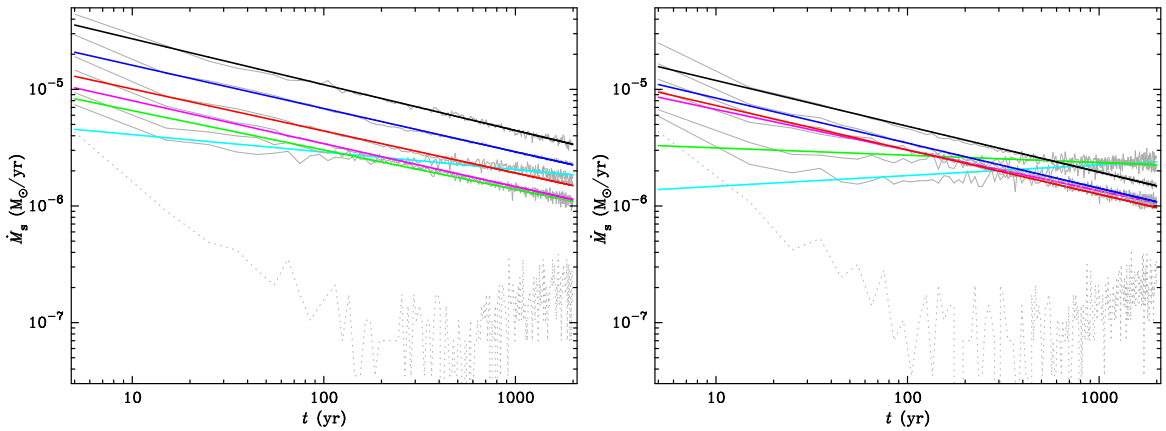

Figure 5.9 Changes in the mass accretion rates against time in the discs with viscosity parameters $\alpha = 0 - 2$. Both subfigures compare the results of using the standard artificial viscosity without Balsara switch (left) and with Balsara switch (right). Straight lines with colours cyan, green, magenta, red, blue, and black are the linear fits to $\log_{10} \dot{M}_s$ versus $\log_{10} t$ of the disc with $\alpha = 0.05, 0.1, 0.3, 0.5, 1$ and 2, respectively. Note that the plot of the disc with $\alpha = 0$ (dotted grey line) cannot be fitted.

Figure 5.5 shows that the effect of artificial viscosity dominating in the inner disc tends to flatten the disc's density profiles from $p = 1/2$ to $p \sim 0$. Changes in density profiles according to artificial viscosity (represented by α) is shown in Figure 5.12 below; we can see that the higher the viscosity the more the alteration in the density profile from the original ($p = 1/2$).

From our simulation results, the mass accretion rate seems to have a rather complicated relation with the viscosity parameter α. Figure 5.9 shows the mass accretion rates of the discs with different selected values of α from 0 to 2. All the plotted data are fitted with straight lines of different colours except that of the disc with $\alpha = 0$ (dotted grey lines in both subfigures). The left and right subfigures are respectively of the discs simulated without and with Balsara switch. Some interesting features are described as follows.

Mass accretion rate

From Figure 5.9, changes in mass accretion rates of low-viscosity discs ($\alpha \lesssim 0.5$) are rather unusual. For better comparison, we plot the mass accretion rates from all cases (see Table 5.3) against α in Figure 5.10. Now, line colours in Figure 5.10 represent time from $t = 0$ (grey) to 2000yr (black) in steps of 250yr. The interesting change in the plots is where $0 < \alpha \lesssim 0.2$. This unusual change may be described by assuming that the efficiency of the inward transfer of angular momentum in a disc increases as α

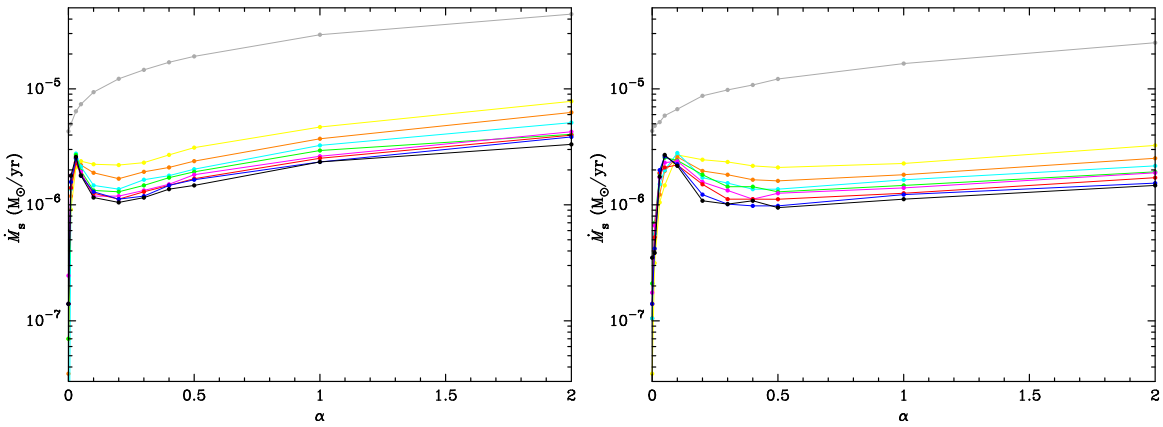

Figure 5.10 Changes of the mass accretion rates in terms of viscosity parameter $\alpha = 0 - 2$. Lines with colours from grey to black correspond to time from $t = 0$ to 2000yr in steps of 250yr. Both subfigures compare the results of using the standard artificial viscosity without (left) and with (right) Balsara switch.

increases. During the transfer process, particles gaining angular momentum flow outwards while particles losing angular momentum flow inwards. The number of particles accreted by the central sink may depend on the interaction between three groups of particles around the surface of the sink: **(1)** particles losing angular momentum near the surface moving inwards, **(2)** particles gaining angular momentum near the surface moving outwards, and **(3)** particles losing angular momentum at radii further away making their way towards the sink.

Let us consider the black line in Figure 5.10(left) where $t = 2000$yr (quasi-steady state). In a very low-viscosity disc ($0 < \alpha \lesssim 0.03$), viscosity would barely influence the exchange of angular momentum between particles throughout the disc. The majority of accreted particle would come from **(3)** as the resistance from the outward flows of **(2)** is not strong enough. The mass accretion rate would increase with α up to the point (the peak at $\alpha \sim 0.03$) where the flows of **(2)** become significant enough to resist the flows of **(3)**. For $0.03 \lesssim \alpha \lesssim 0.2$, the number of particles from **(3)** might decrease considerably as the resistance from **(2)** increases. Although the number of accreted particles increasingly comes from **(1)**, it does not compensate the considerable drop of **(3)**. Therefore, the mass accretion rate decreases as α increases. Until the point where the increasing number of particles from **(1)** begins to dominate, the mass accretion rate begins to rise again. From Figure 5.10(left), this seems to occur at $\alpha \gtrsim 0.2$. The increasing number of particles from **(1)** may be roughly illustrated by the pixel plots in Figure 5.11. Each pixel is rendered by the averaged radial mass-flux (ρv_r) of particles inside the pixel column. The subfigures from (a) to (f) are of the discs

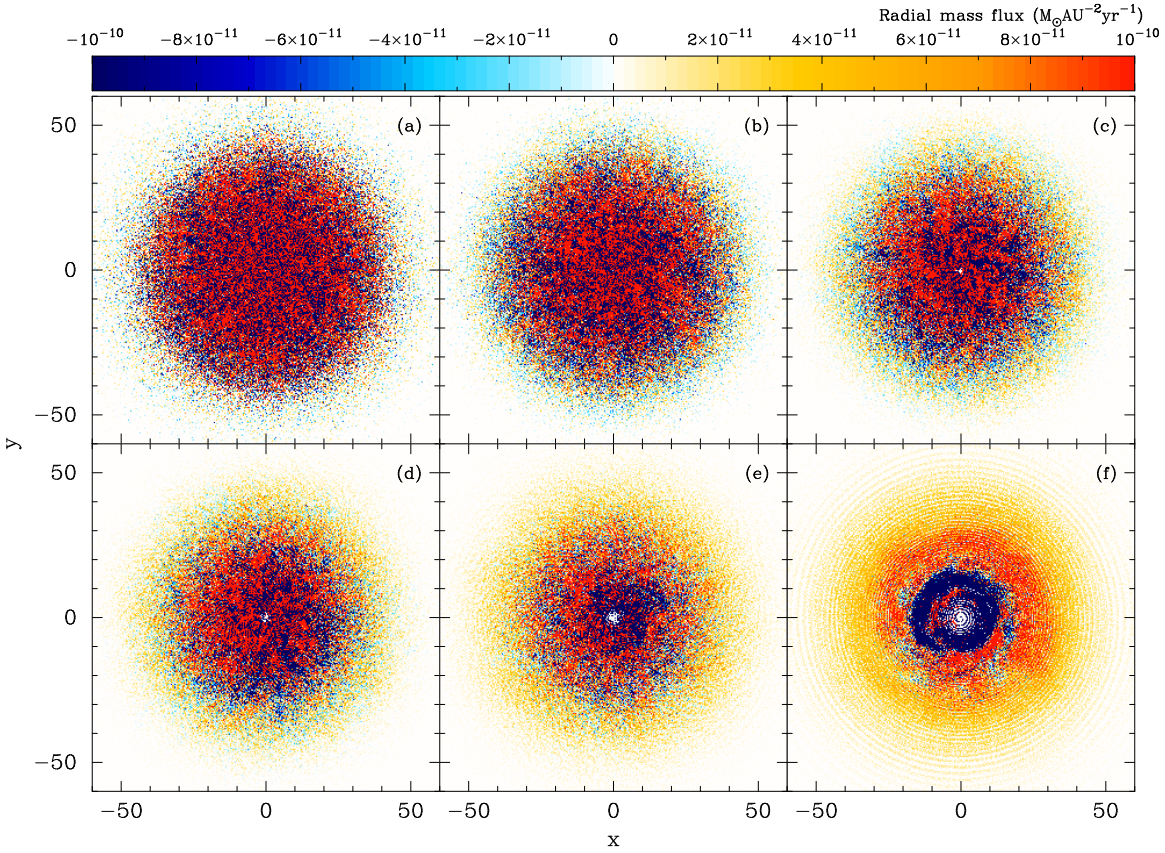

Figure 5.11 Pixel plots of radial mass-fluxes in the discs. Subfigures from (a) to (f) show the discs with $\alpha = 0.05, 0.1, 0.3, 0.5, 1$ and 2, respectively. Each pixel of in the plots is coloured by the average value of radial mass-fluxes of particles inside the pixel column. The magnitude and direction of the average flux are given by a colour bar at the top: blueward colours for inward fluxes and redward colours for the outward.

with $\alpha = 0.05, 0.1, 0.3, 0.5, 1$ and 2, respectively. A pixel containing particles mostly moving inwards has a blueward colour, while that containing particles mostly moving outwards has a redward colour. We can see from the figure that, in a low-viscosity disc (e.g. Figure 5.11(a)), particle fluxes are mostly outward (red) and mixed rather well with inward fluxes throughout the disc. In the higher-viscosity discs (Figure 5.11(b)-(f)), the fluxes begin to be separated especially in the inner parts of the disc where inward fluxes (blue) dominate (Figure 5.11(f)). The high mass accretion rates in high-viscosity discs are due to these inward fluxes in the inner disc. As well as producing the inward fluxes, the exchange of angular momentum in the inner disc also push particles outwards, reducing the surface density in the area. This can be seen from the density plots in Figure 5.12 which are of the same set of discs from Figure 5.11 plus the non-viscous disc ($\alpha = 0$, the orange lines on both subfigures).

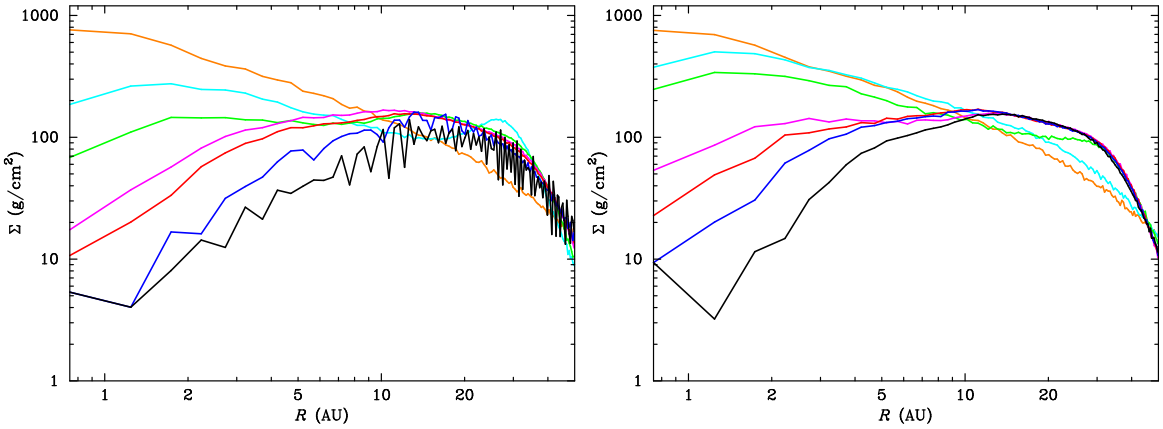

Figure 5.12 Surface density at $t = 2000$yr of the discs with $\alpha = 0, 0.05, 0.1, 0.3, 0.5, 1$ and 2 represented by orange, cyan, green, magenta, red, blue, and black lines, respectively. The two subfigures are from the simulations performed without (left) and with (right) Balsara switch.

Particle stratification in highly viscous discs

As we can see from Figure 5.11(f), particles in the disc are radially stratified in patterns of tightly wound spirals. This can be seen more clearly in the particle plots shown in Figure 5.13. The stratified pattern in the disc corresponds with the zigzag density pattern on the black line in Figure 5.12(left). This stratification of particles is a numerical effect innate to the SPH method. That is, when high viscosity is used in a disc simulation, shear forces between particles of adjacent orbits are high accordingly. As a consequence, particles tend to clump together in the same orbital radii where relative velocities between them are minimized. The orbital radii are discretized by the effective ranges of viscous forces, i.e. approximately two smoothing lengths ($2h$). This can be seen from comparing the gap sizes of stratified rings in Figure 5.13 to the average smoothing lengths of particles in the disc plotted in Figure 5.14. Finally, that the rings are spiral as clearly seen in Figure 5.13(b) is due to the inward drift of the particles in the radial direction.

Simulations with Balsara switch

The role of Balsara switch is to reduce the effect of shear viscosity between particles in adjacent orbits in a disc. Using the Balsara switch seems to reduce the mass accretion rates effectively in high-viscosity discs, for example, the mass accretion rates of the discs with $\alpha \gtrsim 0.2$ in Figure 5.10(left) and (right). Balsara switch also removes the stratification of particles in the disc as the effect of shear forces have been reduced. This can be seen from the black line ($\alpha = 2$) in Figure 5.12(right) which is smoother

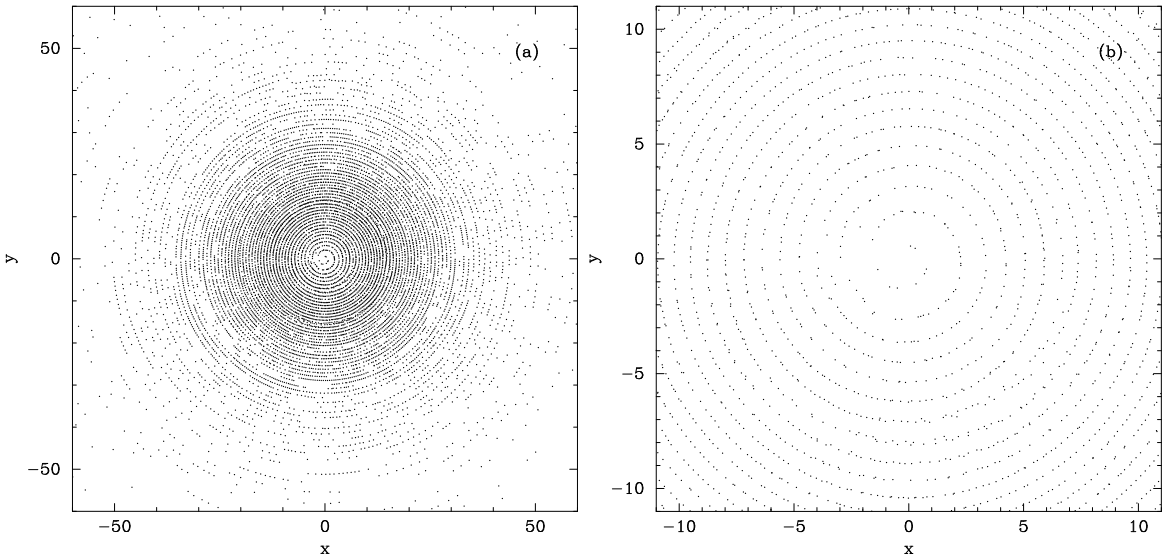

Figure 5.13 Plain particle plots of the disc from Figure 5.11(f) with the same xy-range (a) and the close-up range around the sink (b). Note that only particles within the vertical range $-0.25 \leq z \leq 0.25$AU are plotted.

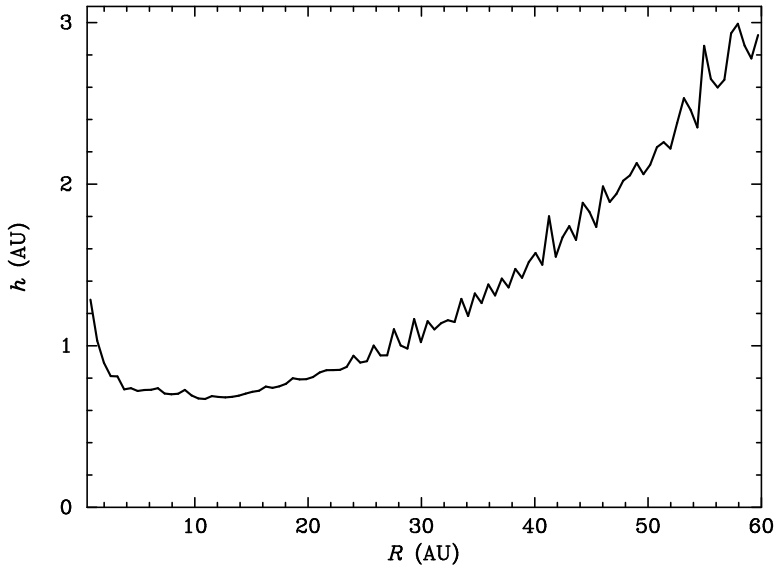

Figure 5.14 Average smoothing length (h) of particles in the disc from Figure 5.11(f).

than that in the left subfigure. However, Balsara switch seems to have adverse effect on the mass accretion rates in some low-viscosity discs ($0.05 \lesssim \alpha \lesssim 0.2$), i.e. the rates are increased slightly.

5.4.4 Disc stability

All discs with initial resolution ~ 190k particles have been evolved 100kyr further from $t = 2$kyr. For convenience, however, we reset the beginning time to $t = 0$. Mass accretion rates of the central sink over 100kyr are shown in Figure 5.15. We can see that the rates become non-linear in the log-log scales after $t \sim 10 - 20$kyr. In terms of lifetimes, the disc with $q = 1/2$ and $T_\circ = 1200$K (orange line in Figure 5.15) is the most short-lived while the disc with $q = 1$ and $T_\circ = 300$K (red line in Figure 5.15) is the most long-lived. Changes in temperature and surface density profiles of the discs are shown in Figure 5.16. As suggested by the accretion rate, the disc with $q = 1/2$ and $T_\circ = 1200$K disperses much quicker than other systems. In all cases, the edges of the discs expand to radii > 100AU. The discs tend to be more stable with age as shown in Figure 5.17 where the Toomre parameter Q and cooling parameter $\beta_{\rm cool}$ of the discs are plotted.

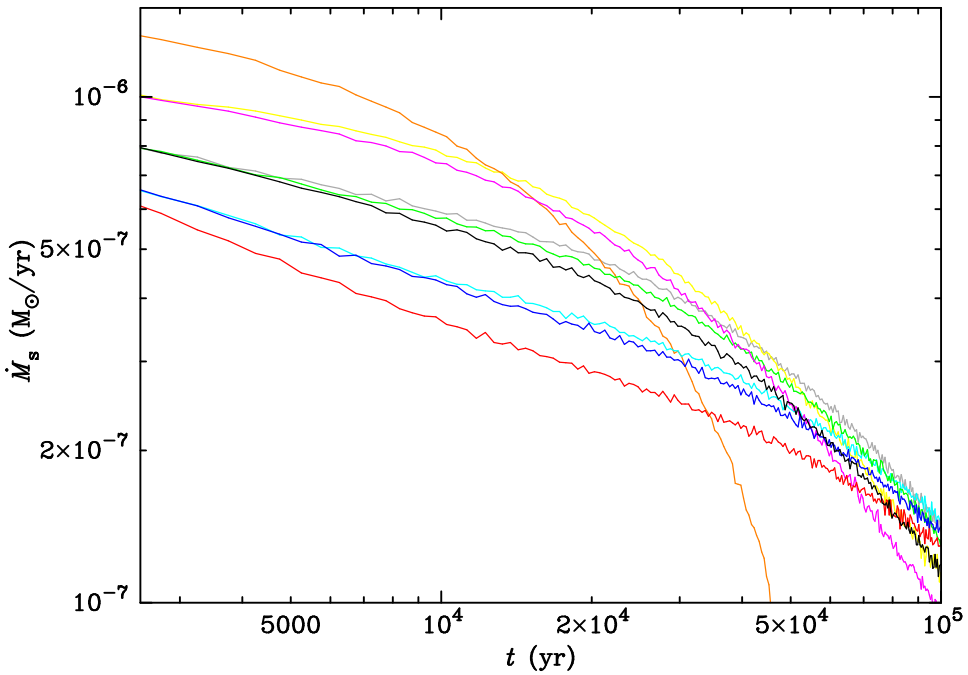

Figure 5.15 Changes in the mass accretion rates of the central sinks of the discs with different q and $T_\circ$. The lines are, in $\{\text{colour}, q, T_\circ\}$ format, $\{\text{grey}, 1/2, 300\text{K}\}$; $\{\text{yellow}, 1/2, 600\text{K}\}$; $\{\text{orange}, 1/2, 1200\text{K}\}$; $\{\text{cyan}, 3/4, 300\text{K}\}$; $\{\text{green}, 3/4, 600\text{K}\}$; $\{\text{magenta}, 3/4, 1200\text{K}\}$; $\{\text{red}, 1, 300\text{K}\}$; $\{\text{blue}, 1, 600\text{K}\}$; and $\{\text{black}, 1, 1200\text{K}\}$.

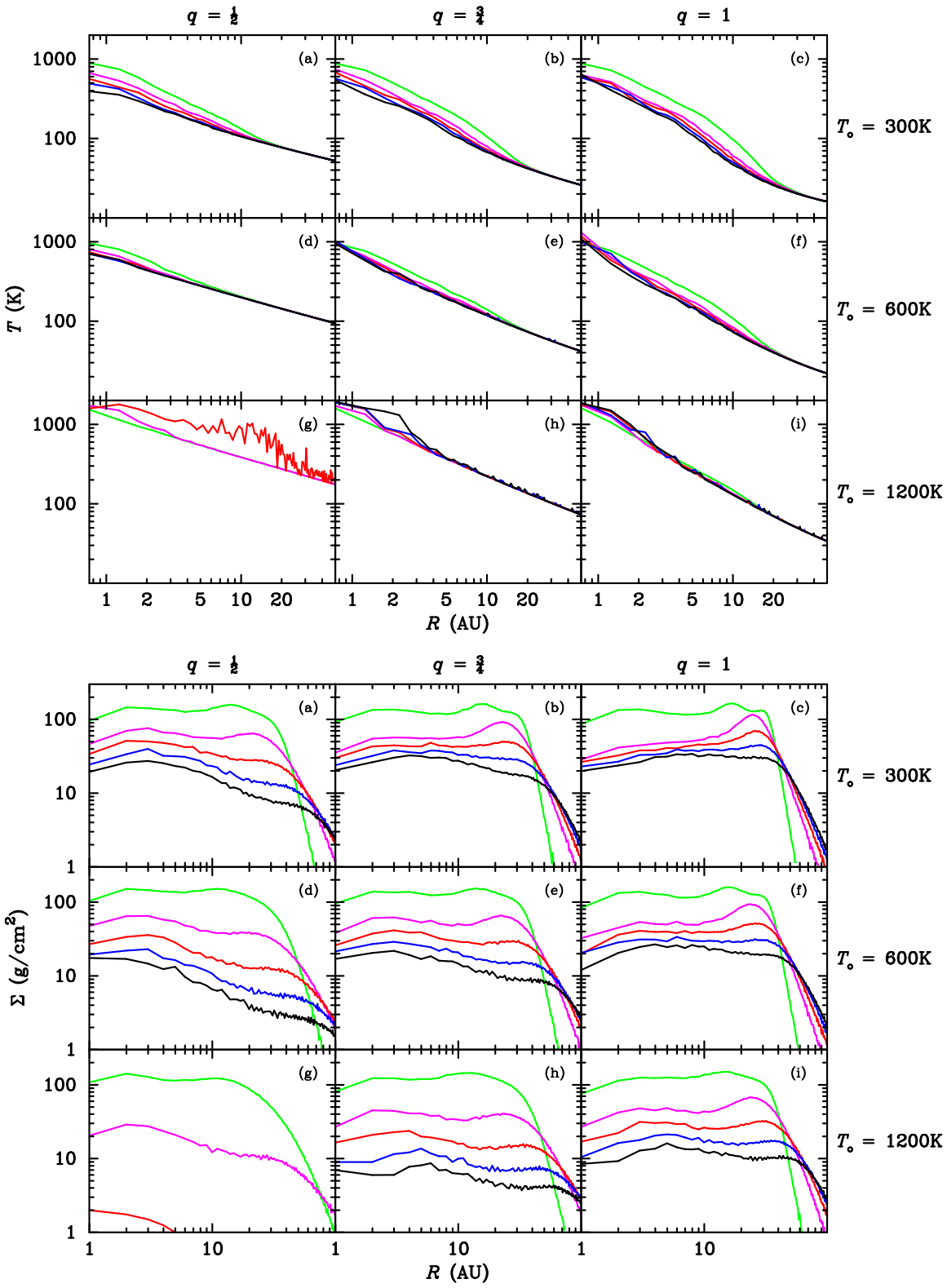

Figure 5.16 Changes in temperature profiles (top group) and surface density profiles (bottom group) of the discs with different values of q and $T_\circ$. Lines with different colours represent the profiles at the time from $t = 0$ (green) to 100kyr (black) in steps of 25kyr.

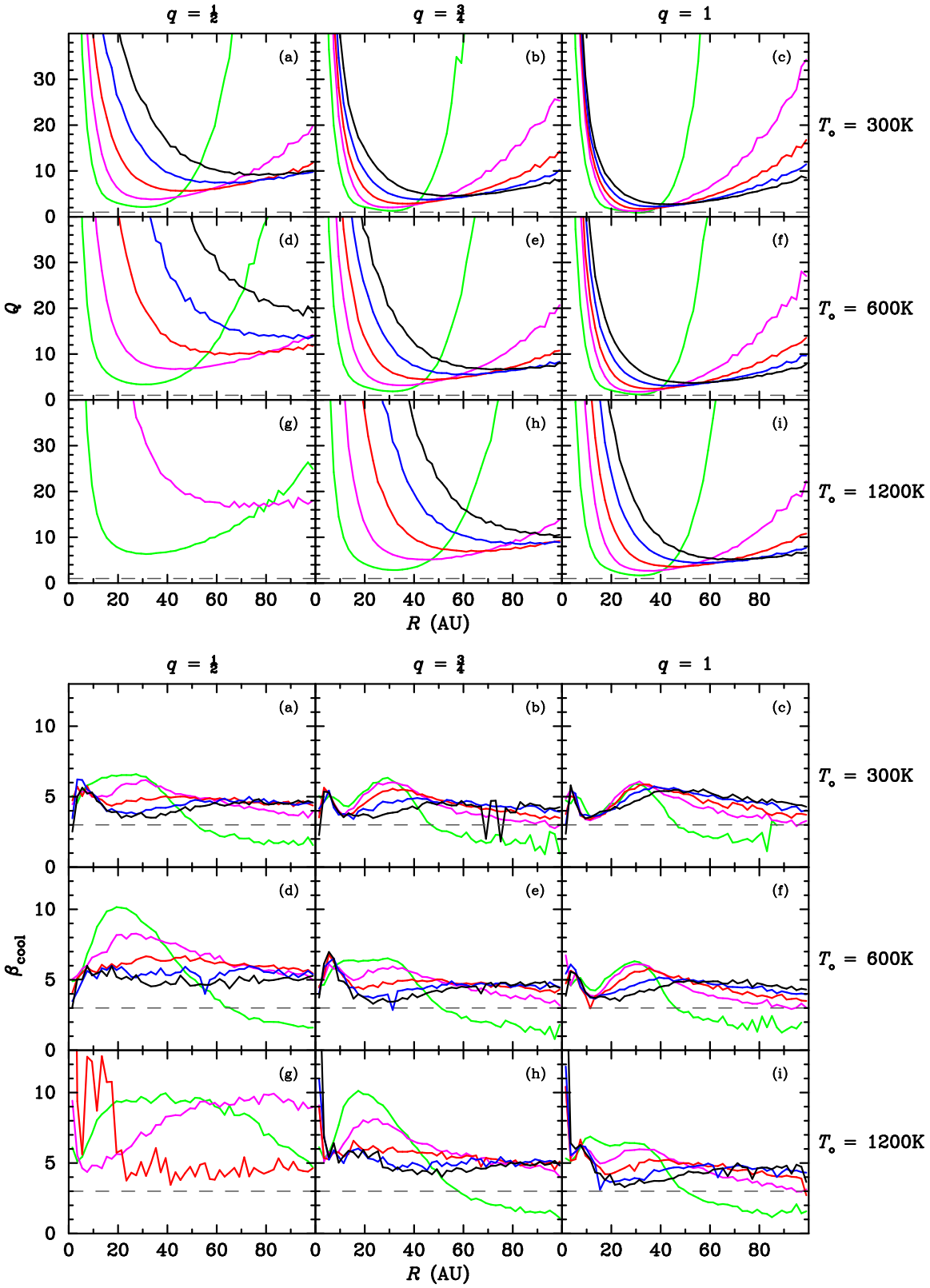

Figure 5.17 Changes in the radial profiles of Toomre parameter (top group) and cooling parameter (bottom group) of the discs with different values of q and $T_\circ$. Line colour description is the same as Figure 5.16.

5.5 The disc for simulations in Chapter 6

In Chapter 6, we will study the effects of tidal perturbations from the companion star in a binary system onto the disc surrounding the primary star (circumprimary disc). A relaxed disc simulated in this chapter work will be used as the initial circumprimary disc. Since we are studying the long-term dynamics of the disc rather than the gravitational instability as a consequence of tidal perturbations, the disc has to be stable against the instability and long-lived. Considering both Toomre parameter and cooling parameter in Figure 5.17, we can see that the disc in subfigure (g) is the most stable disc while the disc in subfigure (c) is the least (marginally stable). However, in terms of disc lifetimes by considering Figure 5.15 and Figure 5.16(bottom group), the disc in subfigure (g) is the most short-lived disc while the disc in subfigure (c) is the most long-lived. It thus appears that the intermediate disc, i.e. the disc in subfigure (e), gives the best compromise between stability and longevity. This disc has $q = 3/4$ and $T_\circ = 600$K. We can also see that the deviation of the disc's temperature from the background after time $t = 2$kyr (see subfigure (e) in the top group of Figure 5.16) is small, meaning that the artificial heating is not very significant. We therefore choose this disc for our simulations in the next chapter.

5.6 Summary

We have performed numerical simulations to study properties of low-mass discs. There are several factors that affect the mass accretion rate onto the central star and the stability of the disc. In this work, we focus on the influence of the resolution, temperature structure, and artificial viscosity that are used in the simulations.

Resolution. We have found that using insufficient resolution can increase the mass accretion rate of the central sink. Low resolution also tends to decrease the cooling time of the disc, but it is still unlikely to result in gravitational instabilities. This is because the Toomre parameter of the disc is well above the critical value and seems to be unaffected by resolution.

Temperature. Temperature structure affects the vertical structure and stability of a disc. A disc with low temperature profile index (q) and high inner edge temperature ($T_\circ$) is fluffy and stable but can be rapidly dispersed. In contrast, a disc with high q and low $T_\circ$ is thin and marginally stable but disperses slowly. Nevertheless, this would

mainly depend on the radiation treatment used in the simulations, i.e. the radiative cooling method (Stamatellos et al. 2007).

Artificial viscosity. The influence of artificial viscosity on disc evolution are rather complicated. We have found that the mass accretion rate of a central sink changes with the viscosity parameter α in an interesting way. We have described this behaviour in terms of viscous interactions between particle fluxes from different sources.

We have also found that high artificial viscosity ($\alpha \gtrsim 1$) can cause particles to stratify in a spiral pattern. This is a numerical effect corresponding to strong shear forces. The stratification of particles can be prevented by using Balsara switch.

We have tested the long-term stability of all discs up to $t = 102$kyr and found that all of them are stable as would be expected from low-mass discs. Finally, from our study in this chapter, we find that the disc that is suitable for simulations in Chapter 6 is the one with $\alpha = 0.1$, $q = 3/4$, and $T_\circ = 600$K.

Chapter 6

Circumstellar discs in misaligned binary systems

In this chapter, we perform simulations to investigate the evolution of a circumprimary disc in a binary star system. We focus on discs whose midplane is misaligned with respect to the orbital plane of the binary. In such a system, the disc is tilted by the influence of tidal forces and tends to be adjusted towards alignment with the binary orbital plane. This process may in some way affect planet formation in the disc. At least, the tilting process would make the orbital axis of planets that are formed from a misaligned disc to be misaligned with respect to the spin axis of the host star.

In binary star formation by core fragmentation, primordial misaligned binaries could be rare as they require highly non-uniform distribution of angular momentum in the natal cores. However, since most binaries are formed in cluster environments, misaligned binaries may be formed at later stages by dynamical interactions between the members in the cluster. The likelihood of this scenario has been shown by Parker and Goodwin (2009) via N-body simulations of star clusters. They have found that up to 20 per cent of binaries in an Orion-like star cluster have orbital planes been misaligned from the originals by an angle $\gtrsim 40^\circ$.

As well as creating misaligned binaries, dynamical interactions can also destroy the systems. One interesting scenario is a binary destruction that occurs to a misaligned binary star whose circumprimary disc is tilted and evolves into a planetary system. If the planet(s) remains bound to the host star after the interaction, this process would create a planetary system whose planetary orbital axis is misaligned with respect to the spin axis of the host star, i.e. a spin-orbit misaligned planetary system.

In Section 6.1, we review the observations, formation mechanisms, and tilting mechanism of discs in misaligned binary systems, followed by a discussion of the implication to planet formation in those discs. The simulation details of discs in misaligned systems are provided in Section 6.2. The results are presented afterwards in Section 6.3. Then, in Section 6.4, we discuss the alignment mechanism(s) and the effect of disc dispersal on planet formation. Finally, the key findings of this chapter work are summarized in Section 6.5.

6.1 Discs in misaligned binary systems

Young stars have discs and are usually found in binaries or multiples with a multiplicity higher than that of main-sequence stars in the field (see Chapter 1). It is interesting to understand how those discs evolve, as this would be beneficial to understanding planet formation occurring within.

In a small multiple system, close encounters among the members can be common and are likely to cause some of the members (usually the least massive ones) to be ejected out of the system (e.g. Anosova 1986; Sterzik and Durisen 1998). During a close encounter between two stars, tidal forces from each star can affect the discs of one another. However, tidal effects from a close encounter are typically transient. The discs may only be disrupted if the periastron separation of the encounter orbit is sufficiently small.

In contrast to the brief perturbations in close encounters, binary stars are the place where disc(s) surrounding each component can be perturbed regularly. In this case, tidal effects would play a significant role in altering some properties of the components such as the mass accretion rates of the stars, the disc's density profiles, and the transfer processes of angular momentum inside the discs and/or between the stellar components. As an example, it has been suggested that rapid accretion of disc mass onto the central star as a result of interactions between binary components may account for strong outburst phenomena such as those produced by FU Orionis objects (Bonnell and Bastien 1992) and Herbig-Haro objects (Reipurth 2000).

In this work, we are interested in the evolution of a *circumprimary disc* in a binary system. The main parameters of the system that we aim to study are the initial inclination and eccentricity of the binary orbit. The system whose orbital inclination of the orbit is non-zero, i.e. *misaligned system*, has several interesting dynamical features. That is, in a misaligned system, the circumprimary disc is tilted by tidal forces from the companion (e.g. Papaloizou and Terquem 1995). To some

extent, tilting process may affect the dispersal rate of the disc and the formation of planets. In this section, we review the observations, formation mechanisms, and tilting mechanism of discs in misaligned binaries. Subsequently, the implication to planet formation in the disc is discussed.

6.1.1 Observations

A number of T Tauri binaries have been found with misaligned discs surrounding the stellar components (e.g. Monin et al. 2006, and references therein). In the Taurus-Auriga and Scorpius-Ophiuchus star-forming regions, mildly misaligned discs with misalignment angles $\lesssim 20^\circ$ are found in wide T Tauri binaries with separations between $200 - 1000$AU (Jensen et al. 2004). As an example from some resolved systems, the protobinary system HH 24 MMS with separation ~ 360AU has been found to have misaligned discs with a relatively large difference in position angles ($\sim 45^\circ$, Kang et al. 2008). Another example is the T Tauri binary system Haro 6-10 where discs surrounding the components separated by ~ 160AU are seen to be strongly misaligned from each other by $\sim 70^\circ$ (Roccatagliata et al. 2011). Indeed, discs surrounding the archetypal T Tauri triple (separation between T Tau N and T Tau Sab $\gtrsim 100$AU) are also found to be relatively misaligned to each other (Skemer et al. 2008; Ratzka et al. 2009). We can see that most observed misaligned systems tend to have separations greater than ~ 100AU. Apart from that misalignment in systems with smaller separations may be difficult to observe, this may tell us something about the formation and evolution of misaligned systems. For example, it is possible that misaligned systems with smaller separations evolve towards alignment faster. We discuss this later in the result section (Section 6.3).

In observations, the orientation of a circumstellar disc may be obtained by means of (a) the polarization map of the sources (e.g. Monin et al. 1998; Wolf et al. 2001; Monin et al. 2006), (b) the directions of the emanated jets (e.g. Davis et al. 1994; Eisloffel et al. 1996; Davis et al. 1997), and (c) the direct observation of the disc (e.g. Koresko 1998; Stapelfeldt et al. 1998; Roccatagliata et al. 2011). However, the tilting motion of the disc may only be inferred from observable bends in the jet flows. This method is based on the fact that jets are usually launched in directions perpendicular to the plane of the inner disc (e.g. Eisloffel et al. 1996; Terquem et al. 1999). A change in the orientation of the disc would cause the directions of the jets to change accordingly. Nevertheless, disc precession is not the only mechanism that can change the direction of jet outflows (e.g. Eisloffel and Mundt 1997).

6.1.2 Formation of misaligned binaries

Young binary systems with misaligned discs can be formed by several mechanisms (e.g. Bate et al. 2000; Monin et al. 2007). The possible mechanisms may be categorized into (a) core fragmentation and (b) dynamical interactions. In binary formation by core fragmentation, the forming protostellar components may have different orientations in their rotational axes if the distribution of angular momentum in the core is considerably non-uniform. Bonnell et al. (1992) have demonstrated that the fragmentation of an elongated cylindrical core with rotational axis anti-parallel to the major-axis can produce protobinary stars with some degree of misalignment between the disc midplanes and the binary orbital plane. For typical prestellar cores with arbitrary shapes, spatial variations in angular momentum distribution may be provided by turbulence in the cores, i.e. turbulent core fragmentation (see Section 1.2.2).

In a young star cluster, it is possible that misaligned binary systems are created from dynamical interactions among the members. From Section 1.2.2, capture process might occur during a close encounter between two stars (in the case of disc capture) or three stars (in dynamical capture). A misaligned system would likely to be an outcome of the capture as the orientations of the discs surrounding the interacting bodies are not necessary aligned. However, as discussed in Section 1.2.2, the likelihood of a binary star paired up by capture process in a star cluster is very low, so to the likelihood of a misaligned system formed by this mechanism. Apart from capture, a misaligned system may be created from an aligned system which experienced a non-coplanar encounter with another star (or star system) in the cluster. The encounter does not disrupt the aligned system but does generate non-coplanar velocities in the components in the system. Parker and Goodwin (2009) have found that dynamical interactions in a typical Orion-like star cluster can alter the orbital inclination of binary stars in the system. Up to 20 per cent of binaries in the system are found with misalignment angles $\gtrsim 40°$. This mechanism could be more efficient in dense star clusters.

In addition, a misaligned system may be created by the combination of core fragmentation and dynamical interactions. This may occur when a prestellar core fragments into an $N \geq 3$ system with all the members having non-coplanar velocity vectors. The dynamical decay of the system might eventually produce a misaligned binary system. In this case, the discs surrounding both components may still be aligned with each other, as they are formed from the same (less turbulent) core, but they are misaligned from the orbital plane of the binary.

6.1.3 Tilting mechanism

Tilting of a misaligned disc is described by the motion of the disc's rotational axis relative to the binary orbital axis. The tilting motion is a combination of precession, alignment, and nutation. However, in this work, we focus on the first two kinds. The details for the nutation (or nodding motion) of the disc may be found in, for example, Katz et al. (1982).

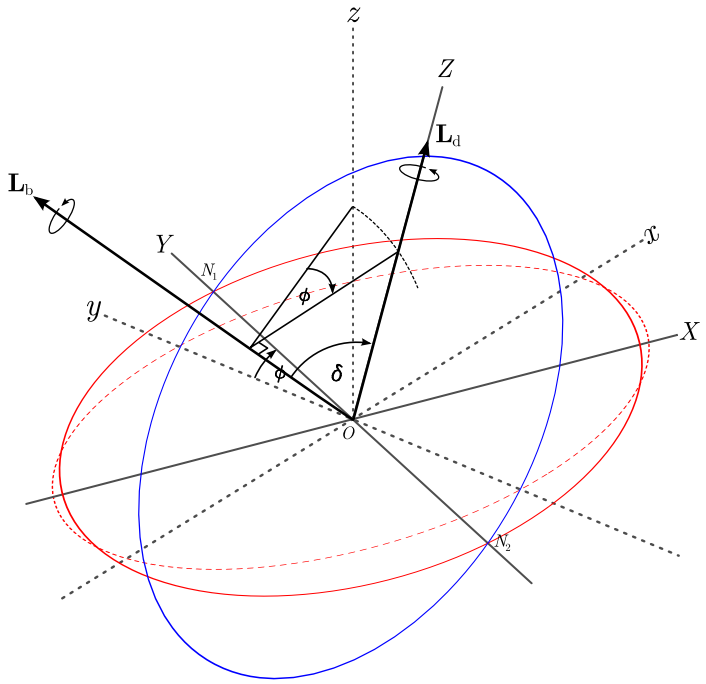

Figure 6.1 Diagram showing the precession angle ϕ and misalignment angle δ for describing changes in orientation of tilting disc. The red circles represent the disc midplane before (dashed circle) and after (solid circle) the disc has been tilted. The blue circle represents the orbital plane of the binary which is also tilted but the movement (not shown) is small compared to that of the disc. The coordinates (x, y, z) are of the rest frame of reference while (X, Y, Z) are of the disc's comoving frame. See text for the definitions of the angles and the comoving coordinates.

Tilting of the circumprimary disc in a binary system is a result of torques exerted perpendicular to the disc's rotational axis, or parallel to the disc midplane. To describe the motion, let us consider the diagram illustrated in Figure 6.1. The blue and red circles in the figure represent the orbital plane of the binary and the rotational plane of the disc, respectively. The intersection of both planes creates a line joining the descending node N_1 and ascending node N_2, i.e. the *line of nodes*. The comoving coordinates (X, Y, Z) are defined by the basis unit vectors $\hat{\mathbf{z}} = \mathbf{L}_\mathrm{d}/|\mathbf{L}_\mathrm{d}|$, $\hat{\mathbf{Y}} = \mathbf{L}_\mathrm{b} \times \mathbf{L}_\mathrm{d}/|\mathbf{L}_\mathrm{b} \times \mathbf{L}_\mathrm{d}|$, and then $\hat{\mathbf{x}} = \hat{\mathbf{Y}} \times \hat{\mathbf{z}}$. The parameters that are used to describe

the precession and alignment processes are the precession angle ϕ and alignment angle δ, respectively. From the diagram in Figure 6.1, the precession angle is obtained from

$$\phi = \cos^{-1}(\hat{\mathbf{Y}} \cdot \hat{\mathbf{y}}) \,, \tag{6.1}$$

while the misalignment angle from

$$\delta = \cos^{-1}\left(\frac{\mathbf{L}_\mathrm{b} \cdot \hat{\mathbf{z}}}{|\mathbf{L}_\mathrm{b} \cdot \hat{\mathbf{z}}|}\right). \tag{6.2}$$

In the disc's comoving frame depicted in Figure 6.1, the precession of the disc is due to the torque $\boldsymbol{\tau}_\mathrm{p}$ exerted along the Y-axis while the alignment process is due to the torque $\boldsymbol{\tau}_\mathrm{a}$ exerted along the X-axis. For precession, the torque $\boldsymbol{\tau}_\mathrm{p}$ is generated by non-symmetric forces acting on both sides of the disc which are separated by the line of nodes (the Y-axis). In the disc's comoving frame, the forces on both sides are the remainders of the gravitational force from the companion and the fictitious forces of the binary co-rotating frame. That is to say, from Figure 6.1, the net force on the $+X$-side of the disc has a component in $+\hat{\mathbf{z}}$ while that on the other side has a component in $-\hat{\mathbf{z}}$. The resulting torque is thus $\boldsymbol{\tau}_\mathrm{p} = -\tau_\mathrm{p}\hat{\mathbf{Y}}$. This component of torque brings the disc's angular momentum $\mathbf{L}_\mathrm{d}$ leaning towards the node N_2 (or towards the $-Y$-axis). When viewing from the rest frame, it appears that the vector $\mathbf{L}_\mathrm{d}$ precesses about the vector $\mathbf{L}_\mathrm{b}$ in a retrograde direction with respect to the rotational direction of the disc.

The rate of change of the precession angle, or the precession rate $\dot{\phi} = \mathrm{d}\phi/\mathrm{d}t$, can be approximated by considering the diagram illustrated in Figure 6.2. From the figure, the infinitesimal change of the angular momentum in the direction of $\hat{\mathbf{Y}}$ is

$$\mathrm{d}\mathbf{L}_Y = -L_\mathrm{d} \sin\delta \, \mathrm{d}\phi \, \hat{\mathbf{Y}}. \tag{6.3}$$

The magnitude of the precession torque ($\boldsymbol{\tau}_\mathrm{p}$) can then be found from

$$\tau_\mathrm{p} = \left|\frac{\mathrm{d}\mathbf{L}_Y}{\mathrm{d}t}\right| = L_\mathrm{d} \sin\delta \, \frac{\mathrm{d}\phi}{\mathrm{d}t}. \tag{6.4}$$

When the orbital average of the torque is considered, the average precession rate may be written as

$$\langle\dot{\phi}\rangle = \left\langle\frac{\mathrm{d}\phi}{\mathrm{d}t}\right\rangle = \frac{\langle\tau_\mathrm{p}\rangle}{L_\mathrm{d}\sin\delta}. \tag{6.5}$$

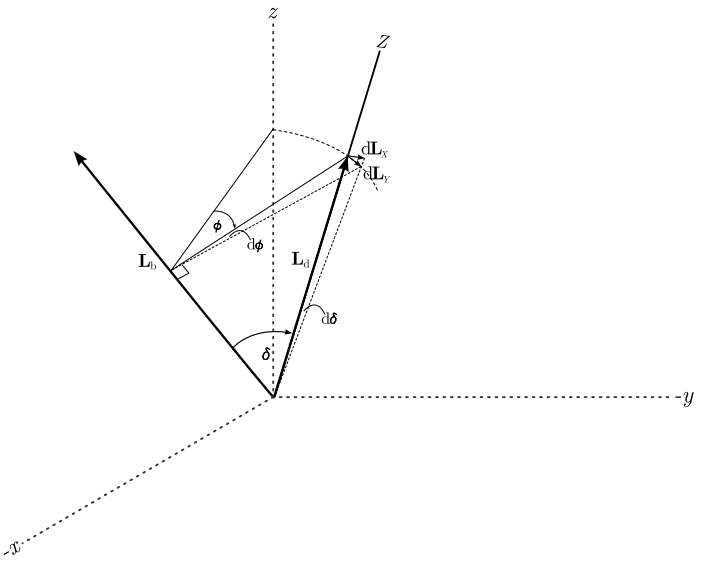

Figure 6.2 Diagram showing the infinitesimal changes $\mathrm{d}\phi$ in the precession angle ϕ, and $\mathrm{d}\delta$ in the misalignment angle δ. For clarity, only the z-axis is depicted for the comoving frame.

We should note that the values of the angle ϕ and $\langle\dot{\phi}\rangle$ are alway positive in our consideration.

Despite the fact that the disc can be treated approximately as a rigid body (e.g. Papaloizou and Terquem 1995; Larwood et al. 1996), deriving an expression for $\langle\dot{\phi}\rangle$ in a mathematically rigorous way is very complicated (see Papaloizou and Terquem 1995). For the sake of simplicity, let us begin by considering a flat disc of radius R_{d}. The time-averaged magnitude of torque exerted on an annulus of mass $\mathrm{d}M$ and inner radius R is given by

$$\left\langle \mathrm{d}\tau_{\mathrm{p}} \right\rangle \simeq \frac{3}{4} G M_{\mathrm{c}} R^2 \mathrm{d}M \left\langle \frac{1}{r^3} \right\rangle \sin\delta\cos\delta, \tag{6.6}$$

where G is the gravitational constant, M_{c} the mass of the companion, and r the binary separation (Bate et al. 2000). By using the surface density profile $\Sigma(R) = \Sigma_{\circ}(R/R_{\circ})^{-p}$ (Equation 5.1) for $\mathrm{d}M = 2\pi\Sigma R\mathrm{d}R$, we have the average torque

$$\begin{aligned} \left\langle \tau_{\mathrm{p}} \right\rangle &\simeq \frac{3\pi}{2} G M_{\mathrm{c}} \Sigma_{\circ} R_{\circ}^{p} \left\langle \frac{1}{r^3} \right\rangle \sin\delta\cos\delta \int_0^{R_{\mathrm{d}}} R^{3-p}\,\mathrm{d}R \\ &\simeq \frac{3\pi}{2} \frac{G M_{\mathrm{c}} \Sigma_{\circ} R_{\circ}^{p} R_{\mathrm{d}}^{4-p}}{(4-p)} \left\langle \frac{1}{r^3} \right\rangle \sin\delta\cos\delta. \end{aligned} \tag{6.7}$$

The time-averaged term of $1/r^3$ can be found from

$$\left\langle \frac{1}{r^3} \right\rangle = \frac{1}{\mathcal{P}} \int_0^{\mathcal{P}} \frac{1}{r^3}\, \mathrm{d}t, \tag{6.8}$$

where $\mathcal{P}$ is the orbital period of the binary. The time $\mathrm{d}t$ in this equation can be written in terms of the orbital angle θ and the angular speed $\dot{\theta}$ of the binary orbit as $\mathrm{d}t = \mathrm{d}\theta/\dot{\theta}$. From Kepler's second law, we have

$$\dot{\theta} = \frac{2\pi a^2 (1-e^2)^{1/2}}{r^2 \mathcal{P}}, \tag{6.9}$$

where a and e are respectively the semi-major axis and eccentricity of the orbit. Also, the orbital separation r as a function of θ is given by

$$r = \frac{a(1-e^2)}{1 - e\cos\theta}. \tag{6.10}$$

Substituting $\mathrm{d}t$ and the relevant variables back into Equation 6.8 and rearranging the terms give us

$$\left\langle \frac{1}{r^3} \right\rangle = \frac{1}{2\pi a^3 (1-e^2)^{3/2}} \int_0^{2\pi} 1 - e\cos\theta\, \mathrm{d}\theta = \frac{1}{a^3 (1-e^2)^{3/2}}. \tag{6.11}$$

The average torque in Equation 6.7 thus becomes

$$\left\langle \tau_\mathrm{p} \right\rangle \simeq \frac{3\pi}{2} \frac{G M_\mathrm{c} \Sigma_\circ R_\circ^p R_\mathrm{d}^{4-p}}{(4-p) a^3 (1-e^2)^{3/2}} \sin\delta\cos\delta. \tag{6.12}$$

The angular momentum L_d required by Equation 6.5 can be calculated from considering the angular momentum $\mathrm{d}L$ of an annulus of mass $\mathrm{d}M$ and inner radius R:

$$\mathrm{d}L \simeq Rv\mathrm{d}M \simeq 2\pi\Sigma\sqrt{GM_\mathrm{s}} R^2 \mathrm{d}R, \tag{6.13}$$

where $v = \sqrt{GM_\mathrm{s}}$ is the orbital speed of the annulus and M_s is the mass of the central star. By using the same surface density profile (Equation 5.1), one can find that

$$L_\mathrm{d} \simeq \frac{4\pi\Sigma_\circ R_\circ^p \sqrt{GM_\mathrm{s}}}{5-2p} R_\mathrm{d}^{5/2-p}, \tag{6.14}$$

where R_d is the radius of the disc. Note that this expression is valid only for star-disc systems with $M_\mathrm{d} \ll M_\mathrm{s}$. Now, substituting $\left\langle \tau_\mathrm{p} \right\rangle$ from Equation 6.12 and L_d from

Equation 6.14 into Equation 6.5 gives us

$$\langle \dot{\phi} \rangle \simeq \frac{3}{8}\left(\frac{5-2p}{4-p}\right)\left(\frac{GM_{\rm c}^2}{M_{\rm s}}\right)^{1/2} \frac{R_{\rm d}^{3/2}\cos\delta}{a^3(1-e^2)^{3/2}}. \tag{6.15}$$

the average precession rate. In this equation, the choice of $R_{\rm d}$ for a typical disc can be rather arbitrary since the density at the outer radii does not drop suddenly but rather attenuates exponentially as the radius increases (see the density profiles of discs in Chapter 5). Nevertheless, we will show later in Section 6.3.2 that $R_{\rm d}$ may be estimated from the characteristic (or effective) radius which scales with the semi-latus rectum of the binary orbit.

From Figure 6.2, one can find that the alignment rate is

$$\dot{\delta} = \frac{{\rm d}\delta}{{\rm d}t} = \frac{\tau_{\rm a}}{L_{\rm d}}, \tag{6.16}$$

where $\tau_{\rm a}$ is the magnitude of the alignment torque exerted along the x-axis. Although finding an expression for $\tau_{\rm a}$ is beyond the scope of this work, we discuss the factors that may involve in determining the value of torque in Section 6.4.1.

6.1.4 Implication for planet formation

Planets are thought to be formed out of protoplanetary discs surrounding young stars (Section 1.4). Since young stars are also commonly found in binary systems (Section 1.2.1), it is possible that the discs surrounding those young binary components can form planets. This seems to be supported by a growing number of observational evidence (e.g. Mugrauer et al. 2007; Daemgen et al. 2009; Desidera et al. 2011) since three exoplanets have been found to orbit the primary component of the three binary stars HR 3522, HR 5185, and HR 458 (Butler et al. 1997). However, it is still difficult to explain how those planet were formed. Planet formation in a binary system could be different from that in a single star mainly because of tidal effects from the stellar components onto the discs. Tidal effects may increase the mass accretion rates of the stars and disperse the disc material, shortening the dispersal timescale of discs. As a consequence, the formation of planets by the core accretion mechanism may be difficult while the formation via disc instabilities is still possible. Nevertheless, if the effect of tidal perturbations on grain growth processes is constructive, the core accretion timescale may be shortened, increasing the possibility of the mechanism.

As discussed above, a disc in a misaligned system tends to have its orientation changed towards alignment by tidal interactions. Planets that might form out of the disc may still have their orbital planes significantly misaligned if the alignment timescale of the system is longer than the planet formation timescale. An example to this is the HD 80606 misaligned planetary system observed by Pont et al. (2009). To sketch the aspect of binaries that might be found with misaligned planetary systems, let us use the estimate alignment timescale from Bate et al. (2000) which is roughly the viscous timescale of the disc: ~ 100 precession periods, and one precession period is ~ 20 binary orbital periods. If we assume that the planet formation timescale of $\sim 10^6$yr is less than a half of the alignment timescale ($\lesssim 50$ precession periods), the expected orbital period of the binary should be $\gtrsim 10^6\text{yr}/50\times 20 = 10^3\text{yr}$. This is equivalent to binary systems with total masses $1M_\odot$ and semi-major axes $\gtrsim 100$AU.

During the past few years, many exoplanets have been found with orbital planes misaligned to the rotational plane of their host star (spin-orbit misaligned planets, e.g. Winn et al. 2009; Pont et al. 2010; Triaud et al. 2010; Johnson et al. 2011; Albrecht et al. 2012); the measurement of the misalignment is usually done via the Rossiter-McLaughlin effect (Rossiter 1924; McLaughlin 1924), see Winn (2011) for details. Several formation mechanisms for those systems have been discussed in Winn et al. (2010). However, we suggest in this work that a spin-orbit misaligned exoplanet could also form from a disc in a misaligned binary system which is later disrupted by a close encounter with other star in the cluster. In this scenario, the misalignment between the rotational axis of the disc and the spin axis of the host star is a result of disc precession. Thus, it is unlikely for both axes to be aligned even though they are aligned at the beginning. Since a misaligned binary with disc(s) is expected to have a wide orbit (see above), the system can be disrupted by a passing star in the cluster. If the planetary system(s) around the disrupted components survives from the interaction, its spin-orbit misaligned orientation remains. In order to justify the plausibility of this scenario, let us consider the encounter timescale of a binary star in a young star cluster, given by

$$t_{\text{enc}} \sim \frac{1}{4\pi r^2 n\sigma}, \tag{6.17}$$

where r is the characteristic radius of the binary (e.g. the semi-major axis), n the number density of the cluster, and σ the velocity dispersion of the cluster (Binney and Tremaine 2008). For example, a young binary star with $r = 300$AU in the Orion Trapezium Cluster with $n \sim 2\times 10^3 - 1\times 10^4 \text{pc}^{-3}$ (e.g. Hillenbrand 1997)

and $\sigma \sim 1.5$km/s (van Altena et al. 1988) would have an encounter timescale $t_{\rm enc} \sim 2.4 - 12.1 \times 10^6$yr. Therefore, given that the average age of Orion is $\sim 2.5 \times 10^6$yr (Jeffries et al. 2011), at least a few tens per cent of the stars in the cluster should have had an encounter at ~ 300AU. This may provide a sufficient possibility for spin-orbit misaligned exoplanets to be created from the disruption of misaligned binaries.

6.2 Simulations

We perform a number of SPH simulations to study the evolution of a circumprimary disc in a misaligned binary star system. The initial system is illustrated in Figure 6.3. The system is prepared by adding a companion star (sink particle) of mass $M_{\rm c} = 0.1 M_\odot$ and accretion radius $R_{\rm c} = 0.5$AU to a relaxed star-disc system prepared in Chapter 5. The position of the primary star is set as the origin with the disc midplane lying on the xy-plane. The companion is initially placed above the $+x$-axis, at apastron radius $r_{\rm max} = 300$AU from the primary, and with initial velocity ($v_{\rm c}$) in the $+y$-direction given by

$$v_{\rm c} = \frac{2\pi a}{\mathcal{P}} \left(\frac{1-e}{1+e} \right)^{1/2}, \tag{6.18}$$

where e is the eccentricity of the orbit, $a = r_{\rm max}/(1+e)$ the semi-major axis, and $\mathcal{P}$ the approximate period of the orbit obtained from

$$\mathcal{P} \simeq \left(\frac{a^3}{M_{\rm s} + M_{\rm d} + M_{\rm c}} \right)^{1/2} \quad {\rm yr}, \tag{6.19}$$

where $M_{\rm s}$ and $M_{\rm d}$ are the masses of the central star and the disc, respectively. Note that, as well as elsewhere in this thesis, the fundamental units of mass, length, and time are, in respective order, $M_\odot$, AU, yr, unless stated otherwise.

A number of systems are set up from the combination of (a) inclination angles $i_{\rm b} = 0°$, 22.5°, 45°, 67.5°, and 90° and (b) eccentricities $e = 0$, 0.2, 0.4, and 0.6. The corresponding semi-major axes and orbital periods for the systems with those eccentricities are presented in Table 6.1. All systems are simulated with the same temperature profile index $q = 3/4$, inner radius temperature $T_\circ = 600$K, and resolution $N_{\rm sph} \sim 190$k particles. Additionally, systems with $i_{\rm b} = 45°$ are also set up and performed on a lower resolution disc with $N_{\rm sph} \sim 47$k particles to test the effects of orbital directions (prograde and retrograde) and the resolution of simulations. The

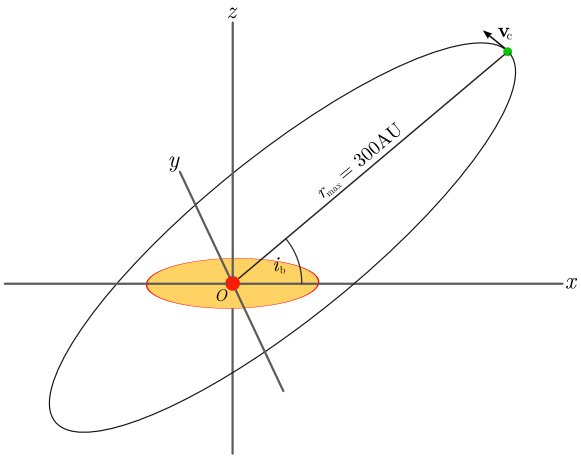

Figure 6.3 Initial configuration of a star-disc-companion system. The primary star (red dot) is at the origin and surrounded by a disc. The companion (green dot) is initially placed above the $+x$-axis with apastron radius $r_{\max} = 300$AU away from the primary and with inclination angle i_b relative to the disc midplane. The companion is given an initial velocity of $\mathbf{v}_c = +v_c\hat{\mathbf{y}}$ (Equation 6.18).

Table 6.1 The semi-major axes and orbital periods corresponding to different values of eccentricity.

Eccentricity	Semi-major axis (AU)	Orbital period (yr)
0	300.0	6348.1
0.2	250.0	4829.2
0.4	214.3	3832.2
0.6	187.5	3136.6

maximum simulation time is 500kyr but most of the simulations may be terminated by this time as their resolution is insufficient.

For concise references, we use some conventions to name the simulation in each case. The label begins with the resolution of the system, followed by some system properties. The label is written distinctively in `monospaced typeface`. For example, the system `200ke2i450` will refer to a system with original resolution of 200k particles, eccentricity $e = 0.2$, and initial inclination $i_b = 45°$. Note that, throughout this chapter, systems with $N_{\rm sph} \sim 47$k and ~ 190k particles will be labelled with their original resolution numbers 50k and 200k (in Chapter 5), respectively.

6.3 Results

The results are divided into two ensembles by the initial inclination of the systems, i.e. aligned systems ($i_{\rm b} = 0°$) and misaligned systems ($i_{\rm b} > 0°$).

6.3.1 Aligned systems

In a coplanar binary system with a circular orbit, i.e. `200ke0i000` ($e = 0$ and $i_{\rm b} = 0°$), tidal perturbations from the companion have a negligible effect on the stability against fragmentation of the disc; the disc is stable through the end of the simulation. The outward transfer of angular momentum in the disc makes the disc expand and fill up its Roche lobe on the plane. The mass at the rim of the disc is then transferred to the companion, as shown in Figure 6.4. The transferred mass forms a secondary disc around the companion. The secondary disc rotates in the same direction as that of the circumprimary disc (counterclockwise).

Figure 6.5 compares the density profiles of the system `200ke0i000` (right) to that of the isolated star-disc system (left) of the same physical properties from Chapter 5. Since some disc material in the system `200ke0i000` has been taken by the companion, the density at the outer radii ($R \gtrsim 100$AU) is lower than that of the disc in the isolated system. The secondary disc created from the transferred material appears as a density peak on the profile of the system `200ke0i000` at radius ~ 300AU. The mass accretion rates of the main star in the binary and the isolated systems are shown in Figure 6.6 as blue and black lines, respectively. We can see that, after $t \sim 50$kyr, the primary star in the binary system accreted mass with higher rate than the star in the isolated system. This suggest that the mass accretion rate of the primary is affected by tidal interactions from the companion.

In a binary system with an elliptical orbit, the companion generates more tidal effects onto the circumprimary disc. Figure 6.7 shows the snapshots of the interaction occurring in the first orbit of the binary systems with three different eccentricities: `200ke2i000` (first column), `200ke4i000` (second column), and `200ke6i000` (third column). We can see from the figure that the degree of interaction increases with the eccentricity. After each pericentric passage of the companion, the mass accretion rate of the primary star increases slightly as shown in Figure 6.8. However, the change is not significant except in the system `200ke6i000` (the black line in Figure 6.8).

Although spiral-arm patterns can be seen on the disc during the pericentric approach in the system `200ke6i000` (Figure 6.7), no fragmentation occurs. This may suggest that protoplanetary discs are rather stable to gravitational instabilities in-

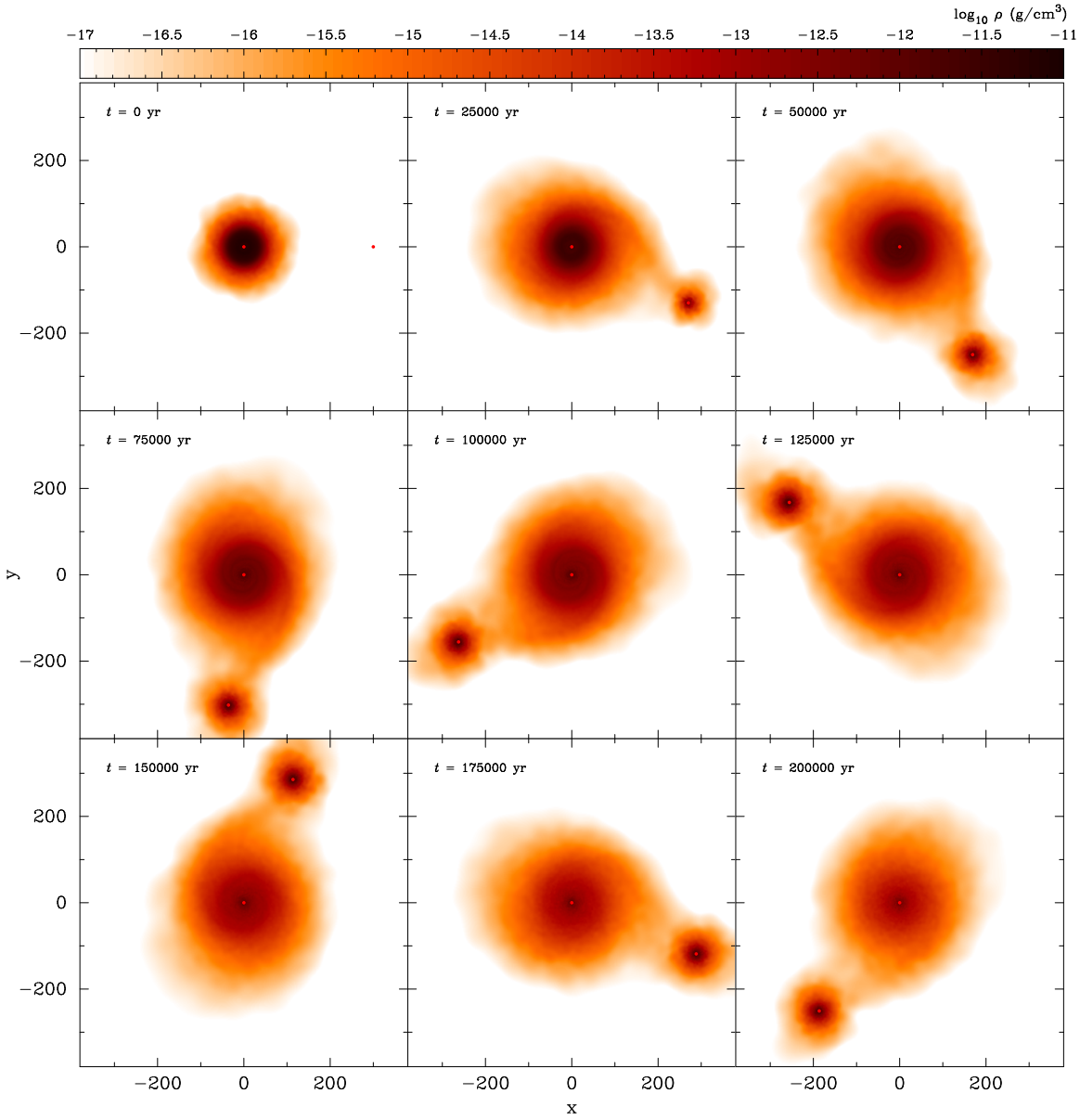

Figure 6.4 Density plots showing the interaction between the circumprimary disc and the companion in the system `200ke0i000` during the first 200kyr. Mass transferring from the outer parts of the disc to the companion can be observed.

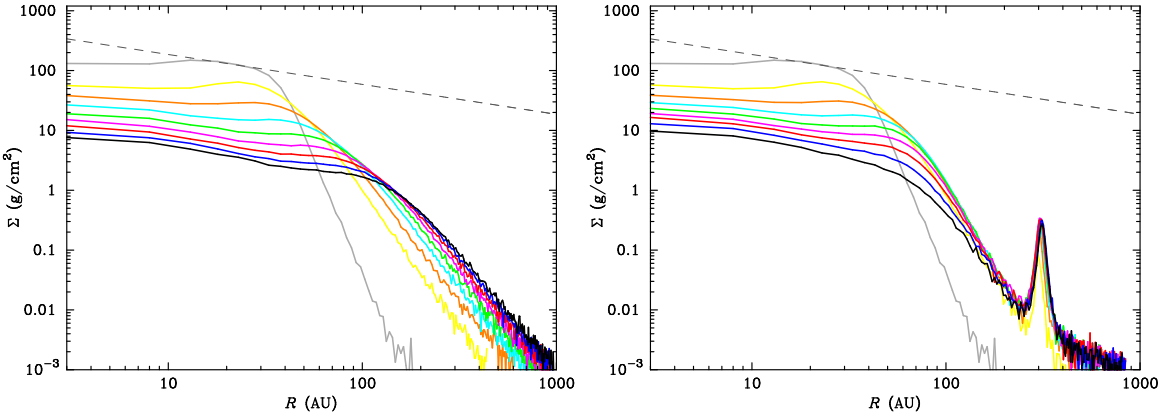

Figure 6.5 Comparison between the surface density profiles of an isolated star-disc system (left) and the system `200ke0i000` (right). Apart from the added companion in the latter system, both have the same physical properties. The grey dashed-lines mark the density profile with index $p = 1/2$. The profiles are shown from $t = 0$ (grey) to 200kyr (black) in steps of 25kyr (see Section 5.4 for colour codes).

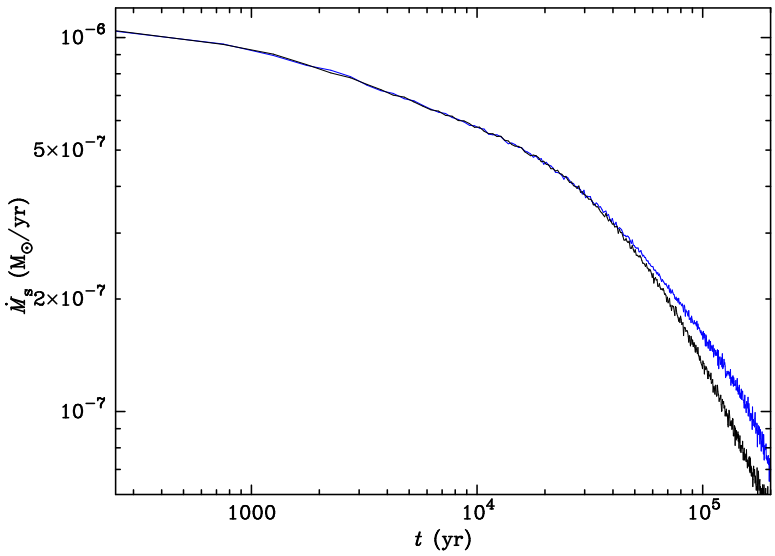

Figure 6.6 Comparison between the mass accretion rates of the main star in an isolated star-disc system (black) and the binary system `200ke0i000` (blue).

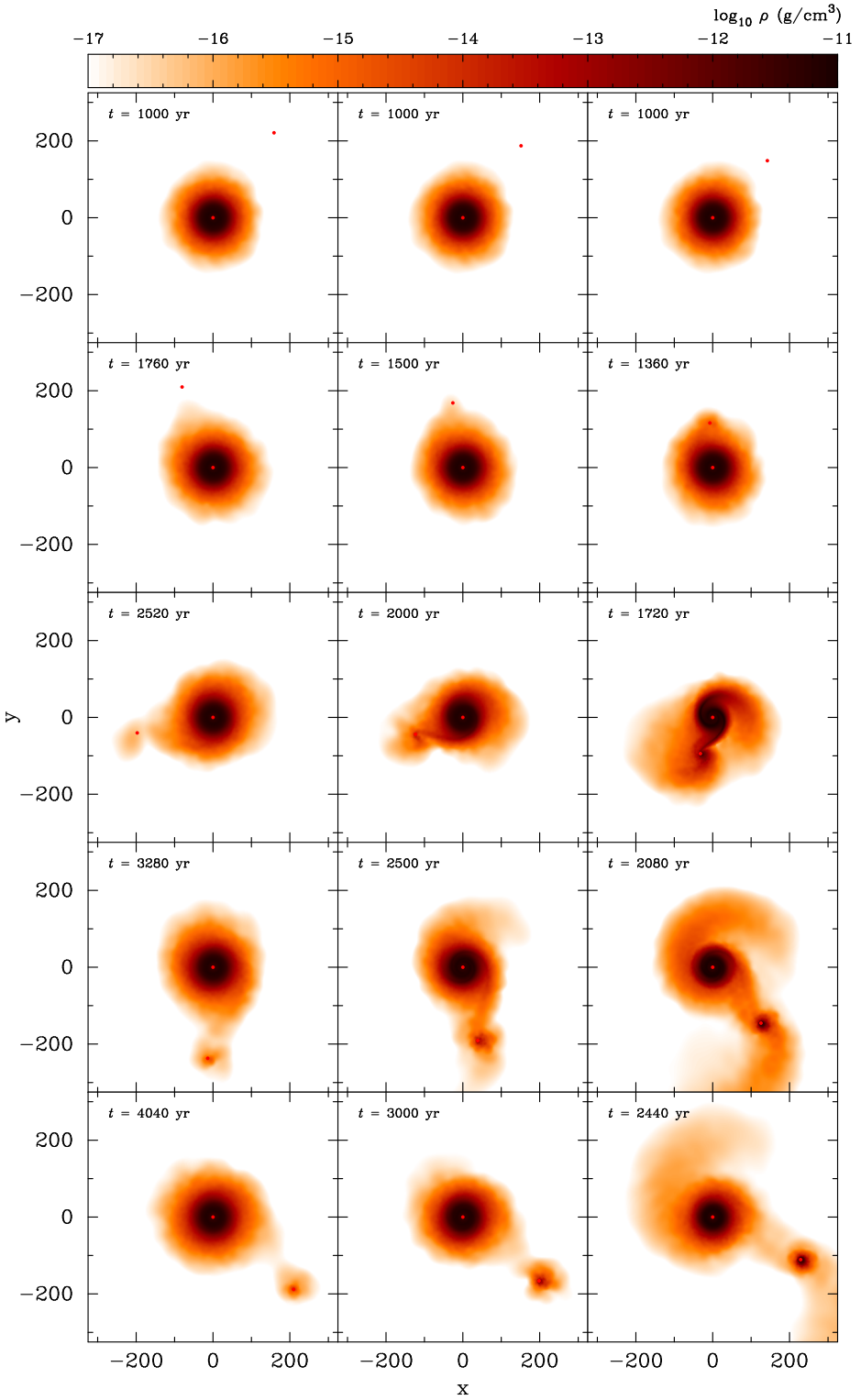

Figure 6.7 Density plots showing the interaction between the companion and the disc during the first orbit of the systems `200ke2i000` (first column), `200ke4i000` (second column), and `200ke6i000` (third column). In a high-eccentricity system such as `200ke6i000`, a large amount of disc material has been taken by the companion during each pericentric passage. The spiral-arm pattern of density can also be seen clearly in the system `200ke6i000` at $t = 1720$yr.

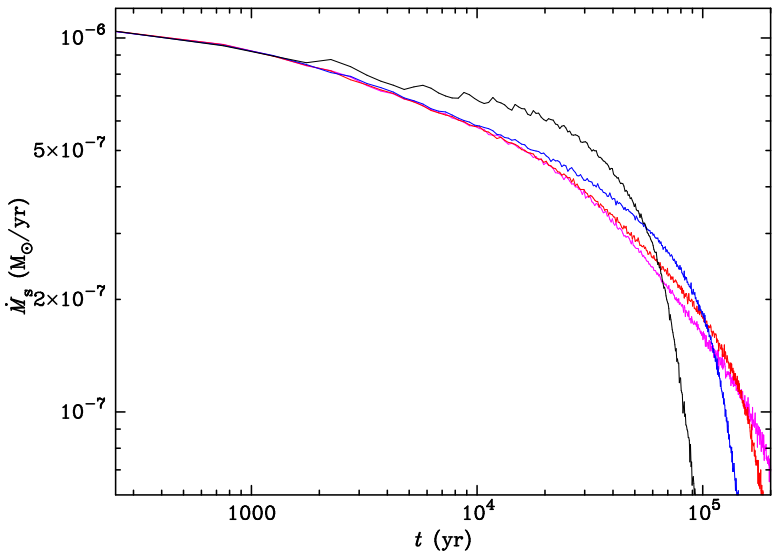

Figure 6.8 Comparison of the mass accretion rates of the primary star in the systems `200ke0i000` (magenta), `200ke2i000` (red), `200ke4i000` (blue), and `200ke6i000` (black). The periodic enhancement on the accretion rate can only be noticeable in the system `200ke6i000`.

duced by the companion, even in a highly eccentric binary system. However, this may not be definitely true since the simulations depend largely on the radiation treatment used in the code (the Stamatellos et al. radiative cooling, see Section 3.4.4). It has been shown recently by Wilkins and Clarke (2011) that the method may systematically underestimate the total cooling rate in a disc simulation by as much as a factor of 200. If this is the case, the results of our disc simulations might change dramatically; that is, the disc might fragment. Nevertheless, this may not be crucial in our work since we focus more on the bulk dynamical properties of a circumprimary disc in a misaligned binary system (see the next section) than the gravitational instability as a consequence of tidal perturbations.

6.3.2 Misaligned systems

Circumprimary discs in misaligned binary systems are tilted by tidal effects from the companion. Figure 6.9 shows the density plots of the circumprimary disc in the system `200ke0i450` viewed along different directions. Subfigures in the first columns show the disc viewed over the xy-plane while the second and the third columns show the cross-sectional plots of the xz- and yz-planes, respectively. Some properties of the system that change with time (t) shown on the right side of the plots include the misalignment angles between: the binary orbital vector and the z-axis, $\delta_{\rm bz}$; the disc's

rotational vector and the z-axis, $\delta_{\rm dz}$; the disc's rotational vector and the binary orbital vector, $\delta_{\rm db}$. The binary orbital vector and the disc's rotational vector are practically the angular momentum vectors of the binary ($\mathbf{L}_{\rm b}$) and the disc ($\mathbf{L}_{\rm d}$), respectively. In Figure 6.9, the vector $\mathbf{L}_{\rm d}$ is represented by the arrow pointing outwards from the primary.

It should be noted that, in this work, the angular momentum vector of the disc is calculated from

$$\mathbf{L}_{\rm d} = m_{\rm SPH} \sum_{R_i \leq R_{\rm d}} \mathbf{R}_i \times \mathbf{V}_i, \tag{6.20}$$

where $m_{\rm SPH}$ is the constant mass for all SPH particles in the simulation, R_i the orbital radius of particle i, V_i the velocity of particle i, and $R_{\rm d}$ the radius of the disc. Since there is no other quantitative use of the vector $\mathbf{L}_{\rm d}$ apart from its direction, the choice of the disc radius $R_{\rm d}$ for calculating the quantity can be arbitrary. We use $R_{\rm d} = 40$AU for all the result analyses henceforth. The reasons for this value are that (a) it contains a sufficient number of the disc particles when the resolution of the disc is low and (b) it is not too far out to be contaminated by the particles associated with the secondary disc in the cases of high eccentric binary systems (the closest separation between the stars is 75AU for the system with $e = 0.6$).

Changes in the precession angle ϕ and misalignment angle δ for each system can be shown in Figure 6.10. In each subfigure, the red pattern is drawn by the vector $\mathbf{L}_{\rm d}$ (or $\hat{\mathbf{z}}$) of the disc that is precessing about the vector $\mathbf{L}_{\rm b}$ of the binary. The pattern is drawn on a plane perpendicular to $\mathbf{L}_{\rm b}$. The angle δ is measured on the scales marked by the concentric circles while the angle ϕ is measured azimuthally clockwise from the vertical axis shown on the plot. The values given in the brackets are δ and ϕ (i.e. (δ, ϕ)) at time $t = 200$kyr, except for the system `200ke6i450` which are at $t = 120$kyr because of the poor resolution beyond that time. The precession and misalignment angles of each system are also plotted against time (up to 500kyr) in Figure 6.11, where the noise due to low resolution is also included. The grey lines linking the data points mark on times where systems lose their resolution by $\sim 10^4$ particles. The following are some details of the results.

Precession rate. From comparing the precession angles in subfigures (a), (b), (c), and (e) in Figure 6.10, or the corresponding data curves (orange, red, blue, and black) in Figure 6.11(top), it appears that the lower the misalignment angle the higher the precession rate ($\dot{\phi}$). Also, we can see the disc in the system `200ke0i900` begins to

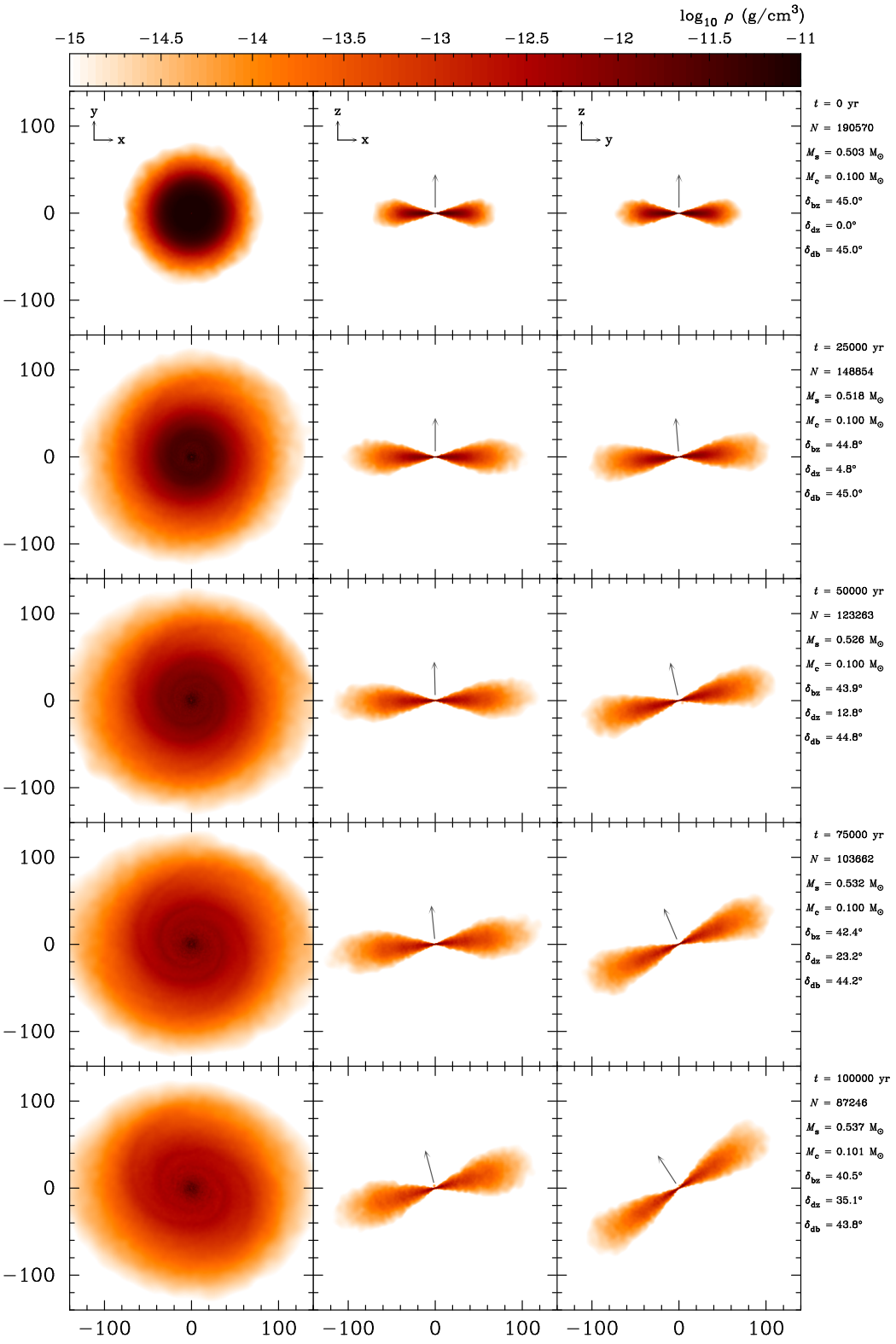

Figure 6.9 Density plots showing the change in the orientation of the circumprimary disc in the system `200ke0i450` over 100kyr. Snapshots in the first column are of the disc viewed from above the xy-plane. Snapshots in the second and the third columns are respectively the xz- and yz-cross-sectional plots of the disc. Snapshot time (t) and other properties of the system including the misalignment angles ($\delta_{\rm bz}$, $\delta_{\rm dz}$, and $\delta_{\rm db}$; see text for the description) are shown on the right side of the plots.

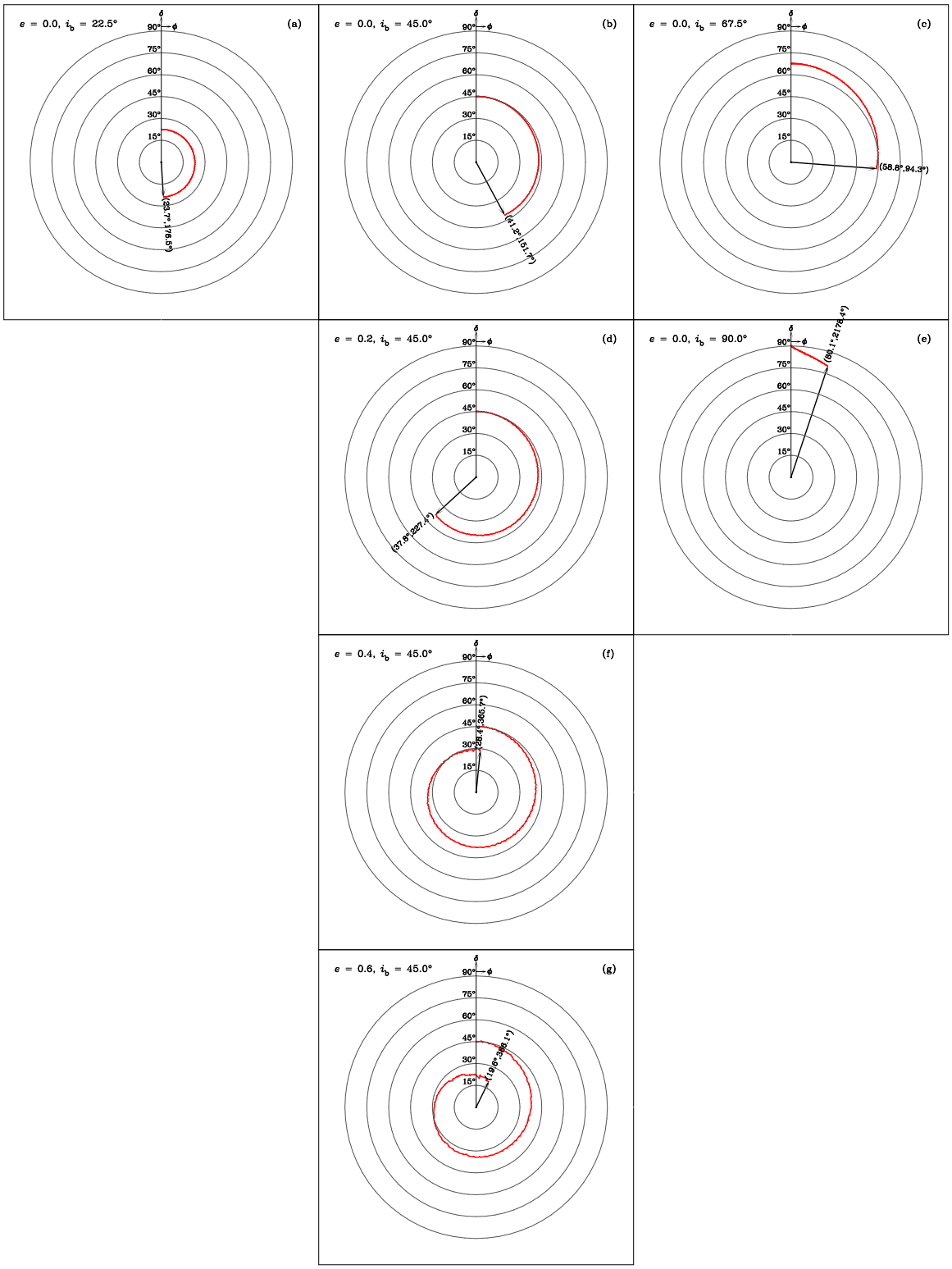

Figure 6.10 Red patterns showing the motions of the vector $\mathbf{L}_{\rm d}$ about the vector $\mathbf{L}_{\rm b}$. The patterns are drawn on a plane perpendicular to $\mathbf{L}_{\rm b}$ and shown as if it were viewed in the direction opposite to $\mathbf{L}_{\rm b}$. The radial scale marked by the concentric circles measures the misalignment angle δ. The precession angle ϕ is measured azimuthally clockwise from the vertical axis shown on the plot. The values in the brackets are of δ and ϕ at time $t = 200$kyr, except in subfigure (g) that shows the values at $t = 120$kyr. The subfigures labelled alphabetically are of the systems (a) `200ke0i225`, (b) `200ke0i450`, (c) `200ke0i675`, (d) `200ke2i450`, (e) `200ke0i900`, (f) `200ke4i450`, and (g) `200ke6i450`; that is, (a)-(c) and (e) are circular-orbit binaries while (d), (f), and (g) are eccentric-orbit binaries.

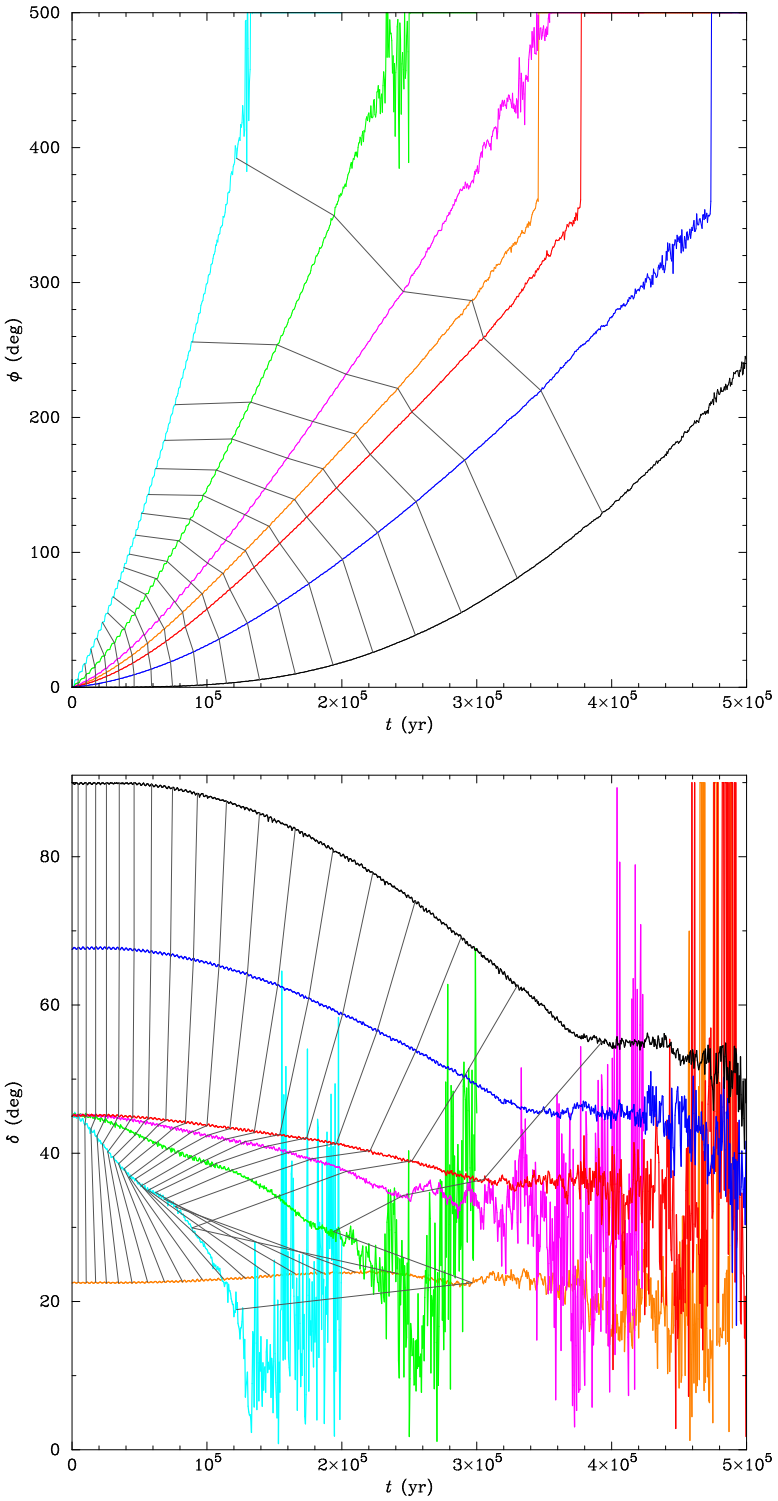

Figure 6.11 Plots of the angles ϕ (top) and δ (bottom) against time t. The data curves with different colours are of the systems `200ke0i225` (orange), `200ke6i450` (cyan), `200ke4i450` (green), `200ke2i450` (magenta), `200ke0i450` (red), `200ke0i675` (blue), and `200ke0i900` (black). The grey lines link the data points where the systems lose their resolution by $\sim 10^4$ particles, i.e. the lines of equal resolution in steps of 10k particles. The noise at the end of each data curve is due to the poor resolution near the end of the simulation.

precess only after it has been tilted, i.e. $\delta < 90°$ at $t \gtrsim 60$kyr. This suggests that no disc precession occurs in the perpendicularly misaligned configuration.

With the same initial inclination, the system with a smaller orbit (or with higher eccentricity) precesses faster. Subfigures (b), (d), (f), and (g) in the second column of Figure 6.10 and the corresponding data curves (red, magenta, green, and cyan) in Figure 6.11(top) show the increasing rate of precession when the value of e increases (orbital size decreases).

Alignment rate. The tilting of the disc seems to be more complicated than the precession. In circular-orbit binaries of the same separation, the disc is tilted towards alignment faster in systems with higher initial inclinations. This can be seen from comparing the changes in the data curves of the systems `200ke0i450` (red), `200ke0i675` (blue), and `200ke0i900` (black) in Figure 6.11(bottom). It is interesting that the disc in the system `200ke0i225` (orange) seems to be tilted towards a more misaligned configuration, suggestive of a turning point of the tilting behaviour at some point where the initial inclination angle is $22.5° < i_{\rm b} < 45°$. Unfortunately, the point cannot be verified by our limited number of simulations.

In eccentric-orbit binaries of the same apastron radius, the disc is tilted faster in systems with higher eccentricities (smaller orbital sizes). The changes can be seen by comparing the data curves of the systems `200ke0i450` (red), `200ke2i450` (magenta), `200ke4i450` (green), and `200ke6i450` (cyan) in Figure 6.11(bottom).

Prograde vs retrograde. The evolution of systems with different directions of the binary orbits are presented in Figure 6.12. The simulations shown in this figure are performed with low resolution (~ 47k) as they are also for investigating the effect of resolution (see below). The subfigures in the first column of Figure 6.12 are of systems `50ke0i450`, `50ke2i450`, `50ke4i450`, and `50ke6i450`. The subfigures in the second column are of the systems with the same initial discs as systems on the first column except that the binary orbits are retrograde. In retrograde systems, the misalignment angle δ is an obtuse angle ($\delta > 90°$). Hence, for convenience in comparing the results, the vector $\mathbf{L}_{\rm d}$ in the second column is shown as if it is viewed in the same direction as that of those plots in the first column. The numbers marked on the concentric circles and those in the brackets show the actual value of δ and ϕ.

From comparing both columns in Figure 6.12, the precession rates in both cases seem to be roughly the same, except for the system `50ke6i450` in the subfigure (g) where the precession rate may be affected by the resolution of the disc (see below).

In terms of the alignment process, both orbital directions tend to bring $\mathbf{L}_\mathrm{d}$ and $\mathbf{L}_\mathrm{b}$ towards alignment in the same direction, i.e. from $\delta > 0°$ to $\delta = 0°$.

Resolution. Comparing the subfigures in the first column of Figure 6.12 (initial resolution $\sim$47k particles) with those in the second column of Figure 6.10 (initial resolution $\sim$190k particles) suggests that a lower-resolution disc tends to precess and tilt towards alignment faster. This is probably due to the hydrodynamic forces being poorly modelled when the resolution is low. That is, the sparse particle distribution in a low-resolution disc might increase relative velocities between particles in adjacent orbits, increasing the artificial-viscosity forces and hence the transfer rate of angular momentum.

Surface density and accretion rate. Changes in the disc's surface density profiles are shown in Figure 6.13 whose figure layout is the same as Figure 6.10. The density profiles are shown at times from $t = 0$ (grey) to 200kyr (black) in steps of 25kyr (see Section 5.4 for colour codes). The small density peak appearing around the rim of the primary disc is of the secondary disc. From the figure, the discs expand to reach the orbit of the companion within $t < 25$kyr. In systems with high eccentricities such as `200ke6i450` in Figure 6.13(g), the discs are truncated by the companion. The mass accretion rate of the primary star in this case is also enhanced, as shown in Figure 6.14(cyan).

Effective radius for precession. If we were to estimate the precession rate of a misaligned binary system by using Equation 6.15, the choice of radius R_d would be crucial, given that other parameters can be measured accurately. This is because the density profiles at outer radii of typical circumstellar discs are not well truncated but rather exponentially attenuated, as can be seen from Figure 6.13. However, by assuming that the precession rate given by Equation 6.15 is correct, we may have some clue for the effective (or characteristic) radius on which the precession mechanism operates. The effective radius (R_deff) of the disc can be obtained from rearranging Equation 6.15, i.e.

$$R_\mathrm{deff} \simeq \left[\frac{8}{3} \left(\frac{4-p}{5-2p} \right) \left(\frac{M_\mathrm{s}}{G M_\mathrm{c}^2} \right)^{1/2} \frac{a^3 (1-e^2)^{3/2} \langle \dot{\phi} \rangle}{\cos\delta} \right]^{2/3} . \tag{6.21}$$

The value of R_deff can be calculated from simulation results where all orbital pa-

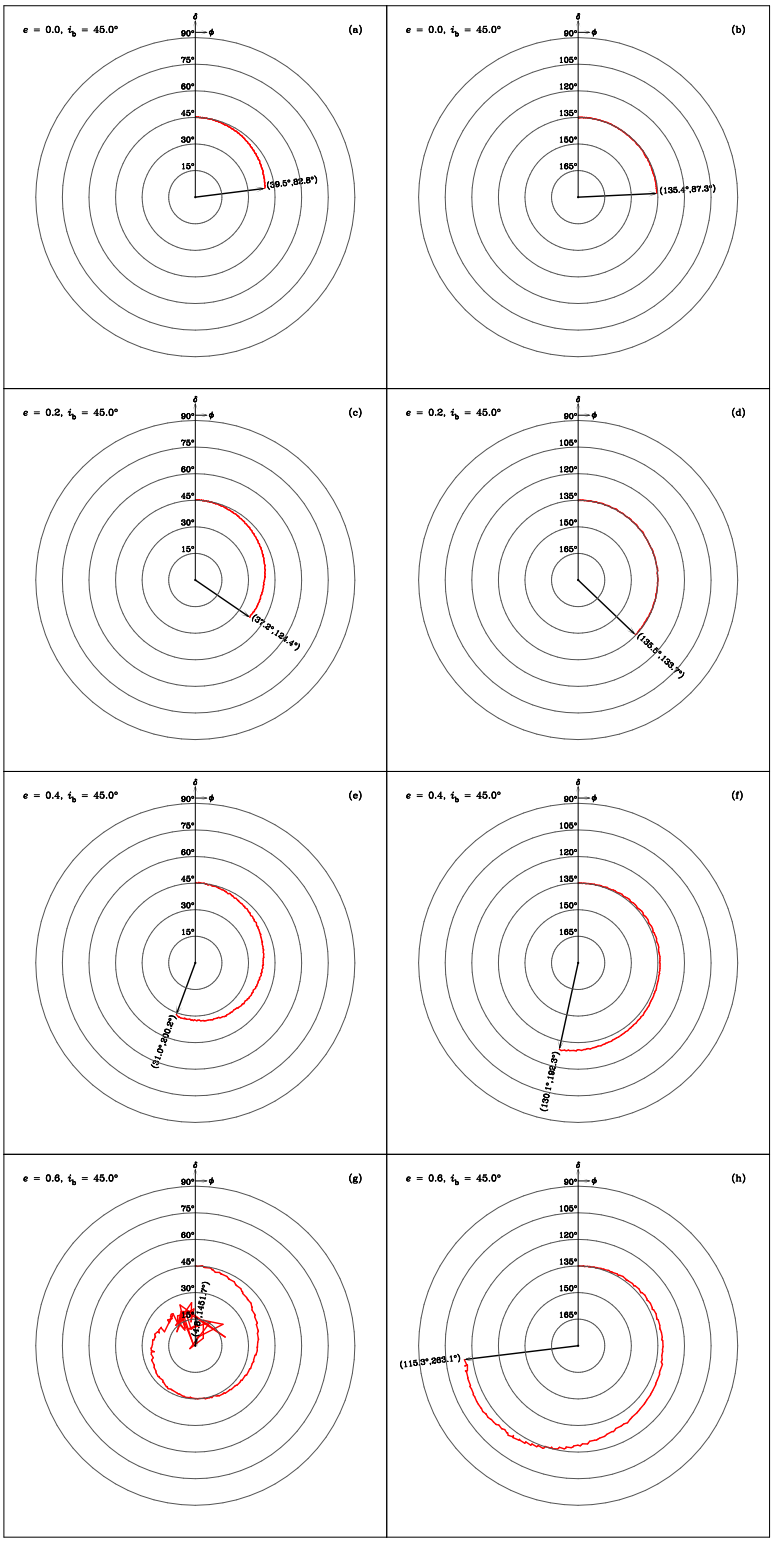

Figure 6.12 Red patterns showing the motions of the vector $\mathbf{L}_{\rm d}$ about the vector $\mathbf{L}_{\rm b}$ under the influence of a prograde companion (first column) and retrograde companion (second column). The simulations are performed with initial resolution of $\sim$47k particles. The values in the brackets are of δ and ϕ at time $t = 100$kyr. The pair of plots in each row are of the systems `50ke0i450` (a and b), `50ke2i450` (c and d), `50ke4i450` (e and f), and `50ke6i450` (g and h).

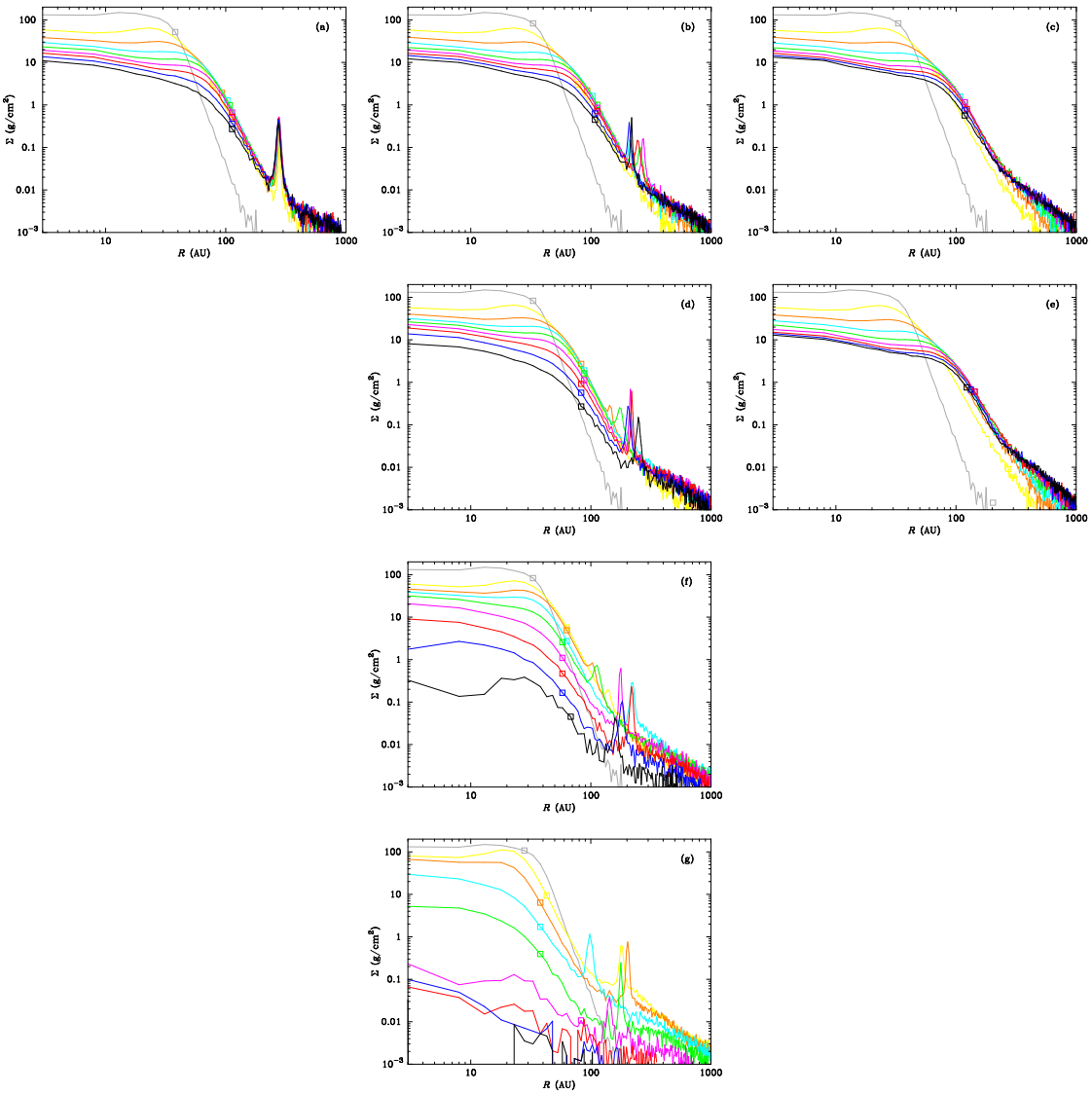

Figure 6.13 Change of the surface density profile of the discs from $t = 0$ (grey) to $t = 200$kyr (black) in steps of 25kyr. The plots are of the systems (a) `200ke0i225`, (b) `200ke0i450`, (c) `200ke0i675`, (d) `200ke2i450`, (e) `200ke0i900`, (f) `200ke4i450`, and (g) `200ke6i450`. The square symbols show the density at the effective radius of precession (see below).

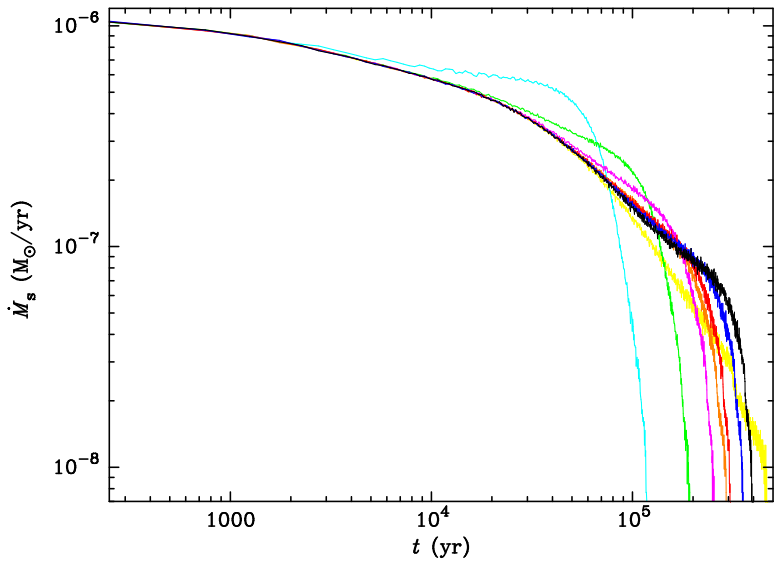

Figure 6.14 Plots comparing the mass accretion rates of the central star in the isolated star-disc system (yellow) and the primary star in the systems `200ke0i225` (orange), `200ke6i450` (cyan), `200ke4i450` (green), `200ke2i450` (magenta), `200ke0i450` (red), `200ke0i675` (blue), and `200ke0i900` (black).

rameters are already known. The value of $\langle\dot{\phi}\rangle$ at any snapshot time t required in Equation 6.21 can be interpolated with the following procedure. First, divide the time range of the whole simulation time equally into n intervals. The size of the intervals is an integer multiple of the snapshot time interval ($\Delta t = 500$yr). Second, calculate the rate of change $\dot{\phi}_i$ at the middle of each time interval (t_i) from a linear fit of the data in the interval, i.e. the slope of the fit is $\dot{\phi}_i$. Finally, the value of $\dot{\phi}$ at any time t is interpolated from using the Lagrange form of interpolating polynomial (e.g. Bradie 2006):

$$\dot{\phi}(t) = \sum_{i=1}^{n} \left(\prod_{\substack{j=1 \\ j \neq i}}^{n} \frac{t - t_j}{t_i - t_j} \right) \dot{\phi}_i. \tag{6.22}$$

Good interpolation may be obtained from adjusting the size of the intervals. The interpolated value of $\dot{\phi}$ should not oscillate or change abruptly if the data (ϕ) does not suggest so.

By assuming that the density profile index $p = 0$ (flat profile), the interpolated value of $\dot{\phi}(t)$ for each system can be calculated and plotted in Figure 6.15. The squares on each curve mark the set of $\dot{\phi}_i$ calculated at the middle of each interval. Note that (a) the interpolation is generally poor near the end of each simulation as the value

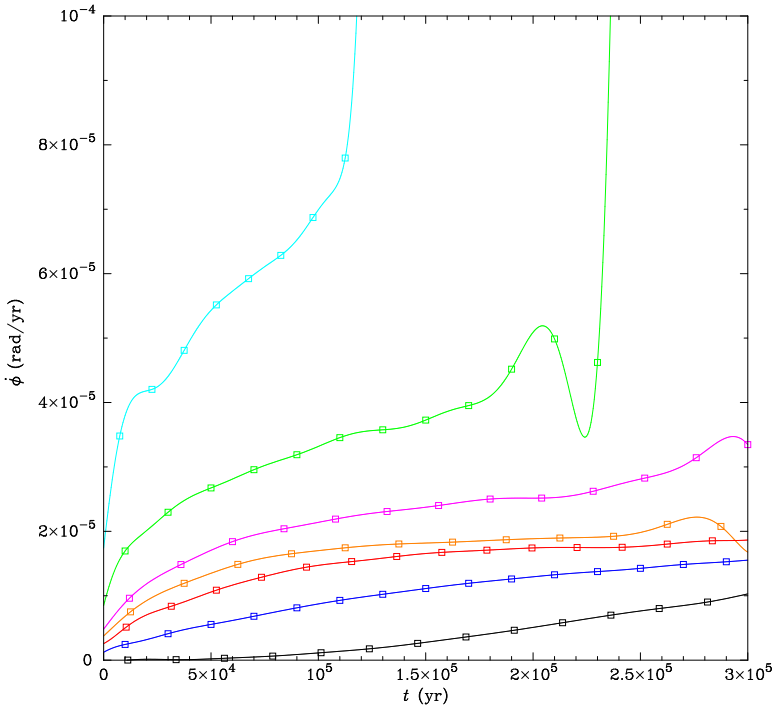

Figure 6.15 Interpolated values for $\langle\dot{\phi}\rangle$ in Equation 6.21. The squares mark the set of $\dot{\phi}_i$ from which the value of $\dot{\phi}(t)$ is interpolated. Line colour-description is the same as that in Figure 6.11.

of ϕ becomes uncertain due to poor resolution and (b) the assumed value of p is not crucial as long as $p < 1$.

With the interpolated value of $\langle\dot{\phi}\rangle$ shown in Figure 6.15, the value of $R_{\rm deff}$ can be calculated and plotted in Figure 6.16(left). The value of $R_{\rm deff}$ at different times can be mapped onto the surface density profiles in Figure 6.13 (the square symbols). We can see from the figure that the characteristic location of $R_{\rm deff}$ on the profiles does not significantly change with time. In most cases, we empirically find that $R_{\rm deff}$ is roughly a linear function of the semi-latus rectum of the binary orbit:

$$R_{\rm deff} = \frac{a(1-e^2)}{\xi}, \tag{6.23}$$

where ξ is a constant of value ~ 2.5. The comparison between $R_{\rm deff}$ calculated from Equation 6.21 and that from Equation 6.23 is also shown in Figure 6.16. The relation seems to break down in the case of high orbital inclination ($i_{\rm b} \to 90°$) and also around the beginning of each case. We discuss the use of this relation later in Section 6.4.2.

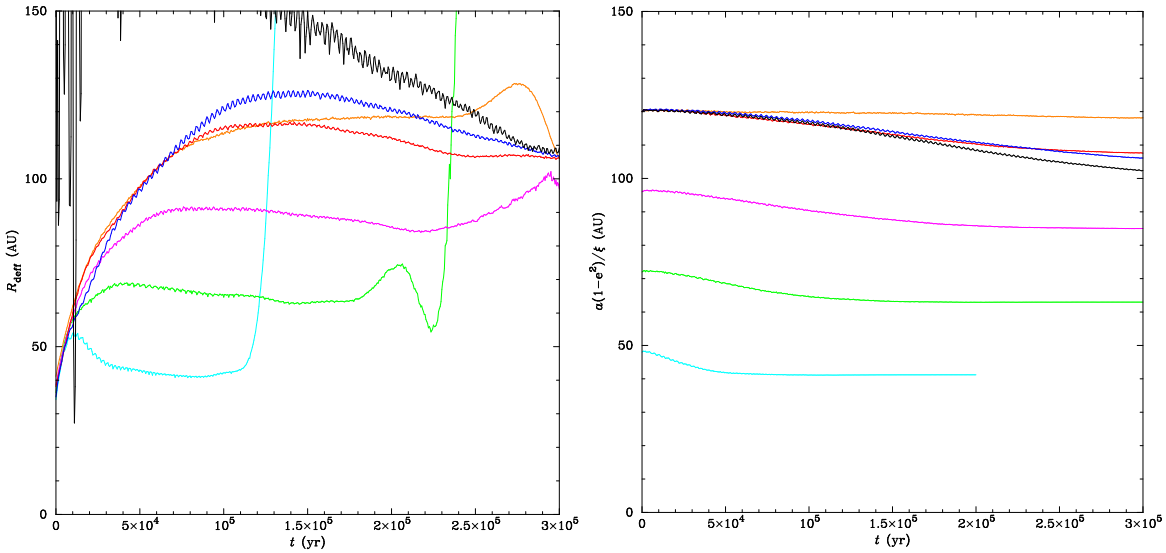

Figure 6.16 Comparison between the effective radius calculated from Equation 6.21 (left) and the value calculated from Equation 6.23 (right) where $\xi = 2.5$. Note that the plot of `200ke0i900` in the left figure is rather chaotic at the beginning due to $\cos\delta \sim 0$. Line colour-description is the same as that in Figure 6.11.

6.4 Planet formation in tilting discs

In this section, we discuss (a) the alignment rate, (b) the dispersal timescale of misaligned discs, and (c) the formation of retrograde planetary systems. For the alignment mechanism of the disc, we intend to describe the process empirically from our simulation results rather than by means of rigorous mathematics as can be found in Papaloizou and Terquem (1995).

6.4.1 Alignment rate

The alignment process may be described partly in terms of the angular momentum transfer from the binary orbit into the disc. The indirect evidence of the transfer can be seen as changes in the binary orbital properties such as the semi-major axis (a) and eccentricity (e) shown in Figure 6.17. The resemblance between the changes in a (Figure 6.17) and δ (Figure 6.11) implies that these parameters are closely related. If we naively assume that the orbital angular momentum loss from the binary was fully transferred to the disc, we would have the alignment rate (from Equation 6.16)

$$\dot{\delta} = \frac{\tau_{\rm a}}{L_{\rm d}} = \frac{\dot{L}_{\rm b} \sin\delta}{L_{\rm d}}, \tag{6.24}$$

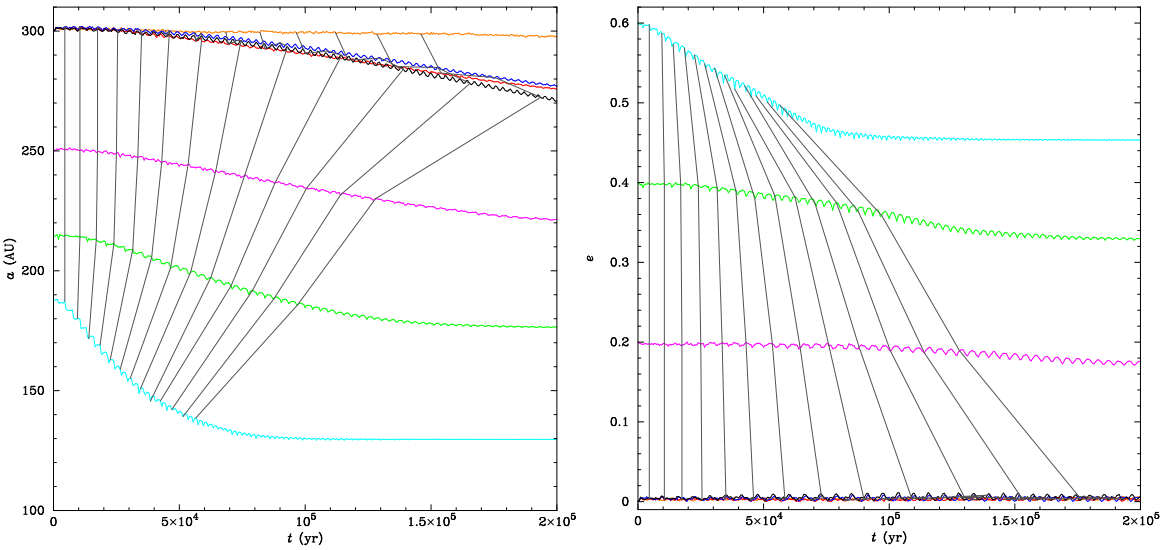

Figure 6.17 Plots showing the changes in semi-major axis (left) and eccentricity (right) of misaligned systems. The lines are of the systems `200ke0i225` (orange), `200ke6i450` (cyan), `200ke4i450` (green), `200ke2i450` (magenta), `200ke0i450` (red), `200ke0i675` (blue), and `200ke0i900` (black). The grey lines are the lines of equal resolution in steps of 10k particles.

where $\dot{L}_\mathrm{b}$ is the rate of change of the binary angular momentum (i.e. torque); the $\sin\delta$ term denotes the projection of the torque onto the x-axis. The orbital angular momentum can be written in terms of the moment of inertia I_b and angular speed ω_b of the orbit as

$$L_\mathrm{b} = I_\mathrm{b}\omega_\mathrm{b}. \tag{6.25}$$

We note that both L_b and $\dot{L}_\mathrm{b}$ belong to the binary centre of mass frame; however, for simplicity in calculation, the quantities are used as if they belonged to the disc's comoving frame. In the centre of mass frame, we have

$$I_\mathrm{b} = \mu r^2 = \frac{M_\mathrm{s}M_\mathrm{c}}{M_\mathrm{s}+M_\mathrm{c}}\left[\frac{a(1-e^2)}{1-e\cos\theta}\right]^2, \tag{6.26}$$

where μ is the reduced mass and r is the binary separation from Equation 6.10. By using $\omega_\mathrm{b} = \dot{\theta}$ from Equation 6.9, we have

$$\omega_\mathrm{b} = \frac{\sqrt{G(M_\mathrm{s}+M_\mathrm{c})}}{a^{3/2}}\frac{(1-e\cos\theta)^2}{(1-e^2)^{3/2}}. \tag{6.27}$$

Substituting I_b and ω_b into Equation 6.25 gives us

$$L_\mathrm{b} = M_\mathrm{s} M_\mathrm{c} \left[\frac{Ga(1-e^2)}{M_\mathrm{s}+M_\mathrm{c}}\right]^{1/2}. \tag{6.28}$$

The torque $\dot{L}_\mathrm{b}$ can be found from

$$\begin{aligned}\dot{L}_\mathrm{b} &= \frac{\partial L_\mathrm{b}}{\partial a}\dot{a} + \frac{\partial L_\mathrm{b}}{\partial e}\dot{e} + \frac{\partial L_\mathrm{b}}{\partial M_\mathrm{s}}\dot{M}_\mathrm{s} + \frac{\partial L_\mathrm{b}}{\partial M_\mathrm{c}}\dot{M}_\mathrm{c} \\ &= \frac{1}{2} M_\mathrm{s} M_\mathrm{c} \left[\frac{Ga(1-e^2)}{M_\mathrm{s}+M_\mathrm{c}}\right]^{1/2} \left[\frac{\dot{a}}{a} - \frac{2e\dot{e}}{1-e^2} + \frac{\dot{M}_\mathrm{s}}{M_\mathrm{s}} + \frac{\dot{M}_\mathrm{c}}{M_\mathrm{c}}\right].\end{aligned} \tag{6.29}$$

With the angular momentum of the disc (L_b) from Equation 6.14, the alignment rate (Equation 6.24) becomes

$$\dot{\delta} = \frac{5-2p}{8\pi\Sigma_\circ R_\circ^p} \left[\frac{M_\mathrm{s} M_\mathrm{c}^2}{M_\mathrm{s}+M_\mathrm{c}} \frac{a(1-e^2)}{R_\mathrm{d}^{5-2p}}\right]^{1/2} \left[\frac{\dot{a}}{a} - \frac{2e\dot{e}}{1-e^2} + \frac{\dot{M}_\mathrm{s}}{M_\mathrm{s}} + \frac{\dot{M}_\mathrm{c}}{M_\mathrm{c}}\right] \sin\delta. \tag{6.30}$$

The consistency of this equation may be verified by integration using Huen's method (the explicit trapezoidal rule):

$$\delta_k \simeq \delta_{k-1} + \frac{\Delta t}{2}(\dot{\delta}_k + \dot{\delta}_{k-1}) \tag{6.31}$$

where $\Delta t = 500$yr is the fixed time interval between snapshots and the index k starts from 1 (at $t = 500$yr) with δ_0 being the initial inclination of the system.

From the simulation results, (1) $\dot{a}$ is generally negative except for `200ke0i225`, (2) $\dot{e}$ may vary around zero in the case of circular orbits but is generally negative in the other cases, and (3) $\dot{M}_\mathrm{s}$ and $\dot{M}_\mathrm{c}$ are always positive. In most cases where the misalignment angle decreases, the alignment rate in Equation 6.30 is expected to be sufficiently negative in order to reproduce the curves that are similar to those from simulations. However, we find that this is not the case: the values vary between slightly negative to slightly positive, making most of the integrated curves flatter than the data curves from simulations. From investigation, we find that the $\dot{a}/a$ term in Equation 6.30 is rather smaller than it should be. Empirically, we also find that the integrated δ curves can be improved by multiplying the $\dot{a}/a$ term with a constant so that the RHS of Equation 6.30 can be more negative; here, we use $5\dot{a}/a$. Also, to obtain the reproduced curves, the radius R_d of the disc has to be assumed; the values are shown in Table 6.2. For a fixed value of initial inclination angle ($i_\mathrm{b} = 45°$), we find

Table 6.2 The assumed values of the disc radius $R_{\rm d}$ for each system. The values of $R_{\rm d}$ enclosed by square brackets tend to decrease exponentially with the eccentricity of the system.

System	$R_{\rm d}$(AU)
`200ke0i225`	120
`200ke0i450`	[180]
`200ke2i450`	[145]
`200ke4i450`	[120]
`200ke6i450`	[105]
`200ke0i675`	155
`200ke0i900`	170

that the value of $R_{\rm d}$ (enclosed by square brackets in the table) decreases roughly as an exponential function of the orbital eccentricity (e), suggesting that the effective radius scales with the size of the binary orbit. On the other hand, the value of $R_{\rm d}$ seems to have no particular relation with the initial inclination angle. Other assumed parameters in the calculations are, for all cases, the inner disc radius $R_\circ = 1$AU and the power-law index $p = 0$ (flat profile) for surface density. The value of $\Sigma_\circ$, for any time t, is taken from the disc's surface density at radius $R \simeq R_\circ = 1$AU. Lastly, those first derivative variables in Equation 6.30 are obtained from a simple approximation method: that is, for any variable x_k at timestep t_k, its first derivative is calculated from

$$\dot{x}_k = \frac{1}{2}\left(\frac{x_{k+1} - x_k}{t_{k+1} - t_k} + \frac{x_k - x_{k-1}}{t_k - t_{k-1}}\right) = \frac{x_{k+1} - x_{k-1}}{2\Delta t}, \tag{6.32}$$

where $\Delta t = t_k - t_{k-1} = 500$yr for any k. Note that the index k runs from $k = 1$ to $n - 1$, where n is the snapshot index starts from 0; and we assume that $\dot{x}_0 \simeq \dot{x}_1$ and $\dot{x}_n \simeq \dot{x}_{n-1}$ for the first and last snapshots, respectively. With all these, the reproduced values of δ can be plotted in Figure 6.18 (the grey curves).

That the $\dot{a}/a$ term in Equation 6.30 has to be modified to give better results simply tells us that our consideration is oversimplified. Nevertheless, this shows us that the missing torque(s) would in some way be proportional to the change in the semi-major axis ($\dot{a}$). This requires more investigation.

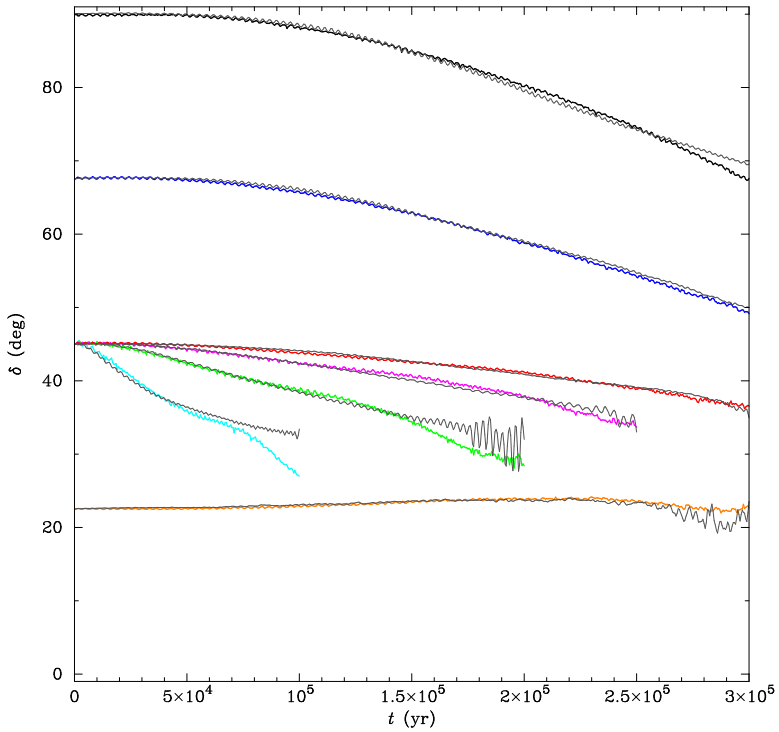

Figure 6.18 Plots showing the comparisons between the values of misalignment angle δ from the integration of Equation 6.30 (grey lines) and from the simulation results (coloured lines). Coloured lines represent the same systems as shown in Figure 6.11. Note that the system `200ke0i000` is not included.

6.4.2 Dispersal timescale of misaligned discs as a constraint for planet formation

Our simulation results suggest two key characteristics of discs in misaligned systems that might have some implication for the formation of planets in the discs. First, we find that it is unlikely for a disc to become aligned with the binary within the disc lifetime. One apparent factor is the $\sin\delta$ term in Equation 6.30, i.e. the misalignment rate becomes very small when δ approaches zero. Another factor is that there seems to be an anti-alignment process that prevents the system from becoming aligned. The existence of this process is suggested by the misalignment angle of the system `200ke0i225` (Figure 6.18) which slightly increases rather than decreases. Without further investigation in this work, we suggest that the anti-alignment mechanism could be related to an outward transfer of angular momentum caused by tidal interactions from the companion. It has been found that the inward propagation of acoustic waves generated by tidal perturbations can transfer angular momentum of the disc outwards (e.g. Larson 2002, and references therein). The transfer process is observed on the

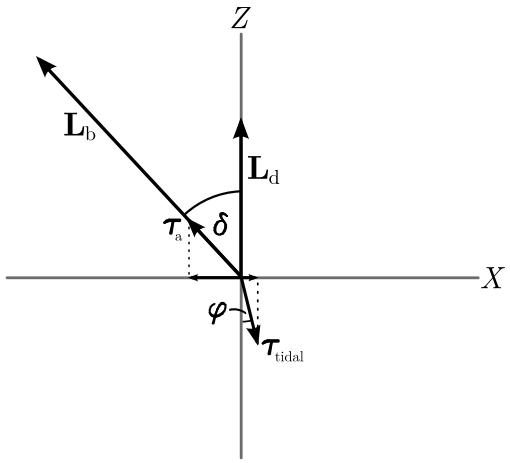

Figure 6.19 Diagram showing the offset direction of the tidal torque $\boldsymbol{\tau}_\mathrm{tidal}$ from the disc's angular momentum $\mathbf{L}_\mathrm{d}$ by an offset angle φ. The component of the tidal torque on the $+x$-axis, as oppose to that of the alignment torque $\boldsymbol{\tau}_\mathrm{a}$, would tend to bring the disc out of alignment.

disc with spiral patterns of density. In aligned systems, tidal torques responsible for redistributing angular momentum in the inner parts of the disc would have a direction opposite to that of the angular momentum $\mathbf{L}_\mathrm{d}$ of the disc. However, this may not necessarily be the case in misaligned systems since the disc material tend to be pulled out of the midplane by tidal forces from the companion. The offset in direction of the tidal torque ($\boldsymbol{\tau}_\mathrm{tidal}$) would have one of the components on the $+x$-axis, as illustrated in Figure 6.19. The component torque varies with the magnitude of $\boldsymbol{\tau}_\mathrm{tidal}$ and the offset angle φ, which are dependent on the misalignment angle δ. The magnitude of $\boldsymbol{\tau}_\mathrm{tidal}$ is expected to be largest in an aligned system and smallest in a perpendicularly misaligned system, while the offset angle φ would vary the opposite way round. It is likely that there is a critical value of misalignment angle (δ_c) where the component of the tidal torque on the $+x$-axis is a maximum, and it is around this critical angle that the alignment mechanism would find difficult to bring the disc through. From the plot of the system `200ke0i225` in Figure 6.18, the angle δ_c would be slightly higher than 22.5° for a misaligned circular system with orbital radius of 300AU. Of course, the value would be different in other systems with different disc properties and orbital configurations. In any case, the anti-alignment mechanism would slow down the alignment process, possibly resulting in the disc remaining significantly misaligned with the binary orbit throughout its lifetime. Therefore, planets that might form from a misaligned disc would have their orbital planes misaligned with respect to the orbital plane of the binary and often the rotational plane of the star they orbit.

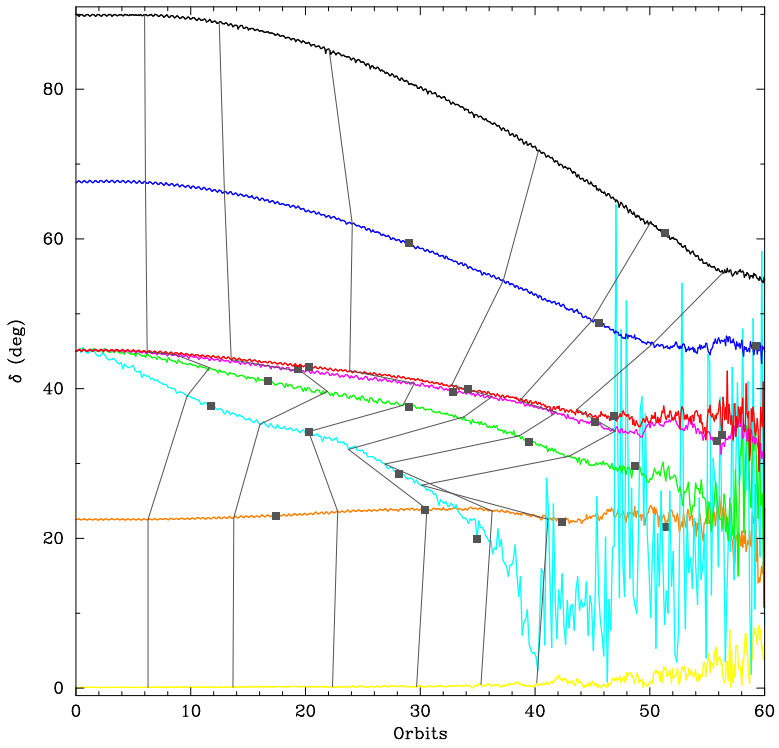

Figure 6.20 Plots of the misalignment angle δ against time in units of the initial orbital period (Orbits). The filled squares mark on the point where the precession angle is a multiple of $\pi/2$. The grey lines mark on the data curves where the disc mass within radius $R \leq 60$AU is reduced by a factor of two. Note that filled-square marks are omitted for the system `200ke0i000` as the precession of the disc is not significantly measurable.

Second, simulations suggest that most of the disc mass is dispersed within a timescale shorter than the precession period of the disc. Let us consider Figure 6.20 where the misalignment angle δ is plotted against time in units of the initial orbital period (labelled as 'Orbits' on the axis). The filled squares on each line mark on the point where the precession angle is a multiple of $\pi/2$, i.e. the first precession round is completed at the fourth mark. The grey lines mark on the data curves where the disc mass within radius $R \leq 60$AU is reduced by a factor of two, i.e. only $1/2^6$ original disc mass is left at time marked by the sixth line. This plot shows that, in all cases, only tiny amount of disc material is left by the end of the first precession round. In other words, the dispersal timescale is shorter than the precession period (a few times 10^5yr) which is rather short compared to the estimate lifetime of isolated T Tauri stars (a few times 10^6yr). This short lifetime might rule out the possibility of planet formation via the core accretion mechanism. Therefore, in misaligned binary systems, disc instabilities may be a major mode of planet formation.

If the dispersal timescale of the disc in any misaligned system is of order the precession period regardless of the variation in several parameters involved, the timescale may be defined as

$$t_{\rm disp} \sim \frac{2\pi}{\dot{\phi}}, \tag{6.33}$$

where $\dot{\phi}$ is the precession rate which may be considered as constant in systems where the initial inclination angle and eccentricity are not too high, for example, the systems `200ke0i225` and `200ke2i450` in Figure 6.15. By using Equation 6.15 for the precession rate $\dot{\phi}$ and using $R_{\rm d} = R_{\rm deff}$ given by Equation 6.23, one can find that

$$t_{\rm disp} \sim \frac{8}{3}\left(\frac{4-p}{5-2p}\right)\frac{\sqrt{M_{\rm s}}}{M_{\rm c}}\frac{\xi^{3/2}a^{3/2}}{\cos\delta}, \tag{6.34}$$

where the constant $\xi \sim 2.5$ and the gravitational constant $G = 4\pi^2$ when $M_\odot$, AU, and yr are used as the units of mass, length, and time, respectively. From this equation, the timescale depends on parameters which are measurable, though with some uncertainties. With more realistic considerations, the dispersal timescale would significantly depend on physical properties of the disc such as viscosity and temperature structure. Further analytical and numerical investigations are thus required in order to find out how significant these properties are to the dispersal timescale.

6.4.3 Formation of retrograde planetary systems

A significant number of retrograde planetary systems has been found over the last few years (e.g. Narita et al. 2009; Anderson et al. 2010; Bayliss et al. 2010; Triaud et al. 2010; Hébrard et al. 2011). These retrograde systems seem unable to be explained by the planet formation models described in Section 1.4, as it is rather unnatural for a circumstellar disc to rotate against the host star. So far, there are three formation scenarios to explain the retrograde systems: (a) close planet-planet interactions (e.g. Naoz et al. 2011), (b) flipping of the orbital plane by the Kozai mechanism in a star-planet-star (or star-planet-planet) triple system (e.g. Kozai 1962; Lithwick and Naoz 2011; Katz et al. 2011), and (c) resonance capture-and-release by an outer planet migrating inwards (Yu and Tremaine 2001). The orbit of the retrograde planet may then be circularized by tidal friction from the host star (e.g. Wu and Murray 2003; Fabrycky and Tremaine 2007). Note that all these scenarios are the dynamical evolution of a ready-formed planet with a third body.

In this work, we suggest that a retrograde planetary system could also be formed from a prograde circumstellar disc in a misaligned retrograde binary. From the results in Section 6.3.2 (see the right column of Figure 6.12), it is possible that the disc can be flipped as it tend to be aligned with the binary orbit. Planets that are formed from the disc would then have retrograde orbits relative to the spin direction of the host star. If the system has close encounters with other stars in the cluster, there is a chance that the binary disruption (see Section 6.1.4) would leave a retrograde planetary system with the host star. The effectiveness of this scenario may depend on several factors that need to be examined in future work.

6.5 Summary

We have performed simulations to investigate the evolution of a circumprimary disc in a binary star system. Various configurations between the disc and the binary components have been studied. In this work, we focus on the disc whose midplane is misaligned from the orbital plane of the binary. We have found that the disc precesses and, in most cases, is brought towards alignment with the binary orbit. This is in line with previous studies by several authors (e.g. Papaloizou and Terquem 1995). The essential results from our work can be summarized as follows.

(1) For the precession process, the effective radius of the disc can be roughly approximated by a linear function of the semi-latus rectum of the binary orbit (Equation 6.23), provided that the initial inclination angle of the orbit is not too high. The relation helps in simplifying the estimate dispersal timescale of the disc (Equation 6.34).

(2) We have derived the alignment rate from the assumption that the corresponding torque is directly related to the change in the orbital angular momentum of the binary. We have found that the derived alignment rate (Equation 6.30) can not reproduce the misalignment angles that fit the simulations. However, by adjusting the term associated with $\dot{a}$ in Equation 6.30, the equation is able to reproduce the misalignment angles that generally agree with the results in most cases. The modified expression may imply the complexity of the alignment mechanism. We aim to investigate this in future work.

(3) From our simulation results, we have found that: (a) a significantly misaligned system might not be able to reach an aligned configuration within the estimated

lifetime of the disc; (b) the dispersal timescale of a disc in a misaligned system could be of orders of the precession period of the disc. We then suggest that, in order to form planets out of a precessing misaligned disc, the formation mechanism has to occur rapidly within the first precession round. Also, it is likely that the orbits of the resulting planets are still misaligned with respect to the orbital plane of the binary and the rotational plane of the star.

(4) We have suggested that a spin-orbit misaligned planetary system could also form from a disc in a misaligned binary system which is later disrupted by a close encounter with other star in the cluster. We have also suggested that this mechanism might be able to form a retrograde planetary system from a misaligned retrograde binary.

To verify the validity of these findings, more analytical and numerical works are required. We discuss our future work in Chapter 7.

Chapter 7

Conclusion

7.1 Main conclusions

We have performed both N-body and SPH simulations to study the dynamics of stars and discs in multiple systems. We have found several interesting features that may be useful for understanding the formation of stars and planets.

7.1.1 Dynamical evolution of young triple systems

In Chapter 4, we have performed N-body simulations to investigate the dynamical evolution of young triple systems. We have found that a collision between the two companions is not uncommon, especially in a compact, coplanar system with equal-mass companions. The chance of companion-companion collisions increases with the radii of the companions. The chance of a collision between one of the companions and the primary star is also non-negligible, especially in a system with a low companion mass ratio.

Those results support our idea that collisions may occasionally play a significant role in the early stages of multiple star formation. From the dramatic nature of collisions, we have suggested that collisions may be an explanation for the age discrepancy in some young multiple star systems with infrared companion(s). That an infrared companion appears younger than other components in the same system may be due to its different accretion history that has been interrupted by collisions in the earlier stages.

In addition, we have also found that the separation distribution of close encounters can be described by the Lévy cumulative distribution function. This finding reveals to us a significantly high chance of head-on collisions.

7.1.2 Stable circumstellar discs

We have studied several properties of low-mass (protoplanetary) discs via SPH simulations in Chapter 5. The main investigations are on the influence of resolution, temperature structure, and artificial viscosity that are used in the simulations. We have found that our low-mass discs are all long-term stable against gravitational instabilities, even in low-resolution simulations where numerical effects could lead to an artificial instabilities. The major factors that make those discs stable are the mass and temperature structure of the discs.

The artificial viscosity affects the mass accretion rate of the central sink. We have found an interesting relation between the mass accretion rate and the viscosity parameter α. We have given an explanation to the relation in terms of the flows of disc particles from various sources. We have also observed and given an explaination to a numerical effect caused by very high viscosity, i.e. the stratification of disc particles. Using the Balsara viscosity switch can remove this effect.

7.1.3 Circumstellar discs in misaligned binary systems

In Chapter 6, we have performed SPH simulations to investigate the evolution of a circumprimary disc in a misaligned binary system. We have found that the disc precesses and, in most cases, is brought towards alignment with the binary orbit, in line with previous studies by several authors.

From analysing the precession process, we have found that the effective radius of a disc is roughly a linear function of the semi-latus rectum of the binary orbit. This relation is useful for estimating the precession rate of a disc.

We have described the alignment mechanism semi-analytically in terms of ideally efficient transfer of angular momentum in the system. Although our assumption of the transfer process is oversimplified, it shows us the aspect of the relevant torque which is mainly related to the rate of change of the orbital semi-major axis.

Simulation results also have suggested that (a) the alignment timescale of a disc may be longer than the disc lifetime and (b) the dispersal timescale of a disc in a misaligned system could be of order the precession period of the disc. These findings could be constraints for planet formation in misaligned systems.

Finally, we have suggested that a spin-orbit misaligned planetary system could also form from a disc in a misaligned binary system which is later disrupted by dynamical interactions with other star in the cluster. This mechanism might also be able to create a misaligned retrograde planetary system if the misaligned binary is retrograde.

7.2 Future work

Our future work will focus on further investigation of misaligned binary systems. The possible work may be listed as follows.

(1) We aim to perform a new set of simulations with higher resolution, i.e. $\geq 3\times10^5$ particles. This is to find out the influence of numerical effects on the disc's dispersal timescales which is found to be rather short (less than one precession period) in this work.

(2) We will investigate the effect of viscosity and temperature structure on both precession and alignment mechanisms. Simulations will be performed with other values of viscosity parameter α and temperature profile parameters q and $T_\circ$.

(3) We aim to investigate how the disc tilting mechanism would affect planet formation in the disc.

(4) We aim to investigate the possibility and effectiveness of the formation scenario for retrograde planetary systems suggested in Chapter 6.

(5) We aim to examine other remaining features of misaligned systems that have not been done in this work, for example, the properties of the secondary disc formed around the companion.

(6) We may also explore other more realistic and complicated configurations of misaligned systems such as a misaligned binary with discs on both components.

Bibliography

Aarseth, S. J., Lin, D. N. C., Palmer, P. L., 1993. *'Evolution of Planetesimals. II. Numerical Simulations'*. ApJ 403, 351.

Adams, F. C., Lada, C. J., Shu, F. H., 1987. *'Spectral evolution of young stellar objects'*. ApJ 312, 788–806.

Agertz, O., et al., 2007. *'Fundamental differences between SPH and grid methods'*. MNRAS 380, 963–978.

Albrecht, S., Winn, J. N., Butler, R. P., Crane, J. D., Shectman, S. A., Thompson, I. B., Hirano, T., Wittenmyer, R. A., 2012. *'A High Stellar Obliquity in the WASP-7 Exoplanetary System'*. ApJ 744, 189.

Alexander, R., 2008. *'From discs to planetesimals: Evolution of gas and dust discs'*. NewAR 52, 60–77.

Alexander, R. D., Clarke, C. J., Pringle, J. E., 2006a. *'Photoevaporation of protoplanetary discs - I. Hydrodynamic models'*. MNRAS 369, 216–228.

Alexander, R. D., Clarke, C. J., Pringle, J. E., 2006b. *'Photoevaporation of protoplanetary discs - II. Evolutionary models and observable properties'*. MNRAS 369, 229–239.

Anderson, D. R., et al., 2010. *'Wasp-17b: An Ultra-Low Density Planet in a Probable Retrograde Orbit'*. ApJ 709, 159–167.

André, P., et al., 2010. *'From filamentary clouds to prestellar cores to the stellar IMF: Initial highlights from the Herschel Gould Belt Survey'*. A&A 518, L102.

Andre, P., Ward-Thompson, D., Barsony, M., 1993. *'Submillimeter continuum observations of Rho Ophiuchi A - The candidate protostar VLA 1623 and prestellar clumps'*. ApJ 406, 122–141.

Andrews, S. M., Williams, J. P., 2005. *'Circumstellar Dust Disks in Taurus-Auriga: The Submillimeter Perspective'*. ApJ 631, 1134–1160.

Andrews, S. M., Williams, J. P., 2007. *'High-Resolution Submillimeter Constraints on Circumstellar Disk Structure'*. ApJ 659, 705–728.

Anosova, J. P., 1986. *'Dynamical evolution of triple systems'.* Ap&SS 124, 217–241.

Armitage, P. J., 2009. *'Planet Formation'.* In: Roig, F., Lopes, D., de La Reza, R., Ortega, V. (Eds.), American Institute of Physics Conference Series, Volume 1192 of *American Institute of Physics Conference Series*, pp. 3–42.

Attwood, R. E., Goodwin, S. P., Stamatellos, D., Whitworth, A. P., 2009. *'Simulating star formation in molecular cloud cores. IV. The role of turbulence and thermodynamics'.* A&A 495, 201–215.

Ballesteros-Paredes, J., Klessen, R. S., Mac Low, M.-M., Vazquez-Semadeni, E., 2007. *'Molecular Cloud Turbulence and Star Formation'.* Protostars and Planets V, 63–80.

Bally, J., O'Dell, C. R., McCaughrean, M. J., 2000. *'Disks, Microjets, Windblown Bubbles, and Outflows in the Orion Nebula'.* AJ 119, 2919–2959.

Bally, J., Sutherland, R. S., Devine, D., Johnstone, D., 1998. *'Externally Illuminated Young Stellar Environments in the Orion Nebula: Hubble Space Telescope Planetary Camera and Ultraviolet Observations'.* AJ 116, 293–321.

Balsara, D. S., 1995. *'von Neumann stability analysis of smooth particle hydrodynamics–suggestions for optimal algorithms'.* Journal of Computational Physics 121, 357–372.

Baraffe, I., Chabrier, G., Gallardo, J., 2009. *'Episodic Accretion at Early Stages of Evolution of Low-Mass Stars and Brown Dwarfs: A Solution for the Observed Luminosity Spread in H-R Diagrams?'* ApJL 702, L27–L31.

Barnes, J., Hut, P., 1986. *'A hierarchical O(N log N) force-calculation algorithm'.* Natur 324, 446–449.

Barsony, M., Koresko, C., Matthews, K., 2003. *'A Search for Close Binaries in the ρ Ophiuchi Star-forming Region'.* ApJ 591, 1064–1074.

Bate, M. R., 1998. *'Collapse of a Molecular Cloud Core to Stellar Densities: The First Three-dimensional Calculations'.* ApJL 508, L95–L98.

Bate, M. R., 2010. *'Collapse of a molecular cloud core to stellar densities: the radiative impact of stellar core formation on the circumstellar disc'.* MNRAS 404, L79–L83.

Bate, M. R., 2011. *'Collapse of a molecular cloud core to stellar densities: the formation and evolution of pre-stellar discs'.* MNRAS, 1310–+.

Bate, M. R., Bonnell, I. A., Bromm, V., 2002a. *'The formation mechanism of brown dwarfs'.* MNRAS 332, L65–L68.

Bate, M. R., Bonnell, I. A., Bromm, V., 2002b. *'The formation of close binary systems by dynamical interactions and orbital decay'.* MNRAS 336, 705–713.

Bate, M. R., Bonnell, I. A., Bromm, V., 2003. *'The formation of a star cluster: predicting the properties of stars and brown dwarfs'*. MNRAS 339, 577–599.

Bate, M. R., Bonnell, I. A., Clarke, C. J., Lubow, S. H., Ogilvie, G. I., Pringle, J. E., Tout, C. A., 2000. *'Observational implications of precessing protostellar discs and jets'*. MNRAS 317, 773–781.

Bate, M. R., Bonnell, I. A., Price, N. M., 1995. *'Modelling accretion in protobinary systems'*. MNRAS 277, 362–376.

Bate, M. R., Burkert, A., 1997. *'Resolution requirements for smoothed particle hydrodynamics calculations with self-gravity'*. MNRAS 288, 1060–1072.

Bayliss, D. D. R., Winn, J. N., Mardling, R. A., Sackett, P. D., 2010. *'Confirmation of a Retrograde Orbit for Exoplanet WASP-17b'*. ApJL 722, L224–L227.

Beckwith, S. V. W., Sargent, A. I., Chini, R. S., Guesten, R., 1990. *'A survey for circumstellar disks around young stellar objects'*. AJ 99, 924–945.

Benson, P. J., Myers, P. C., 1989. *'A survey for dense cores in dark clouds'*. ApJS 71, 89–108.

Benz, W., 1990. *'Smooth Particle Hydrodynamics - a Review'*. In: J. R. Buchler (Ed.), Numerical Modelling of Nonlinear Stellar Pulsations Problems and Prospects, pp. 269–+.

Bergfors, C., et al., 2010. *'Lucky Imaging survey for southern M dwarf binaries'*. A&A 520, A54.

Bertout, C., Basri, G., Bouvier, J., 1988. *'Accretion disks around T Tauri stars'*. ApJ 330, 350–373.

Bhattal, A. S., Francis, N., Watkins, S. J., Whitworth, A. P., 1998. *'Dynamically triggered star formation in giant molecular clouds'*. MNRAS 297, 435–448.

Binney, J., Tremaine, S., 2008. *'Galactic Dynamics: Second Edition'*. Princeton University Press.

Boffin, H. M. J., Watkins, S. J., Bhattal, A. S., Francis, N., Whitworth, A. P., 1998. *'Numerical simulations of protostellar encounters - I. Star-disc encounters'*. MNRAS 300, 1189–1204.

Boley, A. C., 2009. *'The Two Modes of Gas Giant Planet Formation'*. ApJL 695, L53–L57.

Boley, A. C., Durisen, R. H., Nordlund, Å., Lord, J., 2007. *'Three-Dimensional Radiative Hydrodynamics for Disk Stability Simulations: A Proposed Testing Standard and New Results'*. ApJ 665, 1254–1267.

Boley, A. C., Mejía, A. C., Durisen, R. H., Cai, K., Pickett, M. K., D'Alessio, P., 2006. *'The Thermal Regulation of Gravitational Instabilities in Protoplanetary Disks. III. Simulations with Radiative Cooling and Realistic Opacities'*. ApJ 651, 517–534.

Bonnell, I., Arcoragi, J.-P., Martel, H., Bastien, P., 1992. *'Fragmentation of elongated cylindrical clouds. IV - Clouds with solid-body rotation about an arbitrary axis'*. ApJ 400, 579–594.

Bonnell, I., Bastien, P., 1992. *'A binary origin for FU Orionis stars'*. ApJL 401, L31–L34.

Bonnell, I. A., 1994. *'A New Binary Formation Mechanism'*. MNRAS 269, 837–848.

Bonnell, I. A., Bate, M. R., 1994. *'Massive Circumbinary Discs and the Formation of Multiple Systems'*. MNRAS 269, L45–L48.

Bontemps, S., Andre, P., Terebey, S., Cabrit, S., 1996. *'Evolution of outflow activity around low-mass embedded young stellar objects'*. A&A 311, 858–872.

Boss, A. P., 1997. *'Giant planet formation by gravitational instability.'* Science 276, 1836–1839.

Boss, A. P., 2000. *'Possible Rapid Gas Giant Planet Formation in the Solar Nebula and Other Protoplanetary Disks'*. ApJL 536, L101–L104.

Boss, A. P., 2004. *'Convective Cooling of Protoplanetary Disks and Rapid Giant Planet Formation'*. ApJ 610, 456–463.

Boss, A. P., Myhill, E. A., 1995. *'Collapse and Fragmentation of Molecular Cloud Cores. III. Initial Differential Rotation'*. ApJ 451, 218.

Bradie, B., 2006. *'A Friendly Introduction to Numerical Analysis'*. Pearson Education, Inc.

Butler, R. P., Marcy, G. W., Williams, E., Hauser, H., Shirts, P., 1997. *'Three New "51 Pegasi–Type" Planets'*. ApJL 474, L115.

Caillault, J., Patterson, J., 1990. *'On the mass-radius relation of late M dwarfs'*. AJ 100, 825–829.

Calvet, N., Magris, G. C., Patino, A., D'Alessio, P., 1992. *'Irradiation of Accretion Disks around Young Objects. II. Continuum Energy Distribution'*. RevMexAA 24, 27.

Calvet, N., Muzerolle, J., Briceño, C., Hernández, J., Hartmann, L., Saucedo, J. L., Gordon, K. D., 2004. *'The Mass Accretion Rates of Intermediate-Mass T Tauri Stars'*. AJ 128, 1294–1318.

Cameron, A. G. W., 1978. *'Physics of the primitive solar accretion disk'*. Moon and Planets 18, 5–40.

Cesaroni, R., Galli, D., Lodato, G., Walmsley, C. M., Zhang, Q., 2007. *'Disks Around Young O-B (Proto)Stars: Observations and Theory'*. Protostars and Planets V, 197–212.

Cha, S.-H., Whitworth, A. P., 2003. *'The formation and fragmentation of the ring appearing in the collapse of a rotating cloud'*. MNRAS 340, 91–104.

Chiang, E. I., Goldreich, P., 1997. *'Spectral Energy Distributions of T Tauri Stars with Passive Circumstellar Disks'*. ApJ 490, 368.

Clarke, C., 1992. *'Star-Disc Interactions and Binary Formation'*. In: H. A. McAlister & W. I. Hartkopf (Ed.), IAU Colloq. 135: Complementary Approaches to Double and Multiple Star Research, Volume 32 of *Astronomical Society of the Pacific Conference Series*, pp. 176.

Clarke, C., Lodato, G., Melnikov, S. Y., Ibrahimov, M. A., 2005. *'The photometric evolution of FU Orionis objects: disc instability and wind-envelope interaction'*. MNRAS 361, 942–954.

Clarke, C. J., Gendrin, A., Sotomayor, M., 2001. *'The dispersal of circumstellar discs: the role of the ultraviolet switch'*. MNRAS 328, 485–491.

Clarke, C. J., Pringle, J. E., 1991. *'Star-disc interactions and binary star formation'*. MNRAS 249, 584–587.

Cossins, P. J., 2010. *'Smoothed Particle Hydrodynamics'*. ArXiv e-prints.

Daemgen, S., Hormuth, F., Brandner, W., Bergfors, C., Janson, M., Hippler, S., Henning, T., 2009. *'Binarity of transit host stars. Implications for planetary parameters'*. A&A 498, 567–574.

D'Angelo, G., Durisen, R. H., Lissauer, J. J., 2010. *'Giant Planet Formation'*, pp. 319–346.

Davis, C. J., Eisloeffel, J., Ray, T. P., Jenness, T., 1997. *'Prompt entrainment in the variable molecular jet from RNO 15-FIR.'* A&A 324, 1013–1019.

Davis, C. J., Mundt, R., Eisloeffel, J., 1994. *'Near-infrared imaging of the jets and flows associated with Herbig-Haro objects HH 91, HH 110, and HH 111'*. ApJL 437, L55–L58.

Delgado-Donate, E. J., Clarke, C. J., Bate, M. R., 2004. *'The dependence of the substellar initial mass function on the initial conditions for star formation'*. MNRAS 347, 759–770.

Desidera, S., et al., 2011. *'A giant planet in the triple system HD 132563'*. A&A 533, A90.

Dominik, C., Blum, J., Cuzzi, J. N., Wurm, G., 2007. *'Growth of Dust as the Initial Step Toward Planet Formation'*. Protostars and Planets V, 783–800.

Duchêne, G., Bouvier, J., Bontemps, S., André, P., Motte, F., 2004. *'Multiple protostellar systems. I. A deep near infrared survey of Taurus and Ophiuchus protostellar objects'*. A&A 427, 651–665.

Duchêne, G., Bouvier, J., Simon, T., 1999. *'Low-mass binaries in the young cluster IC 348: implications for binary formation and evolution'*. A&A 343, 831–840.

Duchêne, G., Ghez, A., McCabe, C., 2003. *'Non coeval young multiple systems? On the pairing of protostars and T Tauri stars'*. Astrophysics and Space Science Library 299, 223–+.

Duquennoy, A., Mayor, M., 1991. *'Multiplicity among solar-type stars in the solar neighbourhood. II - Distribution of the orbital elements in an unbiased sample'*. A&A 248, 485–524.

Durisen, R. H., Boss, A. P., Mayer, L., Nelson, A. F., Quinn, T., Rice, W. K. M., 2007. *'Gravitational Instabilities in Gaseous Protoplanetary Disks and Implications for Giant Planet Formation'*. Protostars and Planets V, 607–622.

Durisen, R. H., Gingold, R. A., Tohline, J. E., Boss, A. P., 1986. *'Dynamic fission instabilities in rapidly rotating N = 3/2 polytropes - A comparison of results from finite-difference and smoothed particle hydrodynamics codes'*. ApJ 305, 281–308.

Dutrey, A., Guilloteau, S., Duvert, G., Prato, L., Simon, M., Schuster, K., Menard, F., 1996. *'Dust and gas distribution around T Tauri stars in Taurus-Auriga. I. Interferometric 2.7mm continuum and ˆ13ˆCO J=1-0 observations'*. A&A 309, 493–504.

Eisloffel, J., Mundt, R., 1997. *'Parsec-Scale Jets From Young Stars'*. AJ 114, 280–287.

Eisloffel, J., Smith, M. D., Davis, C. J., Ray, T. P., 1996. *'Molecular Hydrogen in the Outflow From CEP E'*. AJ 112, 2086.

Eisner, J. A., Carpenter, J. M., 2006. *'Massive Protoplanetary Disks in the Trapezium Region'*. ApJ 641, 1162–1171.

Eisner, J. A., Hillenbrand, L. A., Carpenter, J. M., Wolf, S., 2005. *'Constraining the Evolutionary Stage of Class I Protostars: Multiwavelength Observations and Modeling'*. ApJ 635, 396–421.

Eisner, J. A., Plambeck, R. L., Carpenter, J. M., Corder, S. A., Qi, C., Wilner, D., 2008. *'Proplyds and Massive Disks in the Orion Nebula Cluster Imaged with CARMA and SMA'*. ApJ 683, 304–320.

Elmegreen, B. G., 2000. *'Star Formation in a Crossing Time'*. ApJ 530, 277–281.

Enoch, M. L., Corder, S., Dunham, M. M., Duchêne, G., 2009. *'Disk and Envelope Structure in Class 0 Protostars. I. The Resolved Massive Disk in Serpens Firs 1'*. ApJ 707, 103–113.

Evans, N. J., II, 1999. *'Physical Conditions in Regions of Star Formation'*. ARA&A 37, 311–362.

Evans, N. J., II, et al., 2009. *'The Spitzer c2d Legacy Results: Star-Formation Rates and Efficiencies; Evolution and Lifetimes'*. ApJS 181, 321–350.

Fabrycky, D., Tremaine, S., 2007. *'Shrinking Binary and Planetary Orbits by Kozai Cycles with Tidal Friction'*. ApJ 669, 1298–1315.

Fischer, D. A., Marcy, G. W., 1992. *'Multiplicity among M dwarfs'*. ApJ 396, 178–194.

Forgan, D., Rice, K., 2009. *'Stellar encounters: a stimulus for disc fragmentation?'* MNRAS 400, 2022–2031.

Forgan, D., Rice, K., Cossins, P., Lodato, G., 2011. *'The nature of angular momentum transport in radiative self-gravitating protostellar discs'*. MNRAS 410, 994–1006.

Fukagawa, M., et al., 2004. *'Spiral Structure in the Circumstellar Disk around AB Aurigae'*. ApJL 605, L53–L56.

Fuller, G. A., Williams, S. J., Sridharan, T. K., 2005. *'The circumstellar environment of high mass protostellar objects. III. Evidence of infall?'* A&A 442, 949–959.

Gammie, C. F., 2001. *'Nonlinear Outcome of Gravitational Instability in Cooling, Gaseous Disks'*. ApJ 553, 174–183.

Gingold, R. A., Monaghan, J. J., 1977. *'Smoothed particle hydrodynamics - Theory and application to non-spherical stars'*. MNRAS 181, 375–389.

Gingold, R. A., Monaghan, J. J., 1982. *'Kernel estimates as a basis for general particle methods in hydrodynamics'*. Journal of Computational Physics 46, 429–453.

Goodwin, S. P., 2010. *'Binaries in star clusters and the origin of the field stellar population'*. Royal Society of London Philosophical Transactions Series A 368, 851–866.

Goodwin, S. P., Kroupa, P., 2005. *'Limits on the primordial stellar multiplicity'*. A&A 439, 565–569.

Goodwin, S. P., Kroupa, P., Goodman, A., Burkert, A., 2007. *'The Fragmentation of Cores and the Initial Binary Population'*. Protostars and Planets V, 133–147.

Goodwin, S. P., Whitworth, A. P., Ward-Thompson, D., 2004a. *'Simulating star formation in molecular cloud cores. I. The influence of low levels of turbulence on fragmentation and multiplicity'*. A&A 414, 633–650.

Goodwin, S. P., Whitworth, A. P., Ward-Thompson, D., 2004b. *'Simulating star formation in molecular cores. II. The effects of different levels of turbulence'*. A&A 423, 169–182.

Goodwin, S. P., Whitworth, A. P., Ward-Thompson, D., 2006. *'Star formation in molecular cores. III. The effect of the turbulent power spectrum'*. A&A 452, 487–492.

Greene, T. P., Wilking, B. A., Andre, P., Young, E. T., Lada, C. J., 1994. *'Further mid-infrared study of the rho Ophiuchi cloud young stellar population: Luminosities and masses of pre-main-sequence stars'*. ApJ 434, 614–626.

Gregersen, E. M., Evans, N. J., II, 2000. *'How to Identify Pre-Protostellar Cores'*. ApJ 538, 260–267.

Gullbring, E., Hartmann, L., Briceno, C., Calvet, N., 1998. *'Disk Accretion Rates for T Tauri Stars'*. ApJ 492, 323–341.

Haisch, K. E., Jr., Lada, E. A., Lada, C. J., 2001. *'Disk Frequencies and Lifetimes in Young Clusters'*. ApJL 553, L153–L156.

Hartigan, P., Kenyon, S. J., 2003. *'A Spectroscopic Survey of Subarcsecond Binaries in the Taurus-Auriga Dark Cloud with the Hubble Space Telescope'*. ApJ 583, 334–357.

Hartigan, P., Strom, K. M., Strom, S. E., 1994. *'Are wide pre-main-sequence binaries coeval?'* ApJ 427, 961–977.

Hartmann, L., 2009. *'Accretion Processes in Star Formation: Second Edition'*. Cambridge University Press.

Hartmann, L., Calvet, N., Gullbring, E., D'Alessio, P., 1998. *'Accretion and the Evolutiion of T Tauri Disks'*. ApJ 495, 385–400.

Hartmann, L., D'Alessio, P., Calvet, N., Muzerolle, J., 2006. *'Why Do T Tauri Disks Accrete?'* ApJ 648, 484–490.

Hartmann, L., Megeath, S. T., Allen, L., Luhman, K., Calvet, N., D'Alessio, P., Franco-Hernandez, R., Fazio, G., 2005. *'IRAC Observations of Taurus Pre-Main-Sequence Stars'*. ApJ 629, 881–896.

Hayashi, C., 1961. *'Stellar evolution in early phases of gravitational contraction.'* PASJ 13, 450–452.

Hayashi, C., 1966. *'Evolution of Protostars'*. ARA&A 4, 171.

Hayashi, C., Nakazawa, K., Nakagawa, Y., 1985. *'Formation of the solar system'*. In: Black, D. C., Matthews, M. S. (Eds.), Protostars and planets II (A86-12626 03-90). Tucson, AZ, University of Arizona Press, 1985, p. 1100-1153., pp. 1100–1153.

Hébrard, G., et al., 2011. *'The retrograde orbit of the HAT-P-6b exoplanet'*. A&A 527, L11.

Heemskerk, M. H. M., Papaloizou, J. C., Savonije, G. J., 1992. *'Non-linear development of M = 1 instabilities in a self-gravitating gaseous disc'*. A&A 260, 161–174.

Heggie, D. C., 1975. *'Binary evolution in stellar dynamics'*. MNRAS 173, 729–787.

Heller, C. H., 1995. *'Encounters with Protostellar Disks. II. Disruption and Binary Formation'*. ApJ 455, 252.

Hennebelle, P., Chabrier, G., 2008. *'Analytical Theory for the Initial Mass Function: CO Clumps and Prestellar Cores'*. ApJ 684, 395–410.

Hennebelle, P., Fromang, S., 2008. *'Magnetic processes in a collapsing dense core. I. Accretion and ejection'*. A&A 477, 9–24.

Henning, T., Pfau, W., Zinnecker, H., Prusti, T., 1993. *'A 1.3-MILLIMETER Survey of Circumstellar Dust around Young Chamaeleon Objects'*. A&A 276, 129.

Henyey, L. G., Lelevier, R., Levée, R. D., 1955. *'The Early Phases of Stellar Evolution'*. PASP 67, 154.

Hernquist, L., 1987. *'Performance characteristics of tree codes'*. ApJS 64, 715–734.

Hernquist, L., 1993. *'Some cautionary remarks about smoothed particle hydrodynamics'*. ApJ 404, 717–722.

Hernquist, L., Katz, N., 1989. *'TREESPH - A unification of SPH with the hierarchical tree method'*. ApJS 70, 419–446.

Hildebrand, R. H., 1983. *'The Determination of Cloud Masses and Dust Characteristics from Submillimetre Thermal Emission'*. QJRAS 24, 267.

Hillenbrand, L. A., 1997. *'On the Stellar Population and Star-Forming History of the Orion Nebula Cluster'*. AJ 113, 1733–1768.

Hillenbrand, L. A., Strom, S. E., Calvet, N., Merrill, K. M., Gatley, I., Makidon, R. B., Meyer, M. R., Skrutskie, M. F., 1998. *'Circumstellar Disks in the Orion Nebula Cluster'*. AJ 116, 1816–1841.

Hills, J. G., 1975. *'Encounters between binary and single stars and their effect on the dynamical evolution of stellar systems'*. AJ 80, 809–825.

Hubber, D. A., Batty, C. P., McLeod, A., Whitworth, A. P., 2011. *'SEREN - a new SPH code for star and planet formation simulations. Algorithms and tests'*. A&A 529, A27+.

Hubber, D. A., Falle, S. A. E. G., Goodwin, S. P., 2011. *'Convergence of SPH and AMR simulations'*. In: J. Alves, B. G. Elmegreen, J. M. Girart, & V. Trimble (Ed.), Computational Star Formation, Volume 270 of *IAU Symposium*, pp. 429–432.

Hubickyj, O., Bodenheimer, P., Lissauer, J. J., 2005. *'Accretion of the gaseous envelope of Jupiter around a 5 10 Earth-mass core'*. Icarus 179, 415–431.

Iben, I., Jr., 1965. *'Stellar Evolution. I. The Approach to the Main Sequence.'* ApJ 141, 993.

Jayawardhana, R., Hartmann, L., Fazio, G., Fisher, R. S., Telesco, C. M., Piña, R. K., 1999. *'A Disk Census for the Nearest Group of Young Stars: Mid-Infrared Observations of the TW Hydrae Association'*. ApJL 521, L129–L132.

Jeffries, R. D., Littlefair, S. P., Naylor, T., Mayne, N. J., 2011. *'No wide spread of stellar ages in the Orion Nebula Cluster'*. MNRAS 418, 1948–1958.

Jensen, E. L. N., Mathieu, R. D., Donar, A. X., Dullighan, A., 2004. *'Testing Protoplanetary Disk Alignment in Young Binaries'*. ApJ 600, 789–803.

Johnson, J. A., et al., 2011. *'HAT-P-30b: A Transiting Hot Jupiter on a Highly Oblique Orbit'*. ApJ 735, 24.

Kalas, P., Graham, J. R., Chiang, E., Fitzgerald, M. P., Clampin, M., Kite, E. S., Stapelfeldt, K., Marois, C., Krist, J., 2008. *'Optical Images of an Exosolar Planet 25 Light-Years from Earth'*. Science 322, 1345–.

Kang, M., Choi, M., Ho, P. T. P., Lee, Y., 2008. *'Millimeter Imaging of HH 24 MMS: A Misaligned Protobinary System'*. ApJ 683, 267–271.

Katz, B., Dong, S., Malhotra, R., 2011. *'Long-Term Cycling of Kozai-Lidov Cycles: Extreme Eccentricities and Inclinations Excited by a Distant Eccentric Perturber'*. Physical Review Letters 107 (18), 181101.

Katz, J. I., Anderson, S. F., Grandi, S. A., Margon, B., 1982. *'Nodding motions of accretion rings and disks - A short-term period in SS 433'*. ApJ 260, 780–793.

Kenyon, S. J., Hartmann, L., 1987. *'Spectral energy distributions of T Tauri stars - Disk flaring and limits on accretion'*. ApJ 323, 714–733.

Keto, E., Wood, K., 2006. *'Observations on the Formation of Massive Stars by Accretion'*. ApJ 637, 850–859.

King, R. R., Parker, R. J., Patience, J., Goodwin, S. P., 2012. *'Testing the universality of star formation - I. Multiplicity in nearby star-forming regions'*. MNRAS 421, 2025–2042.

Kitamura, Y., Momose, M., Yokogawa, S., Kawabe, R., Tamura, M., Ida, S., 2002. *'Investigation of the Physical Properties of Protoplanetary Disks around T Tauri Stars by a 1 Arcsecond Imaging Survey: Evolution and Diversity of the Disks in Their Accretion Stage'*. ApJ 581, 357–380.

Kitsionas, S., Whitworth, A. P., 2007. *'High-resolution simulations of clump-clump collisions using SPH with particle splitting'*. MNRAS 378, 507–524.

Köhler, R., Leinert, C., 1998. *'Multiplicity of T Tauri stars in Taurus after ROSAT'*. A&A 331, 977–988.

Köhler, R., Petr-Gotzens, M. G., McCaughrean, M. J., Bouvier, J., Duchêne, G., Quirrenbach, A., Zinnecker, H., 2006. *'Binary stars in the Orion Nebula Cluster'*. A&A 458, 461–476.

Kokubo, E., Ida, S., 1996. *'On Runaway Growth of Planetesimals'*. Icarus 123, 180–191.

Königl, A., 1991. *'Disk accretion onto magnetic T Tauri stars'*. ApJL 370, L39–L43.

Konopacky, Q. M., Ghez, A. M., Rice, E. L., Duchêne, G., 2007. *'New Very Low Mass Binaries in the Taurus Star-forming Region'*. ApJ 663, 394–399.

Könyves, V., et al., 2010. *'The Aquila prestellar core population revealed by Herschel'*. A&A 518, L106.

Koresko, C. D., 1998. *'A Circumstellar Disk in a Pre-main-sequence Binary Star'*. ApJL 507, L145–L148.

Koresko, C. D., Herbst, T. M., Leinert, C., 1997. *'The Infrared Companions of T Tauri Stars'*. ApJ 480, 741–753.

Kozai, Y., 1962. *'Secular perturbations of asteroids with high inclination and eccentricity'*. AJ 67, 591.

Kraus, A. L., Hillenbrand, L. A., 2009. *'The Coevality of Young Binary Systems'*. ApJ 704, 531–547.

Kraus, A. L., Ireland, M. J., Martinache, F., Hillenbrand, L. A., 2011. *'Mapping the Shores of the Brown Dwarf Desert. II. Multiple Star Formation in Taurus-Auriga'*. ApJ 731, 8.

Kroupa, P., Burkert, A., 2001. *'On the Origin of the Distribution of Binary Star Periods'*. ApJ 555, 945–949.

Krumholz, M. R., Tan, J. C., 2007. *'Slow Star Formation in Dense Gas: Evidence and Implications'*. ApJ 654, 304–315.

Kundurthy, P., Meyer, M. R., Robberto, M., Beckwith, S. V. W., Herbst, T., 2006. *'Mid-Infrared Observations of T Tauri Stars: Probing the Star-Disk Connection in Rotational Evolution'*. AJ 132, 2469–2477.

Kusaka, T., Nakano, T., Hayashi, C., 1970. *'Growth of Solid Particles in the Primordial Solar Nebula'*. Progress of Theoretical Physics 44, 1580–1595.

Lada, C. J., 1987. *'Star formation - From OB associations to protostars'*. In: M. Peimbert & J. Jugaku (Ed.), Star Forming Regions, Volume 115 of *IAU Symposium*, pp. 1–17.

Lada, C. J., 2006. *'Stellar Multiplicity and the Initial Mass Function: Most Stars Are Single'*. ApJL 640, L63–L66.

Lada, C. J., Muench, A. A., Haisch, K. E., Jr., Lada, E. A., Alves, J. F., Tollestrup, E. V., Willner, S. P., 2000. *'Infrared L-Band Observations of the Trapezium Cluster: A Census of Circumstellar Disks and Candidate Protostars'*. AJ 120, 3162–3176.

Lafrenière, D., Jayawardhana, R., van Kerkwijk, M. H., 2008. *'Direct Imaging and Spectroscopy of a Planetary-Mass Candidate Companion to a Young Solar Analog'*. ApJL 689, L153–L156.

Larson, R. B., 1969. *'Numerical calculations of the dynamics of collapsing proto-star'*. MNRAS 145, 271–+.

Larson, R. B., 1972. *'The Collapse of a Rotating Cloud'*. MNRAS 156, 437–458.

Larson, R. B., 1981. *'Turbulence and star formation in molecular clouds'*. MNRAS 194, 809–826.

Larson, R. B., 2002. *'The role of tidal interactions in star formation'*. MNRAS 332, 155–164.

Larwood, J. D., Nelson, R. P., Papaloizou, J. C. B., Terquem, C., 1996. *'The tidally induced warping, precession and truncation of accretion discs in binary systems: three-dimensional simulations'*. MNRAS 282, 597–613.

Lee, C. W., Myers, P. C., 1999. *'A Catalog of Optically Selected Cores'*. ApJS 123, 233–250.

Leinert, C., Zinnecker, H., Weitzel, N., Christou, J., Ridgway, S. T., Jameson, R., Haas, M., Lenzen, R., 1993. *'A systematic approach for young binaries in Taurus'*. A&A 278, 129–149.

Lithwick, Y., Naoz, S., 2011. *'The Eccentric Kozai Mechanism for a Test Particle'*. ApJ 742, 94.

Lodato, G., 2008. *'Classical disc physics'*. NewAR 52, 21–41.

Lodato, G., Meru, F., Clarke, C. J., Rice, W. K. M., 2007. *'The role of the energy equation in the fragmentation of protostellar discs during stellar encounters'*. MNRAS 374, 590–598.

Low, C., Lynden-Bell, D., 1976. *'The minimum Jeans mass or when fragmentation must stop'*. MNRAS 176, 367–390.

Lucy, L. B., 1977. *'A numerical approach to the testing of the fission hypothesis'*. AJ 82, 1013–1024.

Lynden-Bell, D., Pringle, J. E., 1974. *'The evolution of viscous discs and the origin of the nebular variables.'* MNRAS 168, 603–637.

Machida, M. N., Inutsuka, S.-i., Matsumoto, T., 2010. *'Formation Process of the Circumstellar Disk: Long-term Simulations in the Main Accretion Phase of Star Formation'*. ApJ 724, 1006–1020.

Machida, M. N., Matsumoto, T., 2011. *'The origin and formation of the circumstellar disc'*. MNRAS 413, 2767–2784.

Machida, M. N., Tomisaka, K., Matsumoto, T., 2004. *'First MHD simulation of collapse and fragmentation of magnetized molecular cloud cores'*. MNRAS 348, L1–L5.

Masunaga, H., Inutsuka, S.-i., 2000. *'A Radiation Hydrodynamic Model for Protostellar Collapse. II. The Second Collapse and the Birth of a Protostar'*. ApJ 531, 350–365.

Masunaga, H., Miyama, S. M., Inutsuka, S.-I., 1998. *'A Radiation Hydrodynamic Model for Protostellar Collapse. I. The First Collapse'*. ApJ 495, 346.

Mathews, J. H., Fink, K. K., 2004. *'Numerical Methods Using Matlab: 4th Edition'*. Prentice Hall.

Mathieu, R. D., 1994. *'Pre-Main-Sequence Binary Stars'*. ARA&A 32, 465–530.

Mayer, L., Lufkin, G., Quinn, T., Wadsley, J., 2007. *'Fragmentation of Gravitationally Unstable Gaseous Protoplanetary Disks with Radiative Transfer'*. ApJL 661, L77–L80.

Mayer, L., Quinn, T., Wadsley, J., Stadel, J., 2002. *'Formation of Giant Planets by Fragmentation of Protoplanetary Disks'*. Science 298, 1756–1759.

Mayor, M., Duquennoy, A., Halbwachs, J.-L., Mermilliod, J.-C., 1992. *'CORAVEL Surveys to Study Binaries of Different Masses and Ages'*. In: H. A. McAlister & W. I. Hartkopf (Ed.), IAU Colloq. 135: Complementary Approaches to Double and Multiple Star Research, Volume 32 of *Astronomical Society of the Pacific Conference Series*, pp. 73.

McCaughrean, M. J., O'dell, C. R., 1996. *'Direct Imaging of Circumstellar Disks in the Orion Nebula'*. AJ 111, 1977.

McLaughlin, D. B., 1924. *'Some results of a spectrographic study of the Algol system.'* ApJ 60, 22–31.

McMillan, P. J., 2011. *'Mass models of the Milky Way'*. MNRAS 414, 2446–2457.

Mestel, L., Spitzer, L., Jr., 1956. *'Star formation in magnetic dust clouds'*. MNRAS 116, 503.

Metchev, S. A., Hillenbrand, L. A., 2009. *'The Palomar/Keck Adaptive Optics Survey of Young Solar Analogs: Evidence for a Universal Companion Mass Function'*. ApJS 181, 62–109.

Mizuno, H., 1980. *'Formation of the Giant Planets'*. Progress of Theoretical Physics 64, 544–557.

Moeckel, N., Bally, J., 2007. *'Capture-formed Binaries via Encounters with Massive Protostars'*. ApJ 656, 275–286.

Molinari, S., et al., 2010. *'Clouds, filaments, and protostars: The Herschel Hi-GAL Milky Way'*. A&A 518, L100.

Monaghan, J. J., 1992. *'Smoothed particle hydrodynamics'*. ARA&A 30, 543–574.

Monaghan, J. J., 1997. *'SPH and Riemann Solvers'*. Journal of Computational Physics 136, 298–307.

Monaghan, J. J., 2005. *'Smoothed particle hydrodynamics'*. Reports on Progress in Physics 68, 1703–1759.

Monaghan, J. J., Lattanzio, J. C., 1985. *'A refined particle method for astrophysical problems'*. A&A 149, 135–143.

Monin, J.-L., Clarke, C. J., Prato, L., McCabe, C., 2007. *'Disk Evolution in Young Binaries: From Observations to Theory'*. Protostars and Planets V, 395–409.

Monin, J.-L., Menard, F., Duchene, G., 1998. *'Using polarimetry to check rotation alignment in PMS binary stars. Principles of the method and first results'*. A&A 339, 113–122.

Monin, J.-L., Ménard, F., Peretto, N., 2006. *'Disc orientations in pre-main-sequence multiple systems. A study in southern star formation regions'*. A&A 446, 201–210.

Morris, J. P., Monaghan, J. J., 1997. *'A Switch to Reduce SPH Viscosity'*. Journal of Computational Physics 136, 41–50.

Motte, F., André, P., Ward-Thompson, D., Bontemps, S., 2001. *'A SCUBA survey of the NGC 2068/2071 protoclusters'*. A&A 372, L41–L44.

Mugrauer, M., Seifahrt, A., Neuhäuser, R., 2007. *'The multiplicity of planet host stars - new low-mass companions to planet host stars'*. MNRAS 378, 1328–1334.

Mundy, L. G., et al., 1996. *'Imaging the HL Tauri Disk at lambda = 2.7 Millimeters with the BIMA Array'*. ApJL 464, L169.

Myhill, E. A., Kaula, W. M., 1992. *'Numerical models for the collapse and fragmentation of centrally condensed molecular cloud cores'*. ApJ 386, 578–586.

Naoz, S., Farr, W. M., Lithwick, Y., Rasio, F. A., Teyssandier, J., 2011. *'Hot Jupiters from secular planet-planet interactions'*. Natur 473, 187–189.

Narita, N., Sato, B., Hirano, T., Tamura, M., 2009. *'First Evidence of a Retrograde Orbit of a Transiting Exoplanet HAT-P-7b'*. PASJ 61, L35–L40.

Natta, A., Grinin, V., Mannings, V., 2000. *'Properties and Evolution of Disks around Pre-Main-Sequence Stars of Intermediate Mass'*. Protostars and Planets IV, 559.

Natta, A., Testi, L., Neri, R., Shepherd, D. S., Wilner, D. J., 2004. *'A search for evolved dust in Herbig Ae stars'*. A&A 416, 179–186.

O'dell, C. R., Wen, Z., 1994. *'Postrefurbishment mission Hubble Space Telescope images of the core of the Orion Nebula: Proplyds, Herbig-Haro objects, and measurements of a circumstellar disk'*. ApJ 436, 194–202.

O'Shea, B. W., Nagamine, K., Springel, V., Hernquist, L., Norman, M. L., 2005. *'Comparing AMR and SPH Cosmological Simulations. I. Dark Matter and Adiabatic Simulations'*. ApJS 160, 1–27.

Osterloh, M., Beckwith, S. V. W., 1995. *'Millimeter-wave continuum measurements of young stars'*. ApJ 439, 288–302.

Padgett, D. L., et al., 2006. *'The SPITZER c2d Survey of Weak-Line T Tauri Stars. I. Initial Results'*. ApJ 645, 1283–1296.

Padgett, D. L., Strom, S. E., Ghez, A., 1997. *'Hubble Space Telescope WFPC2 Observations of the Binary Fraction among Pre-Main-Sequence Cluster Stars in Orion'*. ApJ 477, 705.

Padoan, P., Nordlund, Å., 2002. *'The Stellar Initial Mass Function from Turbulent Fragmentation'*. ApJ 576, 870–879.

Papaloizou, J. C. B., Terquem, C., 1995. *'On the dynamics of tilted discs around young stars'*. MNRAS 274, 987–1001.

Parker, R. J., Goodwin, S. P., 2009. *'The role of cluster evolution in disrupting planetary systems and discs: the Kozai mechanism'*. MNRAS 397, 1041–1045.

Parker, R. J., Goodwin, S. P., 2012. *'The same, but different: Stochasticity in binary destruction'*. ArXiv e-prints.

Patience, J., Ghez, A. M., Reid, I. N., Matthews, K., 2002. *'A High Angular Resolution Multiplicity Survey of the Open Clusters α Persei and Praesepe'*. AJ 123, 1570–1602.

Persi, P., et al., 2000. *'ISOCAM observations of the Chamaeleon I dark cloud'*. A&A 357, 219–224.

Petr, M. G., Coudé du Foresto, V., Beckwith, S. V. W., Richichi, A., McCaughrean, M. J., 1998. *'Binary Stars in the Orion Trapezium Cluster Core'*. ApJ 500, 825.

Pfalzner, S., Gibbon, P., 1996. *'Many-Body Tree Methods in Physics'*.

Podolak, M., 2003. *'The contribution of small grains to the opacity of protoplanetary atmospheres'*. Icarus 165, 428–437.

Pollack, J. B., Hubickyj, O., Bodenheimer, P., Lissauer, J. J., Podolak, M., Greenzweig, Y., 1996. *'Formation of the Giant Planets by Concurrent Accretion of Solids and Gas'*. Icarus 124, 62–85.

Pont, F., et al., 2010. *'The spin-orbit angle of the transiting hot Jupiter CoRoT-1b'*. MNRAS 402, L1–L5.

Pont, F., et al., 2009. *'Spin-orbit misalignment in the HD 80606 planetary system'*. A&A 502, 695–703.

Prato, L., Greene, T. P., Simon, M., 2003. *'Astrophysics of Young Star Binaries'*. ApJ 584, 853–874.

Price, D. J., 2004. *'Magnetic fields in Astrophysics'*. Ph. D. thesis, Institute of Astronomy, Madingley Rd, Cambridge, CB2 0HA, UK.

Price, D. J., 2007. *'splash: An Interactive Visualisation Tool for Smoothed Particle Hydrodynamics Simulations'*. PASA 24, 159–173.

Price, D. J., 2008. *'Modelling discontinuities and Kelvin Helmholtz instabilities in SPH'*. Journal of Computational Physics 227, 10040–10057.

Price, D. J., 2010. *'Smoothed Particle Hydrodynamics and Magnetohydrodynamics'*. ArXiv e-prints.

Price, D. J., Monaghan, J. J., 2004. *'Smoothed Particle Magnetohydrodynamics - II. Variational principles and variable smoothing-length terms'*. MNRAS 348, 139–152.

Pringle, J. E., 1981. *'Accretion discs in astrophysics'*. ARA&A 19, 137–162.

Prosser, C. F., Stauffer, J. R., Hartmann, L., Soderblom, D. R., Jones, B. F., Werner, M. W., McCaughrean, M. J., 1994. *'HST photometry of the trapezium cluster'*. ApJ 421, 517–541.

Rafikov, R. R., 2005. *'Can Giant Planets Form by Direct Gravitational Instability?'* ApJL 621, L69–L72.

Rafikov, R. R., 2007. *'Convective Cooling and Fragmentation of Gravitationally Unstable Disks'.* ApJ 662, 642–650.

Raghavan, D., McAlister, H. A., Henry, T. J., Latham, D. W., Marcy, G. W., Mason, B. D., Gies, D. R., White, R. J., ten Brummelaar, T. A., 2010. *'A Survey of Stellar Families: Multiplicity of Solar-type Stars'.* ApJS 190, 1–42.

Ratzka, T., Köhler, R., Leinert, C., 2005. *'A multiplicity survey of the ρ Ophiuchi molecular clouds'.* A&A 437, 611–626.

Ratzka, T., Schegerer, A. A., Leinert, C., Ábrahám, P., Henning, T., Herbst, T. M., Köhler, R., Wolf, S., Zinnecker, H., 2009. *'Spatially resolved mid-infrared observations of the triple system T Tauri'.* A&A 502, 623–646.

Rawiraswattana, K., Lomax, O., Goodwin, S. P., 2012. *'Collisions in young triple systems'.* MNRAS 419, 2025–2030.

Reipurth, B., 2000. *'Disintegrating Multiple Systems in Early Stellar Evolution'.* AJ 120, 3177–3191.

Reipurth, B., Guimarães, M. M., Connelley, M. S., Bally, J., 2007. *'Visual Binaries in the Orion Nebula Cluster'.* AJ 134, 2272–2285.

Ressler, M. E., Barsony, M., 2001. *'A Luminous Infrared Companion in the Young Triple System WL 20'.* AJ 121, 1098–1110.

Rice, W. K. M., Armitage, P. J., Bate, M. R., Bonnell, I. A., 2003. *'The effect of cooling on the global stability of self-gravitating protoplanetary discs'.* MNRAS 339, 1025–1030.

Rice, W. K. M., Lodato, G., Armitage, P. J., 2005. *'Investigating fragmentation conditions in self-gravitating accretion discs'.* MNRAS 364, L56–L60.

Rice, W. K. M., Mayo, J. H., Armitage, P. J., 2010. *'The role of disc self-gravity in the formation of protostars and protostellar discs'.* MNRAS 402, 1740–1749.

Roccatagliata, V., Ratzka, T., Henning, T., Wolf, S., Leinert, C., Bouwman, J., 2011. *'Multi-wavelength observations of the young binary system Haro 6-10: The case of misaligned discs'.* A&A 534, A33.

Rossiter, R. A., 1924. *'On the detection of an effect of rotation during eclipse in the velocity of the brigher component of beta Lyrae, and on the constancy of velocity of this system.'* ApJ 60, 15–21.

Rosswog, S., 2009. *'Astrophysical smooth particle hydrodynamics'.* NewAR 53, 78–104.

Sargent, A. I., Beckwith, S., 1987. *'Kinematics of the circumstellar gas of HL Tauri and R Monocerotis'.* ApJ 323, 294–305.

Scally, A., Clarke, C., McCaughrean, M. J., 1999. *'Wide binaries in the Orion nebula cluster'.* MNRAS 306, 253–256.

Scholz, A., Jayawardhana, R., Wood, K., 2006. *'Exploring Brown Dwarf Disks: A 1.3 mm Survey in Taurus'.* ApJ 645, 1498–1508.

Shakura, N. I., Sunyaev, R. A., 1973. *'Black holes in binary systems. Observational appearance.'* A&A 24, 337–355.

Shu, F., Najita, J., Ostriker, E., Wilkin, F., Ruden, S., Lizano, S., 1994. *'Magnetocentrifugally driven flows from young stars and disks. 1: A generalized model'.* ApJ 429, 781–796.

Shu, F. H., Adams, F. C., Lizano, S., 1987. *'Star formation in molecular clouds - Observation and theory'.* ARA&A 25, 23–81.

Shu, F. H., Tremaine, S., Adams, F. C., Ruden, S. P., 1990. *'Sling amplification and eccentric gravitational instabilities in gaseous disks'.* ApJ 358, 495–514.

Sicilia-Aguilar, A., Hartmann, L. W., Hernández, J., Briceño, C., Calvet, N., 2005. *'Cepheus OB2: Disk Evolution and Accretion at 3-10 Myr'.* AJ 130, 188–209.

Simon, M., Close, L. M., Beck, T. L., 1999. *'Adaptive Optics Imaging of the Orion Trapezium Cluster'.* AJ 117, 1375–1386.

Simon, M., et al., 1995. *'A lunar occultation and direct imaging survey of multiplicity in the Ophiuchus and Taurus star-forming regions'.* ApJ 443, 625–637.

Simon, M., Prato, L., 1995. *'Disk Dissipation in Single and Binary Young Star Systems in Taurus'.* ApJ 450, 824.

Skemer, A. J., Close, L. M., Hinz, P. M., Hoffmann, W. F., Kenworthy, M. A., Miller, D. L., 2008. *'Evidence for Misaligned Disks in the T Tauri Triple System: 10 μm Superresolution with MMTAO and Markov Chains'.* ApJ 676, 1082–1087.

Skrutskie, M. F., Dutkevitch, D., Strom, S. E., Edwards, S., Strom, K. M., Shure, M. A., 1990. *'A sensitive 10-micron search for emission arising from circumstellar dust associated with solar-type pre-main-sequence stars'.* AJ 99, 1187–1195.

Springel, V., Hernquist, L., 2002. *'Cosmological smoothed particle hydrodynamics simulations: the entropy equation'.* MNRAS 333, 649–664.

Stamatellos, D., Maury, A., Whitworth, A., André, P., 2011. *'The lower limits of disc fragmentation and the prospects for observing fragmenting discs'.* MNRAS 413, 1787–1796.

Stamatellos, D., Whitworth, A. P., 2008. *'Can giant planets form by gravitational fragmentation of discs?.'* A&A 480, 879–887.

Stamatellos, D., Whitworth, A. P., 2009a. *'The properties of brown dwarfs and low-mass hydrogen-burning stars formed by disc fragmentation'*. MNRAS 392, 413–427.

Stamatellos, D., Whitworth, A. P., 2009b. *'The role of thermodynamics in disc fragmentation'*. MNRAS 400, 1563–1573.

Stamatellos, D., Whitworth, A. P., Bisbas, T., Goodwin, S., 2007. *'Radiative transfer and the energy equation in SPH simulations of star formation'*. A&A 475, 37–49.

Stapelfeldt, K. R., Krist, J. E., Menard, F., Bouvier, J., Padgett, D. L., Burrows, C. J., 1998. *'An Edge-On Circumstellar Disk in the Young Binary System HK Tauri'*. ApJL 502, L65+.

Sterzik, M. F., Durisen, R. H., 1998. *'The dynamic decay of young few-body stellar systems. I. The effect of a mass spectrum for $N = 3$, 4, and 5'*. A&A 339, 95–112.

Strom, K. M., Strom, S. E., Edwards, S., Cabrit, S., Skrutskie, M. F., 1989. *'Circumstellar material associated with solar-type pre-main-sequence stars - A possible constraint on the timescale for planet building'*. AJ 97, 1451–1470.

Tan, J. C., Krumholz, M. R., McKee, C. F., 2006. *'Equilibrium Star Cluster Formation'*. ApJL 641, L121–L124.

Terquem, C., Eislöffel, J., Papaloizou, J. C. B., Nelson, R. P., 1999. *'Precession of Collimated Outflows from Young Stellar Objects'*. ApJL 512, L131–L134.

Testi, L., Natta, A., Shepherd, D. S., Wilner, D. J., 2001. *'Constraints on Properties of the Protoplanetary Disks around UX Orionis and CQ Tauri'*. ApJ 554, 1087–1094.

Thies, I., Kroupa, P., Goodwin, S. P., Stamatellos, D., Whitworth, A. P., 2010. *'Tidally Induced Brown Dwarf and Planet Formation in Circumstellar Disks'*. ApJ 717, 577–585.

Thomas, P. A., Couchman, H. M. P., 1992. *'Simulating the formation of a cluster of galaxies'*. MNRAS 257, 11–31.

Tohline, J. E., 2002. *'The Origin of Binary Stars'*. ARA&A 40, 349–385.

Tohline, J. E., Durisen, R. H., 2001. *'An Update on Binary Formation by Rotational Fission'*. In: H. Zinnecker & R. Mathieu (Ed.), The Formation of Binary Stars, Volume 200 of *IAU Symposium*, pp. 40.

Toomre, A., 1964. *'On the gravitational stability of a disk of stars'*. ApJ 139, 1217–1238.

Triaud, A. H. M. J., et al., 2010. *'Spin-orbit angle measurements for six southern transiting planets. New insights into the dynamical origins of hot Jupiters'*. A&A 524, A25+.

Tscharnuter, W., 1975. *'On the Collapse of Rotating Protostars'*. A&A 39, 207–212.

Tscharnuter, W. M., Schönke, J., Gail, H.-P., Trieloff, M., Lüttjohann, E., 2009. *'Protostellar collapse: rotation and disk formation'*. A&A 504, 109–113.

Uchida, Y., Shibata, K., 1984. *'Magnetically buffered accretion to a young star and the formation of bipolar flows'*. PASJ 36, 105–118.

Uchida, Y., Shibata, K., 1985. *'Magnetodynamical acceleration of CO and optical bipolar flows from the region of star formation'*. PASJ 37, 515–535.

Uzpen, B., Kobulnicky, H. A., Kinemuchi, K., 2009. *'The Frequency of Warm Debris Disks and Transition Disks in a Complete Sample of Intermediate-Mass Glimpse Stars: Placing Constraints on Disk Lifetimes'*. AJ 137, 3329–3338.

van Altena, W. F., Lee, J. T., Lee, J.-F., Lu, P. K., Upgren, A. R., 1988. *'The velocity dispersion of the Orion Nebula cluster.'* AJ 95, 1744–1754.

Walch, S., Naab, T., Whitworth, A., Burkert, A., Gritschneder, M., 2010. *'Protostellar discs formed from turbulent cores'*. MNRAS 402, 2253–2263.

Ward, W. R., 1997. *'Protoplanet Migration by Nebula Tides'*. Icarus 126, 261–281.

Ward-Thompson, D., André, P., Crutcher, R., Johnstone, D., Onishi, T., Wilson, C., 2007. *'An Observational Perspective of Low-Mass Dense Cores II: Evolution Toward the Initial Mass Function'*. Protostars and Planets V, 33–46.

Ward-Thompson, D., Scott, P. F., Hills, R. E., Andre, P., 1994. *'A Submillimetre Continuum Survey of Pre Protostellar Cores'*. MNRAS 268, 276.

Watkins, S. J., Bhattal, A. S., Boffin, H. M. J., Francis, N., Whitworth, A. P., 1998a. *'Numerical simulations of protostellar encounters - II. Coplanar disc-disc encounters'*. MNRAS 300, 1205–1213.

Watkins, S. J., Bhattal, A. S., Boffin, H. M. J., Francis, N., Whitworth, A. P., 1998b. *'Numerical simulations of protostellar encounters - III. Non-coplanar disc-disc encounters'*. MNRAS 300, 1214–1224.

Weidenschilling, S. J., 1977a. *'Aerodynamics of solid bodies in the solar nebula'*. MNRAS 180, 57–70.

Weidenschilling, S. J., 1977b. *'The distribution of mass in the planetary system and solar nebula'*. Ap&SS 51, 153–158.

Weidenschilling, S. J., Cuzzi, J. N., 1993. *'Formation of planetesimals in the solar nebula'*. In: Levy, E. H., Lunine, J. I. (Eds.), Protostars and Planets III, pp. 1031–1060.

Weidenschilling, S. J., Spaute, D., Davis, D. R., Marzari, F., Ohtsuki, K., 1997. *'Accretional Evolution of a Planetesimal Swarm'*. Icarus 128, 429–455.

Weintraub, D. A., Sandell, G., Duncan, W. D., 1989. *'Submillimeter measurements of T Tauri and FU Orionis stars'*. ApJL 340, L69–L72.

Wetherill, G. W., Stewart, G. R., 1989. *'Accumulation of a swarm of small planetesimals'*. Icarus 77, 330–357.

White, R. J., Ghez, A. M., 2001. *'Observational Constraints on the Formation and Evolution of Binary Stars'*. ApJ 556, 265–295.

Whitworth, A. P., Stamatellos, D., 2006. *'The minimum mass for star formation, and the origin of binary brown dwarfs'*. A&A 458, 817–829.

Wilkins, D. R., Clarke, C. J., 2011. *'Testing the accuracy of radiative cooling approximations in SPH simulations'*. ArXiv e-prints.

Williams, H. A., Tohline, J. E., 1988. *'Circumstellar ring formation in rapidly rotating protostars'*. ApJ 334, 449–464.

Williams, J. P., Blitz, L., McKee, C. F., 2000. *'The Structure and Evolution of Molecular Clouds: from Clumps to Cores to the IMF'*. Protostars and Planets IV, 97.

Williams, J. P., Cieza, L. A., 2011. *'Protoplanetary Disks and Their Evolution'*. ARA&A 49, 67–117.

Winn, J. N., 2011. *'The Rossiter-McLaughlin effect for exoplanets'*. In: Sozzetti, A., Lattanzi, M. G., Boss, A. P. (Eds.), IAU Symposium, Volume 276 of *IAU Symposium*, pp. 230–237.

Winn, J. N., Fabrycky, D., Albrecht, S., Johnson, J. A., 2010. *'Hot Stars with Hot Jupiters Have High Obliquities'*. ApJL 718, L145–L149.

Winn, J. N., et al., 2009. *'On the Spin-Orbit Misalignment of the XO-3 Exoplanetary System'*. ApJ 700, 302–308.

Wolf, S., Stecklum, B., Henning, T., 2001. *'Pre-Main Sequence Binaries with Aligned Disks?'* In: Zinnecker, H., Mathieu, R. (Eds.), The Formation of Binary Stars, Volume 200 of *IAU Symposium*, pp. 295.

Woodward, J. W., Tohline, J. E., Hachisu, I., 1994. *'The stability of thick, self-gravitating disks in protostellar systems'*. ApJ 420, 247–267.

Wu, Y., Murray, N., 2003. *'Planet Migration and Binary Companions: The Case of HD 80606b'*. ApJ 589, 605–614.

Wuchterl, G., Guillot, T., Lissauer, J. J., 2000. *'Giant Planet Formation'*. Protostars and Planets IV, 1081.

Yorke, H. W., Sonnhalter, C., 2002. *'On the Formation of Massive Stars'*. ApJ 569, 846–862.

Yu, Q., Tremaine, S., 2001. *'Resonant Capture by Inward-migrating Planets'*. AJ 121, 1736–1740.

Zinnecker, H., Wilking, B. A., 1992. *'Infrared companions: clues to binary star formation.'* In: Duquennoy, A., Mayor, M. (Eds.), Binaries as Tracers of Star Formation, pp. 269–277.